ANALYSIS AND SIMULATION OF
HYPERVELOCITY GOUGING IMPACTS

DISSERTATION

John D. Cinnamon, Major, USAF

AFIT/DS/ENY/06-01

DEPARTMENT OF THE AIR FORCE
AIR UNIVERSITY

AIR FORCE INSTITUTE OF TECHNOLOGY

Wright-Patterson Air Force Base, Ohio

Analysis and Simulation of Hypervelocity Gouging Impacts

DISSERTATION

Presented to the Faculty

Department of Aeronautics and Astronautics

Graduate School of Engineering and Management

Air Force Institute of Technology

Air University

Air Education and Training Command

In Partial Fulfillment of the Requirements for the

Degree of Doctor of Philosophy

John D. Cinnamon, B.S.E., M.S.E., P.E.
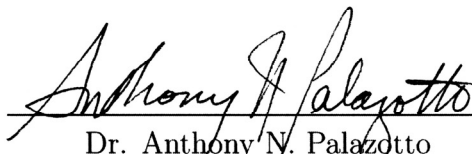
Major, USAF

June 2006

ANALYSIS AND SIMULATION OF HYPERVELOCITY GOUGING IMPACTS
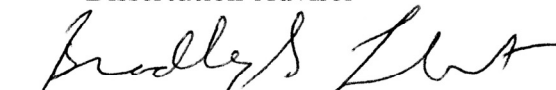
John D. Cinnamon, B.S.E., M.S.E., P.E.

Major, USAF

Approved:

_____   _24 May 06_
Dr. Anthony N. Palazotto   date
Dissertation Advisor
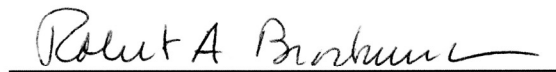
_____   _5/24/06_
Dr. Bradley S. Liebst   date
Dean's Representative

_____   _24 May 06_
Dr. William P. Baker   date
Committee Member

_____   _24 May 2006_
Dr. Robert A. Brockman   date
Committee Member

_____   _24 May 06_
Dr. Michael D. Hooser   date
Committee Member

Accepted:

_____   _31 May 06_
M. U. Thomas   Date
Dean, Graduate School of Engineering and Management

AFIT/DS/ENY/06-01

Abstract

Hypervelocity impact is an area of extreme interest in the research community. The U.S. Air Force has a test facility at Holloman Air Force Base which specializes in hypervelocity impact testing. This Holloman AFB High Speed Test Track (HHSTT) is currently working toward a test vehicle speed above Mach 10. As the sled's speed has increased to Mach 8.5, a material interaction develops which causes "gouging" in the rails or the sled's "shoes" and this can result in catastrophic failure.

Previous efforts in investigating this event have resulted in a choice of the most suitable computer code, (CTH), and a model of the shoe/rail interaction. However, the dynamic stress models of the specific materials were not developed and the model was not validated against experimentation.

In this work, a summary of past and present research efforts, as well as the theoretical foundation of this field of study, are presented. A characterization of gouging is developed from an examination of a gouged rail from the HHSTT. A thermodynamic history of gouging is determined from the experimental evidence and an extensive study is performed that determines the specific material models.

The developed material dynamic strength models are validated utilizing several experimental tests which are successfully simulated using CTH. Additionally, a penetration theory is developed which provides insight into the gouging problem using an analytic approach that does not require the use of computationally intensive codes.

Based on the detailed examination of the materials and the validation of the material models within CTH, an evaluation of the HHSTT gouging phenomenon is performed. These simulations of the gouging problem replicate the experimentally observed characteristics and lead to recommendations to mitigate the occurrence of hypervelocity gouging.

"Fear not, I am with you; be not dismayed; I am your God.
I will strengthen you, and help you, and uphold you with my right hand..."

Isaiah, 41:10

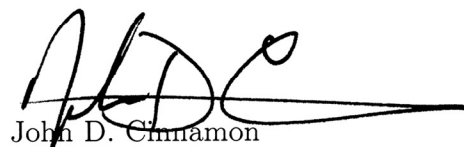*To my wife and children, for your love & support*

John D. Cinnamon

Acknowledgements

Table of Contents

List of Figures

xiv

List of Tables

List of Symbols

xxiv

List of Abbreviations

Analysis and Simulation of
Hypervelocity Gouging Impacts

I. Hypervelocity Gouging Problem Overview

Gouging resulting from hypervelocity impact is an area of interest for the United States Air Force (USAF) and the Department of Defense (DoD). The Holloman High Speed Test Track (HHSTT) serves as the premier USAF facility conducting hypervelocity impact tests. The Air Force Research Laboratory (AFRL) and the Air Force Office of Scientific Research (AFOSR) are interested in increasing the capability of this facility up to the approximately Mach 10. Indeed, this research is being conducted under AFOSR sponsorship.

The HHSTT rocket sled system appears in Figure 1.1. This particular sled is the 192-pound Missile Defense Agency payload tested on April 29, 2003. This fully instrumented test run served to validate the HHSTT hypersonic capabilities and also set the World Land Speed Record of Mach 8.5 (6,416 mph or 9410 fps). The rocket sled in Figure 1.1 rides along the standard railroad rails constructed from 1080 steel on "shoes" or "slippers" fabricated of VascoMax 300 steel. Figure 1.2 is a schematic of the interface between the sled's shoes and the rail. The shoe is formed to wrap around the rail head, leaving a very small gap (on the order of one-half centimeter). The nominal sled configuration is the one in Figure 1.1. This study will be limited to this geometry.

The goal of the HHSTT's current efforts is to increase their velocity capability to approximately Mach 10 ($\sim$10000 fps or $\sim$3 km/s). However, at velocities of approximately 1.5 km/s a phenomenon known as "gouging" occurs. This phenomenon is characterized by either damage (i.e. material removal and/or melting) to the rail and/or shoe, or catastrophic failure of the rocket sled system due to material interaction between the rail and the shoe. As mentioned previously, the shoes are machined
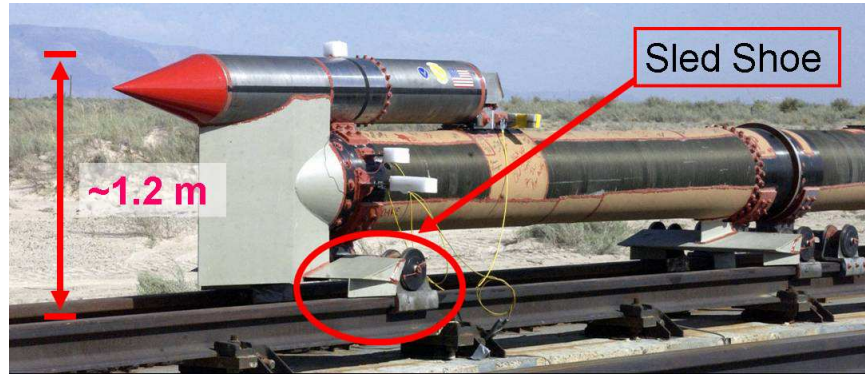
Figure 1.1: **Rocket Sled System at the HHSTT.**
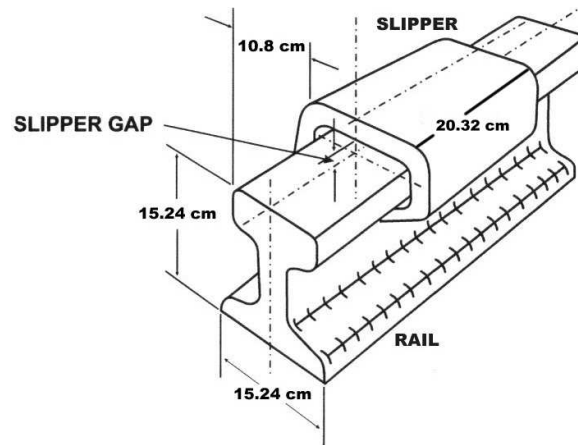
Figure 1.2: **Rocket Sled Shoe-Rail Interface.**

to allow a slight gap between their structure and the rail head. This allows the vehicle to maintain a limited "free-flight" condition as the vehicle accelerates down the track. The consequence of this free flight condition is that the shoe can roll, pitch, or yaw with relation to the rail during the test and this results in intermittent contact between the shoe and the rail. This contact typically creates zones of material removal observed on the rail. Due to the method of sled system braking, the shoes are dramatically altered in the slow down process and therefore are not typically suitable for post-test analysis. While non-catastrophic gouging is costly (in terms of rail repair), it does not necessarily adversely affect the test mission. However, some gouging events either destroy the rail and cause a sled crash, or multiple gouges deteriorate the sled's shoes to the point of catastrophic failure. It is because of this fact that the

mitigation of gouging is a primary concern. Figures 1.3 and 1.4 are of a total rail failure and catastrophic sled failure respectively.

Figure 1.3:   **Typical Total Rail Failure.**

Figure 1.4:   **Catastrophic Rocket Sled Failure.**

A typical gouge in the rail is shown in Figure 1.5. This particular section of rail is coated with an iron-oxide paint developed to mitigate gouging. The shoe section also appears on the rail to further illustrate the geometry. A schematic of a typical gouge is presented in Figure 1.6.

In order to understand the initiation of the gouging phenomenon and hypervelocity speeds, and its mitigation, we will examine the following from both past and current research efforts in the field. Upon establishing this foundation, a detailed examination of the gouging phenomenon will be undertaken, with a metallurgical study of the gouge shown in Figure 1.5. This study will indicate a verifiable thermodynamic history which will aid our understanding of the gouging event. In order to modify past modeling efforts to maximize accuracy, a study which determines the material
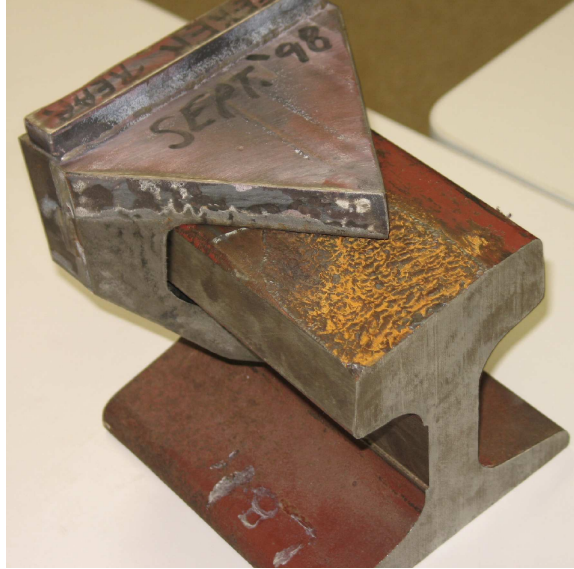
Figure 1.5:   **Typical Rail and Shoe Gouge.**
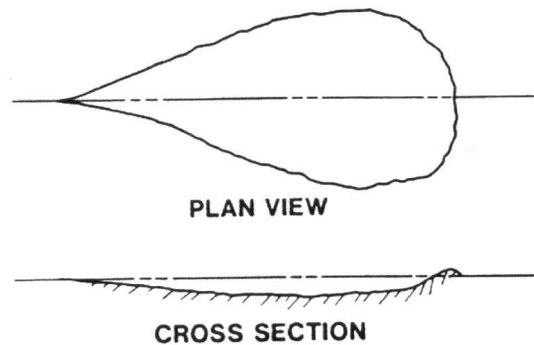
Figure 1.6:   **Schematic of Typical Rail Gouge.**

constitutive models for VascoMax 300 and 1080 steel is presented. These material flow models are then validated using impact experiments and CTH simulations of the experiments. Additionally, a theoretical penetration model is created that indicates the impact energy necessary to initiate gouging, without the need for computationally intensive CTH simulations.

Based on the extensive experimentation with the materials in the HHSTT gouging problem, a validated CTH model of the gouging scenario is conducted. These simulations suggest the mechanism for gouge initiation and design recommendations are made which will improve the probability of success for the HHSTT's goal of achieving

1-4

sled velocities on the order of Mach 10. An greater understanding of the initiation and mitigation of gouging is thereby attained.

II. Previous Research in the Hypervelocity Gouging Phenomenon

Hypervelocity Gouging research has been an area of interest for many years. In fact, this author is following the fruitful work of Laird [68] and Szmerekovsky [108] under AFOSR sponsorship. This chapter will trace the previous research in this field by summarizing the work of Szmerekovsky [108] in the description of this history and providing a summary of his contribution to this research effort. To begin, a brief description of the gouging phenomenon is presented.

2.1 Description of Gouging

In this AFOSR effort to examine gouging, Laird [68] presented the definition of gouging as:

> Gouging is a failure mode found in metals undergoing hypervelocity sliding contact. When inertial forces are so great that the materials exhibit fluid like behavior, shock induced pressure creates a region of plasticity under the location of impact. Tangential motion of one body with respect to the other deforms or shears material at these points and results in deformation of the parallel surfaces that impinge on each other in a continuous interaction. Once this interaction region grows large enough to shear the surface of one of the materials from the bulk material, a gouge has been formed. Continuous interaction of the materials in the region of the gouge will cause the gouge to grow further until the materials are no longer in contact. [68]

This definition has several key aspects that delineate gouging from other types of material deformation. Laird found that the material interaction was characterized by the creating of material "jets." These jets contained thin plastic deformations at high strain rates. These jets would would form from both sections of bulk material and the event would proceed with the material jets mixing. In the HHSTT application, this gouging would involve material from the shoe and the rail. Recall that Chapter I described the catastrophic impact that gouging can have on the sled system. A single gouge can either be insignificant and thereby not cause sled failure and only require rail repair, or it can be large enough to be catastrophic to the test sled run. The

prediction of the type of gouging or severity of the effect remains highly problematic. This interaction is depicted in an early numerical simulation result in Figure 2.1.
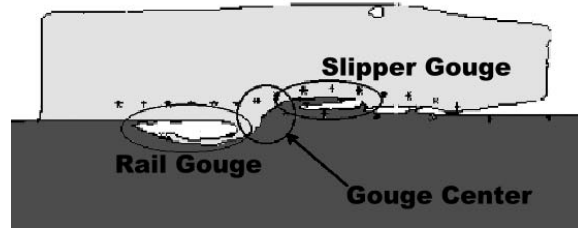
Figure 2.1:   **Typical Material Gouging Interaction.**

Laird also presented a nominal sequence of events in gouge development. In numerical simulations, gouging was preceded by a hump of material being created plastically from the bulk material. This hump precipitated material flow in both the shoe and the rail, led to jetting, and eventual material mixing. This can be seen graphically in Figure 2.2.
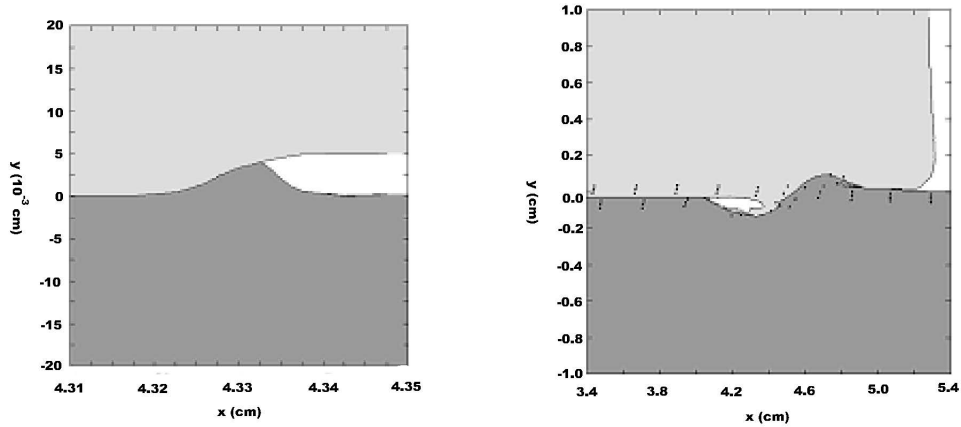
Figure 2.2:   **Gouge Initiation and Development.**

This type of material deformation does not occur at low velocities. The exact definition of hypervelocity and therefore the exact description of when this gouging phenomenon might occur is not a precise endeavor. However, as Laird reports, a widely accepted estimate is as the impact velocity approaches the order of magnitude of the elastic wave speed of the specific material gouging becomes more probable. This elastic wave speed, c_o, is defined as:

Table 2.1: Elastic Wave Speed for VascoMax 300 and 1080 Steel.

Material	E	ρ	c_o
VascoMax 300	190 GPa	8.00 g/cm^3	4.87 km/s
1080 Steel	205 GPa	7.85 g/cm^3	5.11 km/s

$$c_o = \sqrt{\frac{E}{\rho}} \qquad (2.1)$$

where E is the elastic modulus (which is the linear elastic slope of the equivalent uniaxial stress-strain (σ - ε) curve of the material) and ρ is the density of the material. Applying this relationship to the manufacturer reported values (Allvac [3] in the case of VascoMax and US Steel [117] for 1080) for both E and ρ for VascoMax 300 and 1080 steel results in Table 2.1.

Based on these calculations, we would expect gouging to start to occur as the impact speed became greater than 1 km/s. This is, in fact, the velocity range in which the problem begins. This will be discussed in detail later in this chapter.

The high stress concentration present in these hypervelocity impacts leads us to modify equation 2.1 to account for the plasticity of the material in this manner:

$$c = \sqrt{\frac{\frac{\partial \sigma}{\partial \varepsilon}}{\rho}} \qquad (2.2)$$

where c is the plastic wave speed and $\frac{\partial \sigma}{\partial \varepsilon}$ is the local slope of the stress-strain curve. Equation 2.2 becomes significant as the material deforms plastically and indicates that the creation and propagation of shock waves becomes significant [108].

Another depiction of the gouging event was proposed by Szmerekovsky [108] in Figure 2.3 in which:

- Plastic displacement must create a steep amplitude above or below the datum sliding line.

- For a gouge to develop, a relative velocity with respect to the bulk of the displacement must form at the portion of furthest penetration.

- The portion of furthest penetration with a relative velocity is called the boundary layer portion of the plastic displacement.

- The bulk of the displacement closest to the slide line is called the sub layer portion of the penetrating plastic displacement. [108]
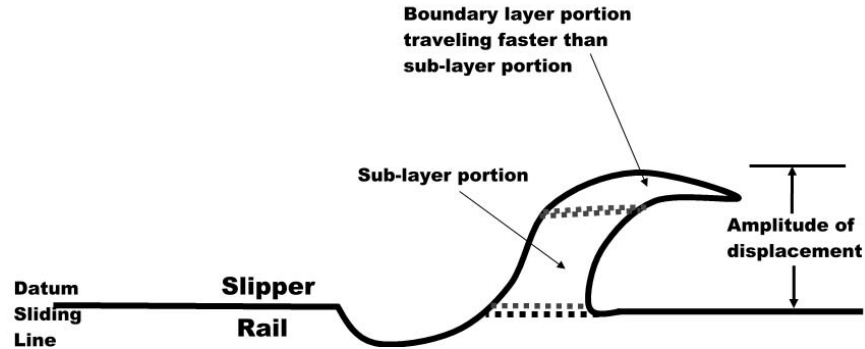
Figure 2.3:   **Depiction of Material Jetting.**

High energy impact problems are therefore concerned with deformations that lead to the generation of both elastic and plastic waves. The plastic waves are created when the stresses present exceed the material yield strength. Beyond the elastic limit, the stress-strain behavior becomes very nonlinear and must be described by the strength model that accounts for this nonlinearity. The choice of constitutive model that describes this relationship becomes critical. Complicating the analysis further is the fact that the rapid deformations lead to high strain rates and possible shock wave creation. Additionally, the description of a material failure criteria also is central to understanding how the impact event will unfold. As mentioned previously, the thermodynamics of the deforming material must also be considered.

In a high energy, temperature, and strain rate deformation, the equation of state (EOS) relationships of the material may dominate the solution. In the EOS, the pressure, density, and temperature relations of the material are defined. These relationships become necessary in the solution of the impact problem and provide the required additional equations that are coupled to the conservation equations to formulate the impact problem. The EOS relationships have the capability to model

shock waves and fluid-like material behavior at high rates of deformation. They are central to numerical codes known as "hydrocodes" (see Zukas [128] and Anderson [4]).

As Laird [68] outlined in his definition of gouging, we are considering a high energy impact event in which shock physics and non-classical mechanics (such as non-linear strength and failure models) dominate. It is within this context that the following summary [108] of research in the field of hypervelocity impact phenomena is presented.

2.2 Previous Hypervelocity Gouging Research

Previous research in this field can be delineated into the following six focus areas [108]:

1. Test track observations and gouging tests.

2. Laboratory gouging tests.

3. Numerical modeling of gouging.

4. Aerodynamic sled analysis.

5. Load and failure analysis.

6. Methods for gouge mitigation.

2.2.1 Test Track Observations and Gouging Tests. One of the areas of examination in this field of hypervelocity gouging is the investigation of the test track runs and their resulting post-gouge structures. The gouging phenomenon has been present at the HHSTT for over 50 years. The effort to understand the initiation of gouging and to take actions to mitigate it has been ongoing for that long as well.

In the late 1960s and early 1970s, Gerstle [40–42] examined this effect using a monorail test sled at the Sandia National Laboratory. One of his focus areas was to define the kind of rail characteristic that would initiate gouging. The thought, at that time, was that rail roughness (uneven rail height, either at a rail section joint or in

the middle of a section) or debris on the rail (an asperity) would initiate the gouging process.

He found that gouges frequently occurred downstream from discontinuities in the rail surface (such as discrete rail section interfaces), but that three-dimensional, small radius (and thereby non-sharp), irregularities such as weld beads across the width of the rail did not cause gouging. This indicated that a discontinuity across the rail head would distribute the stress, cause uniform deformation, and prevent the development of a uniaxial strain condition. This condition would create a sharp wave front and would allow the formation of a shock wave (which is a plastic wave of uniaxial strain) [80]. The uniform deformation frustrates the shock wave formation by relaxing the stress wave created by high speed impact. Without this shock wave, the high pressure gradients required for plastic flow and gouging are prevented.

Gerstle also performed a metallurgical study on the damaged rail section from his testing and discovered that the gouges had a surface layer of 304 stainless steel (sled shoe material used in his tests) deposited on top of martensitic 1080 steel (the rail material). The presence of martensite in the 1080 steel demonstrated that the temperatures were high enough to austenitize the steel and then the steel rapidly quenched. He references several studies in [42] that indicates similar heating and quenching has been shown in punch tests. He also observed that the rail material was severely strained and microcracked. Gerstle believed this to be evidence of catastrophic thermoplastic shear (or adiabatic slip). Thermoplastic shear "occurs when the local rate of temperature change is such that the resulting strength decrease exceeds the rate of increase in strength due to effects of strain hardening [42]." In other words, a large temperature change in a small localized area softens the material in that same area quicker than strain hardening strengthens it. It then becomes an area of local weakness in the material, and thus a likely spot of shear fracture. During adiabatic slip in steel, for example, local heat generation is large enough to austenitize the material, but the large mass of metal around that thin shear zone of the austenite material will quench it quickly enough to turn it into martensite.

Gerstle also found shoe material (stainless steel) in the examined rail section. This indicated material mixing that is a characteristic of gouging. He also reported that the non-gouged sections showed no damage, except for evidence of surface decarburization - indicated exposure to a high temperature source (over 800 K typically).

Gerstle also examined the variations in cracking within the gouged region. He found evidence of adiabatic shear bands that formed normal and parallel to the direction of sled motion. This indicated that stress waves were interacting within the plastically deformed material. He found the most significant fracture on the gouge centerline (in the deepest section of the gouge). Additionally, he found martensite within these fracture areas, indicating a high thermal load, followed by rapid quenching.

In his investigations, Gerstle found that the high energy impact event created a large thermodynamic event that allowed the material to experience phase change and rapid temperature variation. Additionally, the thermal energy imparted by the plasticity of the material may have been relieved by the creation of shear bands – which can be thought of as a thermal sink. Therefore, some of the energy in the event was absorbed by the material in this fashion.

Gerstle's work suggests that gouging is a thermodynamic event. The creation of shear bands is not necessarily an adiabatic process, but may involve heat transfer within the material. Shear band formation which leads to material failure also provides the impact event an internal method of heat absorbtion that needs to be investigated.

A summary of sled development and the associated problems with rail damage, gouging, and shoe wear was produced by Krupovage and Rasmussen [64] in 1982. They summarized research that has been done at Holloman AFB is various in-house reports. They identified gouging as being the result of impact between the shoe and the rail and that these impacts seemed to indicate a large bearing load. That is, the vibration of the sled as it travels down the rail results in a large compressive load on

the rail as the sled comes down from an oscillation. They note that efforts to reduce this vibration by controlling the aerodynamic forces had been somewhat successful. They also describe the fact that the shoe/rail interaction is one of constant wearing contact, as evidenced by "slipper fire." This slipper fire is a constant stream of bright effluents from the back end of the slipper as it travels downrange. They attributed this intense light/fire to aerodynamic heating of the shoe and rail and the oxidation of the eroding shoe and rail material (i.e. from wear and not necessarily gouging).

The authors proposed the following relationship for the rate of work developed by friction that could create this frictional heat:

$$\dot{w} = C_f N v \qquad (2.3)$$

where C_f is an empirical friction coefficient, N is the normal force, and v is the sled velocity. This equation assumes that the work is converted exclusively to frictional heat. Therefore, determination of the other parameters could provide an estimate of the energy acting as a heat input.

This extreme contact heat can cause the materials to melt. The authors, however, observed that melted metal acted more like an abrasive than as a lubricant. Because the concept of coating the rail to prevent gouging has been successfully implemented to some extent at the HHSTT, this discussion concerning the desirable properties of the coating becomes critical. If the liquid metals are abrasive and therefore increase the likelihood of damage, then the prevention of this melting is a goal of their effort.

In 1984, Krupovage [65] again examined rail gouging. He summarized numerous test sled runs with varying sled geometry, test conditions, and velocities. The largest gouge that he reported was one that measured 4 inches long, 3 inches wide, and .4 inches deep. Gouge location varied widely. Gouges were found at rail section interfaces and on the inside of the shoe surface. Some of the gouges contained shoe

material and, in some cases, copper that originated from an aerodynamic wedge fixed to the front of the shoe.

Krupovage also noted that at high speed (above 5000 fps) that sled material was shed from the forward section of the sleds. In these high speed runs the aerodynamic heating effect was also observed. From these facts, Krupovage concludes that gouging is a function of the high aerodynamic heating load, liberation of shoe and rail materials from high heat and oxidation (i.e. wear products from shoe and rail) and debris from either the deterioration of the sled components or an outside source. He argues that gouging is initiated from this debris (referred to as an asperity in other references) interacting inside the gap between the shoe and the rail. Krupovage did not believe that simple (vibratory) impact would be sufficient to cause gouging in itself. An important distinction is that his definition of debris would also include rail section interfaces and rail surface roughness as asperities.

Krupovage also reported more gouging in the sled coast phase (this is the phase in which the sled is no longer under propulsive acceleration). On many of these test runs, the sled enters a large helium bag at the terminal end of the run (where the target of the sled payload resides). In this environment, he found no material loss from aerodynamic heating. From these observations, Krupovage proposes that a dynamic model consisting of the shoe undergoing vibratory impact with the rail should be constructed to model this gouging phenomenon.

Krupovage's work points to the importance of the aerodynamic heating to this vibratory type impact problem. Additionally, his observations that gouging is initiated by an asperity of some kind is also key to describing this high energy event.

Barber and Bauer [8] compared the phenomenon of sliding contact at low, high, and hypervelocity (velocity at which interaction forces are predominantly inertial) in 1982 (see also a summary of contact mechanics by Barber, et al. [7] in 2000). They argued that there existed a threshold velocity for hypervelocity gouging. Additionally,

they developed a model for hypervelocity gouging that included the concept of impact with an asperity. Their description of gouging is:

> When two solids are brought together, actual physical contact occurs only at a small number of discrete contact points. The normal load between the two solids is supported by these discrete areas. The number and size of the contact points increases with increasing applied load. Adhesion between two bodies in contact occurs at the contact spot and "cold welds" are formed. Tangential motion of one body with respect to the other deforms or shears material in the contact spots and results in further asperity contact. Frictional forces develop because of the ability of the contact spots to resist this deformation (wear results from material fracture due to excessive straining in the contact spot region.) During contact spot shearing, energy is dissipated into the deformation zone and then removed from the deformation zone by thermal conduction into the material substrate.
>
> As sliding velocity increases, the rate of energy dissipation in the deformation zone exceeds the conduction rate out of the deformation zone, causing the deformation zone temperature to rise. As sliding velocity increases still further, the temperature of the entire surface of a slider may reach the melting point, at which point a liquid interface is formed between the sliding surfaces, greatly reducing the frictional forces observed and the coefficient of friction. The liquid interface behaves as a hydrodynamic bearing. Viscoshearing of the liquid film dissipates energy, which causes intense heating of the slider surface and results in surface melting. Surface recession occurs, providing an influx of melted material from the slider surface equal to the efflux from the interface due to slider motion, and a steady-state hydrodynamic interface is established. The development of this hydrodynamic fluid layer depends upon the material properties of the slider and guider, the sliding velocity, the normal load, and possibly the geometry of the slider.
>
> At hypervelocity, if a fluid interface forms, velocity gradients in the interface will increase, as will the frictional force, energy deposition, surface recession, slider wear, and interface temperature. At some velocity, it is likely that the temperature of the interface region becomes so high that the interface material is vaporized, with a resultant drop in viscosity and frictional force. If a fluid interface does not form, asperity contact continues to occur at very high velocities. The asperities, however, can no longer come into contact in a steady or quasi-steady mechanical mode. Instead, they impact generally in an oblique manner, generating shock stresses. [8]

This description contradicts Krupovage and Rasmussen's [64] assertion that a liquid metal interface acts as an abrasive rather than to reduce interface friction.

At hypervelocity, however, both investigations agree that frictional forces increase between a liquid and metal. Laird's description of gouging compares favorably with this (see Section 2.1 [68]). Laird's description of gouging centers on the development of a high pressure core generated from the plasticity of the impact. The plasticity of the material interacting with the motion of the shoe shears material from both the rail and the shoe and this process initiates gouging.

While this description by Barber and Bauer does consider the contribution of thermal loads/diffusion and shear stresses in the development of plasticity, it is somewhat incomplete it its description of gouging. The phenomenon of shear band formation, for instance, is not addressed. However, the emphasis on the heat transfer aspects (i.e. the thermodynamics) points to the importance of this specific area of research.

Barber and Bauer define a "hypervelocity sliding threshold velocity" at which the stress created by impact exceeds the material ultimate strength. The impact stress, and thereby this threshold velocity, is described as being a function of impact velocity with an asperity, angle of impact, material density and shock speed. They proposed that this impact created a very localized material defect (like a crater) that travels with in the direction of the shoe at approximately 1/2 the shoe's velocity. This would then result in the typical gouge shape. While this mechanistic description offers to explain an asperity impact scenario, it does not address the simple vibratory impact case - known as an oblique impact. In this type of scenario, a gouge is created by the shoe impacting the rail at a shallow angle and creating a gouge without the necessity of an asperity. Additionally, Barber and Bauer's approach does not account for material mixing reported (e.g. in the metallurgical findings of Gerstle [42]).

Barber and Bauer did not report significant correlation between their theories and quantitative data. They did, however, point to the work of Graff, et al. [44], in which it was noted that there appeared to be a minimum shoe velocity and normal load required to initiate gouging. Therefore, a hypervelocity sliding threshold velocity

was supported by the data. Barber and Bauer also noted that in some rail gun gouging studies (see Section 2.2.2) a threshold velocity was discovered.

The concept of a minimum horizontal velocity required to initiate gouging is borne out in the experience of the HHSTT. However, many other variables enter into this analysis that make such a simple generalization somewhat problematic.

In 1997, Mixon [81] performed a survey of the literature and experimental data and created a detailed review of the gouging phenomenon. He examined a database of test runs and resulting gouging and summarized the common elements to describe the factors that contribute to gouge creation. These elements included high stress from dynamic loading, high sled velocity, asperities on the rail surface, heating due to friction, deterioration of the shoe and creation of debris that lodges in the slipper gap, and ejection of sled material due to aerodynamic heating (high temperature behind the normal shocks).

Mixon reviewed three types of tests for his analysis. They included the Low Mass Interceptor (LMI), Medium Mass Interceptor (MMI), and Patriot PAC3. Each of these test series consisted of discrete sled sections, with the payload being carried by the forebody sled and pushed by the pusher section. The shoes of the forebody, as well as the shoes of the final stage pusher rocket (called the Roadrunner), could initiate gouging.

The LMI tests (two of them were available) examined by Mixon made use of the terminal helium bag described previously. The test runs had a peak velocity of 6863 fps and experienced gouging beginning at approximately 5800 fps. The majority of the gouges (75% to 83%) occurred past peak velocity and all of them occurred in the helium environment. In this regime, the aerodynamic heating and oxidation is kept to a minimum, but the deterioration of the shoes has already occurred.

Seven MMI test runs were evaluated, with a peak velocity of 6660 fps. The location of the gouging on the railhead was recorded for four of these runs. The onset of gouging occurred at about 5400 fps and a total of 408 gouges were discovered

(with 24 being significant enough to require welding to repair). Figure 2.4 depicts the velocity profile (represented by the line) of the sled, as well as the location and number of the resulting gouges (shown as bars indicating the number of gouges per 500 ft section of rail). It is clear from Figure 2.4 that most of the gouges are in the region of maximum velocity. The fact that the largest number of gouges occurs after peak velocity points to shoe degradation as a possible cause of the phenomenon. A majority of the gouges were found to occur at the rail corners - where stress and temperature concentrations are a maximum.
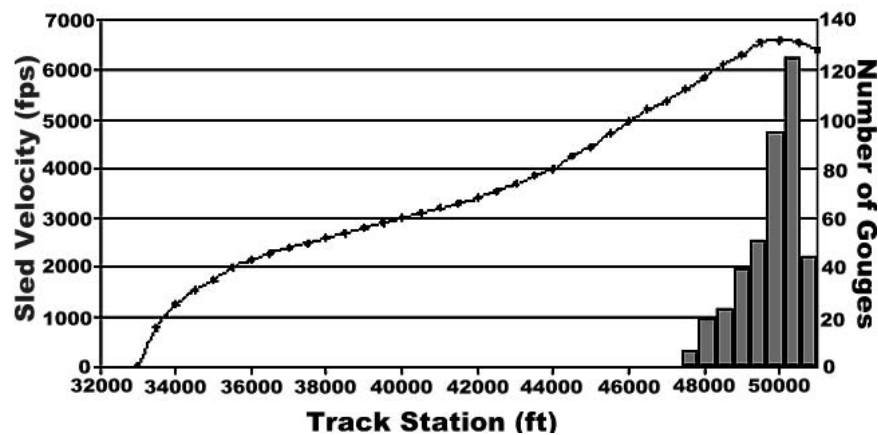
Figure 2.4:   **Sled Velocity v. Number of Gouges (MMI Tests).**

Mixon presented diagrams of the gouge locations and noted that there were sections of rail that had multiple gouges. Additionally, there were runs in which gouging was particulary prevalent. For instance, the worst run included 114 (27.9%) gouges, nine (37.5%) major gouges, and a large six inch gouge that broke the rail and led to catastrophic failure.

The Patriot (PAC3) tests included fourteen runs with a peak velocity in the 6000-6100 fps range. This series of tests also included an aggressive rail repainting effort. The track was sandblasted and repainted with 6 mils ($\pm$ 1 mil) paint every four test runs. The rail was also spot painted after every run, where needed. In this test series, gouging began at 5750 fps and gouging seemed unrelated to whether the vehicle was before or after the peak velocity. All the gouging was in the helium

environment. This test series only suffered two major gouges (both on the same run). This same run ended with catastrophic failure of the Roadrunner.

Mixon argues from this analysis of the test record that gouging is related to the roll forces in the vehicle. He concludes that the location of the gouges shows that the sled experiences roll or lift during the run and that gouging leads to more excessive roll moments that contribute to total system failure. Mixon also notes that the fact that gouging occurs late in the test run indicates shoe wear/deterioration is a factor in gouge initiation. However, this region is also where velocity and aerodynamic heating is at a maximum, so clear causality may not be easily established. Additionally, the dynamic nature of propulsion cut-off (i.e. a sudden drag load imposed on the vehicle once the propulsion system turns off) is not addressed in the analysis. Mixon did find that the highest gouge rates were found in a small band of velocities ($\pm$ 50 fps) around the peak velocity.

Mixon concluded that high stress, high velocity, rail imperfections, deteriorated slipper surfaces, and frictional heating were the significant contributors to gouging. His summary pointed to the fact that rail coatings can reduce the onset of gouging. Therefore, as we will see in Section 2.2.6, gouging mitigation efforts have focused on this area. In fact, Mixon asserts that and accurate gouging model is needed to study these rail coatings. However, he noted that the model needs to be capable of considering various coating material properties and to ascertain their effect on the gouging event.

In this section, analysis of gouged materials from hypervelocity test track runs has produced some theories on the causes and mechanisms of hypervelocity gouging. These include the formation of adiabatic shear bands and thermoplastic shear, high temperature effects (both from aerodynamic heating and plasticity of the material), inertial effects of hypervelocity impact, and shock wave formation. In addition, formation of a plastic zone, high strain rates, viscoshearing, and hydrodynamic bearing may also be mechanisms causing hypervelocity gouging based on analysis of gouged

test track materials. Clearly there are numerous variables at play in this gouging phenomenon. From the research in this section, there appears to be a strong relationship between the velocity of the sled and the onset of gouging. These various observations and contributing factors point to the need for a robust and validated model to evaluate the phenomenon of hypervelocity gouging.

2.2.2 Laboratory Gouging Tests. In addition to the experimental testing available using test tracks as outlined in Section 2.2.1, experimental data for hypervelocity gouging is available from laboratory gouging tests. In these tests, gouges are created under laboratory conditions by impacting a projectile into a target at high velocity. The materials are typically carefully studies in their "virgin" state and after the gouging has occurred.

As early as 1968, Graff, et al. [44] created a gun experiment that generated a high velocity sliding impact with velocities up to 9000 fps. In this effort, projectiles were shot at a shallow (grazing) angle against flat or curved plates (targets).

The authors began with a review of all available test sled data from the HHSTT. Their conclusions, based on the gouging information, was that factors such as rail and slipper materials, slipper geometry, rail roughness, airflow in the slipper gap, sled velocity, and contact stresses played a role in gouge development. They argued that gouging was the result of high velocity sliding contact (impact) between two metallic bodies (surfaces). They noted that gouging seemed to initiate in the 5200 to 5550 fps range and that the typical gouge was tear shaped (2-4 inches long, one inch wide, 1/16 inch deep).

Graff, et al. noted that the gouges seemed to exhibit evidence of discoloration and material mixing (i.e. metal deposits within the gouge). They also observed that the largest number of gouges occurred after peak velocity was attained and that about 80% of the gouges were on the side or top edges of the rail, 15% were on the undersides, and only 5% were on the top surface of the rail. They argued that although shoe deterioration plays a role, sled velocity was the primary factor in the

gouging phenomenon. In addition, in those runs in which canards on the sled were set to push the sled down into the track (and thereby reduce vibration) there was less gouging. Also, the advent of high strength maraging steel for the shoe material reduced gouging.

In order to create laboratory gouging, Graff, et al. focused on the variables of impact velocity, shoe and rail materials, and interface stresses. They created gouges in a steel target with projectiles fabricated from brass, copper, steel, and aluminum. They found that a 3 foot radius curved steel target concentrated the stresses sufficiently (note: a 20 foot radius plate did not) to create gouges similar to those at the HHSTT.

Graff, et al. noted that the projectiles marked the target plate during the impact and that a layer of mixed projectile and target material was created. This indicated that gouging involved material mixing and that the temperature reached the melting point.

Graff, et al. also postulated that aerodynamic heating during a sled run could, in itself, could raise the temperature of the shoe enough to cause material melting without the necessity of an impact. They argued that there was evidence that the coating material acts as a lubricant and thereby prevents the transmission of shearing forces to the rail. In this fashion, the cause for gouge initiation was avoided. They also proposed that melting products could, like the coating material, act as lubrication and prevent gouging. The rationale was that the liquid interface would only transmit the spherical (volume changing) stresses and not the deviatoric (shape changing) stresses. The only shear forces transmitted, then, would be within a narrow viscous boundary layer on the shoe.

Graff, et al. presented analytical computations that demonstrated that steady pressure dominated the impact event and that the transient stresses were relatively insignificant (based on projectile size and velocity). The magnitude of these normal stresses were, for a .27 ounce steel projectile, around 78,000 psi.

They also demonstrated that gouges could be initiated by putting discontinuities on the target surface. These locations would experience stress concentrations and that would lead to gouging. Gouging could be increased by something as simple as orienting the surface finish transverse to the projectiles motion as compared to having the grain parallel to the velocity vector. It was due to this study that they concluded the surface preparation was an essential contributor to the gouging process.

Graff, et al. proposed that gouging occurred when metal to metal contact begins between the projectile and the target. This means that the impact must possess sufficient normal stress and impact velocity to allow the projectile to penetrate the oxide film on the target and the molten layer on either surface to create a metal on metal interface. They argue this contact would create a "weld" between the materials and precipitate gouging.

The penetration described by Graff, et al. could be initiated by a stress concentration resulting from the target surface condition. This would begin the mixing type process described in Section 2.1 by Laird in which material from both bodies begins to rotate about a high pressure core. The authors here proposed that the gouge would start very small, but would grow as the metal to metal contact persisted and shear of the material continued. The gouge would terminate with passage of the projectile back end beyond the affected area.

In 1970, Graff, et al. [45] continued the study of gouging by examining various projectile and coating materials to make some generalizations concerning the onset of gouging. They found that:

- All metallic projectiles caused gouging

- Hard metals have a higher threshold gouging velocity

- Hard maraging steel gouged least, but excessive hardness could result in machining action

- A shoe with hardness slightly higher than the rail would give the best results

- Best coating results were from low strength, low density, non-metallic materials

- Low strength coatings allowed shear to occur in coating, not in target or projectile

- Gouging was prevented if metal to metal contact could be prevented

The work by Graff, et al. points to the importance of a coating to prevent the metal to metal contact that appears necessary to initiate the gouging event. The characteristics of the coatings and a more detailed discussion can be round in Section 2.2.6.

In 1995 and 1997, Tarcza [113,114] studied this concept of a minimum threshold gouging velocity by shooting projectiles at a relatively low velocity. He proposed that gouging could occur a low velocity and that it was a function of material properties. His aim was to demonstrate this correlation to predict the onset of gouging. Tarcza created an experiment that related gouging to impact velocity and material strength. He also sought to demonstrate that there was a threshold gouging velocity, but that it was much lower than previously reported. Additionally, he wanted to design an experimental protocol that would be inexpensive and fairly easy to duplicate.

Tarcza's review of the relevant gouging literature, in particular those that related to the rocket sled and rail guns, resulted in a list of common theoretical contributions to the hypervelocity gouging phenomenon. All of these varied sources acknowledged the role of shoe velocity, stress between the contacting surfaces, and the material properties of the structures in the initiation of gouging.

Tarcza examined the past gouging data and proposed a linear relationship between the threshold gouging velocity and the specific yield strength (yield strength divided by density). This is depicted in Figure 2.5. Extrapolating this relationship, he argued that a lead on lead impact scenario should allow gouging to occur at approximately 715 fps. A common thread throughout the literature that Tarcza found was that the gouging was characterized by the various different impact configurations as having a high pressure core that was created by the impact and continued to grow.

This core was required to grow in size from the time of impact, or gouging would not commence.
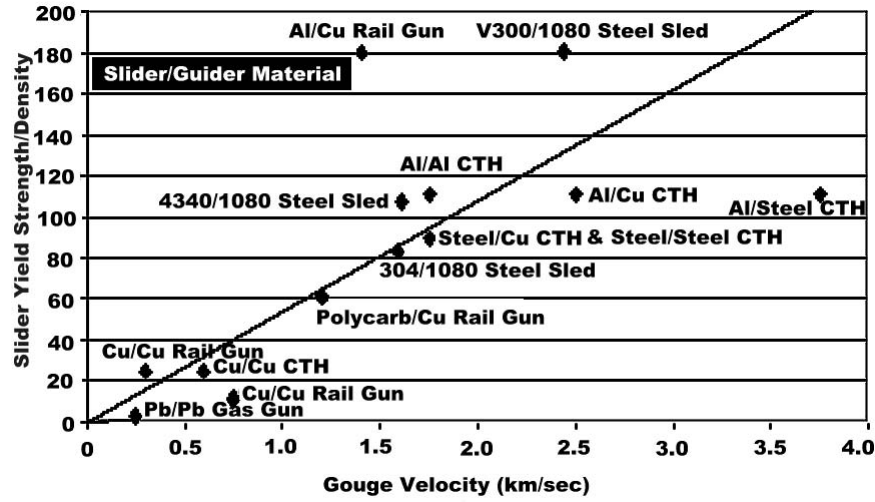
Figure 2.5:   **Slider Specific Yield Strength v. Gouge Velocity.**

Tarcza postulated that gouging was possible below the threshold gouging velocities reported in literature given a particular set of impact conditions and material properties. He argued that hypervelocity gouging occurred at velocities at which the inertial forces dominated the event and not necessarily at high relative striking speeds. He then sought a material combination that would make gouging possible in his laboratory environment.

Tarcza selected lead on lead as his material combination. He set up a light gas gun and shot .22-caliber projectiles at a curved target in a similar configuration to Graff, et al. [44]. He found that gouging occurred at striking (sliding) velocities of approximately 890 fps ($\approx$ 270 m/s). He found gouges in shapes similar to those reported in the literature for hypervelocity gouging events. Additionally, he found that gouging was related to the surface condition (i.e. irregularities, scratches, etc.), although not exclusively. While these surface discontinuities contributed to gouging in most cases, other gouging events seemed simply the product of the material interaction. Counterintuitive to some thinking, a uniform seam across his lead target

(much like a weld bead between rail sections) seemed to discourage gouging. Recall that this agrees with Gerstle's work in [40, 41].

Tarcza observed a form of deformation that lies between gouging and non-gouging behavior. He called this "incipient" gouging. In this kind of interaction, gouges had been initiated, but had not fully developed. Additionally, as opposed to previous impact studies, Tarcza concluded that the presence of an oxide layer did not affect gouging. He argued that gouging was a results of sustained material contact and that the uniform target discontinuity (seam) prevented such sustained contact and thereby frustrated gouge development.

Although Tarcza was able to create gouging far below the widely held definition of hypervelocity (i.e. where impact velocity is close to the material sound speed) it does not invalidate aspects such as shock waves as be contributors to gouging. It does demonstrate, however, that material properties and impact conditions play a significant role in this study also.

Tarcza also concluded that the normal force level was a crucial component to the development of gouging. This normal force is generated by an oblique impact angle with the target or impact with a surface asperity. Graff, et al. [44] and Tarcza both found that a curved target plate was necessary to initiate this gouging - i.e. that sufficient normal force was required. The normal force is assumed to be a function of the projectile (sled/shoe) velocity, but no data on the normal force generated is available. Therefore, assumptions with regard to the dynamic environment, amplitudes of oscillation, and sled orientation must be made to compute an estimate for the normal force of impact.

Ramjaun, et al. [91] investigated the field of hypervelocity impacts with regard to space debris bumper shields in 2000. They examined hypervelocity impact craters formed at various striking angles at around 5 km/s. Their research discussed failure mechanisms that can apply to the shoe/rail interaction at very similar velocities. They discovered adiabatic shear band formation in the impact damaged area.

Ramjaun, et al. detail a failure mechanism in which the compressive shock wave of impact propagates within the projectile and the target (in our case, the shoe and the rail) and reflect off of the free surface. These wave reflections leave the material in a highly energetic state that can lead to fragmentation, melting, or vaporization.

The oblique impact scenarios performed by these authors is the most applicable to our gouging problem. The author's examination of the impact craters from the oblique angle shots reveal a gouge-like shape and characteristic material melting, mixture, and thermoplastic shear. Metallurgical evaluation determined the existence of adiabatic shear bands and intense plastic deformation. The authors concluded a large temperature excursion was experienced by the material.

Ramjaun, et al. concluded that the shear bands were the result of shear instabilities created under high stress and strain rates. This plasticity generates heat that concentrates in these shear band areas and cause thermal softening. When the shock wave reflections return to the area, tensile stresses are produced that fracture the material along these lines of shear instability. These shear bands can link up and cause section to break from the bulk material. Additionally, this seems to indicate a potential thermal sink mechanism as the thermal energy concentrates here and then is released.

These authors cited the primary cause of hypervelocity impact damage to be the formation of adiabatic shear bands. They conclude that to mitigate damage, the material chosen should "have no tendency to form adiabatic shears." [91] The material to best resist hypervelocity impact damage would:

- have uniform and homogenous flow properties during viscoplastic deformation to prevent formation of adiabatic shear bands caused by uneven formation of viscoplastic zones

- have a high melting point to prevent cracking in case of adiabatic shear band formation

- and not transform into a brittle phase during shock loading which increases the likelihood of fracture under loading.

These authors, then, describe specific material properties that should be kept in mind as we evaluate shoe/rail designs to mitigate hypervelocity gouging. This is applicable in our problem because as Gerstle reported, and as we will see in Section 4.2, shear band formation is prevalent in this gouging phenomenon.

These laboratory experiments in the field of gouging are extremely valuable and, unfortunately, rare. This is due to the high cost of performing such tests. To gain better insight into the phenomenon and because of the high cost of creating and running such tests, numerical investigation of gouging has taken place in parallel with experimental procedures such as test track observations and laboratory testing. These numerical simulations can offer insight into the creation of gouging and challenge us to recreate the experimental results within a model.

2.2.3   Numerical Modeling of Gouging.   Due to the high cost of experimental work in the gouging field and the desire to create models for predicting/mitigating hypervelocity gouging, numerical models or simulations form an important basis of the field of research. These numerical approaches are typically based on, and validated by, the experiment work described in Sections 2.2.1 and 2.2.2. Numerical models can offer valuable insights into the physical understanding of the impact event. They also allow theoretical considerations to be tested without the expense of actual experimentation. Of course, it must be recognized that the models inherit the inaccuracies of our limited understanding of all the physical processes involved in hypervelocity gouging.

Traditional computational methods in structural mechanics are based upon Hamiltonian mechanics in which the forcing function $F(t)$ is known. Thus, the system of equations based on Hamilton's equations of motion can be represented by

$$F(t) = [M]\{\ddot{u}\} + [C]\{\dot{u}\} + [k_{nonlinear} + k_{linear}]\{u\} \qquad (2.4)$$

where $[M]$ is the mass matrix, $[C]$ is the viscous damping matrix, $[k_{linear} + k_{nonlinear}]$ is the stiffness matrix containing both linear and nonlinear terms, $\{\ddot{u}\}$ is the acceleration vector, $\{\dot{u}\}$ is the velocity vector, $\{u\}$ is the displacement vector, and $F(t)$ is the forcing function (a.k.a. vector of the applied forces). This equation is the result of solving the three fundamental conservation equations (a detailed explanation of which appears in Chapter III).

These Hamiltonian dynamics are considered under traditional (non-shock) load conditions. Therefore, numerous aspects of a hypervelocity impact are not accounted for. For instance, material failure, viscoplasticity, large material movement, shock waves, thermal effects and the like are not modeled. The forcing function, $F(t)$ in Equation 2.4 is assumed to be applied in rates below the wave speed of the material. However, we know this is not the case in hypervelocity impact problems. Inertial effects are more dominant in the solution of the fundamental laws of conservation and equilibrium. Additionally, at hypervelocity, high pressure can cause the materials under consideration to behave as inviscid fluids [80]. At these impact pressures, the equation of state begins to dominate the solution of the material deformation (see Chapter III) - which can account for the non-equilibrium thermodynamics and related effects that arise from this high energy event.

Therefore, the numerical modeling of hypervelocity impacts must take into account this non-classical material behavior and consider rapid loading and material response. As mentioned previously, the high energy impact event requires consideration of the EOS of the materials, as well as the constitutive modeling.

Boehman, et al. [15] in 1977 published the earliest computational hypervelocity gouging model. Their computer model attempted to capture friction, wear, and gouging between the shoe and the rail. Their efforts to establish gouging criteria were largely unsuccessful, yet they were able to identify velocity regimes that were more stable.

Barker, et al. [11] continued this numerical work in 1987 at the Sandia National Laboratory using the predecessor to CTH, CSQ. A Parallel Impact Thermodynamics (PIT) model was created to model the shoe/rail impact problem. The name indicated the nature of the impact (parallel to the rail) and for the use of a thermodynamics (i.e. a hydrocode) solution of the gouging event. Barker utilized an elastic/perfectly-plastic constitutive formulation that generated a viscoplastic response beyond the yield strength. The gouging was initiated in this model by the use of an asperity on the rail surface. Figure 2.6 shows this model and the small gap between the shoe and the rail.
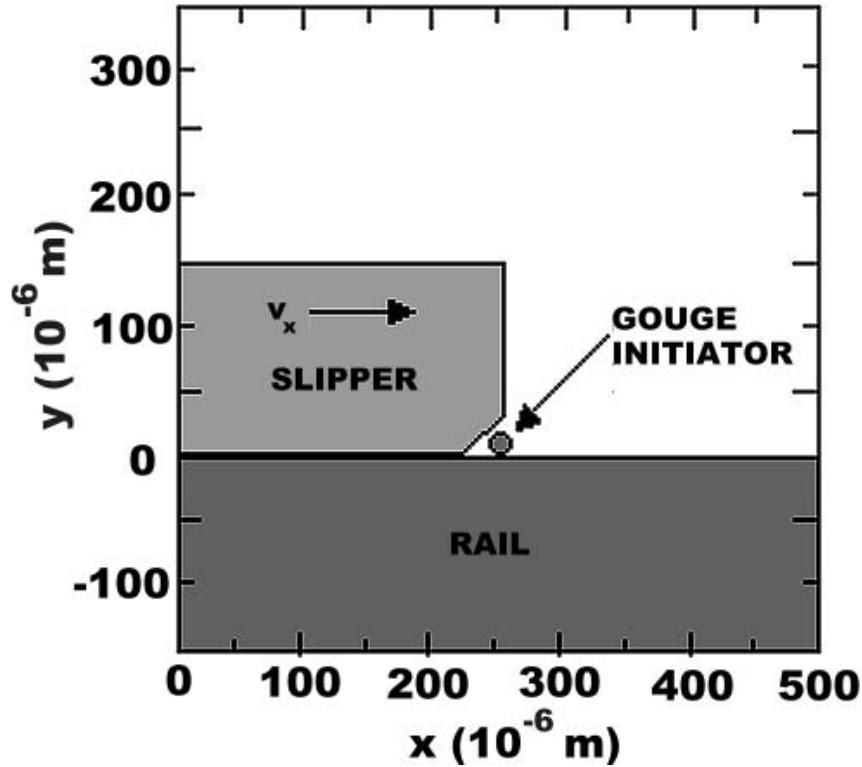
Figure 2.6:   **Barker's PIT Model for Gouging.**

Barker, et al. believed the gouging phenomenon to be an impact related event and created the PIT model and theory proceeding from that assumption. The hydrocode solved this impact problem considering shock wave physics and thermodynamics. In order to quantify the frictional heat generated, they relied on experimental work involving a 30 mm diameter steel ball shot down a barrel (with a curvature of

1 mil per 10 inches) at 3 km/s. This resulted in the surface of the ball melting after 2000 microseconds (60 cm of travel) to a depth of 6.7 mm.

Barker, et al.'s model was validated in that it produced gouging when the shoe impacted an asperity at high velocity. The leading edge of the shoe was necessarily created at a 45° angle to crush the asperity under the shoe during the impact sequence. In addition to this 2-D model, they created a 3-D model in which gouging was shown to occur, but only if the gap between the shoe and the rail was removed. Since gouging was successfully recreated in the code, they authors felt the PIT model was validated.

Their study of the PIT model showed that the gouging was characterized by extreme local deformation (of the asperity in particular), high heating and subsequent melting/vaporization of the materials, and the creation of a high-pressure region. They theorized that this high pressure interaction would deform the otherwise parallel material interfaces in such a manner that they impinged on each other and began to mix, thus producing a gouge. They postulated that once this interaction began, it could become self-sustaining and would continue until the back end of the shoe past the interacting region. (This matches the description proposed from the experimental work in Sections 2.2.1 and 2.2.2.) They also noted the importance of the shock interaction within the gouging event.

Barker, et al. performed a parametric study on his model results to better quantify the contributions to gouging from various variables and to offer suggestions on gouge mitigation. This study also served to verify the validity of the PIT model assumptions. The study concluded that in order to mitigate gouging one needed to:

- increase the gap size between the shoe and rail

- increase the shoe yield strength with respect to the rail

- use plastic as the shoe material

- pitch the shoe to create a small angle between the shoe and rail

- decrease the normal load between the shoe and rail

Interestingly, the effect of the normal force in the creation of gouging was recognized as a key component.

Barker, et al. ran his model without friction to test the hypothesis concerning gouging proposed by Graff, et al. [44]. Recall that this theory was that gouging was the outgrowth of metal on metal contact resulting from the projectile penetrating the oxide layer and the layer of melted material between the projectile and the target. In Barker, et al.'s model, gouging occurred with or without friction. The friction was removed by considering a layer of frictionless material between the shoe and the rail. Therefore, the presence or absence of the frictionless material between the projectile and the target did not significantly affect gouge initiation. This indicated that the inertial forces dominated the impact event rather than the formation of a welded junction as proposed by Graff, et al.

With this analysis in place, Barker designed a laminated shoe that specifically allowed release waves to travel faster and thereby relieve the pressure in the high pressure core. This served to decrease peak normal pressure and also allowed for melt lubrication at high velocity. This design was fielded and reached 1.9 km/s without gouging in testing.

While the PIT model offered insight into the gouging event, there were several shortcomings. The shoe design in the model was not accurate, and the actual shoe (with a much less steep angle of attack to the track) still was thought to lead to gouging where that geometry in the model would not. Additionally, an asperity was required for gouge initiation where it was thought that gouging was possible without one.

Another area where hypervelocity gouging occurs is in the development of rail gun technology or high speed multiple-stage gas guns. In these applications, gouging can occur during the projectiles movement down the gun barrel, resulting in very undesirable outcomes. Barker, et al., in 1989 [12], reviewed Susoeff and Hawke's 1988 report [103] on rail gun gouging. Barker, et al. concluded that although the source of

gouging damage was not certain, it was possible that the projectile had shed molten material that had impinged into the barrel and precipitated the damage. The lack of gouging at very high velocity could be due to the projectile completely vaporizing whereas at lower shot velocities the projectile survives to damage the barrel.

Barker, et al. also presented another parametric study of CTH conditions that lead to gouging within the PIT model. The materials of copper, steel, aluminum, and plastic were evaluated in all combinations and in the velocity range of 1/2 to 12 km/s. The aim of the study was to describe whether an asperity would results in a growing interaction (pressure) region and create gouging or not. Barker concluded that there was a minimum and maximum velocity range in which gouging would occur. That is, the previously discussed threshold gouging velocity also had an upper limit according to the model. (It is noteworthy that this upper limit has not been demonstrated in experimentation.) The upper limit occurred when the impact velocity exceeds twice the wave velocities of the materials. Apparently the material has insufficient time to be moved into the interacting region and therefore the high pressure core fails to grow. Additionally, the lower threshold velocity could be raised by increasing the material yield strengths.

Again the critical nature of material yield strength, normal force, shock physics, and material interaction was noted in the investigation into hypervelocity gouging.

Tachau continued the effort to model hypervelocity gouging in 1991 [112]. He began with a summary of the literature in the field and identified Barker, et al.'s model as a starting point. He noted that the PIT model required an asperity, a gap between the shoe and the rail, and a downward crushing of the asperity to initiate gouging. He also noted that the PIT model neglected the effects of sliding friction.

Tachau argued that gouging could be initiated by an oblique impact and that a gap and an asperity were not required elements. Tachau created this model in CTH and improved on the PIT model by giving the shoe an initial vertical (downward) velocity into the rail surface (see Figure 2.7). Given the high horizontal (downrange)

velocity of the shoe, this model would create highly oblique (very shallow angles) impacts. Tachau postulated that this would create the antisymmetric humps as described by Abrahamson and Goodier in 1961 [1] and would begin the gouging event.
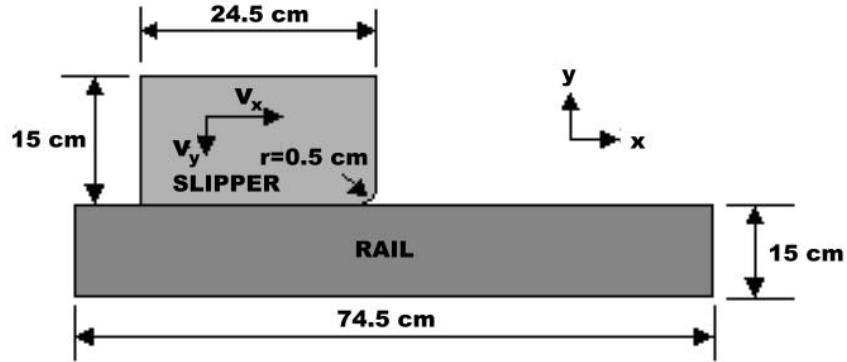
Figure 2.7:   **Tachau's Model for Gouging.**

Tachau's initial conditions were 2 km/s horizontally and 100 m/s vertically (It should be noted at this point that Tachau's assumption of a 100 m/s downward vector was significantly high. In 2000, Hooser [48, 49], using the Dynamic Analysis and Design System (DADS), showed that a more realistic vertical impact velocity is approximately 1 to 2 m/s.) Tachau observed that the resulting crater depths were deeper than those created in the actual sled tests. Additionally, his model showed very high temperatures (1800 K) resulting from plastic deformation near the material interface. This thermal input heated the surface to the melting point. Also, the core pressures generated in the resulting gouge region was around 5 GPa.

Tachau examined the model output for aluminum and steel shoes and varying velocities. He found that a high pressure core is characteristic of gouging and that the initial velocities played a major role in whether or not gouging occurred. For example, for steel on steel, the 2 km/s horizontal and 100 m/s vertical velocities did cause gouging, but reducing the horizontal velocity to 1 km/s did not.

The results of Tachau's model led him to surmise that the high temperatures generated at the contact surface are sufficiently high to cause the interacting materials to thermally soften and flow. This interacting region of plastic material then allows the

formation of a high-pressure core. The source of this high temperature, he argues, is from frictional effects and the energy of impact. These would be higher with increased impact velocities and normal loads.

For the oblique impact, this zone of viscoplastic material allows deformation and creation of the hump of material previously discussed. This would then lead to material mixing and growth of the high pressure core. This would be similar in nature to the gouging generated by the PIT model. For the impact with an asperity, Tachau demonstrated than as long as the asperity had a sloped surface, the impact would impart sufficient downward velocity that gouging would commence. This indicates that the vertical velocity of the shoe does not need to be significant in order to create a gouge in this model.

Once more, the topics of surface condition, frictional effects, normal force, and vertical impact velocity are the factors which alter the probability of gouging within this particular model.

Tachua extended his study in 1994-1995 [110, 111] along a similar vein. He concluded that a series of CTH studies showed that the gouging phenomenon was initiated by an oblique impact that causes a sharp temperature rise. This high temperature thermally softened the target and caused the characteristic hump of material to form the precedes gouging. The high pressure core formed next and the gouge was thereby created. It should be noted that in his work, Tachau relied on an elastic-perfectly plastic constitutive law due to the fact that a more complex relationship was not available in CTH at that time.

Following up on Tachau's work in 1998, Schmitz [95] developed another model based on CTH results to examine gouging and wear. This particular model proposed to predict shoe wear and the onset of gouging based on empirical data and set initial conditions. Schmitz had the expectation that additional experimental testing would be performed to validate his model. In the creation of his model, he utilized an asperity impact simulation (see Figure 2.8) based on Barker's model as described in [11].

Schmitz found that gouging was dependent on the creation of a growing high pressure core within the first 4 microseconds of impact. He was able to correlate gouging in varying material combinations to experimental HHSTT data, which appears in Figure 2.9.
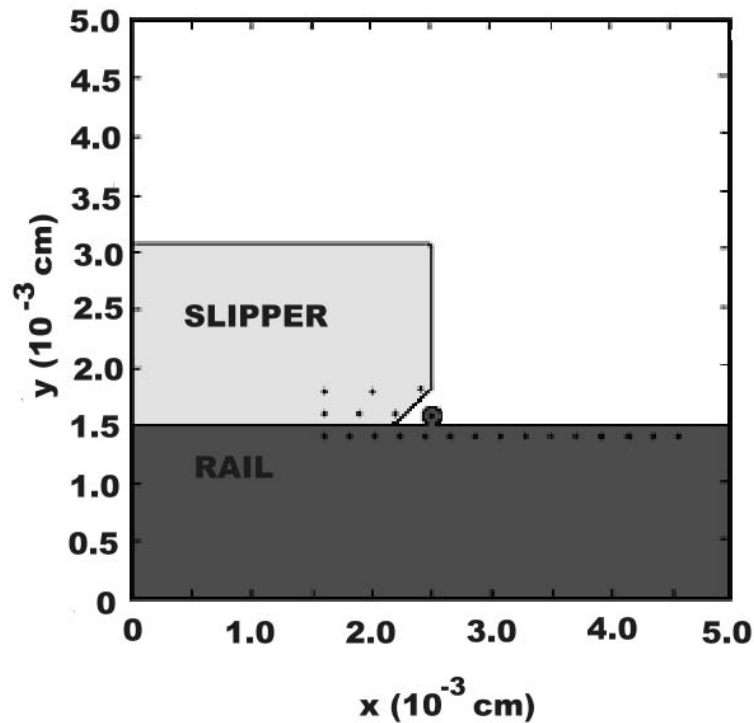
Figure 2.8:   Schmitz's Model for Gouging.
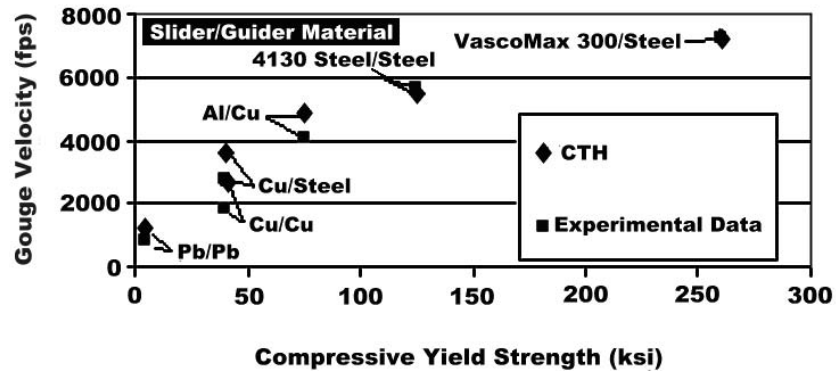
Figure 2.9:   Schmitz's Validation of CTH to Experimental Data.

In 2002, Laird [68] extended this investigation of hypervelocity gouging with an emphasis on understanding the fundamental physics of the phenomenon. Laird's focus was on understanding gouge initiation (in terms of material jetting) and the effect of temperature on the resulting gouging. In this undertaking, he performed a numerical study of gouging using the CTH hydrocode [70]. He also investigated the effect that high temperature had on the resulting gouge [67]. Laird's model was created after scaling down Tachau's model by an order of magnitude. While his work offers a comprehensive examination of the factors involved in gouging, his model was not scaled down using the Buckingham Pi approach or similar mathematical scaling law [108].

The key elements of gouging identified by Laird include the plastic deformation of the materials, their strength, and the normal force. These factors must appear in combination (i.e. one alone is not sufficient) to initiate a gouge. The essential feature was a material jet (see Figure 2.3) in both the shoe and the rail that began a material interaction that led to material mixture and eventual gouging. The jets were characterized by viscoplasticity of both materials.

He also argued that when these jets begin to form and initiate the gouging process, the reflected shock waves had not had sufficient time to return as tensile waves and therefore a spall or tensile fracture is unlikely. He did note, however, that the high compressive stresses created an environment conducive to gouge development.

Laird also performed numerical examination of the high temperatures involved in the gouging event. He argued that these temperatures caused thermal softening and thereby reduced resistance to gouging. Indeed, while a room temperature impact would lead to gouging, one in which the shoe had been pre-heated (by aerodynamic heating in front of the sled, for instance) had a "jump-start" to these higher temperatures and thereby making gouging more likely. The major difference between these two cases was that the pre-heated shoe created gouging earlier in time than the room temperature case.

Additionally, Laird found that a redesigned shoe leading edge with a very shallow angle (less than 1.790°) did not gouge under the same conditions that a shoe with a rounded leading edge - due to a shallow slope at the material interface. Therefore, the geometry of the shoe could, in itself, prevent the formation of material jets and therefore gouging.

Laird also discovered that increasing the material yield strength of the rail would also inhibit gouging to some extent. This analysis fit with previous work that showed that each of these parameters played a role in where the threshold gouging speed would be for a given geometry. While this increased rail yield strength did not decrease the total penetration of the shoe into the rail, it decreased the viscoplastic interaction, and therefore the high pressure core, the leads to gouge formation.

In 2004, Szmerekovsky [104–108] extended this research area by creating a CTH model of the impact using actual test sled dimensions. The details of his investigation will be discussed in Section 2.3.

While Szmerekovsky addressed the previous limitations in modeling by creating a numerical model based on the actual test sled dimensions, several other limitations are inherent in these past simulations. Primary among them is that CTH models which most accurately model the hypervelocity impact event do not contain material property values or strength models specific to the materials used at the HHSTT. As a complement to this numerical study, another focus area for research has been on the aerodynamic effects of these hypervelocity speeds on the gouging problem.

2.2.4 Aerodynamic Sled Analysis. As we have seen in the previous sections, the thermodynamics of impact plays a significant role in the gouging phenomenon. As some of the researchers have noted in previous years, the thermal environment is not only limited to the heat generated from plastic material flow, but originates also from the aerodynamics of the sled traveling down the rail at speeds of Mach 5 and higher. The high speed passage of the sled through the air creates strong shock fronts that raise the stagnation temperature behind the shock and flows heat into the

shoe/rail system. Based on the time scale required for heat conduction, however, the shoe is the only element of the interaction that will experience significant temperature effects.

As early as 1968, Korkegi and Briggs [62,63] developed a 2-D analytical model to study the shoe/rail gap region under this high flow condition. They divided the flow region into four discrete areas:

- a laminar flow near the stagnation point at the front of the slipper

- a turbulent boundary layer region before the upper and lower boundary layers merge

- a merged region

- a Couette flow asymptote (flow between a moving plate and parallel stationary plate).

By performing this analysis, they found that the air that flows through the gap is compressed by the shock front to significantly high temperatures and pressures. This results in high lift loads and heat gradients along the inner surface of the shoe. In the speed range we are examining (Mach 5 to Mach 10) that confined flow in the gap reaches temperatures equivalent to those on the leading edge stagnation points and also on the same order as those generated by sliding friction. For example, at 10,000 fps, the heating rates were on the order of 100 Btu/ft^2-sec, which was reported to be close to that of a frictional heating when the shoe and rail are in sliding contact. This indicates that extreme heating will be present in this analysis, whether the shoe is in contact with the rail or not. Based on the conduction analysis presented in Chapter IV, however, there is insufficient time for this generated heat to conduct into the rail. The shoe, on the other hand, can heat over the duration of a test run and may experience elevated temperatures. An examination of the effect of a heat shoe on a hypervelocity impact is examined in Chaper IX.

Korkegi and Briggs developed an expression for gap pressure p as a function of the distance from the slipper leading edge x (see Figure 2.10) from one-dimensional

isentropic flow relations relating effective area to local Mach number and pressure as follows:

$$\frac{p(x)}{p_\infty} = \left(\frac{(\gamma+1)M_\infty^2}{2+(\gamma-1)M^2(x)}\right)^{\frac{\gamma}{\gamma-1}} \left(\frac{\gamma+1}{2\gamma M_\infty^2 - (\gamma-1)}\right)^{\frac{\gamma}{\gamma-1}} \tag{2.5}$$

where p_∞ is the pressure at the free stream, $M(x)$ is the Mach number as a function of the downstream distance from the slipper leading edge x, M_∞ is the Mach number at the free stream, and γ is the ratio of the specific heats. The model is valid from the leading edge of the slipper to location where the upper and lower boundary layers meet. The model was developed for $M >> 1$, and should therefore be valid in the velocity regime being studied. This equation is also valid for the helium environment when the proper Mach number and value of γ is applied.
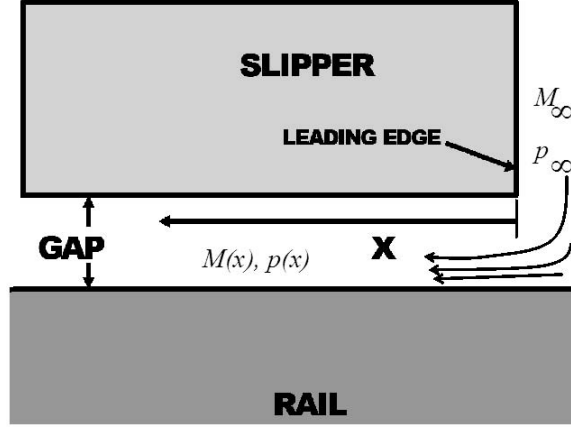
Figure 2.10: **Dimensional Model for Korkegi and Briggs Equation.**

Korkegi and Briggs' concluded that the flow conditions varied dramatically between a cold shoe and a heated one. After the shoe heats up, which happens fairly quickly, a state of constant pressure exists between the shoe and the rail. However, a state of dynamic instability results with regard to pressure and the gap between the shoe and the rail. They showed that as the gap narrowed, the pressure dropped off. Conversely, as the gap widened, the pressure increased. This instability results in the bouncing of the shoe against the rail and sets up the vibratory impact scenario observed in test runs. Therefore, not only does heat play a major role in the gouging event, but the aerodynamics also set up a dynamically unstable system the creates the

environment for the vertical impacts and high normal stresses highlighted by other authors as key mechanisms for gouge initiation. This instability leads to the vertical impact velocities used in Chapter IX in the modeling effort.

An external flow analysis was performed by Lofthouse, et al. [73] in 2002 on the sled currently being used at the HHSTT. His computations were limited to an inviscid computational fluid dynamics solution over a velocity range of Mach 2 to Mach 5. He discovered the highest pressure gradients generated by the sled occurred on the outer shoe surfaces. He considered the flow through the shoe/rail gap and predicted the pressure between the shoe and the rail to be characterized by shock interactions and sharp rises in pressure (jumps up to 75 psi). These pressure differentials could drive large temperature flows on the slipper. Again, this solution was inviscid. The addition of viscous flow could increase this effect significantly.

In the consideration of the aerodynamic effects on the gouging phenomenon, the literature shows a large heat flow in the problem. This additional source of heat adds to that already being generated by the plasticity and magnifies the thermodynamic contribution to gouge creation. Additionally, the aerodynamics have been shown to induce instability that causes the oscillatory impacts observed as one of the mechanisms responsible for gouging.

2.2.5 Load and Failure Analysis. Added to the numerous consideration presented above in the high energy impact environment of one of material loading and subsequent failure. The high pressures and loads experienced by the structures necessitates a good description of the material failure mechanisms. The creation of shear bands and material jetting and/or mixing demonstrates the existence of material failure in this gouging phenomenon. Failure and damage research is focused primarily on developing the theory used for setting criteria for material failure, including thermodynamics of deformation and damage.

In 1961, Abrahamson and Goodier [1] noted that moving loads on soft or viscous materials were often preceded by "humps" of material. These humps were argued to

be the result of inelastic material behavior. They postulated that if the material were elastic, the deformation would create equal bumps before and after the moving load. If the material is moving relative to the load, the leading hump is drawn under the load. The resulting profile is a function, then, of the penetration into the target material and the horizontal velocity of the load. This characteristic hump is a key feature of the gouging process.

Voyiadjis, et al. [118–121] and Abu Al-Rub [2] have developed a framework for analysis of heterogenous media that assessed a strong coupling between viscoplasticity and anisotropic viscodamage evolution for impact problems using thermodynamic laws and nonlinear continuum mechanics. Their proposed development included thermo-elastic-viscoplasticity with anisotropic thermo-elastic-viscodamage, a dynamic yield criterion of a von Mises type and a dynamic viscodamage criterion, the associated flow rules, nonlinear strain hardening, strain rate hardening, and thermal softening. The model presented in the research offers to be considered as a framework to derive various nonlocal and gradient viscoplasticity and viscodamage theories by introducing simplifying assumptions.

This theoretical development of a framework for a damage model is an example of development of a thermodynamic damage and failure model that could be used to improve the definition of failure for high velocity problems such as hypervelocity gouging. Subsequent use of this model could aid in the understanding of the failure mechanisms involved in gouging. The primary limitation of this approach is the integration of this analysis into CTH or other shock physics codes. While this failure model has been added to a Lagrangian finite element type code, its inclusion in an Eulerian shock physics code seem unlikely in the near term. This essentially makes this approach have no application to this type of analysis - since all meaningful solutions use shock codes. Additionally, because it is not available in a shock wave code, there is no linkage to an equation of state model - which could account for the non-equilibrium thermodynamic phenomenon.

In a related vein of research, Hanagud [46, 53, 74] is currently investigating a set of constitutive equations for high energy impact under a state of non-equilibrium thermodynamics. The objectives of this research are:

- To formulate constitutive models and equations of conservation, for metallic projectile materials, in appropriate continuum mechanics and non-equilibrium thermodynamics framework. The formulated models should be able to explain shock induced phase changes (including melting).

- To simplify the constitutive model, as found necessary, and use the model, with other equations of conservation and interface conditions, to understand the penetration mechanism of metallic projectiles into isotropic and granular media at high initial impact velocities (e.g., 850 to 2000 m/sec). The term understanding the penetration mechanism includes the projectile phase changes, melting, any failure of the projectile and deviation of the trajectory from the intended trajectory.

- To determine the parameters of the constitutive model and the penetration mechanism through testing.

- To design new materials, their microstructure and the spatial variation of the thermomechanical characteristics and structural design of the projectile to avoid trajectory deviation and any failure of the projectile.

The Hanagud constitutive models may be used to better describe the thermoplastic failure mechanisms of gouging. To accurately describe phase transition and non-equilibrium thermodynamics in which the first and second laws of thermodynamics are of uttermost importance, the Hanagud constitutive model is required. Most constitutive model assume adiabatic or isothermal states of thermodynamics. A similar limitation in application also applied to this work as had applied to Voyiadjis in that inclusion of these developing theories into usable code is a problematic process. In addition, most of the non-equilibrium thermodynamic effects are at pressures and

strain-rates where the equation of state dominates the solution, not the constitutive model.

Central to this discussion is the recognition that in the areas deforming at high pressure and temperature, the EOS relationships tend to dominate the solution - which incorporate non-equilibrium thermodynamic characteristics. This would lead us to focus on shock physics codes and analysis to describe the material interaction. However, the material flow model contributes significantly to the solution of the remaining areas that are deforming at lower pressures and temperatures [129]. Therefore, a poor constitutive model for the material could render the code simulations of the entire problem useless.

This area of performing load and failure analysis is central to the effort to understand and mitigate gouging. Current gouge mitigation can be summarized in the following section.

2.2.6   *Methods for Gouge Mitigation.*   As described in the preceding sections, the high energy of impact can be absorbed by the materials in the form of a damage mechanism. Shear bands are one such mechanism examined already. Current gouge mitigation effort revolve around coating the materials to improve their resistance to gouging. A coating and/or a change in material hardness/strength might be used to improve the material's resistance to impact deformation. In addition, the coating may prevent the transmission of shearing loads to the underlying bulk material or may change the thermal resistance of the material to the extreme thermal loads of impact. The thermal cycling of the coating may also affect its properties. Therefore, the area of coatings that can mitigate gouging by altering the impact environment is one of intense interest.

The HHSTT has successfully used coatings to reduce the occurrence of gouging. The analysis presented later in this section suggests that this is due to the reduction of frictional effects (heat), the sacrificial nature of the coating to disallow shear stress

from transmitting through it, the property of coatings to mask rail roughness, and its ability to protect the materials from the high thermal loads present in impact.

Coating fall into one of two categories. The first is refractory. These coatings typically protect sled components from the harsh thermodynamic conditions, but can also be used on the shoe or the rail. Refractory coatings such as tantalum, nickel-aluminum, zirconium oxide, tungsten, and cobaltech have been used on rocket sleds in the past [64]. Other coating materials have been applied to the rails using sprayers. While the application process is tedious and requires care, it has been somewhat successful in mitigating gouging. Currently, the HHSTT uses an iron oxide (hematite) coating on the low speed section of the track, and an epoxy coating on the latter half.

The second coating type is ablative, such as Teflon, carbon-carbon, and carbon-phenolic coatings. These coatings have been used for speed exceeding Mach 6 with some success. Unfortunately, these materials do not offer good shock resistance (i.e. they fracture under shock loading) and they may cause detrimental configuration changes [64].

Both Barker, et al. [11] and Tachau [112] proposed redesigned shoes based on varying the material properties of the shoes in order to reduce shock wave effects and reduce the likelihood of creation of the high pressure gouging core. These efforts were focused on system materials, while Schmitz's work [95] centered on gouge mitigation using coatings on the existing system materials.

Schmitz performed a study using CTH on various coatings and thicknesses and compared these conditions to the gouging threshold velocity. His results demonstrated that coatings made of aluminum, epoxy, polyethylene, polyurethane, and teflon raised the threshold gouging velocity substantially more than the other coatings including hematite, molybdenum, and zinc. These results from Schmitz's work appear in Figures 2.11 and 2.12. Schmitz's definition of gouging, however, was limited to the creation and growth of the high pressure core discussed previously in this chapter.

Gouge Velocity

Legend: Molybdenum, Zinc, Hematite, Aluminum, Teflon, Epoxy, Polyurethane, Polyethylene
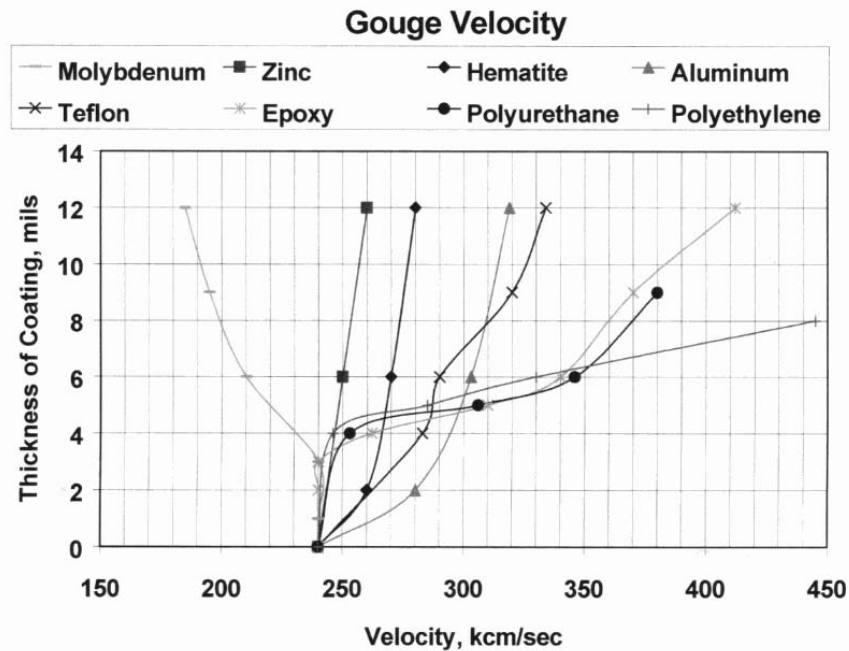
Figure 2.11: **CTH Analysis of Various Coatings/Thicknesses v. Gouging Velocity.**

Coating Effectiveness

Legend: 0 mil, 1 mil, 3 mils, 5 mils, 6 mils, 9 mils, 12 mils

(Polyurethane/Steel)
(Epoxy/Steel)
(Teflon/Steel)
(Aluminum/Steel)
(Hematite Primer/Steel)
(Zinc/Steel)
(Molybdenum/Steel)
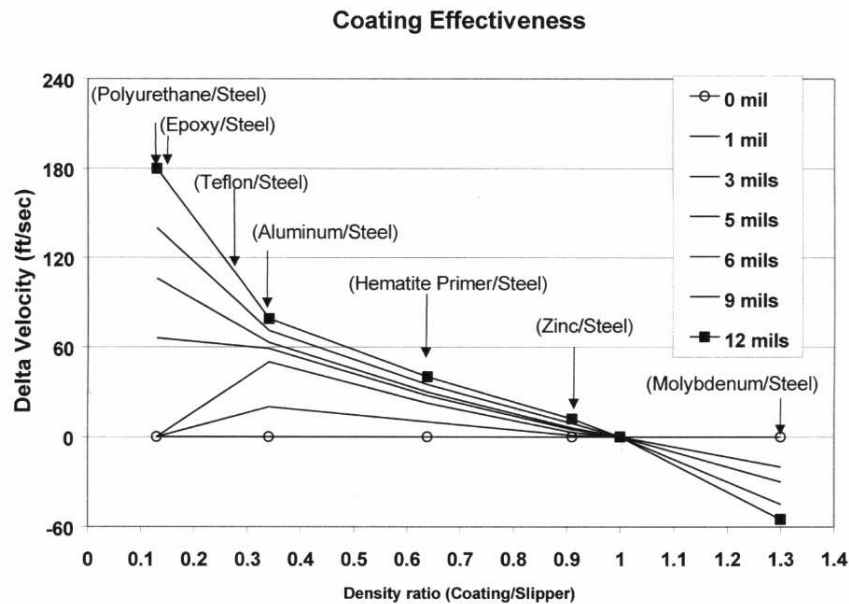
Figure 2.12: **CTH Analysis of Various Coatings Effectiveness.**

A number of approaches have been attempted to mitigate gouging. The use of coatings and redesign of the sled's shoes are among these approaches. With a

2-40

clearer understanding of the mechanisms that initiate gouging and allow it to develop, more effective mitigation schemes can be developed. Certainly the past research has indicated that coating material choice and thickness, as well as impact geometry, play key roles in this field.

2.3 Szmerekovsky Model

Szmerekovsky [104–109] advanced the understanding of the hypervelocity gouging problem by:

- Investigated the most appropriate numerical simulation tool for hypervelocity gouging research.

- Performed a mesh refinement study and created a gouging model in CTH

- Developed a mathematically sound technique to scale the shoe/sled model

- Examined some of the thermodynamics in the gouging problem

- Demonstrated, by using a scaled approach, that higher horizontal velocity created conditions more conducive to gouging

- Examined coating material selection and thickness resulting in a proposal for application parameters to mitigate gouging

In an effort to confront the gouging problem in general and the HHSTT geometry as a specific example, Szmerekovsky first evaluated a number of the available numerical codes to ascertain which one was the most appropriate for gouging study. Classic finite element formulations with Lagrangian meshes were found to lack the capability to deform and allow the material mixing seen in actual gouges. Additionally, the need to include thermodynamics and an extensive EOS database, drove Szmerekovsky to choose CTH as the best code for this analysis. While there are Eulerian codes that may have similar capabilities available, CTH provides unparalleled EOS data and shock physics capabilities with make it uniquely suited for this research.

Upon selecting CTH, the author constructed a model of the shoe and rail interaction problem at the HHSTT. As discussed in Section 2.2, a plane strain (2-D) model was considered a valid representation of the impact problem. In addition, a 3-D model in CTH was not computationally feasible. Therefore a plane strain model was created. Szmerekovksy then performed a mesh refinement study and discovered solution convergence at cell sizes of 0.002 cm. This also matched the material length scales described by Abu Al-Rub [2] and Voyiadjis [119], indicating that mesh sizes smaller than that would be outside the realm of continuum mechanics. The sled/rail model was created using the entire mass of the sled system, distributed to one shoe and depicted in plain strain. This included significantly more momentum than the Laird [68] model.

Szmerekovsky also applied the Buckingham Pi Theorem to the gouging problem to ensure a mathematically sound method of scaling the problem. He showed his model could replicate the results of Laird and that he could create a dimensionally accurate model of the shoe/rail interaction (in real dimensions) at the HHSTT.

Szmerekovsky's analysis included an initial look at the thermodynamics of the impact event. He concluded that friction and plasticity could generate the temperatures on the order of those needed to make the material phase changes and shear bands observed by Gerstle [40–42]. Szmerekovsky also noted that CTH's heat conduction algorithm had the capability to model heat transport during the impact event away from the zones of heat generation into the bulk material. However, this effect was small and did not contribute significantly to the overall solution [109].

By applying the Buckingham Pi scaling between impact scenarios at 1.5 km/s and 3.0 km/s, he demonstrated that the 3.0 km/s impact generated gouging earlier than a scaled time history would predict. This showed that the characteristics leading to gouging were enhanced by the increased velocity. His model also created the typical high pressure core necessary for gouge initiation and development.

Finally, Szmerekovsky concluded that coating selection and thickness could reduce shear stresses and pressure under the shoe and thereby reduce the probability of gouging. Additionally, the coating could act as a sacrificial layer that would effectively mask rail roughness (surface discontinuities or asperities) and allow the shoe to avoid a gouging scenario.

There are, however, several limitations to the work of Szmerekovsky and some areas that require further study. Primary among these is that CTH did not have the two specific materials, VascoMax 300 and 1080 steel, in its constitutive model material database. CTH has a EOS model for VascoMax 300 and an EOS model for iron (which can be argued to be very close to a low carbon steel like 1080 in terms of state relationships). However, neither material has a strength model in CTH. In addition, the previous models that were used relied on a strain-rate independent strength model, which poorly reflects the ability of the material to support higher stress levels while deforming at high rates. The fact that CTH used a strain-rate independent formulation was not known to Szmerekovsky. Secondly, the CTH model of the sled impact was never validated against experimental tests or shown to be accurate in its depiction of hypervelocity impact. Finally, available gouges from the HHSTT were not evaluated in terms of microstructure in order to quantify the thermal effects during gouging. A more thorough investigation of those thermal characteristics in the CTH environment would be helpful to both validate the model and to more fully understand the gouging process to devise mitigation methods.

2.4   *Summary of Previous Research*

The field of hypervelocity gouging has experienced a rich history of research. These efforts have ranged from experimentation on test tracks and laboratory examinations to numerical analysis, aerodynamic effects, load & failure analysis, and gouge mitigation. In these various approaches, a number of mechanisms for the initiation of gouging and the continued development of the gouge during the impact have been postulated.

Applying the conclusions of previous research to the HHSTT sled problem, one must consider the following areas:

- Experimental examination of hypervelocity gouges to ascertain characteristics of this kind of deformation.

- Close investigation of the thermodynamic effect on material microstructure, to include the creation of shear bands due to high thermal load. Consideration of non-equilibrium thermodynamic effects.

- Material properties of the sled and rail, considering their ability to resist gouge initiation. Specifically, the material flow models must be determined for the materials in the HHSTT impact scenario.

- Examination of the coatings used at the HHSTT to determine their ability to reduce friction in sliding impacts

- Integrating as much of these phenomenon into a numerical simulation that can be validated using experimental data and utilized to provide additional insight into the mitigation of gouging.

- Creation of a sled model that can be utilized to examine the various causes of gouge initiation (i.e. vertical impact, angled impact, and rail discontinuity).

These areas are ones in which further research must be done to characterize the gouging phenomenon and allow judgements to be made concerning gouge mitigation.

III. Theoretical Background

As the previous investigations indicated, the gouging phenomenon is dominated by a viscoplastic material deformation and shock wave phenomenon. Therefore, attempts to accurately model these hypervelocity impacts revolve around determination of accurate material constitutive models and Equations of State (EOS). Inherent in these two topics are the foundational elements upon which the solutions of these impacts rest. In addition, a brief discussion concerning the failure criterion within these solutions will be essential to understanding. While it appears counterintuitive at first, one can begin the topic by outlining how a computer code, such as CTH, solves these types of problems. Of course, the solution techniques were derived prior to code implementation, but a discussion on the code solution procedure will establish a framework upon which we can rely to guide the discourse on theory.

3.1 Hypervelocity Impact Solution Procedure

Szmerekovsky in [108] outlines the theoretical basis for viscoplasticity and summarizes the key points that are germane to the development of a solution to the type of material deformations discussed in Chapter II. He then describes how, in general, CTH solves such a problem. A summary of that description is provided in this section for ease of reference.

CTH, like most hydrocodes, uses the three conservation equations (mass, momentum, and energy), a description of the material EOS and the constitutive relationships to solve the forcing function [129]. These three fundamental equations can be expressed in Lagrangian (material) or Eulerian (spatial) frames of reference [4]. A complete treatment of this can be found in Malvern's text [75] and a more specific application to these kind of problems can be found in [13] and [59].

CTH solves these high energy impact problems by performing a Lagrangian step in which the material mesh is allowed to deform. The rationale for this is that the solution in the Lagrangian sense avoids the difficulty in solving the convective portion of the Eulerian representation. That is, the equations that must be solved

to resolve material flow through the Eulerian (spatial) mesh are significantly more difficult than solving the material flow in the Lagrangian (material) sense. In terms of computational time, the difference between the approaches is significant [4]. After the deformation is computed in the material sense, the deformed material is then remapped back to an Eulerian mesh and the time step is complete. Using this technique, the material distribution is first solved using the Lagrangian coordinate system and then mapped back into the Eulerian coordinate system [4]. The relationships required for this process are presented here.

In the following equations, the summation convention is adopted for the repeated indices. The Lagrangian (material) expression of the conservation of mass in terms of measurements in the Eulerian (spatial) coordinate system is:

$$\frac{D\rho}{Dt} + \rho\frac{\partial v_i}{\partial x_i} = 0 \tag{3.1}$$

where ρ is the material density, v_i is the velocity (evaluated in the spatial or Eulerian coordinate system for a specific particle), x is a measure of position (in the spatial coordinate system), t represents time, and

$$\frac{D}{Dt} = \frac{\partial}{\partial t} + v_i\frac{\partial}{\partial x_i} \tag{3.2}$$

which is known as the material derivative, substantial derivative, or the total time derivative (in which the measurements of position and velocity are in the Eulerian or spatial coordinate system). This definition establishes how a Lagrangian (material) description can be formed from quantities measured in the Eulerian (spatial) coordinate system.

The conservation of mass can therefore be expressed in the Eulerian reference frame, in which we are tracing density as it flows through a specific point, as:

$$\frac{\partial \rho}{\partial t} + \frac{\partial}{\partial x_i}(\rho v_i) = 0 \tag{3.3}$$

3-2

The conservation of momentum can be expressed also, with σ_{ij} representing the stress tensor, and f_i denoting the external body forces per unit mass. In the Lagrangian (material) sense, the relation is:

$$\frac{Dv_i}{Dt} = f_i + \frac{1}{\rho}\frac{\partial \sigma_{ji}}{\partial x_j} \tag{3.4}$$

and in the Eulerian frame is becomes:

$$\frac{\partial v_i}{\partial t} + v_j \frac{\partial v_i}{\partial x_j} = f_i + \frac{1}{\rho}\frac{\partial \sigma_{ji}}{\partial x_j} \tag{3.5}$$

The conservation of energy, with e representing the specific total energy, can be expressed in the Lagrangian (material) sense as:

$$\frac{De}{Dt} = f_i v_i + \frac{1}{\rho}\frac{\partial}{\partial x_j}(\sigma_{ij}v_i) \tag{3.6}$$

and in the Eulerian frame it can be written as:

$$\frac{\partial e}{\partial t} + v_i \frac{\partial e}{\partial x_i} = f_i v_i + \frac{1}{\rho}\frac{\partial}{\partial x_j}(\sigma_{ij}v_i) \tag{3.7}$$

The total specific energy is defined as:

$$e = \frac{1}{2}v_i v_i + E \tag{3.8}$$

which comprises the kinetic energy and the specific internal energy, E. With this expression, Equation 3.6 becomes:

$$\frac{DE}{Dt} = \frac{P}{\rho^2}\frac{D\rho}{Dt} + \frac{1}{\rho}s_{ij}\dot{\varepsilon}_{ij} \tag{3.9}$$

and Equation 3.7 becomes:

$$\frac{\partial E}{\partial t} + v_i \frac{\partial E}{\partial x_i} = \frac{P}{\rho^2}\left(\frac{\partial \rho}{\partial t} + v_i \frac{\partial \rho}{\partial x_i}\right) + \frac{1}{\rho} s_{ij} \dot{\varepsilon}_{ij} \qquad (3.10)$$

where s_{ij} is the stress deviator tensor, $\dot{\varepsilon}_{ij}$ is the strain-rate tensor, and P is the hydrostatic pressure.

Another way to state this is that the total stress tensor is considered in its two components, the symmetric deviatoric stress tensor, $\mathbf{D}$, and the spherical stress tensor, $\mathbf{S}$ (in which the stress tensor is spatial or Cauchy stress).

These conservation equations are not sufficient to solve the deformation problem. Two additional equations are necessary. The first is the equation of state, which relates the hydrostatic pressure to state variables such as density and specific internal energy. The other is the material constitutive model, which describes the material flow stress as a function of strain, strain-rate, and temperature.

The standard solution method is to allow the EOS to provide the solution for the spherical (sometimes referred to as volumetric) stress, and the constitutive model to provide the solution to the deviatoric (sometime referred to as shear) stress.

In hypervelocity impact, where impacts occur at speeds on the order of magnitude of the material sound speed, the spherical stresses tend to be much higher than the deviatoric stresses. Therefore, it is easy to err and assume that the EOS is the primary consideration for creating accurate solutions. However, even in these high energy impacts, the pressures quickly drop (especially away from the impact interface) to regimes in which the deviatoric stresses dominate. Therefore, an accurate model must have both a robust EOS and an accurate constitutive model to generate good results [129].

3.2 Equation of State

Stated simply, the equation of state bridges traditional continuum mechanics and thermodynamics. Continuum mechanics solves the three conservation equations (in terms of pressure, P, density, ρ, energy, E, and particle velocity, u) in a contin-

uous field with respect to time, t and space. Of course, these three relationships are incomplete - requiring a fourth relation. Continuity equations can provide the missing relationships in traditional static mechanics. In this high energy regime, an equation of state, $P(\rho, E)$, can also provide the required fourth relationship [4, 47, 77, 128].

Let us assume, for the moment, that $P(\rho, E)$ is a unique function. This implies that ρ and E are state variables, and P is a state function. If this is true, then P is independent of the process that generated the conditions, and is only a function of the $\rho - E$ state.

If these state variables exists, and are unique, then the process of thermodynamics can be applied to the problem. If we consider an equilibrium thermodynamic condition, the other thermodynamic quantities must also exist (i.e. temperature, T and entropy, S). The full complement of state equations would then become: $P(\rho, T)$, $E(\rho, T)$, and $S(\rho, T)$. This set is sometimes referred to as the temperature-based EOS – as opposed to the energy-based formulation presented above.

Pressure and internal energy can be derived from the Helmholtz free energy relationship, which states:

$$A = E - TS \tag{3.11}$$

where A is the Helmholtz free energy. The pressure and internal energy can then be expressed by:

$$P = -(\frac{\partial A}{\partial V})_T = \rho^2(\frac{\partial A}{\partial \rho})_T \tag{3.12}$$

$$E = A - T(\frac{\partial A}{\partial T})_\rho \tag{3.13}$$

where $V = 1/\rho$. Combining equations 3.12 and 3.13, we arrive at the following relationship (sometimes referred to as the thermodynamic consistency relation):

$$-(\frac{\partial E}{\partial V})_T = \rho^2(\frac{\partial E}{\partial \rho})_T = P - T(\frac{\partial P}{\partial T})_\rho \tag{3.14}$$

Once again, this formulation assumes a state of thermodynamic equilibrium. Note that in equation 3.12, the work done by PdV does not exclusively go into strain energy. Some of this work is converted into entropy, or heat. If we were considering an isentropic problem, then the equation would reduce (noting $dS = 0$ and $-PdV = dE$) to:

$$P = -(\frac{\partial E}{\partial V})_S = \rho^2 (\frac{\partial E}{\partial \rho})_S \qquad (3.15)$$

Now, let us consider a situation in which $P(\rho, E)$ is not a unique solution. Experimentation provides us evidence that this is true. Therefore, in order to create an EOS, more variables must be introduced to create a unique solution. Two primary cases apply to our problem (others involving explosive products are beyond this investigation). One is that the material's microstructure can have an impact on the EOS (like grain boundaries, defects, phase changes, etc.)– requiring the addition of flow variables that average the effect of inhomogeneous microstructure. The second case is that of time-dependent behavior in which the time required to reach equilibrium is not available in the given problem. This tends to "overdrive" the EOS into a state of thermodynamic non-equilibrium until the required time to reach equilibrium has been satisfied. Rapid deformation and heating can cause this second case.

In order to extend the concept of the EOS to handle these additional cases (which apply to the HHSTT problem, described in detail later in this work), some additional variables need to be considered. These variables are sometimes referred to as "internal state variables." This is due to the fact they do not appear in the conservation equations. These internal state variables modify the EOS relationships - specifically the thermodynamic relations - to account for these other effects.

Complicating this matter further are impacts in which shock waves are generated. Szmerekovsky [108] details the basics of shock waves. Briefly, a shock wave is generated when an impact creates disturbances which propagate faster than the material speed of sound. A sharp discontinuity is created in which material states vary significantly across a moving shock wave. In this case, the solution must consider

the Rankine-Hugoniot jump conditions [128]- where the states across the wave front must relate via the shock conservation equations (here the subscript 0 refers to the initial, at rest condition):

$$\mu = 1 - \frac{\rho_0}{\rho} = \frac{u_P}{U_S} \tag{3.16}$$

$$P_H = P_0 + \rho_0 U_S u_P = P_0 + \rho_0 U_S^2 \mu \tag{3.17}$$

$$E_H = E_0 + \frac{1}{2}u_P^2 = E_0 + \frac{(P_H + P_0)\mu}{2\rho_0} \tag{3.18}$$

where ρ is the density, P_H is the pressure, and E_H is the entropy of the shocked material, U_S is the shock wave velocity through the undisturbed material, and u_P is the particle velocity behind the shock front. These jump conditions must also be satisfied by the EOS in solutions which consider shock waves.

Beyond these considerations are those which advanced EOS' handle. To this point, a state of non-equilibrium thermodynamics could be achieved by creating rapid deformation and heating [4–6]. In fact, many mechanisms exist that can create this state of non-equilibrium. Some of them that apply to hypervelocity impact are material phase changes that non-conservatively remove energy from the solution and generate multiple shock fronts, thermal electronic excitation and ionization, and non-constant heat capacity. Other mechanisms, such as chemical reactions, are not contributors to the HHSTT problem. Recognizing that these advanced considerations must be accounted for in the EOS (typically through internal state variables), the EOS becomes much more involved [6].

Because the creation of a single EOS formulation that encompasses a large body of materials remains elusive, equations of state tend to be developed for a specific material - and even specific impact conditions. These EOS formulations are then validated against experimentation (high energy impact).

Fortunately, CTH not only possesses many analytical EOS formulations, with the appropriate constants for specific materials, but it also includes a very powerful, and frankly unique, database of experiments for many materials. These experiments

have measured the state variables for hypervelocity impacts, explosions, and other high energy events. The states are recorded in a table which CTH can reference in the solution procedure. These tables create a solution surface in state variable space that includes all of the higher order effects noted above. In essence, the EOS is not so much an equation, as a state look-up table. Therefore, all the advanced conditions and cases are inherently included due to the nature of the experimentation.

For the materials in the HHSTT gouging problem, CTH has EOS tables for VascoMax 300 and iron. The iron EOS is considered very accurate for low carbon steels, like 1080 steel - and includes the phase transitions that occur at high pressure and temperature. Therefore, from an EOS point of view, CTH is uniquely suited to solve the gouging problem. Additionally, the EOS tables include non-equilibrium thermodynamic effects that occur in these hypervelocity impacts.

With the EOS solving the volumetric (spherical) stress components of the impact, we require a constitutive model of the materials to handle the deviatoric portion of the deformation.

3.3 Constitutive Models

In order to solve the deviatoric stress portion of the high energy impact problem, a constitutive model is required. A constitutive model is a relationship defining the dynamic yield strength (also known as material flow stress) of the material. This is, of course, much different than the static yield strength of the same material. As the concept of the material constitutive model has developed over the last several decades, more aspects of the problem have been considered in the model. Most of the modern formulations of material flow models have recognized the effects of strain (ε_{ij}), strain-rate $(\dot{\varepsilon}_{ij})$, and temperature [129]. This can be expressed as:

$$\sigma_{ij} = f(\varepsilon_{ij}, \dot{\varepsilon}_{ij}, T) \tag{3.19}$$

Figure 3.1 illustrates the basic relationships. Increasing strain and strain-rate lead to higher flow strength (strain hardening and strain-rate dependency respectively), while increasing temperature results in lower dynamic yield strength (thermal softening). Note that we are now discussing quantities known as "effective stress" and "effective strain/strain-rate." This is due to the fact that creating constitutive models that are functions of the entire stress tensor is very cumbersome. Therefore, an isotropic material is assumed, and stress is taken to be a function of scalar quantities [129].
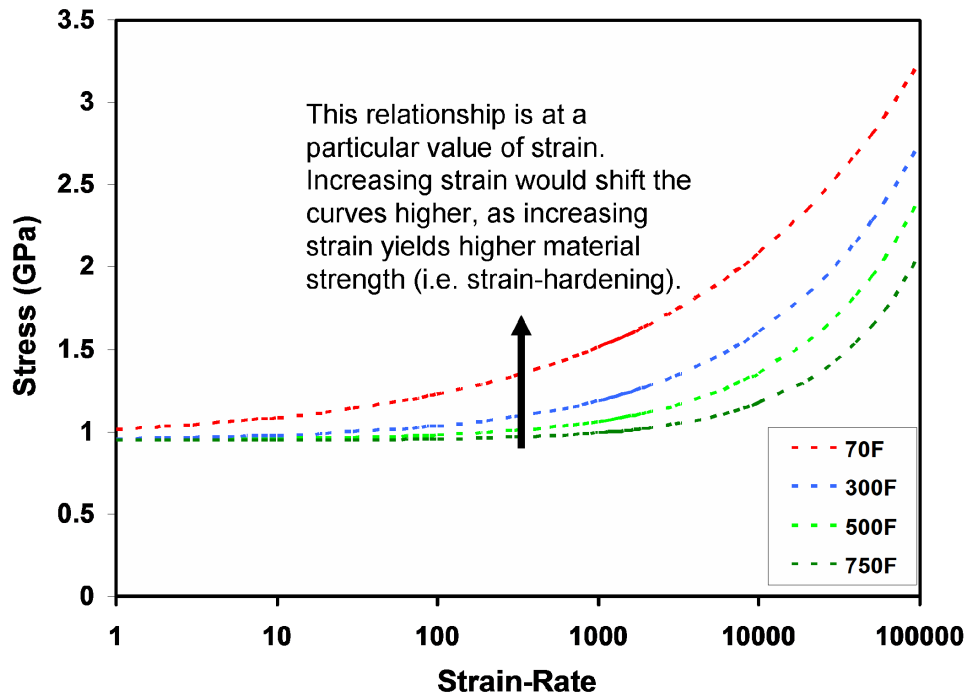
Figure 3.1:   **General Constitutive Model Relations.**

There are numerous constitutive models available in the literature and within the CTH code. The major differences between them revolve around being able to manipulate the strength curve with respect to the above-mentioned parameters to create desired results, or on how linked the specific formulation is with material properties/characteristics. Some of them attempt to account for non-continuum effects, such as material microstructure and defects. Others are simply empirically based flow models based on experimentation.

Two of the most widely used constitutive models are the Johnson-Cook and the Zerilli-Armstrong formulations. The strength of these particular models is the strong success that they have historically enjoyed in modeling material behavior, while being straightforward enough to be determined for a specific material without inordinate expense.

Previous modeling efforts by Szmerekovsky were based on the Steinburg-Guinan-Lund model [100–102] for VascoMax 250 and the Johnson-Cook model for iron. Unfortunately, CTH's implementation of the Steinburg-Guinan-Lund model for VascoMax 250 was a rate-independent version - a fact not known to the researcher. Therefore, the results generated by his models are limited to a single value of flow stress (given constant temperature and strain) over the wide range of strain-rates. Additionally, the Johnson-Cook model for iron is limited in its applicability to a relatively high strength steel, such as 1080 steel, which has very different strain-rate dependency. These factors prompt this author to seek specific, verifiable material flow models for VascoMax 300 and 1080 steel.

The Johnson-Cook model was formulated first in 1983, and was proposed as predominately an empirical model [54]. Later work on the model highlights the fact that some of the constants show trends based on material properties and families of materials (i.e. all steels may share a certain range for a particular constant). The Johnson-Cook model relates the material flow stress (dynamic yield strength), σ, as:

$$\sigma = [A + B\varepsilon^n][1 + C\ln\dot{\varepsilon}^*][1 - T^{*m}] \tag{3.20}$$

where ε is the equivalent plastic strain, $\dot{\varepsilon}^*$ is the dimensionless strain-rate ($\dot{\varepsilon}^* = \dot{\varepsilon}/\dot{\varepsilon}_0$ and $\dot{\varepsilon}_0 = 1.0 \ s^{-1}$), and T^* is the homologous temperature defined as:

$$T^* = (T - T_{room})/(T_{melt} - T_{room}) \tag{3.21}$$

3-10

The constants A, B, C, m, and n are determined via experimental testing. The Johnson-Cook model is somewhat easier to experimentally determine because of the discrete parts that account for the various parameters. The first portion is the static yield strength and a modification for strain. The second portion adds the strain-rate dependency. The final portion adds the temperature effects. By performing experiments in a state of uniaxial strain, over a range of temperatures and strain-rates, one can create the model for chosen values of strain.

The primary limitation to the Johnson-Cook model is that is creates a flow stress curve that is linear with respect to strain-rate. That is, the curves represented in Figure 3.1 cannot be produced by the Johnson-Cook model. Rather, those curves would be linear. For some applications, this model is sufficient - especially if the strain-rates under consideration remain at 10^4/sec or less.

The type of constitutive model that generated the curves in Figure 3.1 is the Zerilli-Armstrong model. The Zerilli-Armstrong formulation was first proposed in 1987 [126]. This model is based more upon microstructural characteristics of the materials - yet still retains an empirical basis similar to the Johnson-Cook model. In the Zerilli-Armstrong model, the flow stress, σ, for a face-centered cubic (FCC) crystal lattice is:

$$\sigma = \Delta\sigma'_G + c_2\sqrt{\varepsilon}\,e^{(-c_3 T + c_4 T \ln \dot{\varepsilon})} + k\sqrt{\ell} \qquad (3.22)$$

where $\Delta\sigma'_G$ is a stress component accounting for dislocation density, $k\sqrt{\ell}$ is an incremental stress term which includes the microstructural stress density, k, and the average grain diameter, ℓ. As with the Johnson-Cook formulation, ε is the effective plastic strain, $\dot{\varepsilon}$ is the effective plastic strain-rate, and T is temperature. The terms c_2 through c_5 are experimentally determined for each specific material. It is important to note that the units of these constants must be reported, and that the units of c_3 and c_4 must cancel the selected units of T. This formulation is modified slightly for the body-centered cubic (BCC) lattice material:

$$\sigma = \Delta\sigma'_G + c_1 e^{(-c_3 T + c_4 T \ln \dot{\varepsilon})} + c_5 \varepsilon^n + k\sqrt{\ell} \tag{3.23}$$

Note that the some of the terms were slightly modified. It is possible to combine Equations 3.22 and 3.23 into one expression, in which either $c_1 = 0$ for FCC materials, or $c_2 = 0$ for BCC materials (which is the case for the two which are considered in this work). Additionally, one can combine the material specific terms which do not rely on experimentation into a single expression by allowing $A = \Delta\sigma'_G + k\sqrt{\ell}$. The combined expression then becomes:

$$\sigma = A + (c_1 + c_2\sqrt{\varepsilon})e^{(-c_3 T + c_4 T \ln \dot{\varepsilon})} + c_5 \varepsilon^n \tag{3.24}$$

This is the formulation which will be used in this study. Therefore, the terms A, n, and c_1 through c_5 (with $c_2 = 0$) are those that will be determined for the specific materials.

These two constitutive models establish the viscoplastic flow stress for the materials under dynamic deformation. They both are strain-rate dependent and include the characteristics of strain-hardening and thermal softening. These two particular constitutive models are the most widely used within the field due to the fact that some straight-forward experimentation can be employed to determine the model constants. Additionally, they have a history of generating accurate results if they are judiciously applied to impact problems.

With the deviatoric stresses being solved via the material constitutive relationships, the final element of the theoretical approach is the delineation of the failure model.

3.4 Failure Model

The topic of failure models and their application in the solution of hypervelocity impact, especially within computational codes, is a particularly wide-ranging topic

[127–129]. There are many different approaches to the concept of defining the criteria (such as pressure, temperature, shear stress, etc.) which lead to material failure. Unfortunately, even the most complex theories, based on microstructural factors, are inadequate to apply across a range of materials [129]. There are very few that gain acceptance by the community of hypervelocity impact researchers and therefore become placed into the computational codes.

One of the most accurate approaches for the failure of metals, specifically, is the establishment of a hydrostatic failure pressure at which the material fractures. In the absence of accepted theory on the determination of this pressure, it is typically determined from experimentation. In this case, isentropic material properties are assumed, and an uniaxial fracture stress is used to estimate the failure pressure. The Von Mises failure criterion is the most common, and most accurate, for metals undergoing deformation [17]. Using the notation of this Chapter:

$$(\sigma_1 - \sigma_2)^2 + (\sigma_2 - \sigma_3)^2 + (\sigma_3 - \sigma_1)^2 = 2\sigma^2 \tag{3.25}$$

where σ is the uniaxial flow stress and σ_1, σ_2, and σ_3 are the principal stresses.

CTH, in its solution procedure, uses this hydrostatic failure pressure, called the fracture pressure within the code, to delineate the failure criterion. Cells with mixed material will take on a volume averaged failure pressure, unless specifically specified otherwise.

As discussed in Chapter II, many contemporary researchers are attempting to create more advanced failure criteria and damage algorithms [2, 46, 118–122]. However, these approaches have not yet achieved widespread acceptance nor have they been made available within the major hydrocodes. Therefore, their utility is limited. Additionally, these investigators have not yet proven their theories, when applied to hypervelocity impact cases, will replicate experimental results with greater accuracy than the current approach.

Therefore, for the purpose of this study, the hydrostatic failure pressure approach will be utilized. The determination of the specific quantity of this failure pressure from experiment will be described in Chapter V.

This brief theoretical overview, then, establishes the framework upon which this study rests. In order to accurately model hypervelocity gouging, we need to determine the constitutive models for VascoMax 300 and 1080 steel. The EOS for these materials within CTH is extremely accurate, experimentally-based, and includes non-equilibrium thermodynamic characteristics. However, there are no accurate constitutive expressions for the material in question. Once we arrive at the constitutive models, a validation of CTH's ability to model impact scenarios needs to be conducted. Using this approach, we can be assured that we have created the most accurate computational model of the HHSTT problem.

Additional theory will be presented as it specifically applies to the study being discussed. In this way, the clarity of the approach will be maintained.

Before the constitutive models for VascoMax 300 and 1080 steel are determined, the characteristics of gouging needs to be explored via an experimental examination of a gouged rail from the HHSTT.

IV. Characterization of Gouging

In order to more fully understand the phenomenon of hypervelocity gouging, a section of gouged rail from the HHSTT was examined. As previously described in Chapter II, the sled experiences catastrophic deceleration at the end of a successful test. Therefore, gouged shoes are not available for examination.

The gouged rail was examined using the most modern techniques in order to understand the characteristics of gouging and to develop experimental elements for CTH to replicate as a part of the model validation process. The examination of the gouged rail revealed a thermal profile that can used to compare against simulation results [29–31].

Based on the results of examining the gouged rail, and the resulting evidence of thermally-induced microstructure change, an examination of additional rail sections was undertaken. A slightly damaged section and three sections of undamaged rail were investigated to determine if microstructure changes are evident in these as well.

4.1 Methodology for Examining Gouge

The HHSTT has changed materials for the hypervelocity sled's shoes many times in an effort to mitigate gouging. For example, in 1973 [42], the rail (fabricated of ANSI 1080 steel) and the shoes (at that time constructed of 304 and 17-4 PH stainless steel) were examined following a 1.77 km/s test run. The microstructure of the damaged area was examined and the authors concluded that shear bands and distorted pearlite comprised a majority of the subsurface effects. This treatment, however, was limited to optical microscopy and did not make an examination of the microstructure into the depth of the rail (away from the impact interface).

Similar to this previous work, a section of rail (featured in Figure 1.5) damaged at approximately 2.1 km/s was sliced normal to the direction of motion to prepare specimens for metallographic analysis. The slice was removed from the center of the gouge, as measured in terms of the gouge's orientation down the rail, in the direction of the sled's motion. Figure 4.1 is of the slice of damaged rail, with the velocity vector

of the sled shown. This rail section has an iron-oxide coating applied to aid in the mitigation of the gouging event.
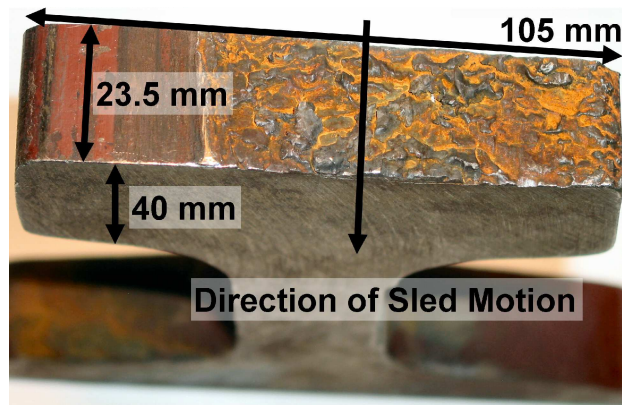
Figure 4.1:   **Section of Gouged Rail.**

The top of this rail section was removed, and made into four separate specimens, denoted as specimens B1 through B4. An undamaged rail section was likewise sectioned to serve as the experimental control. Figure 4 indicates the orientation of these samples. For samples B1, B2, and B3, the face examined is the one pictured in Figure 4.2. The face examined for specimen B4 was the face shared with B3, or the plane of the specimen along the velocity vector of the sled (lengthwise down the gouge).
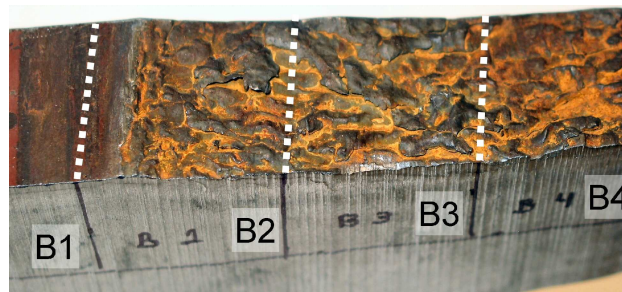
Figure 4.2:   **Gouged Rail Specimen Location (specimens are approximately cubic, with 25mm sides).**

The samples were mounted in conducting material and polished to a 0.05-micron finish using standard techniques. The fine polishing was limited to using diamond. It was noted that if the samples were further polished using 0.05-micron colloidal silica,

the samples partially etched, even though the preparation was at a neutral pH. The best results for examining the microstructure of the 1080 steel were obtained using an electro-polishing technique instead of the silica as the last step. In addition, etched specimens (with a standard 3% nital etch) were prepared.

Therefore, three different preparations were available for examination. The first was created by polishing the specimens to a 0.5-micron finish with diamond and finishing them with silica - which will be referred to as the "as-polished" state. The second was created by finishing them with an electro-polish instead of silica - which will be referred to as "electro-polished." Finally, the third preparation was created by etching the specimens finished with silica - which will be referred to as "etched."

The specimens were examined in polarized light, in bright field, and using a scanning electron microscope (SEM) as appropriate to the final finish. Micro hardness testing and Energy Dispersive X-Ray Spectroscopy (EDS) was performed on the specimen in the as-polished state and Orientation Imaging Spectroscopy (OIM) in the electro-polished state. Table 4.1 summarizes the various preparations, what examination techniques were applied, and provides their nomenclature – which is used for the balance of this work. The facilities at the Air Force Material Laboratory, Materials Division, at Wright-Patterson AFB were generously made available for this analysis.

4.2 Results of the Examination of Gouged Specimens

The examination of the gouge specimens indicated a large thermal event that permanently changed the microstructure of the steel. This change was evident to the naked eye, as well as through the many examination techniques applied.

Specimens in the as-polished state exhibited a partial etch of the surface that was visible to the naked eye. Putting a camera at a slight angle to the surface of the specimen and taking a flash photograph revealed a clear impact affected area. It should be observed that not only is a plastically deformed region present, but also a zone that appears to be affected by the heat of the event (see Figure 4.3). Figure

Table 4.1:   Summary of Specimen Preparation/Examination Techniques.

	Polished with diamond to .05 micron, finished with silica - partial etch	Polished with diamond to .05 micron, finished with silica, etched with 3% nital	Polished with diamond to .05 micron, electro-polished
Optical Microscopy, Polarized Light	X		X
Optical Microscopy, Bright Field Light		X	
Scanning Electron Microscopy (SEM), both primary and backscatter modes	X		X
Energy Dispersive X-Ray Spectroscopy (EDS)	X		
Orientation Imaging Spectroscopy (OIM)			X
Nomenclature	As-polished	Etched	Electro-polished

4.4 provides a comparison of specimen B4 to specimen A4 (from the undeformed rail) and the differences are clear. The lower right section of B4 shows a crack that was present down to a rail depth of 31 mm. In addition, the removal of approximately 5 mm of material from the rail is evident in this figure.
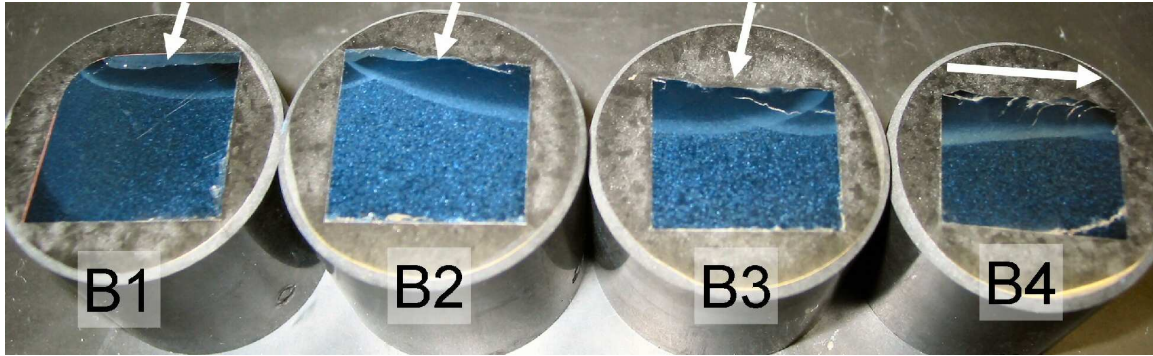
Figure 4.3:   **Overview of Heat Affected Zone (velocity vector of sled shown by the arrows).**
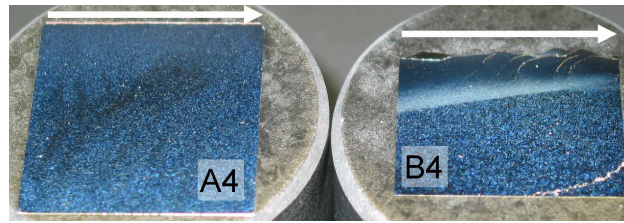
Figure 4.4:   **Comparison of Rail Specimens (A4 and B4, sled velocity vector shown by arrows).**

Closer to the surface in the same specimen are some clear shear bands (further justified and described later in this work) and indications that the material flowed in the direction of the sled's travel to modify the top of the typical cracking in the gouged area that was previously reported in [42]. That is, the curvature of these shear bands being concave against the sled's motion in [42] is modified at the top to follow the plastic flow of the material. In specimen B4, seven such discrete bands are present (with similar shape) indicative of the material flowing close to the surface, and thereby modifying the shear band curvature. This material flow indicates that the surface melted during gouging impact [42].

It is helpful, at this point, to note that all of the 1080 steel specimens contained inclusions and flaws in the microstructure due to the manufacturing. In addition, after metallurgical examination of all the deformed rail specimens, it was concluded that all of their microstructures were significantly similar - therefore the results for B4 are representative. Finally, where available, the microstructure reported was matched against published micrographs elsewhere in the literature (in particular in [38] and [99]).

When the entire specimen B4 is examined, the zone affected by the thermal characteristics of the hypervelocity impact is evident. Figure 4.5 shows B4 in an etched state (and is in the plane of motion examined by the computer modeling, see Section 2.3).

The structural variation from the impact interface down into the body of the rail is very evident. In this preparation, the longitudinal "roll marks" from manufacturing process are clear (in Figure 4.5 they are the black horizontal striations and black spheroids through the thickness of the specimen). It appears at this magnification that there are some clear zones of different microstructures. Also, there is a very clear demarcation between the affected zone and the unaffected rail below. This figure is marked with those microstructures identified, along with Rockwell Hardness test C (HRC) values through the depth of the specimen. The justification and presentation of these microstructures appear in the remainder of this section.

The top of the specimen (i.e. the top of the gouge), was characterized by a significant amount of material flow, mixing (addressed later in this work), and evidence of rapid cooling - martensite. This is consistent to the previous results in [42]. Determination that this layer is martensite comes from the etch-resistant nature of the material, the measured HRC values (which correspond to the value for martensite appearing in literature [38,99]), and an Orientation Imaging Spectroscopy (OIM) test. The OIM evaluation identified the characteristic body-centered tetragonal (BCT) crystal structure, small grain size, and a lack of a preferred grain orientation (which

Martensite
(HRC 55)
Split Trans
(HRC 42)
(HRC 40)
Fine Pearlite
(HRC38)

(HRC 40)
Split Trans
(HRC 41)
(HRC 34)
Coarse Pearlite
(HRC 30)

Coarse Pearlite
(HRC 30)

1 mm
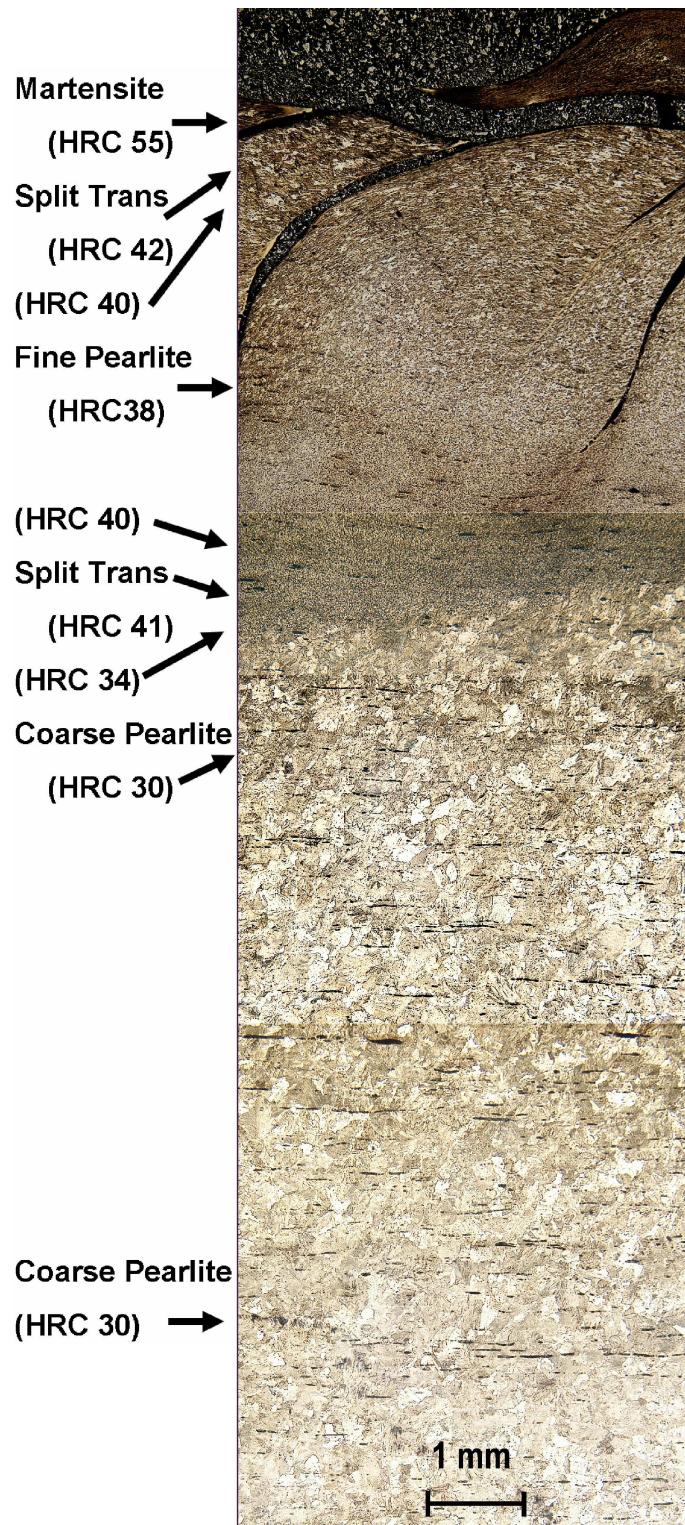
Figure 4.5:   Specimen B4 - Overall View (etched, sled travel is left to right).

implies rapid cooling, consistent with martensite formation [38, 99]). The carbon content of 1080 steel (0.8 %) restricts residual austenite concentration to a maximum of 10%. The OIM analysis indicated the presence of austenite's face-centered cubic (FCC) crystal structure, but not in significant amounts. While this phase is present, its inclusion does not affect the conclusion of this analysis. Figure 4.6 shows the top of the specimen and the layer of martensite. The back scatter mode of the SEM is denoted as BSE (back scatter emitter).
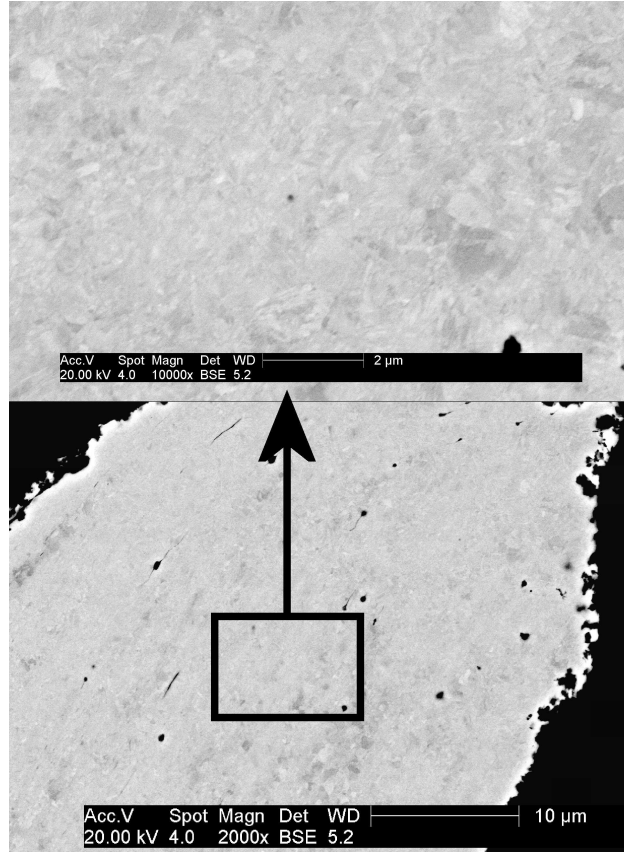
Figure 4.6:   **Top of Deformed Specimen (as-polished, SEM, BSE [2000x and 10000x]).**

Immediately below this top layer of martensite is a very distinct zone of microstructure that is a split transformation. A split transformation is a mixture of martensite and extremely fine pearlite that results from cooling from the austenizing temperature for 1080 steel (or eutectoid steel) of about 725°C. This kind of microstructure is very similar to that reported in [99] for rapidly/continuously cooled eutectoid

steel. The HRC value for this zone of microstructure is 42, which corresponds to a split transformation hardness value. Additionally, the OIM detected a mixture of BCT (martensite) and body-center cubic (BCC) crystal structure with a trace of FCC components (austenite). The BCC constituents represent ferrite (alpha phase), which along with cementite, form the fine pearlite. The grain sizes were small and showed no orientation preference - indicating a fast cooling rate [38, 99]. Figure 4.7 shows this microstructure, while Figure 4.8 depicts the transition from this zone to one of fine pearlite. In these pictures, the lighter colored structures are martensitic and the darker are pearlitic. A similar microstructure can be generated through an extended period of tempering (measured in many hours), in which carbides precipitate out of the ferrite in a process known as spheriodization. However, we know from the HHSTT that these gouges cool to the touch in minutes due to rapid cooling. Additionally, the extreme energy of these hypervelocity impacts and evidence of melting on the railhead [42] allow us to conclude that the affected steel completely austenizes and that this microstructure is, in fact, a split transformation.

Examination, through the depth, below the top zone of split transformation revealed a zone characterized by fine pearlite. The HRC in this area also matches what has been reported in the literature for a fine pearlitic microstructure [38, 99]. The OIM examination yielded a predominant BCC crystal structure which indicates pearlite, and larger grain sizes. The grains had more of a preferred alignment, but were still indicating variability associated with fairly rapid cooling from austenite. Figure 4.9 illustrates this microstructure. Figure 4.10 is of one of the major shear bands in this area, with a layer of martensite along the fracture surface, and matches results reported in [42]. The presence of martensite was verified by hardness testing and optical metallurgy. This martensite forms as the material heated from plastic deformation rapidly cools when the material fractures.

Below the area of fine pearlite, at the edge of the zone that is visible in both Figures 4.4 and 4.5, is another zone of split transformation. The HRC was measured as the higher value associated with the mixture of martensite and pearlite. The OIM
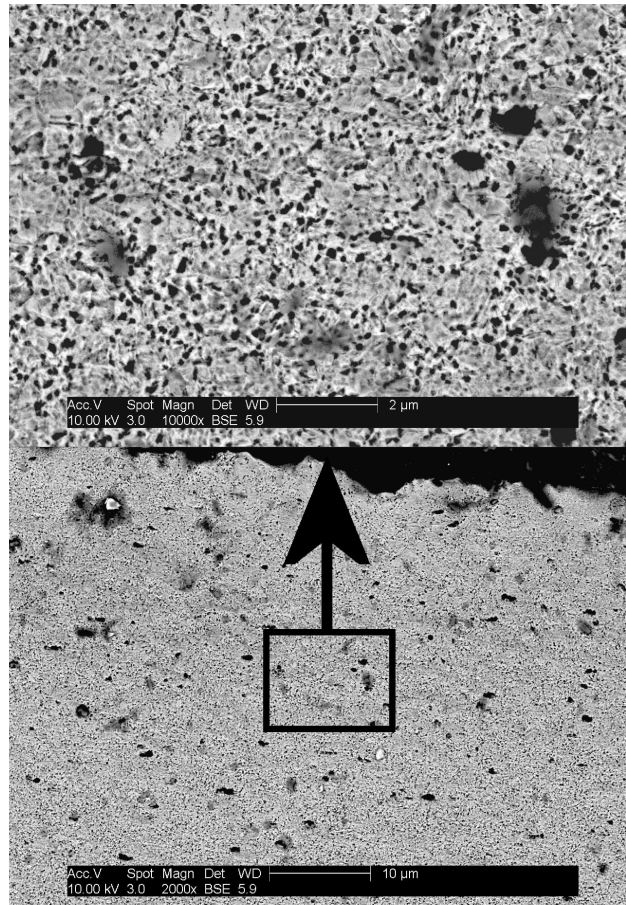
Figure 4.7:   **Top of B4 - Split Transformation (electro-polished, SEM, BSE [2000x and 10000x]).**
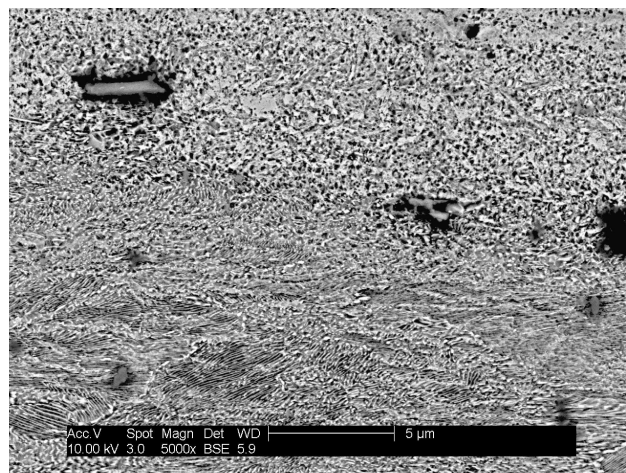
Figure 4.8:   **Top of B4 - Split Transformation Transition (electro-polished, SEM, BSE [5000x]).**
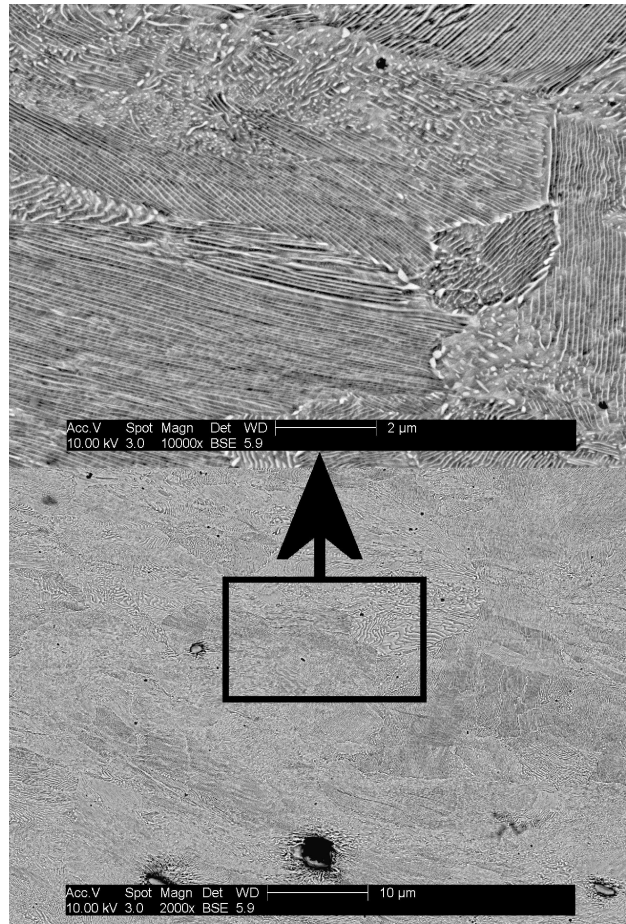
Figure 4.9:   **Top of B4 - Fine Pearlite (electro-polished, SEM, BSE [2000x and 10000x]).**

again returned a zone of mixed crystalline structures and smaller grain sizes. Again, the grains showed no preferred orientation. This microstructure appears in Figure 4.11.

Examination below this heat affected zone revealed microstructure that transitioned immediately to coarse pearlite. This area yielded a HRC value consistent with typical coarse pearlite. The OIM analysis confirmed this with predominate BCC structure, large grains, and preferred orientations that characterize steel that has cooled slowly. The coarse pearlite observed continues throughout the depth to the bottom of the specimen. Figure 4.12 shows this coarse pearlitic microstructure and it is virtually identical to Figure 4.13 - which depicts the microstructure of specimen
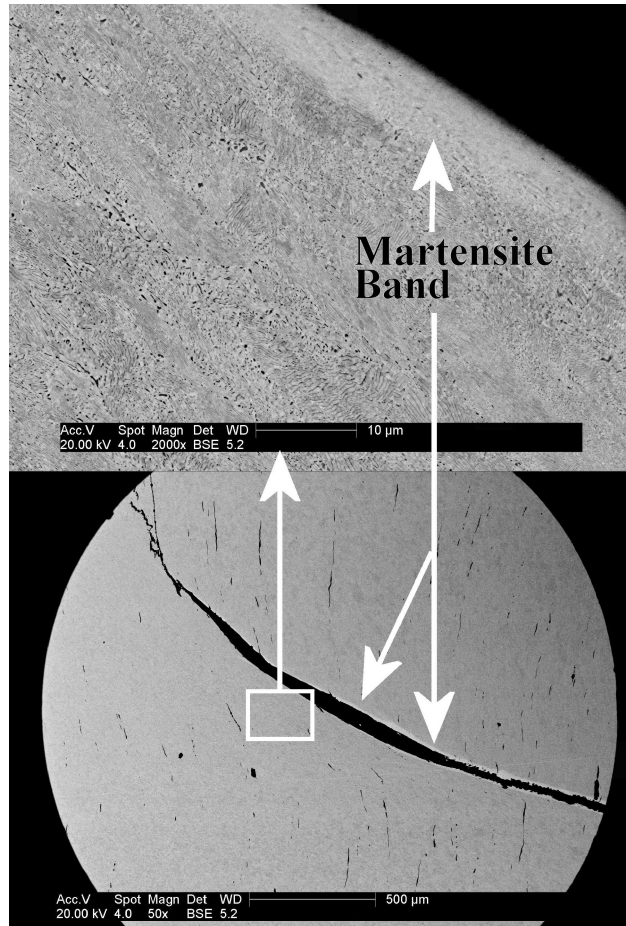
Figure 4.10: **Specimen B4 - Shear Band (electro-polished, SEM, BSE [50x and 2000x]).**

A4's undamaged microstructure. A reference OIM analysis performed on specimen A4 yielded similar results to those of the coarse pearlite in specimen B4.

This examination, through the depth, of the gouged rail has indicated various microstructures that match those in literature [38,99]. The HRC hardness results and the OIM analysis match the microstructures identified by metallography. Unfortunately, a similar study with the sled shoes is not possible, due to the destructive sled slow-down technique applied at the HHSTT.

In order to ascertain the material composition of the impact zone, Energy Dispersive X-Ray Spectroscopy (EDS) was performed on the damaged rail, and on undamaged specimens of the rail (1080 steel) and shoe (VascoMax 300). The damaged
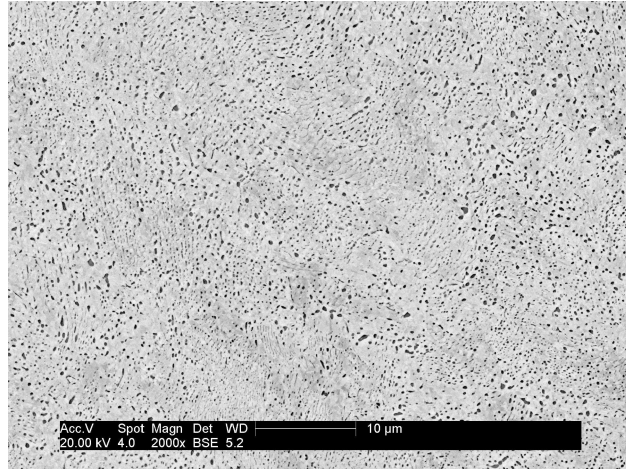
Figure 4.11: **Edge of Heat Effected Zone - Split Transformation (as-polished, SEM, BSE [2000x]).**
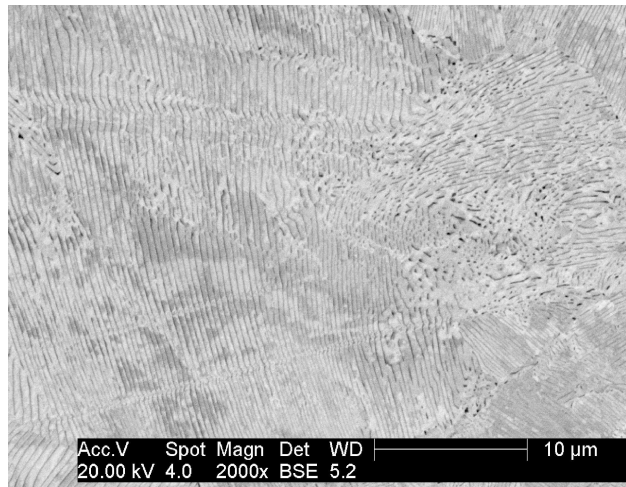
Figure 4.12: **Specimen B4 - Below Heat Affected Zone (as-polished, SEM, BSE [2000x]).**

specimen matched the composition of the undamaged rail exactly with the exception of the area near the surface. At the top of the damaged rail, constituents such as nickel and cobalt (which is part of the composition of the shoe and not the rail steel) were found. This confirms a mixture of shoe and rail material that characterizes the gouging phenomenon.

Figure 4.13:   **Specimen A4 Microstructure (as-polished, SEM, BSE [2000x]).**

4.3   Analysis of Gouge Results

In the examination of this damaged rail section, it became clear that a large thermodynamic event was the mechanism that created a significant portion of the phenomenology present. There are microstructural changes in the deformed rail that indicate a large thermodynamic input into the event. That is, the material damage must include a large temperature effect to account for the metallurgical results presented above.

From a macroscopic perspective, the shear bands resulting from catastrophic thermoplastic shear reported in [42] were verified. It is interesting to note that these shear bands match the character of the bands predicted by computer modeling of the impact event in [104–106, 108, 109]. The shear bands show evidence of martensite formation along the fracture surfaces consistent with thermoplastic activity followed by rapid quenching [42].

The experimentally observed microstructure suggests a thermodynamic history. The various types of final structure are the result of cooling from an austenizing temperature. In some applications, this quenching is done with oil or water baths. In others applications, the steel is allowed to air cool, which quenches the surface and the interior at different rates [38, 99]. The continuous (i.e. non-isothermal) cooling

diagram for 1080 steel was obtained [99] and verified by the rail manufacturer for the HHSTT. This diagram, adapted from [99], appears as Figure 4.14. Table 4.2 summarizes the microstructure resulting from various cooling rates when the steel starts above the austenizing temperature of 725°C.
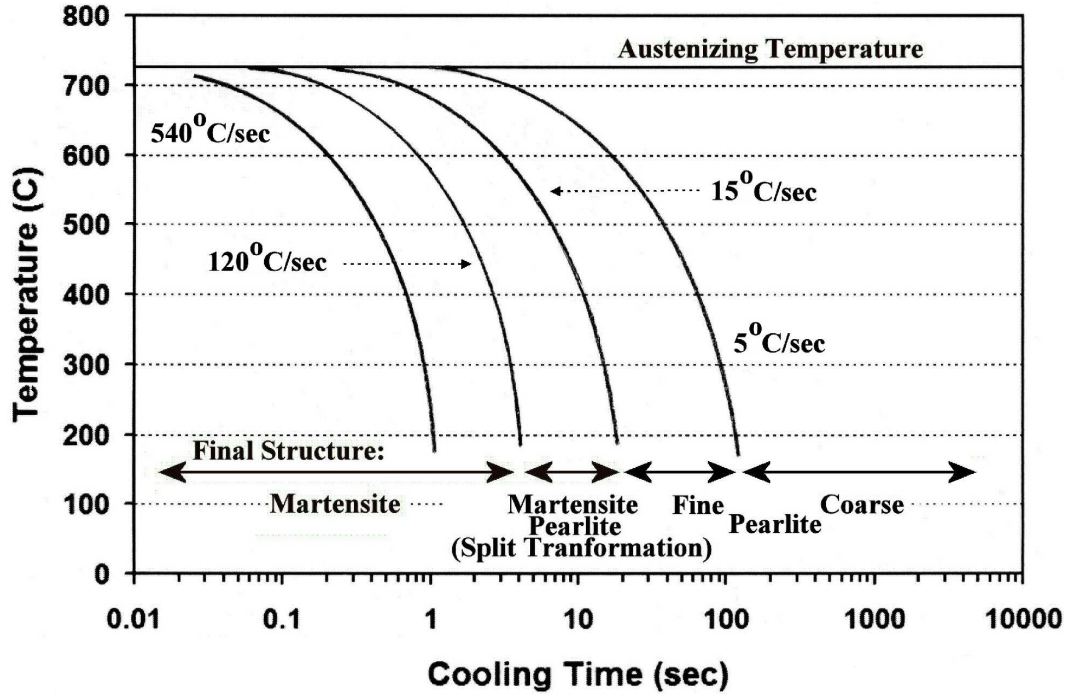
Figure 4.14: **Continuous Cooling Curve for 1080 Steel (adapted from [99]).**

Both the reports in [42] and our examination of the rail gouge indicate the surface of the rail had reached the melting temperature of 1480°C and therefore having the rail begin this process above the austenizing temperature seems very plausible. In addition, the models in [104–106, 108, 109] predict high temperatures into the rail at these depths.

Examining these events in terms of thermodynamics with continuous cooling, a description of the impact event that explains the microstructure revealed in experimentation can be proposed. The rail, undergoing plastic impact, heats above the melting temperature (1480°C) on the surface, and that material flows and partially sloughs off (seen in [42]). The rail heats above the austenizing temperature (725°C)

Table 4.2: Summary of Resulting Microstructure
from the Continuous Cooling of 1080 Steel.

Microstructure	Cooling Rate	Rockwell C Value (HRC)
Martensite	120°C/sec or faster	50 - 65
Martensite/Fine Pearlite (split transformation)	15°C/sec - 120°C/sec	40-50
Fine Pearlite	5°C/sec - 15°C/sec	35-40
Coarse Pearlite	5°C/sec or slower	30-35

down to a depth of approximately 7 - 10 mm below the original rail surface (or approximately 3 mm to 5 mm down into the remaining material below the gouge). Because this impact event only lasts in the neighborhood of 20 microseconds, the material below the heated zone is at the ambient temperature. That is, insufficient time (i.e. several seconds) is available for the conduction of the heat to occur and no plastic deformation has occurred to generate viscoplastic temperature change.

When the deformation event has concluded (and the shoe has moved downrange) the rail immediately begins to cool. The heat is able to quench quickly into the air above the rail and into the steel below the austenized region - which explains the rapid cooling-related microstructure at the railhead and down at the lowest depth of the heat affected zone. Rapid quenching into the air is aided by the turbulent airflow generated by the test sled traveling at speeds above 2 km/sec. The ability of steel to quench rapidly both into the air and depth (when a part of a contiguous structure that was plastically deformed beyond the austenizing temperature) was noted in [42]. The area between these zones would cool more slowly.

The area below the heat affected zone would not have heated during impact, but would heat as the thermal pulse travels into the depth of the rail. If this heat pulse was insufficient to increase the rail's temperature above the austenizing limit, then no appreciable microstructure change would occur. This section of the rail would

be indistinguishable from the undamaged rail. Figure 4.15 illustrates this proposed thermal history.
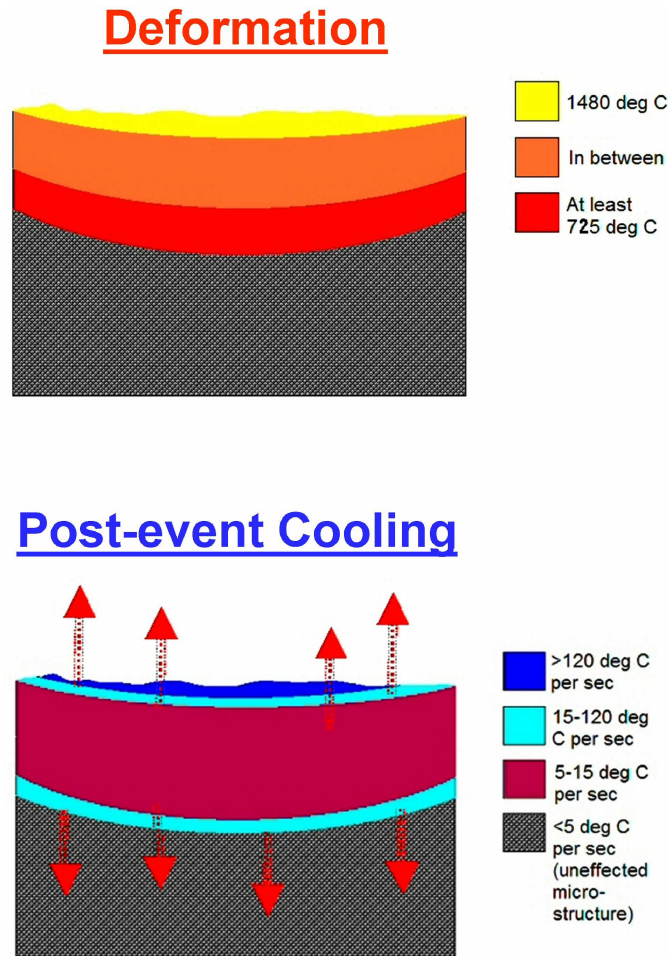
Figure 4.15:   **Proposed Thermal History of Hyperveloc-ity Gouge.**

A one-dimensional heat conduction analysis can be used to validate the cooling rates suggested by the observed microstructure. Taking a one-dimensional slice through the depth, with the initial heat distribution noted in Figure 4.15, creates the depiction appearing in Figure 4.16. Note that x is defined as zero at the surface, down to ℓ. Due to the similarity of the heat profile and conduction across the gouge, this one-dimensional slice is a fairly accurate representation of the heat transfer path.

By applying Newton's Law of Cooling, we can arrive at the familiar heat conduction relationship:
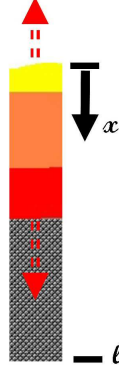
Figure 4.16:   **One-Dimensional Slice of Cooling Gouge.**

$$\frac{\partial T}{\partial t} = \frac{1}{\rho C_\nu} \nabla \cdot (K \nabla T) \tag{4.1}$$

where T is temperature, t is time, ρ is density, C_v is specific heat at constant volume, and K is the thermal conductivity.

The one-dimensional form of this equation becomes:

$$\frac{\partial T(x,t)}{\partial t} = \frac{1}{\rho C_\nu} \frac{\partial}{\partial x} (K \frac{\partial T}{\partial x}) \tag{4.2}$$

In Equation 4.2, the x coordinate is defined in Figure 4.16, and we note that K is a function of temperature. Typical solutions for this equation rely on establishing boundary conditions and holding K constant. As an example, let us consider a constant K and T to represent temperatures above ambient (300 K) – therefore the boundary conditions are zero at the rail surface and the bottom of our specimen.

Solving Equation 4.2 in the standard manner, we arrive at the solution:

$$\begin{aligned} T(x,t) &= \sum_{n=1}^{\infty} [\tfrac{2}{\ell} \int_0^\ell f(x) \sin(\tfrac{n\pi x}{\ell}) dx] \cdot \sin(\tfrac{n\pi x}{\ell}) e^{-\lambda_n^2 t} \\ where \quad \lambda_n &= \sqrt{\tfrac{K}{\rho C_\nu}} \cdot \tfrac{n\pi}{\ell} \end{aligned} \tag{4.3}$$

where $f(x)$ represents the initial thermal profile estimated from knowing that the railhead was at the melt temperature (from [42] and experimental observations), and

Table 4.3:   Summary of Thermal Conductivity of 1080 Steel [52].

Temperature (°C)	K {W/(m K)}
0	49.8
100	48.1
200	45.2
300	41.4
400	38.1
500	35.1
600	32.6
700	30.1
800	24.3
1000	26.8
1200	30.1

that the lowest depth of microstructure change must necessarily have been above the austenizing temperature. We can create an estimated temperature profile at time $t = 0$ by fitting a smooth curve through these known end conditions, and forcing it to go rapidly to zero beyond the austenizing limit. This form matches those created by previous numerical simulation [104–106, 108, 109]. Our assumption that K is constant can be modified with experimental data concerning the thermal conductivity as a function of temperature. Table 4.3 summarizes this data.

Equation 4.2 was solved numerically, with K varying with temperature per Table 4.3. A linear fit was assumed between the discrete experimental points reported in Table 4.3. The results of this evaluation indicate that the estimated cooling rates needed to generate the presented microstructure are created. Figure 4.17 is a depiction of the entire range of dimensionality, from railhead to the bottom of the specimen. The various curves represent the temperature, through the specimen depth, at particular moments in time. The profile at time $t = 0$ was estimated as described above. Note

that although the heat pulse moves down into the rail, the pulse does not move an austenizing temperature (700°C above ambient) lower into the depth.
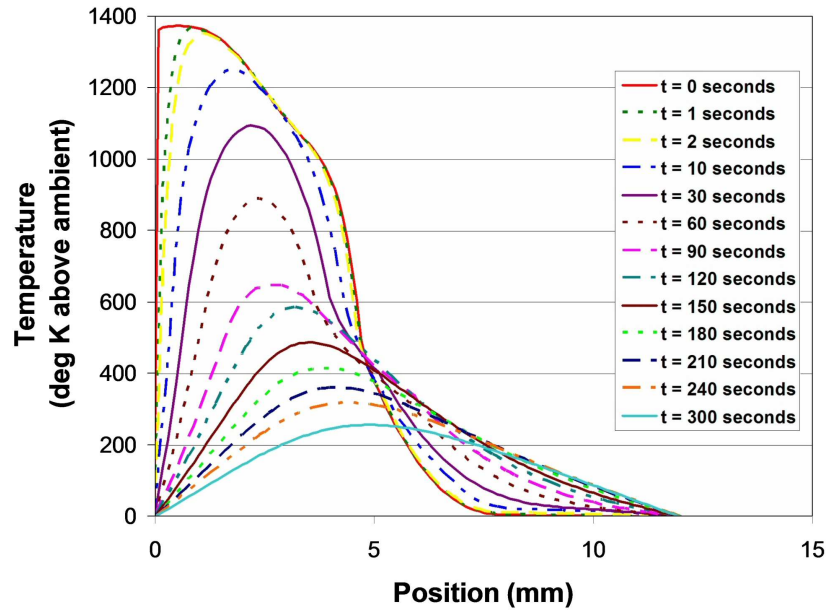
Figure 4.17:   **1080 Steel Specimen Cooling.**

If we examine the area of our concern, at temperature above the austenizing limit, we arrive at Figure 4.18. More time points are represented in this figure to aid in our discussion.

It is clear from the closer view that there is a thermal gradient established though the depth as the heat travel to either the rail top or down into the rail depth. Figure 4.19 depicts the gradient as the temperature passes the critical austenizing limit. The figure also indicates the cooling rates required to generate the various microstructures and the cooling time for that particular rail depth position to cool below the austenizing temperature. Clearly, the thermal conductivity of 1080 steel is sufficient to create the microstructures identified from the HHSTT gouge. The layer of martensite at the gouge surface, the split transformation directly below the martensite, and the zone of fine pearlite are predicted exactly as we observed. Additionally, the split transformation within the depth of the specimen is predicted, along with the abrupt transition to unaffected microstructure.
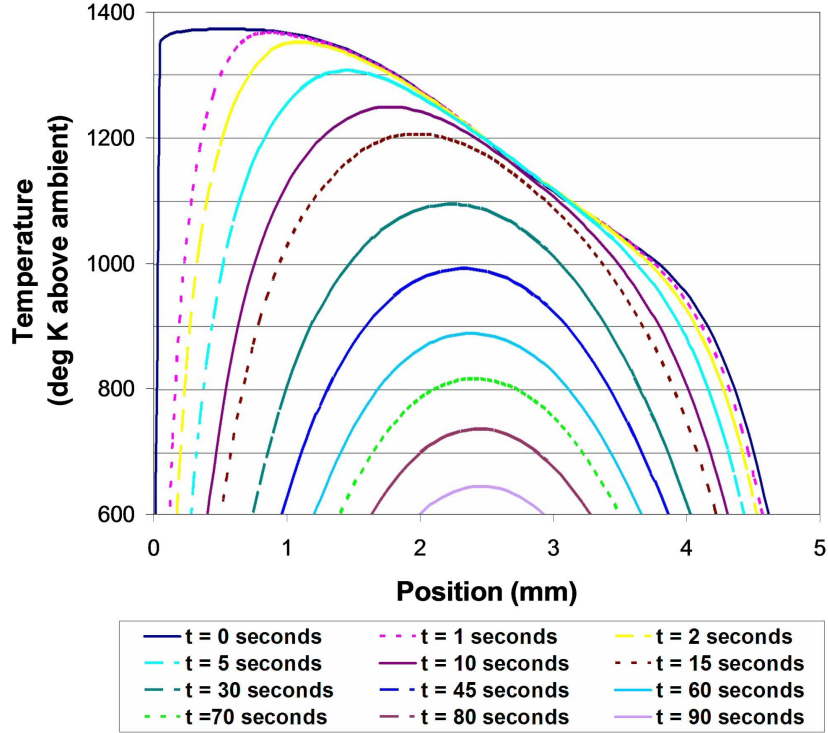
Figure 4.18:   **Specimen Cooling through Austenizing Temperature.**

An argument can be made that our boundary conditions do not account for the thermal conductivity to the air or are too aggressive. However, the observed microstructures indicate that this cooling did, in fact, take place. Additionally, the presented solution allows for a cooling rate that assumes the turbulent air of the sled passage could enforce an ambient air temperature. However, slower cooling rates are possible that still create martensite on the rail surface. The minimum cooling rates required to match our experimental results would only serve to adjust our model. That is, for martensite to be created on the gouge surface, the minimum thermal gradients required would match our model at any point down to 0.5 mm. Therefore, we could consider the gouge surface to be at 0.5 mm in our computational model, thereby making that amount of the model to be a thermal boundary layer, and still generate the microstructure experimentally observed throughout the depth of the specimen. The other boundary condition, within the depth, was varied to be at ambient temperature at distances further away from the surface, with little effect on
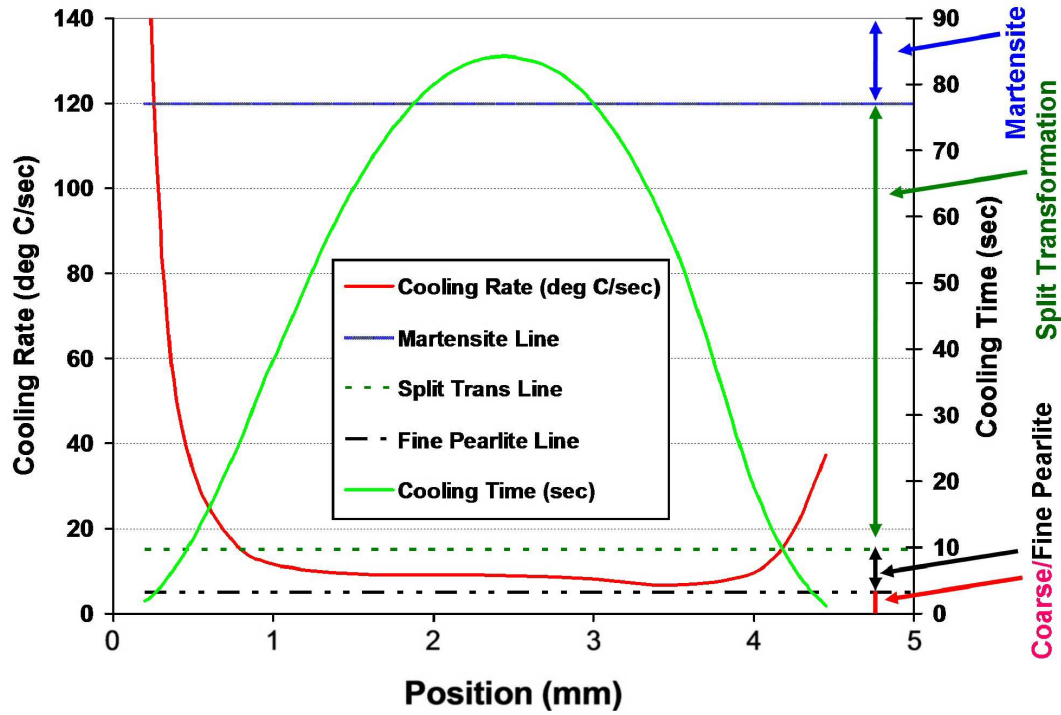
Figure 4.19:   **Specimen Cooling Gradient and Resulting Microstructure.**

the model. Therefore, our confidence that this one-dimensional model is sufficiently accurate to validate our experimental metallurgical results is very high.

An additional result of this analysis was to verify that the capability of conduction to transport temperature on the time scale of the impact event, as opposed to the cooling event, is very limited. Over the course of a typical impact, measured in the tens of microseconds, heat conduction results in only 1 - 2 degrees (K) of temperature change. So while conduction during cooling is capable of causing the microstructure changes found in the experimental examination of the gouged rail, it is not a significant mechanism in the impact/deformation event. This fact was verified within previous CTH simulations of the impact event in [109] and in a related analysis of heat conduction during deformation [125].

4.4   Conclusions on Gouged Specimen Examination

A metallographic examination was conducted on a damaged rail having undergone hypervelocity gouging impact. The microstructure was shown to vary significantly from the specimen top down into the unaffected structure. A temperature history is suggested from the microstructural evidence. Material mixing in the region of the gouging, and the creation of shear bands from the heat generated by catastrophic thermoplastic shear is confirmed in the micrographs. A one-dimensional heat conduction model is created that exactly predicts the microstructure identified in the metallography.

The results of this analysis will serve to improve the numerical gouging model and further the effort to mitigate hypervelocity gouging at the HHSTT [32]. The results of this metallurgical study establish a thermal profile that can be matched against computer simulations of the gouging event. These code models of hypervelocity gouging can thereby be validated.

4.5   Examination of Rail Condition

The discovery of such a large heat affected zone and the associated thermal history that creates the observed microstructure prompted an investigation into other sections of rail from the HHSTT. In particular, two sections of rail that were not ever put into service were examined, as well as two sections that had been in service. One piece has no visible damage, and the other had a "scrape" under the flange where the shoe had contacted it as the sled had pitched or moved up. Table 4.4 summarizes the samples examined, their condition, and their nomenclature. All of these specimens were prepared per the "etched" procedure outlined in Table 4.1 and evaluated using bright-field microscopy. All rail samples were examined through the depth away from the surface into the bulk of the material.

Both of the virgin rail sections showed no thermally-induced microstructure change, except at the rail head surface. A standard manufacturing process is to

Table 4.4:   Summary of Non-gouged Rail Specimens.

Type of Rail	Coating	Damage	Sample Location	Nomenclature
Unused	None	None visible	Rail Head	e2k
Unused	Iron Oxide	None visible	Rail Head	e2kr
In Service	None	None visible	Rail Head	is
In Service	Iron Oxide	None visible	Rail Head	isrt
In Service	Iron Oxide	Scrape	Under flange	isrb

spray the rail heads with water during the cooling period, called head hardening, to create a thin, martensitic layer on the top surface [38]. This increases resistance to wear through the enhanced hardness of the top surface. Although this result was not expected by the HHSTT engineers (as the rails were not supposed to be head hardened), this small microstructural variance most likely has little impact on the gouging phenomenon. This judgment is based on the small dimensionality of the variation. Figures 4.20 and 4.21 are of these virgin rail sections. The black horizontal line in Figure 4.20 denotes a break in the microscopy and the microstructure far away from the rail head appears below that line. A similar technique could have been applied to Figure 4.21, but was not necessary, the unaffected microstructure (as with the previous figure) looked identical as one proceeded through the depth away from the rail head.

The in-service rails were examined in the same fashion. However, it became immediately clear that microstructure changes similar to those appearing in Figure 4.5 were present in these in-service rails.

Figure 4.22 is of an in-service rail that had no coating. The rail had no visible damage. A section of the rail head was examined and an area of altered microstructure was found. This indicates that a microstructural change was caused by this rail section heating to above the austenizing temperature of 725°C and then cooling at a sufficiently rapid rate to generate the changes. The heating conduction analysis earlier
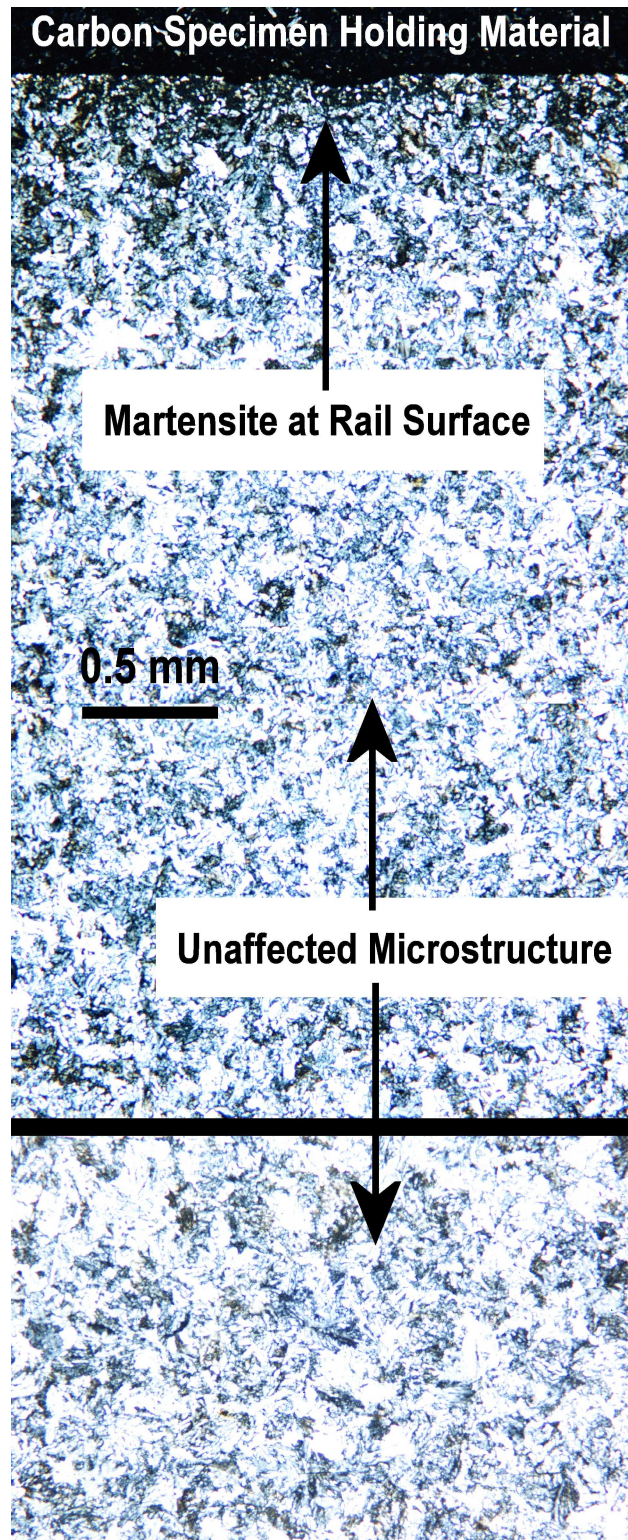
Figure 4.20:   Specimen "e2k" Microstructure.
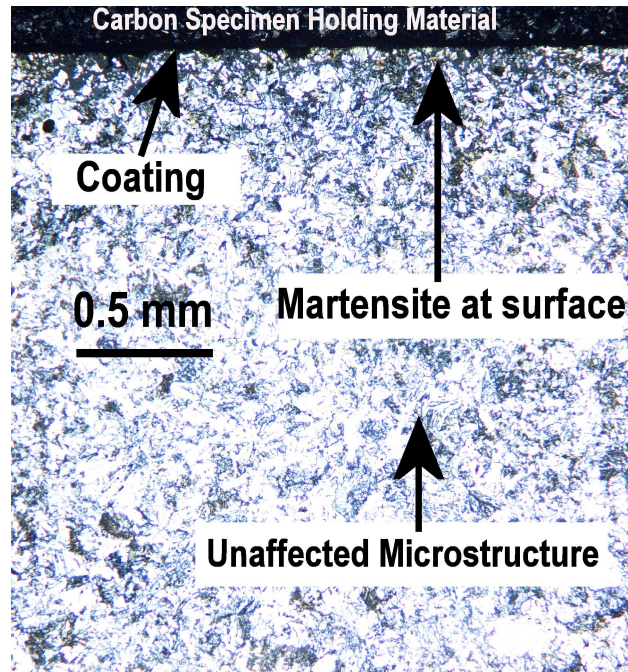
Figure 4.21:   Specimen "e2kr" Microstructure.

in this chapter indicates that insufficient time exists during shoe passage to conclude the heat pulse was a conduction-related event. Therefore, some small amount of plasticity or viscoelasticity may have occurred that accounts for the heat input into the depth of the rail while not resulting in obvious damage. This discovery also establishes a validation point to compare against a computational solution.

Another in-service rail was also examined. This particular rail section had a visible "scrape" on the underside of the flange. This was caused by the sled shoe rising and striking the underside of the rail head. The scrape was painted over again with iron oxide coating, so a visible evaluation was not possible. This scraped section was removed and examined through the "depth" - which in this case was away from the ground and toward the top surface of the rail. Figure 4.23 depicts the microstructure observed. Once again, a section of altered microstructure exists near the rail surface which indicates a thermal pulse that austenized the steel, followed by rapid cooling.
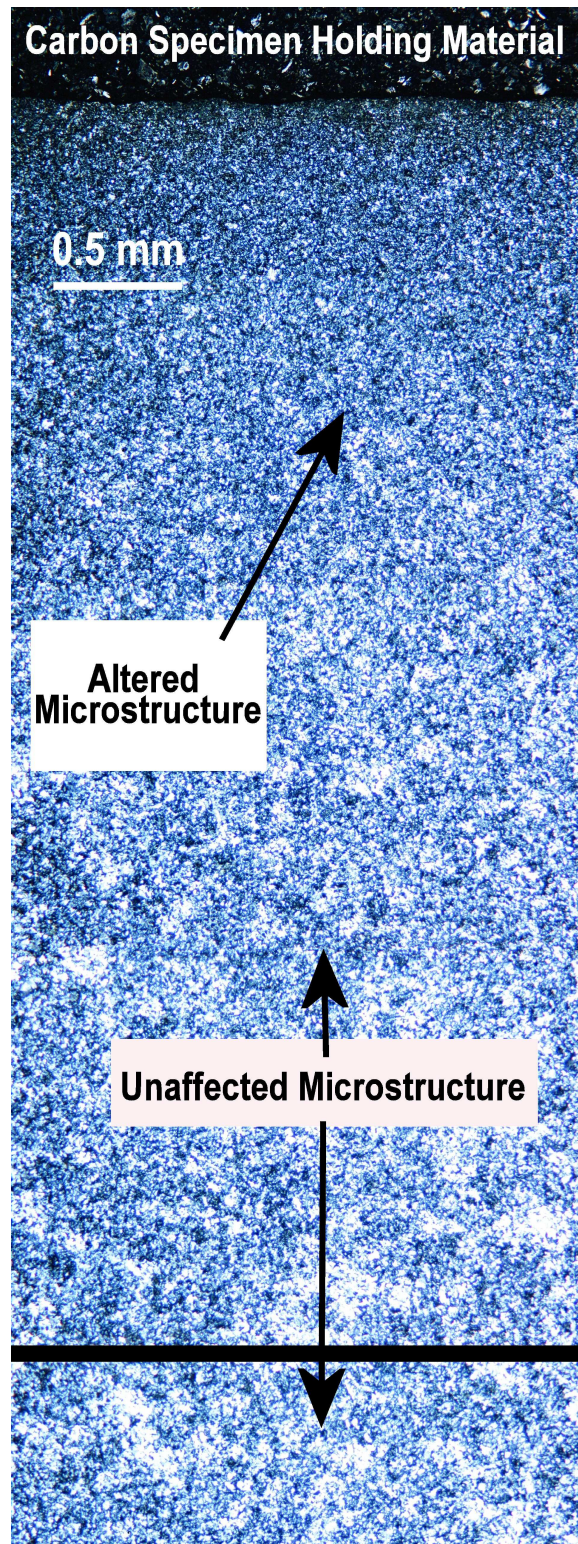
Figure 4.22:   Specimen "is" Microstructure.
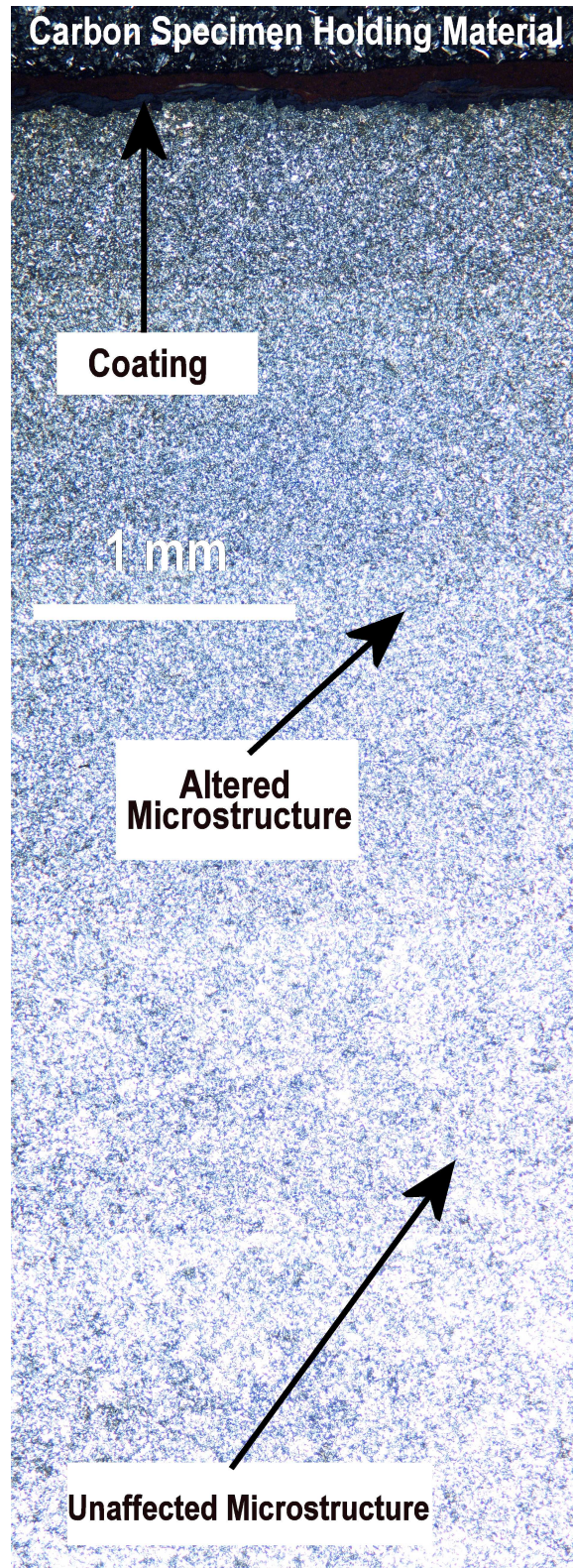
Figure 4.23: Specimen "isrb" Microstructure.
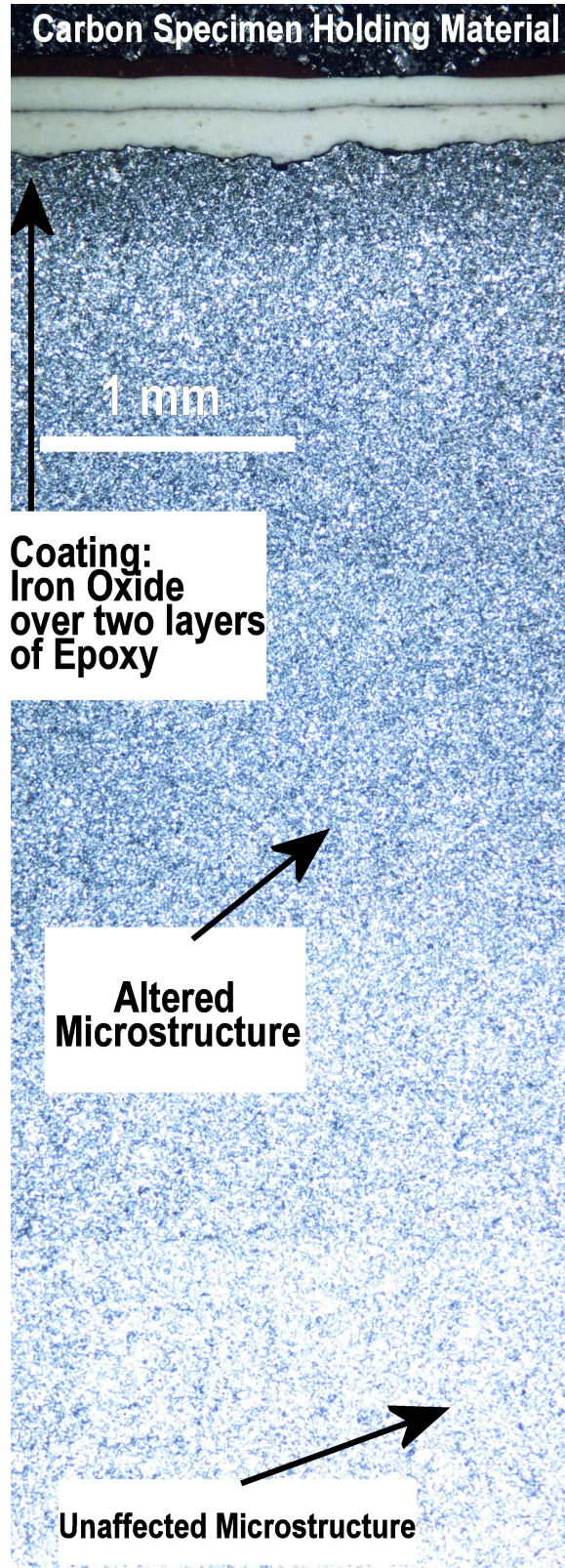
Figure 4.24: Specimen "isrt" Microstructure.

The scraped section of rail was also examined in an area away from the damage and where no visible damage was present. A section of the rail head was evaluated and appears in Figure 4.24. While this section did not show visible damage, the altered microstructure is also present in this sample.

Earlier in this chapter, specimen A4 was also examined through the depth and used as a control for the evaluation of the hypervelocity gouge. The section of rail that specimen A4 came from was also a section of in-service and undamaged rail. Yet this rail showed no sign of microstructural change. Therefore, we can conclude that not all in-service rail has encountered heat pulses. However, some sections have suffered from this kind of thermal effect - most likely the result of small amount of plastic deformation.

4.6   Gouge Characterization Conclusions

In this chapter, several rail sections were examined using metallurgical techniques in order to better understand gouging. One section had experienced a hypervelocity gouge. Other sections were virgin specimens, or had been in-service on the HHSTT.

Based on the in-depth examination of the gouged rail, a thermodynamic history was developed and analytically verified that explained the observed altered microstructure. Material mixing, shear band development, and thermally-induced phase changes were confirmed. Using the same approach, microstructural changes (very similar to those observed in the gouged rail) were discovered in the in-service rails. The time scales involved in these sled tests preclude the origin of these thermal pulses to be heat conduction from a heated shoe. Therefore, some relatively small amounts of plasticity or viscoelasticity must have caused the thermally-induced microstructural changes observed.

These thermal profiles quantify, in some sense, the amount of heat that must have been generated by either a gouging impact, or a less severe material interaction,

between the HHSTT sled and the rail. This information will serve as a validation point for the CTH simulations to replicate in the process of creating a usable impact model.

V. Constitutive Model Development

An essential element in the effort to accurately model hypervelocity gouging is the development of specific material constitutive models. In the HHSTT scenario, all previous work in the field has relied on material flow models that were not specific to VascoMax 300 and 1080 steel. In many cases, the material models available to the investigators significantly differed from these.

As discussed in Chapter III, the material constitutive model is a very important element in the solution of hypervelocity impact [129]. While the EOS tends to dominate the solution in some aspects, a significant portion of the solution depends on the material flow model. In this chapter, an extensive experimental study is detailed that investigates the flow characteristics of these specific materials.

5.1 Constitutive Model Overview

As noted in Chapter III, the two constitutive model formulations that will be utilized are the Johnson-Cook and the Zerilli-Armstrong. Both of these approaches capture the major parameters that must be accounted for in a modern material flow model. That is, the dynamic yield strength of the material must be a function of strain, strain-rate, and temperature. Therefore, an experimental approach that aims at resolving the constants in either of these constitutive models must vary these variables (see Equations 3.20 and 3.24).

The strain-rate variation in the development of a constitutive model becomes the key in this effort. This is because the higher strain-rate tests are typically beyond the scope of most facilities and become expensive to conduct. Yet this higher strain-rate regime is exactly where these hypervelocity impacts occur [88]. Previous modeling efforts indicated that strain-rates in the 10^3/sec to 10^6/sec range were common in these hypervelocity impacts [104–106, 108, 109]. Even though the EOS begins to dominate the solution at these higher pressures and strain-rates, the material constitutive model makes a significant contribution to the solution [129].

In order to capture the maximum range of strain-rates in the model development effort, two major tests are conducted. The first is the traditional SHB test. This test can generate states of uniaxial strain-rate up to 10^3/sec. The second test is a flyer impact plate experiment, which creates uniaxial strain-rates from 10^4/sec to 10^6/sec. These two tests span the entire range of interest and form the experimental basis upon which an accurate constitutive model can be formulated for VascoMax 300 and 1080 steel.

5.2 Split Hopkinson Bar Test

A series of SHB tests were conducted using VascoMax 300 and 1080 steel from the HHSTT. Because the HHSTT performs the heat treatment for the VascoMax 300 and to ensure we were testing the exact material from the field, the SHB specimens were prepared by the HHSTT machine shops.

5.2.1 SHB Test Background. A typical Split Hopkinson Bar (SHB) test apparatus was used to test specimens of 1080 steel and VascoMax 300 [32, 34, 35]. The facility at the University of Dayton Research Institute (UDRI) was used. Figure 5.1 is an overall view of the test apparatus. The manner in which the specimens are heated in the test section of the apparatus is illustrated in Figure 5.2. The test section, with a tested specimen, appears in Figure 5.3.

The bars in this SHB apparatus are 0.5 inch diameter Inconel 718. The striker bar was capable of generating stress pulses that created strain-rates in the test specimens of up to ~1500/sec. The stress pulse is assumed to be:

$$\sigma = \rho c_0 V_s \tag{5.1}$$

where ρ is the material density (7900 kg/m^3), c_0 is the material sound (elastic wave) speed, and V_s is the striker bar velocity. The striker bar velocity can be measured
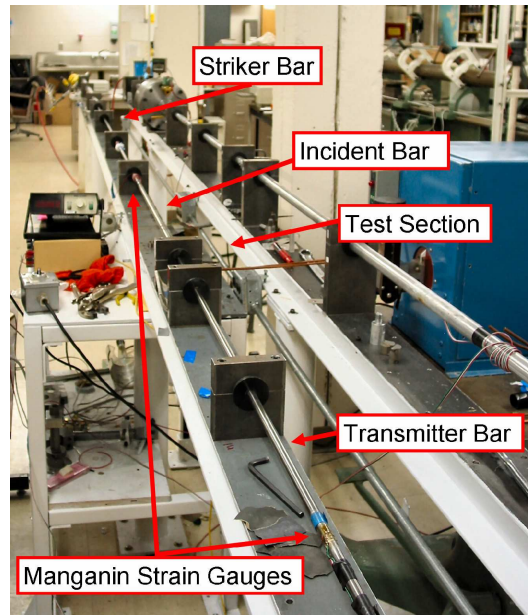
Figure 5.1:   **UDRI SHB Test Apparatus.**
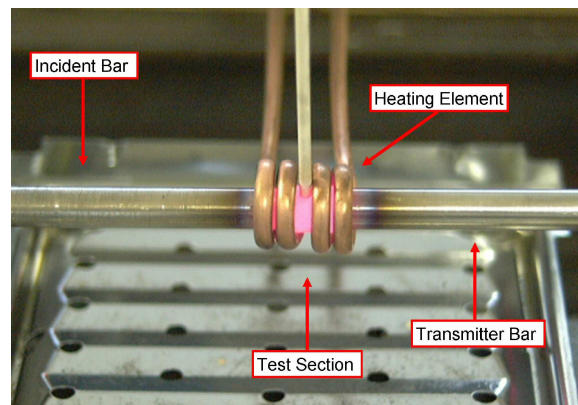
Figure 5.2:   **SHB Test Apparatus Heating Element.**
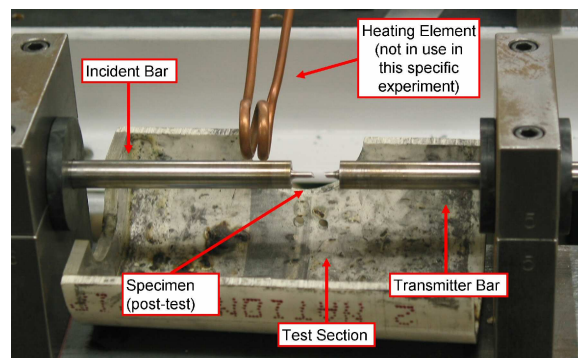
Figure 5.3:   **SHB Apparatus Test Section.**

(using laser breaks) and the elastic wave speed can be found using (where E is the Inconel 718 bar elastic modulus):

$$c_0 = \sqrt{\frac{E}{\rho}} = \sqrt{\frac{195 \, GPa}{7900 \, kg/m^3}} = 4968 \, m/s \tag{5.2}$$

The created compressive stress pulse travels through the incident bar, through a collar surrounding the test specimen, to the end of the transmitter bar. The free end reflects the pulse back as a tensile wave that arrives back at the specimen (where the collar now has no effect because the collar is not attached to either bar). Figure 5.4 is a schematic of the test apparatus and shows this arriving tensile wave as ε_i, the incident strain wave. The incident wave is partially reflected as ε_r and transmitted as ε_t. The manganin strain gauges on the apparatus bars allow for the measurement of these strain pulses.
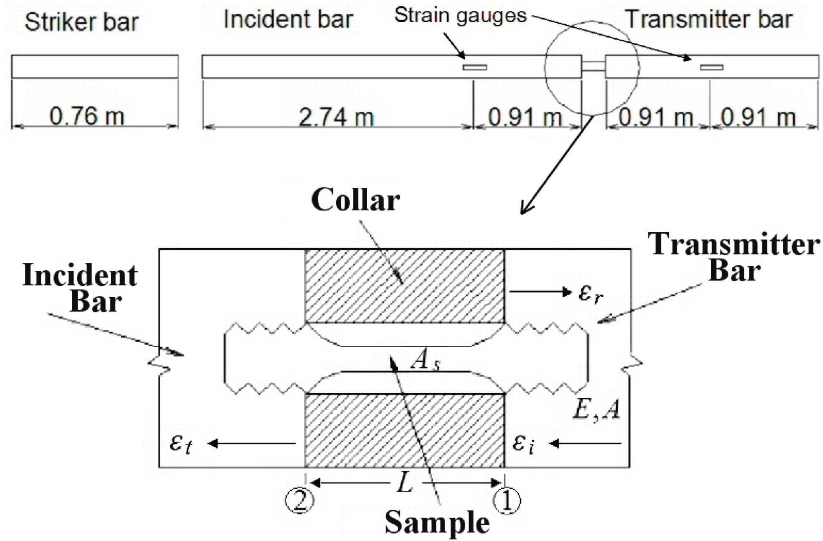
Figure 5.4:   SHB Test Apparatus Schematic.

Following the theory developed in $[39, 72, 78, 79, 87, 129]$, the values of specimen strain-rate and stress can be computed from these strain measurements.

The displacements of the ends of the specimen in Figure 5.4 can be expressed in Equation 5.3, where $\varepsilon = \partial u / \partial x$ and $\sigma = E\varepsilon$, where u is displacement, σ is uniaxial

stress, and ε is uniaxial strain. The average strain in the specimen can be found from Equation 5.4, where L is the length of the specimen test section. The forces, P, at the ends of the specimen can be computed in Equation 5.5 from noting that $\sigma = E\varepsilon = P/A$, where E is the test material elastic modulus and A is the Hopkinson bar cross-sectional area.

$$\left\{ \begin{array}{l} u_1 = \int_0^t c_0\varepsilon_1 dt = c_0 \int_0^t (\varepsilon_i - \varepsilon_r) dt \\ u_2 = \int_0^t c_0\varepsilon_2 dt = c_0 \int_0^t \varepsilon_t dt \end{array} \right\} \tag{5.3}$$

$$\varepsilon_s = \frac{u_1 - u_2}{L} = \frac{c_0}{L} \int_0^t (\varepsilon_i - \varepsilon_r - \varepsilon_t) dt \tag{5.4}$$

$$\left\{ \begin{array}{l} P_1 = EA\varepsilon_1 = EA(\varepsilon_i + \varepsilon_r) \\ P_2 = EA\varepsilon_2 = EA\varepsilon_t \end{array} \right\} \tag{5.5}$$

Assuming the forces are the same at both ends of the specimen, Equation 5.5 implies that $\varepsilon_i + \varepsilon_r = \varepsilon_t$ and therefore from Equation 5.4:

$$\varepsilon_s = \frac{c_0}{L} \int_0^t (\varepsilon_t - \varepsilon_r - \varepsilon_r - \varepsilon_t) dt = -\frac{2c_0}{L} \int_0^t \varepsilon_r dt \tag{5.6}$$

which is the specimen strain. This is available from the strain gauge measurements of ε_r. The force at the specimen ends must equal the force in the bars, which requires:

$$\sigma_s = \frac{A}{A_s}\sigma_b = \frac{A}{A_s}E\varepsilon_t \tag{5.7}$$

where σ_b is the stress in the bar and A_s is the gauge cross-sectional area of the test specimen. The specimen strain-rate is obtained from Equation 5.6 (by differentiating with respect to time) as:

$$\dot{\varepsilon}_s = -\frac{2c_0}{L}\varepsilon_r \tag{5.8}$$

With these relationships a set of material data (stress and strain) can be gathered at varying strain-rates and temperature. From this data, a constitutive model can be created.

5.2.2 SHB Test Results. A series of SHB tests were conducted on material specimens machined at the HHSTT to be identical to those materials in use in the field. The specimens were machined to the specifications appearing in Figure 5.5 - note that in this figure all dimensions are in inches.
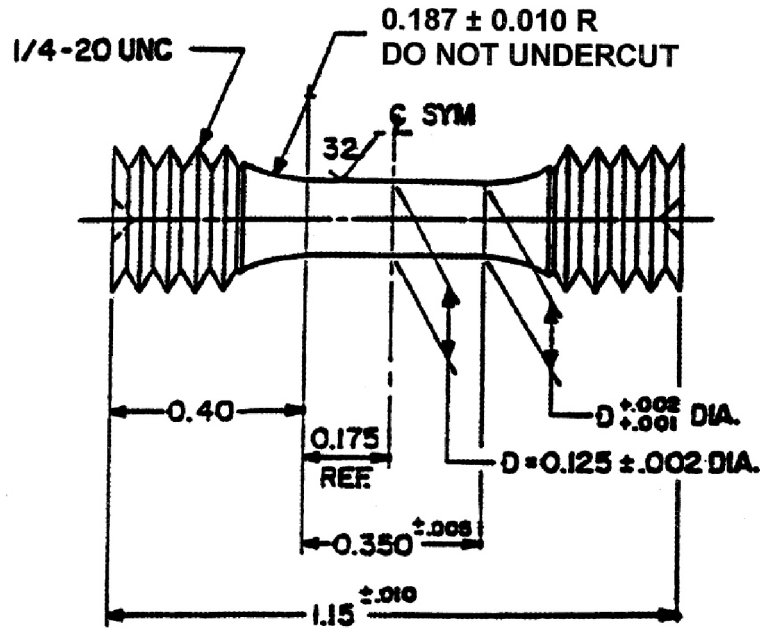
Figure 5.5: **Specifications for the SHB Specimens (units are inches).**

The 1080 steel test results were typical of a strain-hardening material. Figure 5.6 shows a typical stress-strain curve generated by the SHB. The full report of the results is available in [60]. Consistent with the assumptions within the SHB relationships, the 1080 steel specimens showed no measurable necking in the specimens. Therefore, the material stress can be computed, via Equation 5.7, from the measured strain - and the curves can thereby be constructed. Table 5.1 summarizes these tests results. It should be noted that the quasi-static tests (at a strain-rate of ~1/sec) were conducted using the SHB specimens and a standard quasi-static pull test machine.

Table 5.1:   Summary of 1080 steel SHB Results.

Test No.	Test Temp (°F)	Strain Rate (s^{-1})	Flow Stress at $\varepsilon \sim .06$ (GPa)
Q1, Q2	70	$\sim$1	1.048
3, 4	70	$\sim$500	1.22
11, 12	300	$\sim$500	1.01
16, 17	500	$\sim$500	.89
18, 20	750	$\sim$500	1.00
6, 7	70	$\sim$1000	1.27
13, 14	300	$\sim$1000	.88
23, 24	500	$\sim$1000	.75
22, 31	750	$\sim$1000	.99
25, 26	70	$\sim$1500	1.18
33, 34	300	$\sim$1500	1.26
27, 28	500	$\sim$1500	1.12
36, 38	750	$\sim$1500	.82
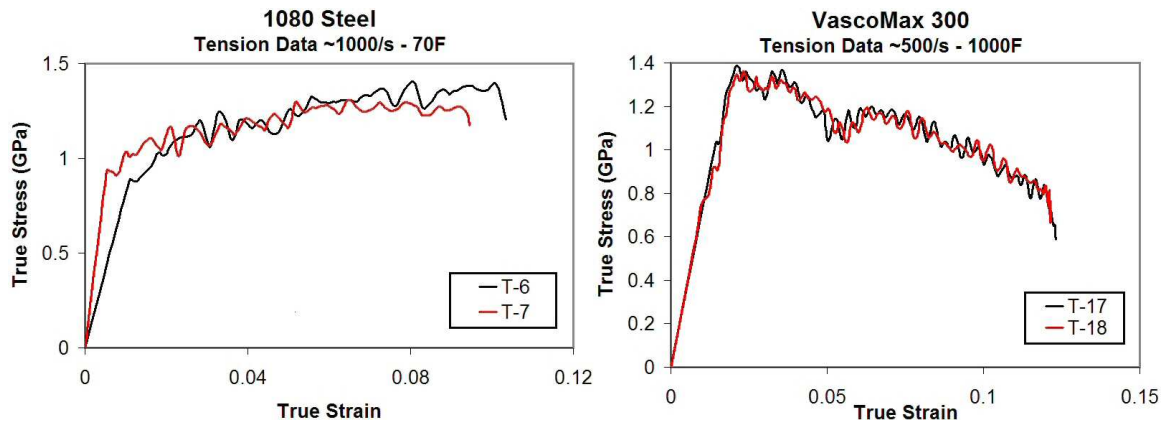
Figure 5.6:   **Comparison of Stress-Strain Behavior of Subject Materials under Tensile SHB Test.**

VascoMax 300, on the other hand, did not behave as a typical strain hardening material. Figure 5.6 shows a typical VascoMax 300 stress-strain profile. It exhibits little strain hardening before the material begins to fail. Additionally, the specimens experienced significant necking during the testing process. Table 5.2 summarizes the VascoMax test results.

Early in this research process, a technique was applied that adjusted the results of these tests for the necking observed in the VascoMax 300 specimens [32, 34, 35]. It was thought that the necking process was part of the strain-hardening process and that the material was capable of carrying more stress as a result. However, it became clear during additional testing that VascoMax 300, in its current state of heat treatment used at the HHSTT, has very little strain capability prior to failure. Therefore, the necking process is part of the failure of the material and the strain-hardening portion is a small area prior to the drop in the true stress curve [125].

5-8

Table 5.2:   Summary of VascoMax 300 SHB Results.

Test No.	Test Temp (°F)	Strain Rate (s^{-1})	Flow Stress at $\varepsilon \sim .01$ (GPa)
Q1, Q2	70	$\sim$1	2.15
3, 4	70	$\sim$500	2.2
15, 16	500	$\sim$500	1.78
19, 20	750	$\sim$500	1.75
17, 18	1000	$\sim$500	1.4
1, 2	70	$\sim$1000	2.18
9, 28	500	$\sim$1000	1.88
10, 11	750	$\sim$1000	1.63
12, 13	1000	$\sim$1000	1.33
6, 7	70	$\sim$1500	2.38
21, 23	500	$\sim$1500	1.95
24, 25	750	$\sim$1500	1.68
26, 27	1000	$\sim$1500	1.65

5.2.3 SHB-Based Constitutive Model Development. At this point, it is possible to develop a constitutive model based on the strain-rate data from 1/sec to 1500/sec. The rationale for developing the models at this point, as opposed to constructing them considering the flyer plate tests, is that one must sacrifice accuracy in matching the mid-range strain-rates of the SHB tests to match the high strain-rate flyer plates. Later in this chapter, it will become clear that perfectly matching all the experimental data is not possible. Therefore, because constitutive models for these materials (VascoMax 300 and 1080 steel) have not been presented in the literature, the mid strain-rate range models will be computed.

The procedure for reducing the SHB data and determining the constants for the material flow models appears in another work [60]. Essentially, by considering each portion of the flow model separately, a systematic approach can be made in determining the constants. For instance, evaluating the SHB experiments at room temperature and at 1/sec strain-rate, the first set of Johnson-Cook constants can be determined. Next, one can hold the strain constant and examine the SHB tests at varying strain-rates to determine the next constant. Finally, the last constant is determined from examining the SHB tests are various temperatures. Finding the Zerilli-Armstrong constants is performed in a similar manner. In addition, the typical values for other metals like those considered can be used as a guide in the iteration process.

Using this approach, the model constants for both materials can be developed for VascoMax 300 and 1080 steel, based on the experimental data from the SHB tests. The typical manner in which the constitutive model is presented in the literature in through the use of an effective flow stress versus effective strain-rate diagram at a particular value of strain. In this way, the critical elements of strain-rate dependency and thermal softening are presented. Table 5.3 summarizes the physical properties and the Johnson-Cook (denoted by JC) and Zerilli Armstrong (denoted by ZA) constants derived from the SHB data, where E is the elastic modulus, ν is poisson's ratio, T_{melt} is the melting temperature in Kelvin, ρ is material density, and eV are units of electron-

Table 5.3: Summary of Physical Properties and Model Constants from SHB.

Property/Constant	1080 Steel	VascoMax 300
E (GPa)	202.8	180.7
ν	0.27	0.283
T_{melt} (K)	1670	1685
ρ (kg/m^3)	7800	8000
JC: A (GPa)	0.525	2.17
JC: B (GPa)	3.59	0.124
JC: C	0.029	0.0046
JC: m	0.7525	0.95
JC: n	0.6677	0.3737
ZA: A (GPa)	0.75	1.0
ZA: c_1 (GPa)	2.5	2.5
ZA: c_2 (GPa)	0	0
ZA: c_3 (eV^{-1})	110.0	40.0
ZA: c_4 (eV^{-1})	5.5	2.0
ZA: c_5 (GPa)	0.266	0.266
ZA: n	0.289	0.289

volts. A conversion between electron-volts and degrees Kelvin can be performed, if necessary, by noting that $1eV = 11605K$.

Figures 5.7 and 5.8 are the resulting diagrams from the SHB data. In these diagrams, the "Exper." notation refers to the SHB experiments at specific temperatures in °F, while JC and ZA refer to the Johnson-Cook and Zerilli-Armstrong model predictions respectively.

The validation of these models will be discussed in detail in the next Chapter. These mid-range strain-rate constitutive models would be extremely useful in a lower energy impact simulation or other scenario in which the strain-rates are in the
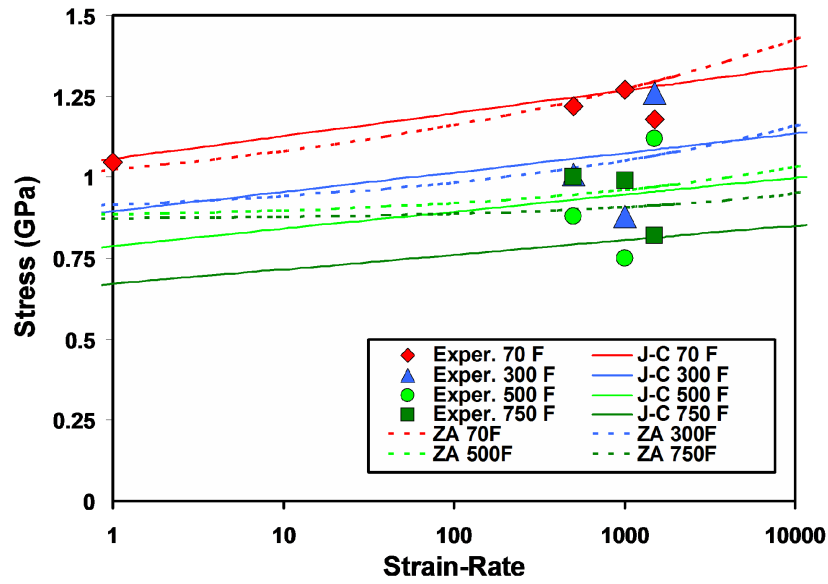
Figure 5.7:   **Effective Flow Stress v. Strain-Rate, 1080 Steel, SHB.**
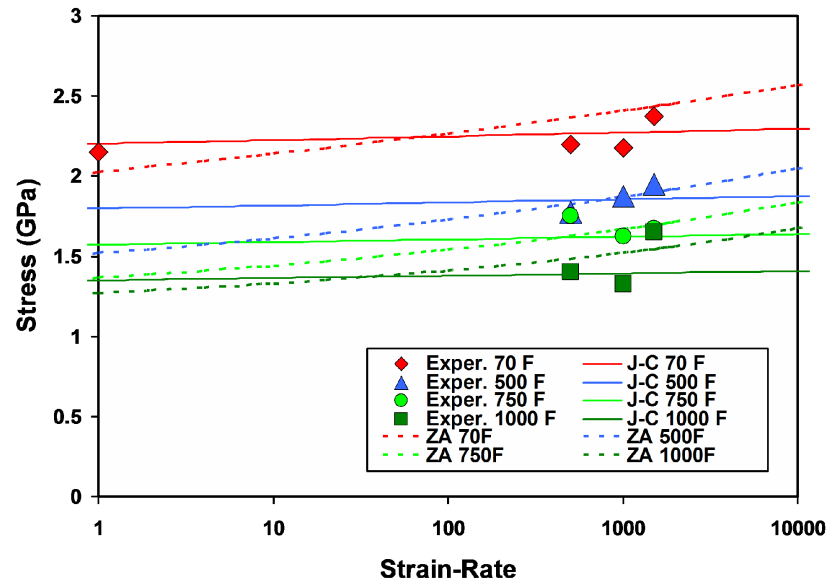
Figure 5.8:   **Effective Flow Stress v. Strain-Rate, VascoMax 300, SHB.**

neighborhood of 10^3/sec or lower. For the computational simulation of the shoe/rail impact, however, a higher strain-rate regime model is necessary. Therefore, high strain-rate tests were conducted.

Another element that the SHB tests can provide is an estimation of the ultimate pressure/stress of the material. This value is the maximum stress measured from the stress-strain diagrams before the materials begins to fail and the stress drops. For VascoMax 300 and 1080 steel, the values are approximately 2.5 GPa and 2.0 GPa respectively.

5.3 Flyer Impact Plate Experiments

In order to generate data to extend previously developed flow models, a higher strain-rate uniaxial test is required. The maximum strain-rate that can be generated in the SHB scenario is on the order of 10^3/sec. The magnitudes required to extend the constitutive model are in the 10^4/sec - 10^5/sec range. The type of test that is typically employed is the flyer plate impact experiment [85]. These high velocity impact tests can provide stress measurements with respect to time for a given impact [86]. These stress curves are characterized by an elastic precursor wave, followed by the plastic deformation wave, as illustrated in Figure 5.9. The magnitude of the elastic precursor wave is known as the Hugoniot elastic limit (HEL). This value provides one of the accepted estimates for the dynamic yield (flow) stress of the material. The flyer plate experiments can be performed in such a manner as to yield both the HEL and the peak stresses at given impact velocities.

The elastic precursor wave travels at the material sound speed (see Equation 2.1). The plastic deformation wave moves at a slower speed behind the elastic precursor. At a particular point in the material, the peak stress will be the summation of the plastic and elastic deformation waves, until the elastic release wave returns from the far-field boundary. The reason that the HEL is used to estimate the flow stress at a given strain-rate is that uniaxial strain simulations of the impact event will rely on the material constitutive model to adjust the magnitude of the HEL - and thereby the total peak stress.

Therefore, these flyer plate experiments provide unique information in the formulation of a material constitutive model. The Johnson-Cook or Zerilli-Armstrong
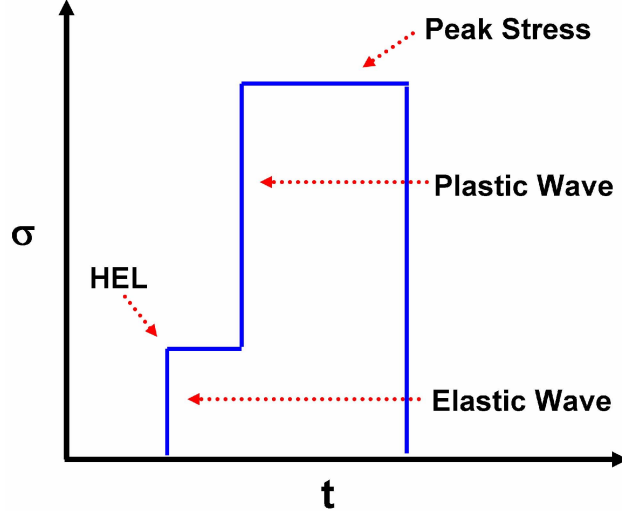
Figure 5.9: **Idealized Stress versus Time Plot for a Uni-axial Planar Impact.**

models serve to establish the magnitude of the HEL, while the material equation of state (EOS) governs the material behavior at the stresses experienced in the plastic deformation wave. Therefore, these experiments require a uniaxial strain code simulation of the impact conditions, with the capability to adjust the material constitutive models and the equation of state. Both of these elements could be adjusted to refine the material models to match the experimental results.

For our experiments, the HHSTT facility once again manufactured the test specimens for the flyer impact plate experiment.

5.3.1 Flyer Plate Experiment Background.   In order to extend the previously determined material models for VascoMax 300 and 1080 steel to the higher strain-rate regime, a series of flyer plate experiments was conducted [33]. The tests were conducted at the University of Dayton Research Institute (UDRI). The test facility appears in Figure 5.10.

One of the two test configurations performed appears in Figure 5.11. This first set of tests (one each for the specific materials) were conducted with the goal of recording the HEL. The flyer plate (3 mm thickness) was shot against a 6 mm thick
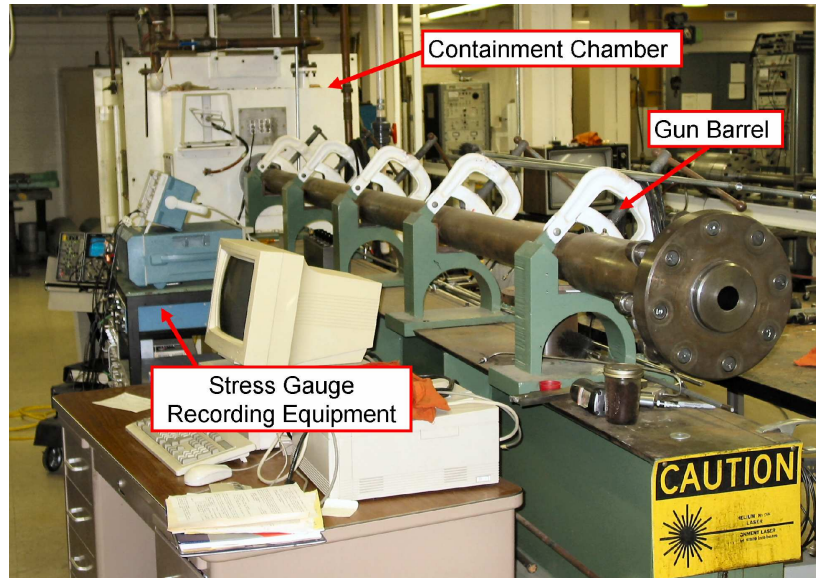
Figure 5.10:   **UDRI Flyer Plate Testing Facility.**

target of the same material, with a manganin stress gauge attached to the back of the
plate, held by 12 mm of polymethyl methacrylate (PMMA). Because of the sufficient
target thickness, the elastic precursor wave was able to separate from the plastic wave
of deformation. This allowed measurement of both the HEL and the peak stress wave
that followed it.
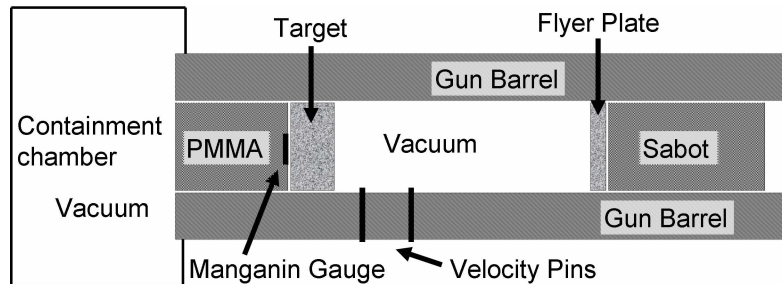
Figure 5.11:   **Schematic of flyer plate experimental tests
7-1878 and 7-1879.**

Two additional experiments were conducted for each material in the second
test configuration. For these tests, the target was composed of 2 mm of material,
a stress gauge, and 12 mm of additional material. These shots were performed to
record the stress wave within the material as it passes. The rationale for performing
these additional tests was to establish an experiment to record the in-material stress

Table 5.4:   Summary of Flyer Plate Tests.

Test	Flyer	Velocity	Target
7-1874	3 mm VascoMax 300	685 m/s	2 mm + gauge + 12 mm VascoMax 300
7-1875	3 mm 1080 Steel	669 m/s	2 mm + gauge + 12 mm 1080 Steel
7-1876	3 mm VascoMax 300	450 m/s	2 mm + gauge + 12 mm VascoMax 300
7-1877	3 mm 1080 Steel	437 m/s	2 mm + gauge + 12 mm 1080 Steel
7-1878	3 mm VascoMax 300	891 m/s	6 mm VascoMax 300 + gauge + 12 mm PMMA
7-1879	3 mm 1080 Steel	891 m/s	6 mm 1080 Steel + gauge + 12 mm PMMA

waves for model validation at lower impact velocities – and therefore lower peak stresses. This geometry did not result in the detection of the HEL (due to a thickness that was not sufficient for the elastic wave to separate from the plastic wave), and is illustrated in Figure 5.12. In both types of tests, the manganin stress gauge was electrically insulated from the steel by a Mylar sheet of 0.025 mm thickness. Table 5.4 summarizes the test conditions described above.
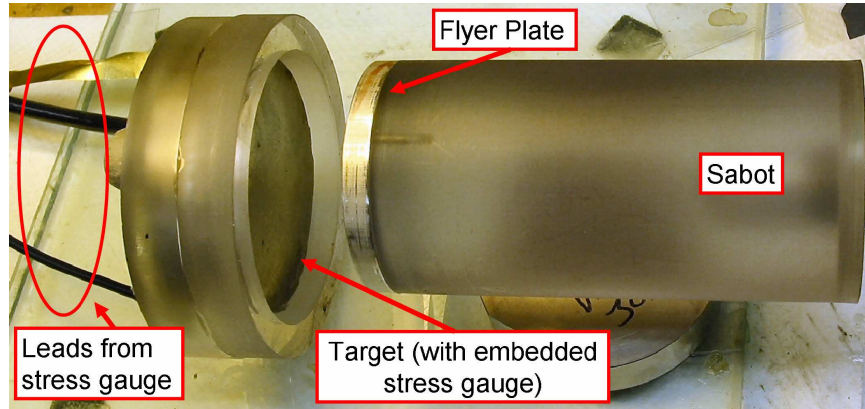
Figure 5.12:   **UDRI Flyer Plate and Target.**

The stress gauge measurements were taken for each of the cases, as well as impact velocity information from the velocity pins. The stress measurement was

recorded as a function of time as the elastic and plastic waves traveled through the gauge.

    5.3.2 Flyer Plate-Based Constitutive Model Development.   In order to formulate a constitutive model for these materials, a 1-D wave code is necessary. This is because the HEL and the peak stresses need to be simulated as a function of time and compared to the experimental results. The hydrocode, CTH, was chosen to simulate these impacts through a 1-D model. Because CTH will be used in hypervelocity impact simulations, using this particular code and its EOS formulation was essential to building an accurate constitutive model.

    Based on previous research, a mesh convergence study has indicated that a mesh size of 0.002 cm is where the CTH solution converges for these impact simulations - and which is at the edge of where continuum mechanics is considered to end for these metals [108]. Therefore, a mesh size was chosen to be 0.002 cm throughout the model of the flyer impact scenarios, except where the Mylar sheet is against the gauge. In those cases, the mesh size chosen was 0.0001 cm. Figures 5.13 and 5.14 depict the CTH models used for these two flyer test geometries.
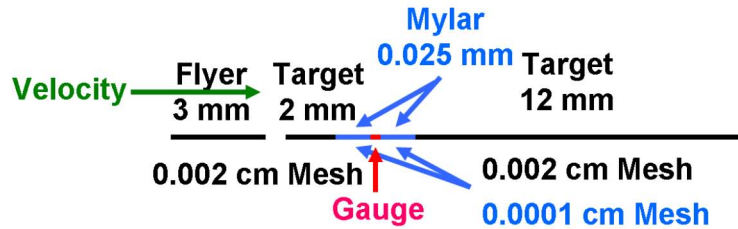
Figure 5.13:   **CTH Model for Flyer Test Configuration One.**

    Tests 7-1878 and 7-1879 were simulated first. The modification of the constitutive model affected the magnitude of the HEL prediction, as well as the peak stress. Figures 5.15 and 5.16 depict the CTH simulation of the stress pulse as it travels through the gauge for Test 7-1878 (VascoMax 300) based on the baseline Johnson-
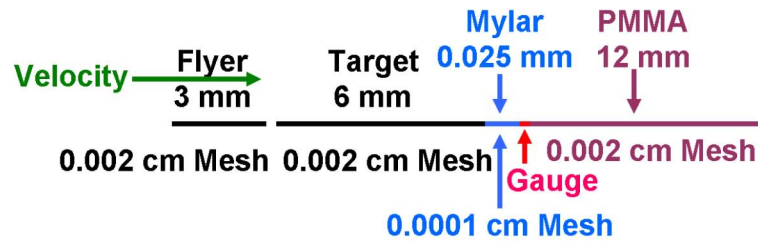
Figure 5.14: **CTH Model for Flyer Test Configuration Two.**

Cook (JC) and Zerilli-Armstrong (ZA) models developed from the SHB tests (see Table 5.3). The experimental data is plotted on the same figure - as well as annotations for the HEL, predicted HEL, and where the material failed during testing. It is important to note that the HEL and the peak stress predictions are fairly close, but could be improved. The difference between simulation and experiment is far more dramatic in Figure 5.17 and 5.18. These figures depict the baseline JC and ZA predictions for the stress in the 1080 steel tests. The HEL is significantly under-predicted, as is the peak stress.
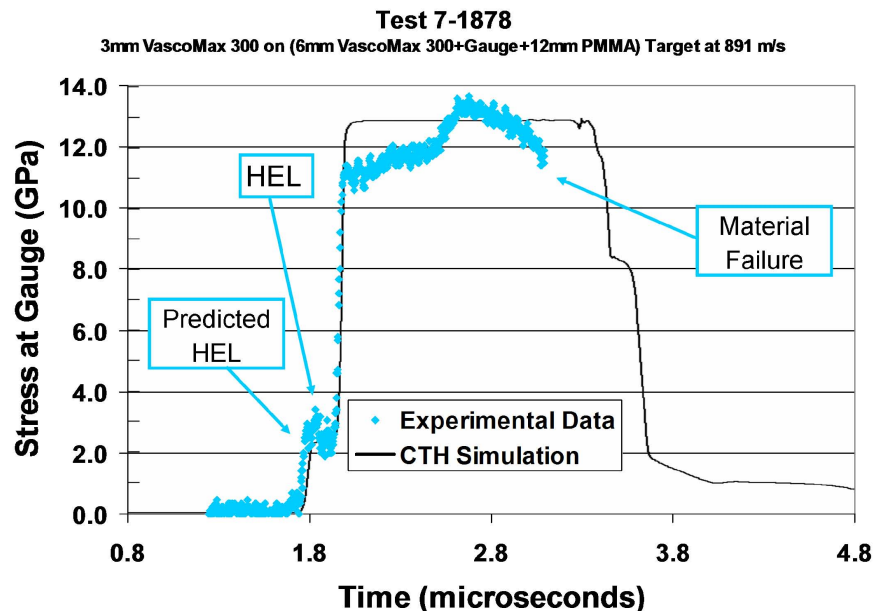
Figure 5.15: **Baseline JC, CTH Simulation, Test 1878.**
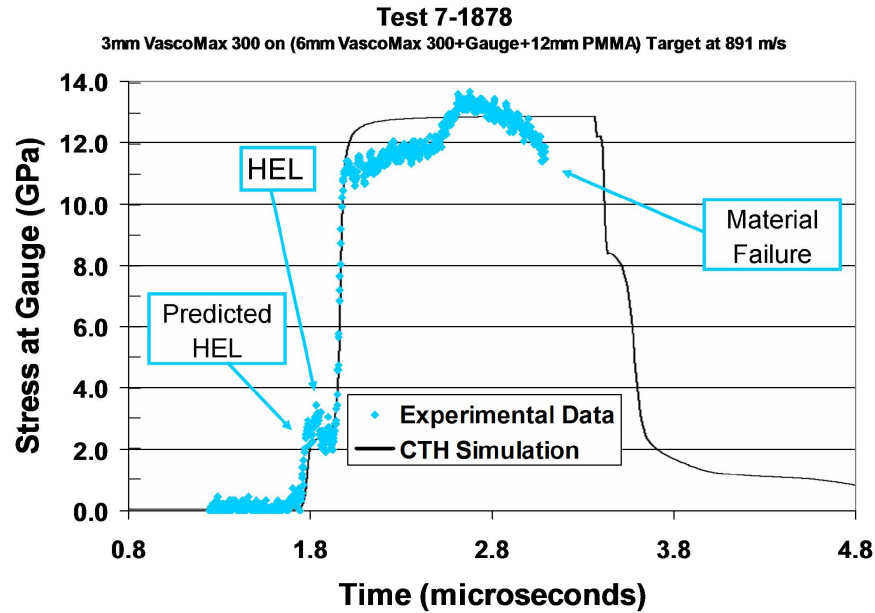
Figure 5.16:   Baseline ZA, CTH Simulation, Test 1878.
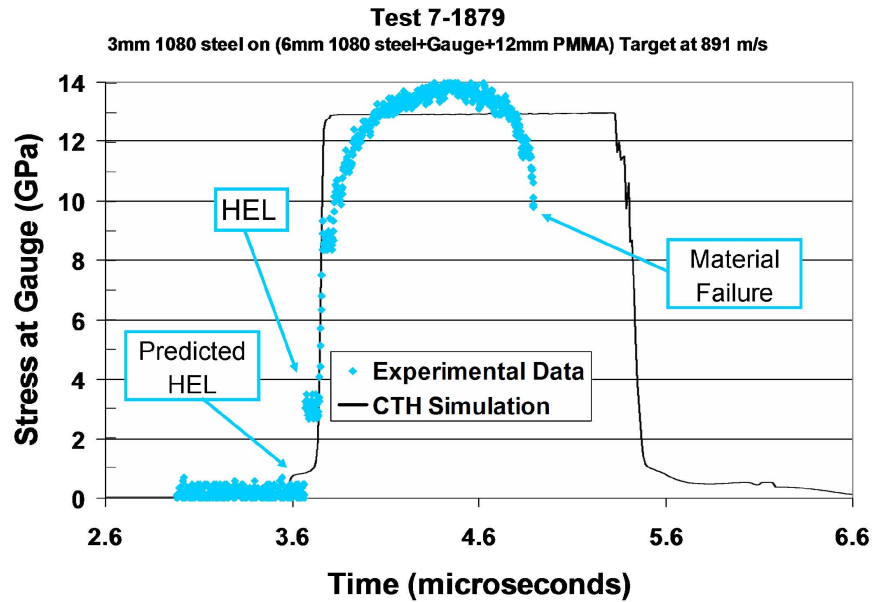
Figure 5.17:   Baseline JC, CTH Simulation, Test 1879.

By modifying the constitutive models in the higher strain-rate regime, the CTH predictions for the stress wave could be adjusted. While the EOS dominated the solution, up to a 10% modification could be made to the peak stress by allowing for higher strengths at strain-rates of 10^5/sec (which is the level computed by CTH as the strain-rate of the flyer plate tests). As expected, these modifications to the consti-

Test 7-1879
3mm 1080 steel on (6mm 1080 steel+Gauge+12mm PMMA) Target at 891 m/s
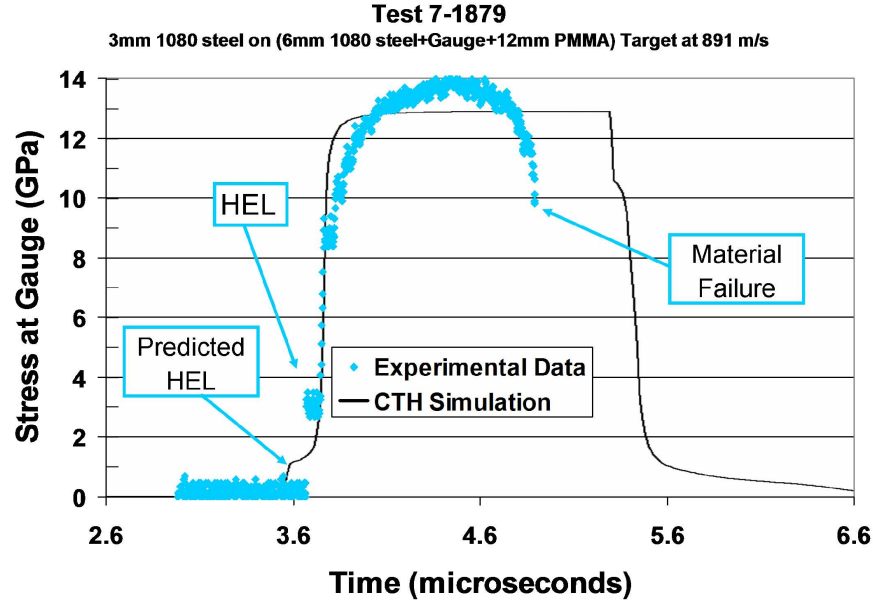
Figure 5.18:   Baseline ZA, CTH Simulation, Test 1879.

tutive model were necessary to make the HEL prediction match the flyer plate exper-
iments. The previous models, developed from the SHB tests, were under-predicting
the flow stress at the strain-rate levels experienced in the flyer plate impacts. By
requiring these adjustments, the flyer plate experiments were effectively bridging the
gap between the lower strain-rate SHB tests, and the very high strain-rate impacts
dominated by the EOS calculations.

An iteration process was undertaken to adjust the parameters of the Johnson-
Cook and Zerilli Armstrong models to find a best match between the CTH simulations
and the experimental flyer plate tests. That is, the constants of these models were
adjusted, then the CTH code was used to simulate the flyer plate tests, and a com-
parison was made between the measured stress and the CTH predicted stress. The
model constants were iterated to create a "best-fit" match for all three tests available
for each material (1878, 1874, & 1876 for VascoMax 300 and 1879, 1875, & 1877 for
1080 steel).

Initially, it appeared as if the Johnson-Cook model (which had been employed
previously [32, 34, 35, 84, 94, 125]) might continue to be sufficient as the constitutive

model for these materials. However, because of the linear relationship between effective stress and strain-rate, the higher stress estimates for 10^5/sec strain-rate required to match the flyer plate tests made the model over-estimate the SHB regime data (illustrated later in this section). Because of this, the greater flexibility of the Zerilli-Armstrong model became important. It was possible to construct a Zerilli-Armstrong model that came close to matching the SHB data, and still made the fit to the flyer plate data possible.

Figures 5.19 and 5.20 illustrate the Johnson-Cook (JC) and Zerilli-Armstrong (ZA) "best-fit" CTH simulations for VascoMax 300 (test 1878) that matched all the flyer plate data as much as possible. They depict the CTH simulation of the shock stress as a function of time for the models developed to match all the flyer plate experiments. On the figures, the experimental stress gauge data is depicted on the simulation. In addition, where the material failed during the experiment is annotated on the figure. Figures 5.21 and 5.22 illustrate the same information for 1080 steel (test 1879).

Test 7-1878
3mm VascoMax 300 on (6mm VascoMax 300+Gauge+12mm PMMA) Target at 891 m/s
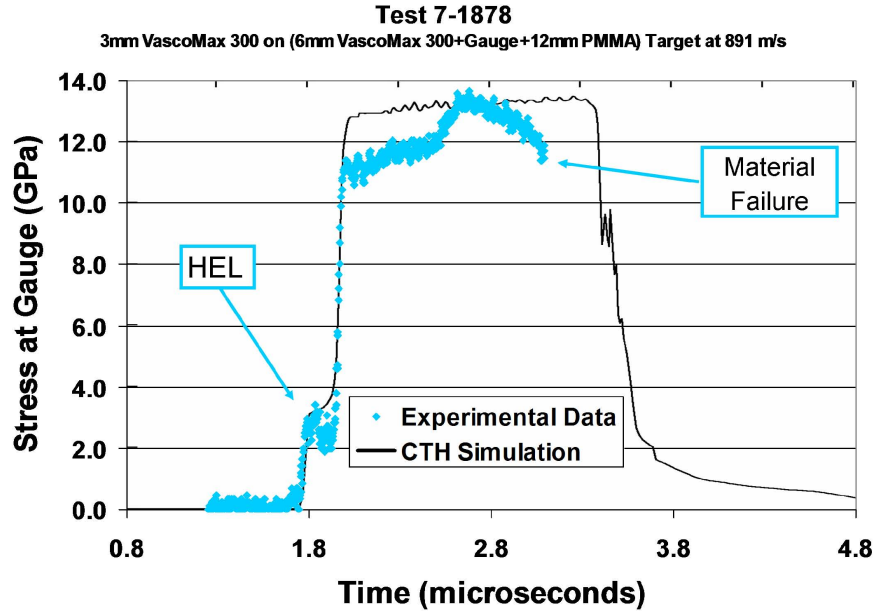
Figure 5.19:   **Best-Fit JC, CTH Simulation, Test 1878.**

Test 7-1878
3mm VascoMax 300 on (6mm VascoMax 300+Gauge+12mm PMMA) Target at 891 m/s
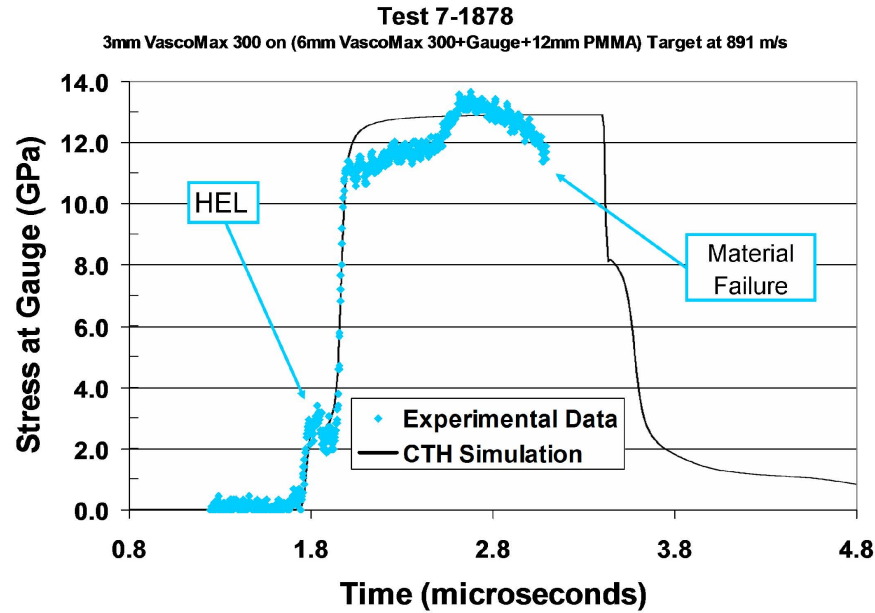
Figure 5.20:   Best Fit ZA, CTH Simulation, Test 1878.

Test 7-1879
3mm 1080 steel on (6mm 1080 steel+Gauge+12mm PMMA) Target at 891 m/s
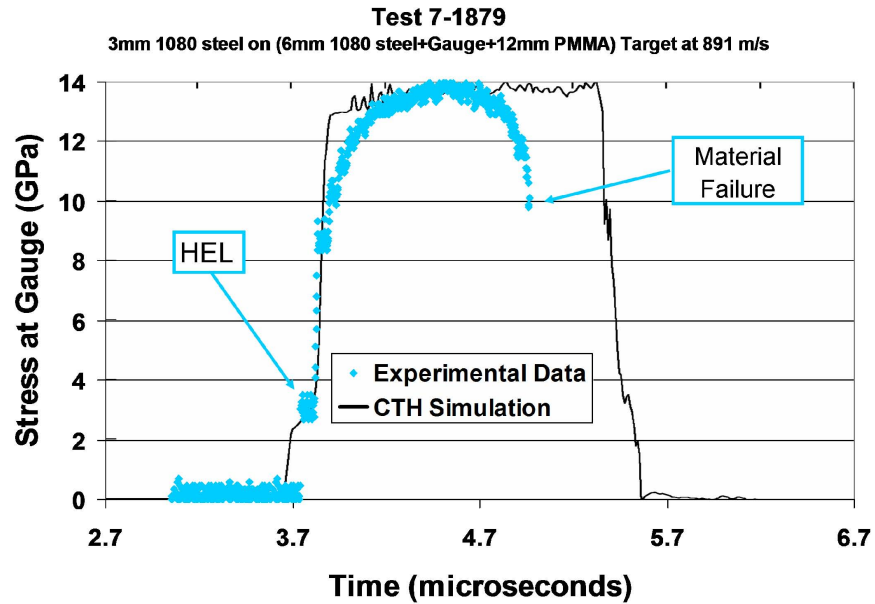
Figure 5.21:   Best Fit JC, CTH Simulation, Test 1879.

In comparing Figures 5.19 to 5.22, both the Johnson-Cook and Zerilli-Armstrong formulations appear capable of matching the experiment tests fairly well. However, the difference between these formulations is far more evident when we examine the effective stress versus strain-rate plots for these models.

Test 7-1879
3mm 1080 steel on (6mm 1080 steel+Gauge+12mm PMMA) Target at 891 m/s
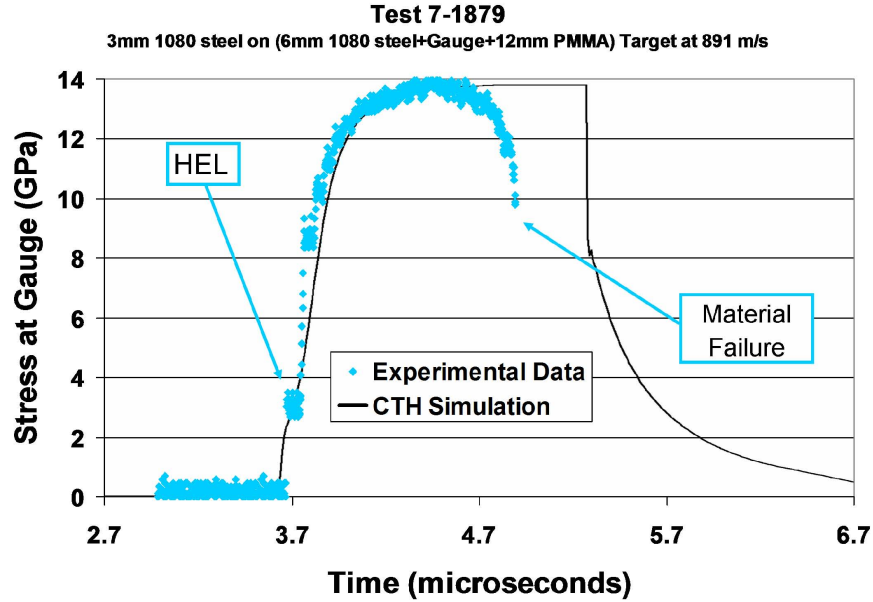
Figure 5.22:   Best Fit ZA, CTH Simulation, Test 1879.

Figures 5.23 and 5.24 illustrate the resulting constitutive relationships developed from matching the flyer plate data. In order to match the measured stress wave, the Johnson-Cook formulation must abandon the mid-range strain-rate data from the SHB tests to a greater extent. Based on the requirement to develop a constitutive model that can estimate material flow stress across the entire strain-rate range, it is clear that the Zerilli-Armstrong formulation is superior in its ability to maintain better matches to both sets of experimental data.

Table 5.5 summarizes the constants for both models that were determined to match the flyer plate stress data. Because of the better fit to the SHB data, the Zerilli-Armstrong model was chosen as the optimum model for the remainder of the investigation.

Figures 5.25 through 5.28 illustrate the fit that the Zerilli-Armstrong model and the EOS in CTH are able to make to the experimental flyer plate tests 1874 through 1877 - which were performed in the second configuration (with the "embedded" stress gauge). The stress wave was measured within the material, as opposed to at the rear of the target. Additionally, these tests were conducted at a lower velocity to provide

Table 5.5: Summary of Physical Properties and Model Constants from Flyer Plate Tests.

| Property/Constant	1080 Steel	VascoMax 300
E (GPa)	202.8	180.7
ν	0.27	0.283
T_{melt} (K)	1670	1685
ρ (kg/m^3)	7800	8000
JC: A (GPa)	0.7	2.1
JC: B (GPa)	3.6	0.124
JC: C	0.017	0.03
JC: m	0.25	0.8
JC: n	0.6	0.3737
ZA: A (GPa)	0.825	1.42
ZA: c_1 (GPa)	4.0	4.0
ZA: c_2 (GPa)	0	0
ZA: c_3 (eV^{-1})	160.0	79.0
ZA: c_4 (eV^{-1})	12.0	3.0
ZA: c_5 (GPa)	0.266	0.266
ZA: n	0.289	0.289
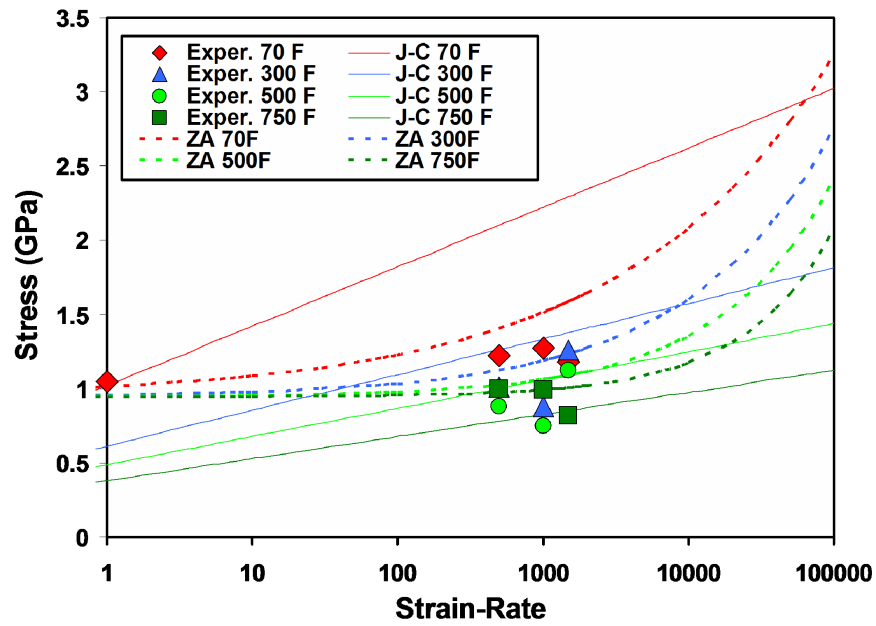
Figure 5.23:   **Effective Flow Stress v. Strain-Rate, 1080 Steel.**
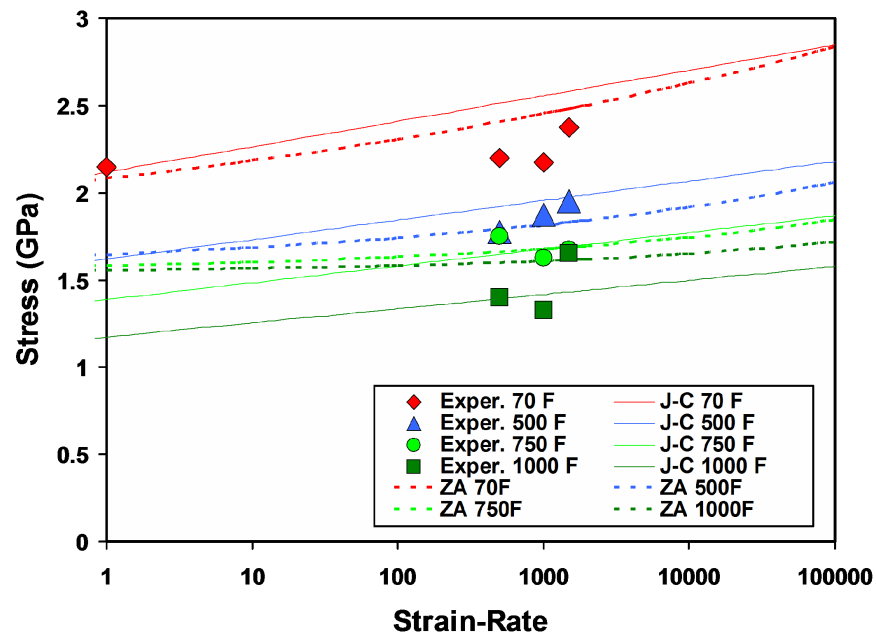
Figure 5.24:   **Effective Flow Stress v. Strain-Rate, VascoMax 300.**

varying peak stresses to match the models against. On these figures, an annotation is made where the gauge failed - which occurred in the VascoMax 300 experiments.

This was further experimental evidence, akin to the SHB results, that VascoMax 300 has very little strain capability prior to failure.

Test 7-1874

3mm VascoMax 300 on (2mm+Gauge+12mm) VascoMax 300 Target at 685 m/s
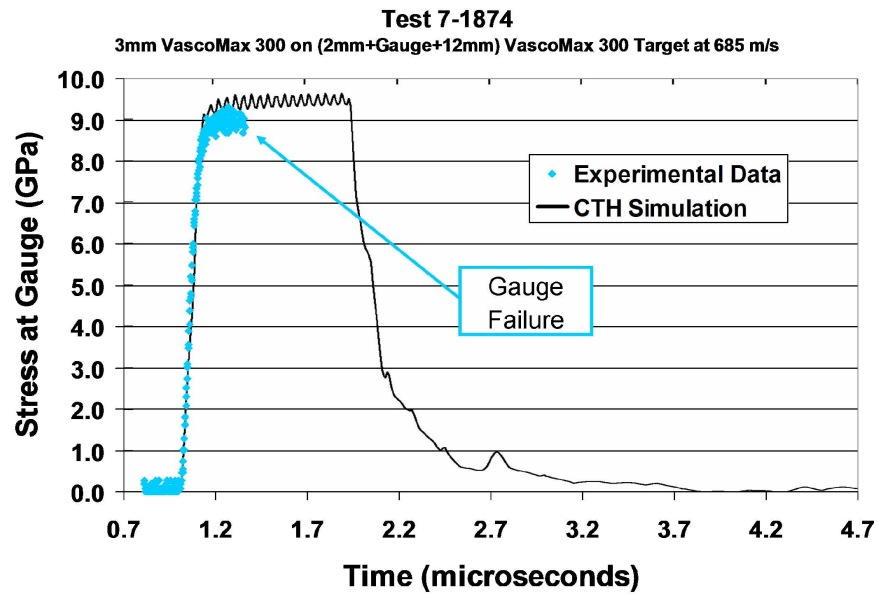
Figure 5.25:   **CTH Simulation, Test 1874.**

Test 7-1875

3mm 1080 Steel on (2mm+Gauge+12mm) 1080 Steel Target at 670 m/s
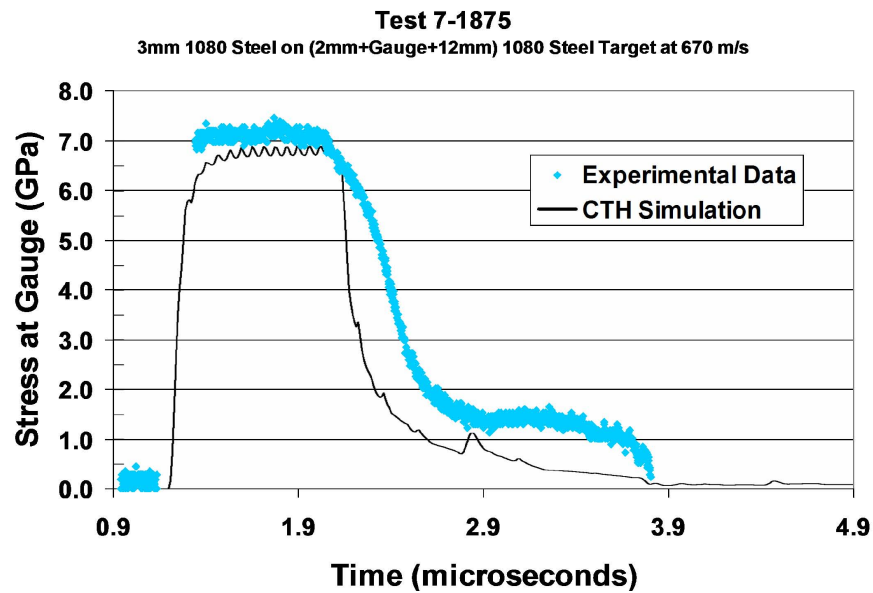
Figure 5.26:   **CTH Simulation, Test 1875.**

Based on the results, a very accurate constitutive model has been developed that creates a close match to the flyer plate impact test data and the previously performed SHB tests. While the JC model developed from the flyer plate experiments tended to

Test 7-1876

3mm VascoMax 300 on (2mm+Gauge+12mm) VascoMax 300 Target at 450 m/s
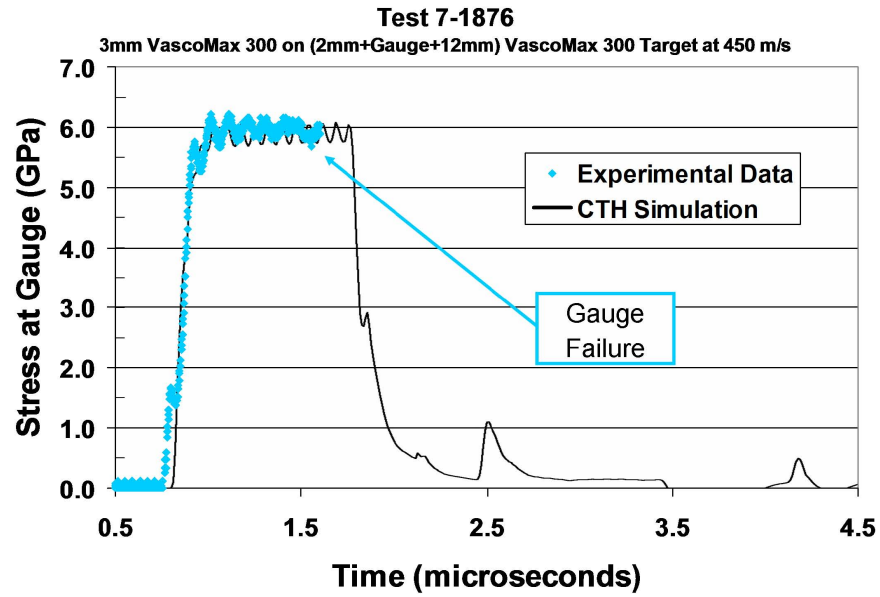
Figure 5.27:   **CTH Simulation, Test 1876.**

Test 7-1877

3mm 1080 Steel on (2mm+Gauge+12mm) 1080 Steel Target at 437 m/s
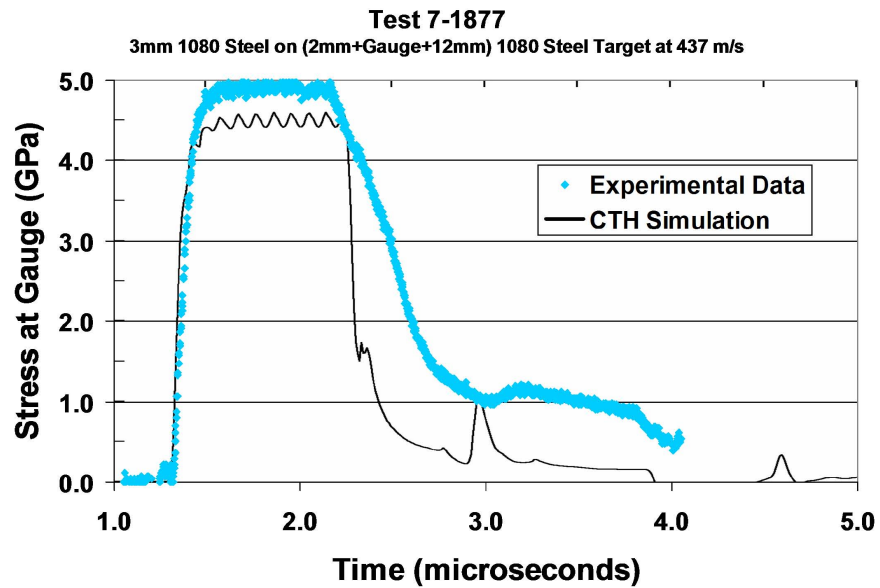
Figure 5.28:   **CTH Simulation, Test 1877.**

produce similarly good results to those appearing in Figures 5.25 through 5.28, the poor fit to the SHB data was a concern. This comparison necessitates the use of the Zerilli-Armstrong model for further simulations in CTH of these materials undergoing dynamic deformation.

5.4 Constitutive Model Summary

By conducting a series of experiments on the materials present in the HHSTT gouging problem (VascoMax 300 and 1080 steel), the material constitutive models were developed. In an attempt to create flow models which are experimentally based across the entire strain-rate range from 1/sec to 10^5/sec, the Zerilli-Armstrong formulation is chosen to continue the effort to model hypervelocity gouging. With these models, the next logical step is to validate them. This was accomplished by comparing CTH simulations to experimentation and ensuring that CTH replicates them reasonably well.

VI. Validation of Constitutive Models for Mid-Range Strain-Rates

In order to validate the material flow models developed for VascoMax 300 and 1080 steel in Chapter V, different approaches must be used for mid-range strain-rates (1/sec to 10^3/sec) and high strain-rates (10^4/sec to 10^6/sec). This is due to the desire to ensure the constitutive model is valid across the entire range so that a CTH model of the hypervelocity gouging phenomenon is accurate. A single high strain-rate experiment might mask the mid-range contribution to the solution. A perfect example is the flyer plate experiments - in which a Johnson-Cook constitutive model was developed which matched those tests, but which abandoned the mid-range Split Hopkinson Bar (SHB) data. This necessitated the use of the Zerilli-Armstrong model in order to fit both sets of experiments.

We know from the discussion in Chapter III that the flow stress model is critical to the solution accuracy for these hypervelocity impacts. While a portion of the gouge is at the high strain-rate range, a good portion of the deforming material is undergoing plasticity in the mid-range strain-rate regime [108]. This will be illustrated in detail in Chapters VIII and IX.

Therefore, the mid-range strain-rate range will be examined first. The constitutive models will be validated first with the SHB test model. A Taylor Impact Test was conducted to validate the models in a mid-range strain-rate impact scenario. The validity of the flow models will be verified for this strain-rate regime.

6.1 Modeling the SHB Tests

To model the SHB tests presented in Chapter V, a slightly different approach needs to be applied. Due to CTH being an Eulerian shock wave code, creating model of the SHB test is difficult [47,71,77,96,97]. Materials in CTH are given properties, such as velocity, which apply to all material at the cell center. Therefore, establishing a non-moving boundary condition at one end of a specimen is problematic. Consequently,

a traditional finite element code with constitutive model modification capability was chosen for this particular part of the constitutive model validation.

An axi-symmetric finite element model of the SHB tensile specimen was carried out using ABAQUS/Explicit (version 6.5) which allows wave propagation to occur as a time function [125]. This particular code is limited to the Johnson-Cook model. Therefore, an evaluation of the Johnson-Cook model developed in Table 5.3 from the SHB data exclusively is compared against the Johnson-Cook model appearing in Table 5.5 which incorporated the flyer plate data.

This numerical approach can thus be used to evaluate a strain pulse effect on the SHB test. The numerical analysis is performed for 1/4 of the specimen due to the symmetry nature (see Figure 6.1). The applied conditions for numerical analysis are the velocity of 5m/sec at the end of the specimen (equivalent to a strain rate of 10^3/sec of the SHB test) and room temperature.
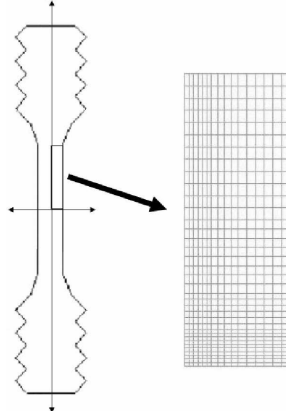
Figure 6.1: **Finite Element model of SHB Specimen.**

In using the models from Table 5.3, the post-test geometry of the SHB specimens was matched. In particular, the significant necking of the VascoMax 300 steel specimens was replicated [32, 34, 35] (see Figure 6.2). Additionally, the relatively uniform plastic deformation of 1080 steel was also successfully recreated (see Figure 6.3). It should be pointed out that since necking occurs with VascoMax 300 and causes the simulation to terminate, the numerical results are associated with the results at 225 microseconds (from a total time span of 306 microseconds). The resulting defor-

mation of SHB specimens match the experimentally observed results of the SHB test well.
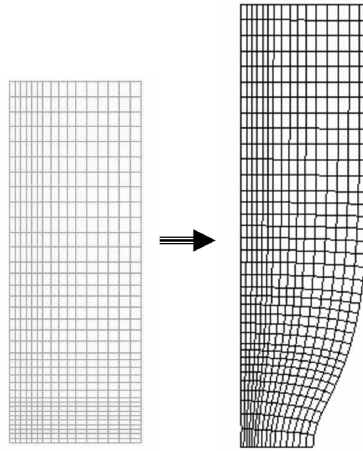
Figure 6.2:   **Finite Element Results for VascoMax 300 SHB Specimen.**
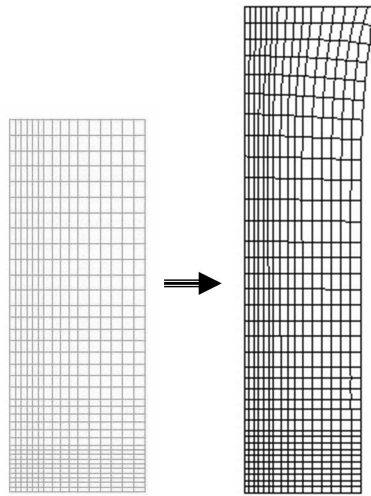
Figure 6.3:   **Finite Element Results for 1080 Steel SHB Specimen.**

Figures 6.4 and 6.5 show the development of viscoplasticity and the associated temperature rise (shown in degrees K) in the deformed material. The localized temperature rise clearly appears at the center of VascoMax 300 tensile specimen. Furthermore, the amount of temperature increase from room temperature is around 800°C.

On the other hand, the temperature rise for the 1080 steel specimen is relatively moderate ($\sim160°$C) and its distribution is fairly uniform.
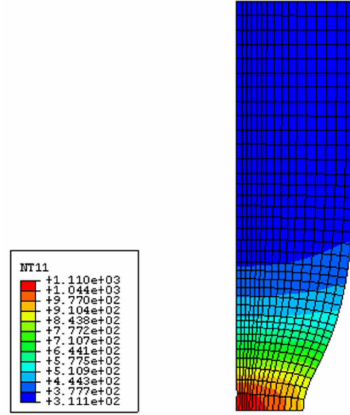
Figure 6.4: **Finite Element Thermal Results for Vasco-Max 300 SHB Specimen.**
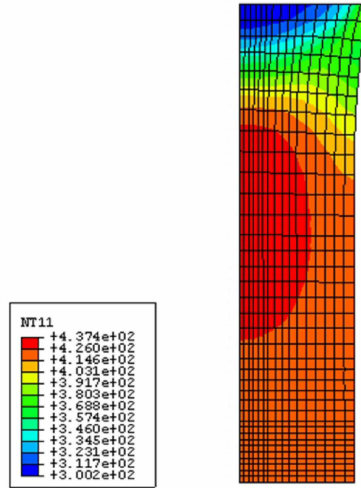
Figure 6.5: **Finite Element Thermal Results for 1080 Steel SHB Specimen.**

This temperature concentration would make the specimen more prone to thermal softening in a localized region – leading to shear band creation. In the next section, a metallurgical confirmation of this will be presented.

When the Johnson-Cook model presented in Table 5.5 (which is the full-range strain-rate model, considering the flyer plate data) was applied to the same simulation, the results no longer matched the post-test measurements of the SHB specimens. The

required linear relationship between effective flow stress and strain-rate forced the model to miss these mid-range strain-rate experimental points. Figure 6.6 highlights the difference in the results for VascoMax 300. In this figure, the effective stress is displayed in units of Pascals. The flyer-plate modified Johnson-Cook model appears on the right. Note that the necking is reduced, due to the higher dynamic yield strength estimate.
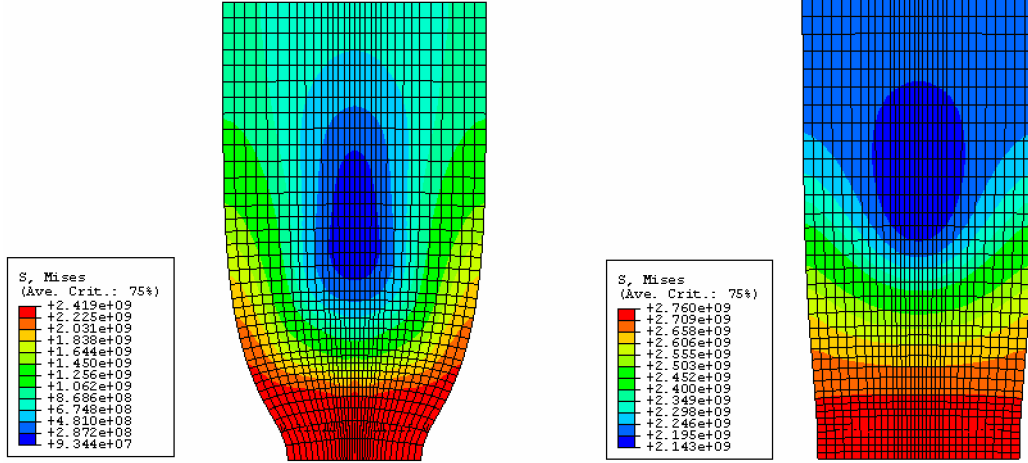
Figure 6.6:   **Finite Element Result Comparison for VascoMax 300 SHB Specimen.**

When the constitutive model matches the SHB data better, the results are a better fit to the experimental measurements. Therefore, the more closely the full strain-rate range models are to those SHB data points, the better the mid-range strain-rate results will be. Consequently, the Zerilli-Armstrong formulation is a superior choice in order to optimize the model's reflection of the entire range of experimental data. Because the full range model, appearing in Table 5.5, was developed using the high strain-rate data, it reflects the entire strain-rate range. Additional experiments are presented in this work to justify the claim that the constitutive models developed are capable, within CTH, of successfully modeling high energy impact events.

An additional result of this particular study was noting that the temperature concentration present in this finite element simulation of the SHB test provides an explanation for the unusual necking observed in the VascoMax 300 specimens. This

result prompted a metallurgical study of the SHB specimens to verify this viscoplastic phenomenon.

6.2 Metallurgical Verification of SHB Model Results

In order to validate predictions regarding shear band formation within the plastically deformed SHB specimens, a metallurgical study was performed on the specimens, similar to that presented in Chapter IV and [28–32, 125]. Four specimens were sliced in half and examined using optical microscopy techniques. As noted in Chapter IV, the final polishing step of colloidal silica partially etched the surface of the specimens - making optical comparisons easier. Additionally, the same procedure was followed in examining 1080 steel specimens so that heat-affected zones could be identified if they exceeded the austenizing temperature.

Figure 6.7 shows a micrograph of a 1080 steel specimen (test T-12, 150°C, 500/sec) at the fracture surface. There is a region of shear deformation, but no evidence of a heat zone and no localized region of shear damage. Note that the material damage is oriented at 45° to the axis of tension.
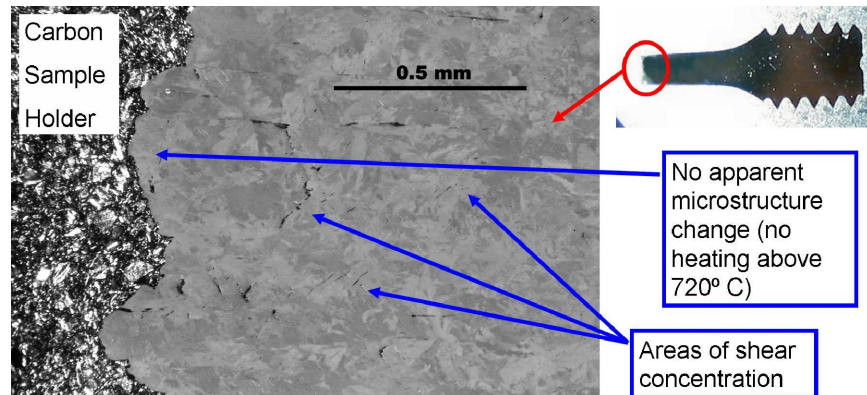
Figure 6.7:   **SHB Specimen T-12, As-Polished, Tip.**

Figure 6.8 shows shear concentrations along the specimen length, away from the fracture surface. Again, the shear effects not being localized in a narrow band closely corresponds with the predictions made by the finite element results. Another 1080 specimen was examined (test T-38, 400°C, 1500/sec) in which lower numbers

of shear concentrations were observed. This matches a related study concerning the effect initial temperature has on shear band creation [125].
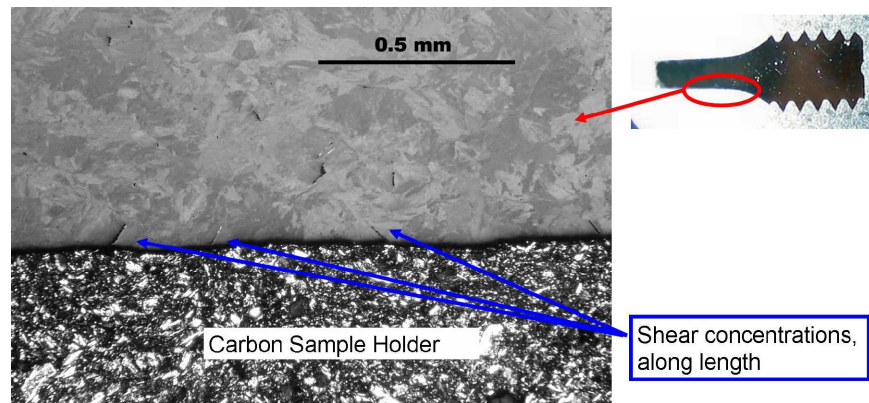
Figure 6.8:   **SHB Specimen T-12, As-Polished, Side.**

A somewhat different result was noted when an examination of the VascoMax 300 specimens was performed. Figure 6.9 shows a micrograph of the necked region (test T-4, room temp, 500/sec) of a VascoMax 300 SHB specimen. A large concentration of voids can be observed in the necked region, and nowhere else. Furthermore, some shear concentrations were observed in Figure 6.10 near the fracture surface - which did not occur elsewhere on the specimen.
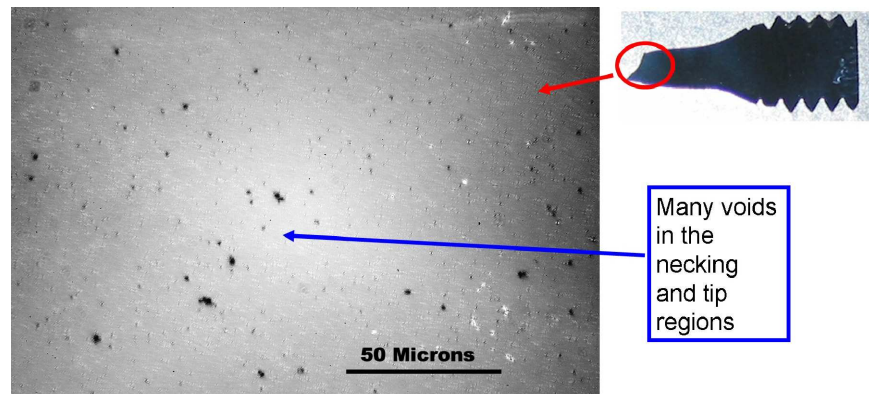
Figure 6.9:   **SHB Specimen T-4, As-Polished, Tip Region.**

These features contrast sharply with those away from the necked region, as shown in Figure 6.11. Away from this region, there are no significant concentrations of voids and no shear concentrations. Another VascoMax 300 specimen was examined
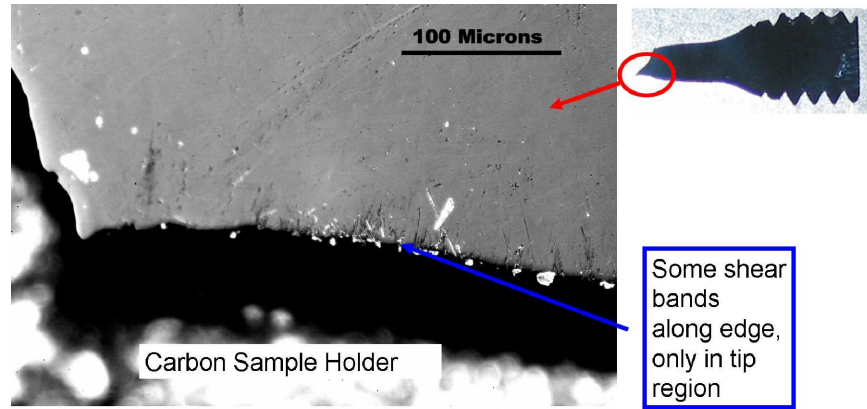
Figure 6.10:   **SHB Specimen T-4, As-Polished, Tip.**

(test T-27, 540°C, 1500/sec), which represents a higher temperature and strain-rate, and the necked area of that specimen appears in Figure 6.12. Note that the number of voids observed was less than test T-4. This again points to reduced shear localization as the initial temperature is increased [125].
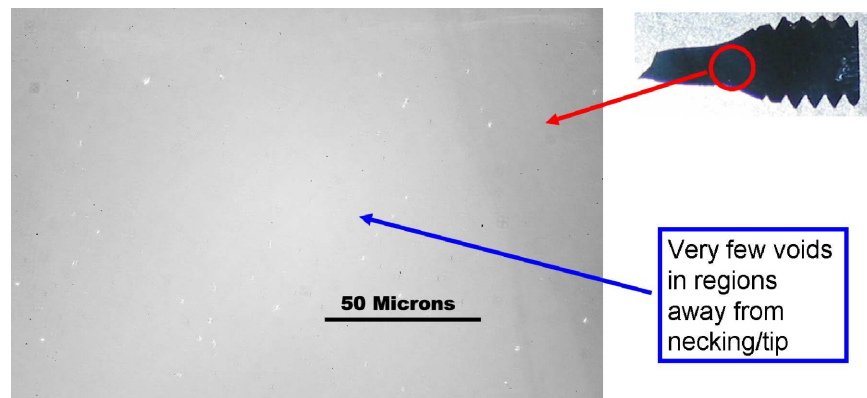
Figure 6.11:   **SHB Specimen T-4, As-Polished, Middle.**

These metallurgical results from the VascoMax 300 specimens compare favorably to the analysis presented in this work. Not only was the shear concentration localized in the necked region as predicted, but the unaffected nature of the microstructure away from that region was also reflected. Additionally, the higher initial temperature of test T-27 appears to have resulted in less shear generation within the resulting deformed material [125].
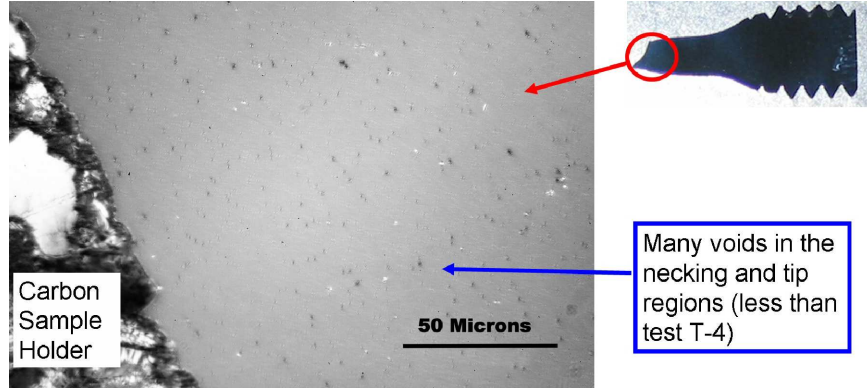
Figure 6.12:   **SHB Specimen T-27, As-Polished, Tip.**

The micrographic examination of the SHB specimens appears to validate both our constitutive model and the resulting shear band prediction based on those constitutive relationships. Although this simulation could not be accomplished within CTH, it does provide verification that the constitutive model based on the SHB tests could replicate those same tests within a computational code. Again, the full-range constitutive model, developed in the Zerilli-Armstrong formulation, is as close as possible to those mid-range strain-rate experimental data points while accurately estimating the high strain-rate regime.

The next set of experimental tests conducted were mid-range strain-rate impact tests that could be modeled within CTH.

6.3   Taylor Impact Tests

The Taylor Impact test involves shooting a cylindrical projectile against a non-deforming target and making judgements concerning material characteristics based on the deformation of the projectile. G. I. Taylor first proposed this test in 1948 [116] along with Whiffen [123]. Since then, the test has been used to estimate yield stress and to validate constitutive models in numerical codes (see Cinnamon, et al. [24, 25], House [51], Wilson, et al. [124], Jones, et al. [55, 58] and Nicholas [88]). This is because the test is more available to investigators than other more costly experiments. Additionally, this test can generate impact strain-rates on the order of 10^3/sec - which

serve to validate models created using the SHB test. Some researchers have used the Taylor test themselves to generate the material constitutive models [55, 58].

6.3.1 *Taylor Test Overview.* A Taylor Impact test facility was created using the 1/2 inch barrel light gas gun pictured in Figures 6.13 (the back end of the gun, including the compressed gas bottle and firing solenoid) and 6.14 (the exit end of the barrel with a sabot stripper plate, the target and fiducial). The target was a block of VascoMax 300 heat treated by the HHSTT to be metallurgically identical to the shoe material and then highly polished. A set of projectiles were manufactured with a nominal diameter of 6 mm and lengths of 30 mm, 60 mm, and 90 mm. They were constructed of 1080 steel (from as-received rail stock) and VascoMax 300 (heat treated in the same fashion as the sled shoes). These material, then, possess the same properties as the sled and rail materials in the HHSTT hypervelocity gouging problem.
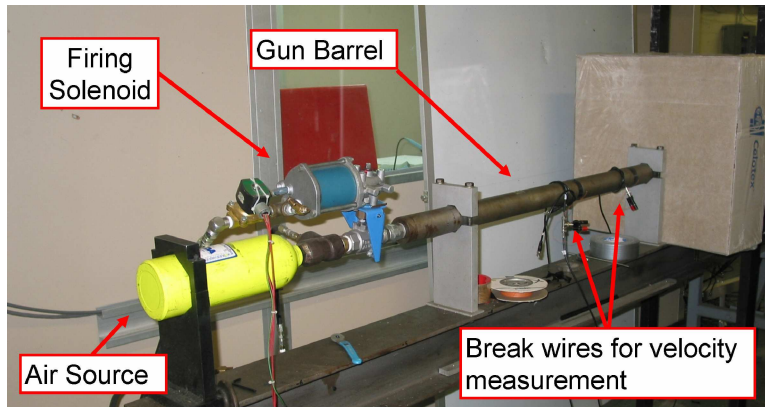
Figure 6.13:   **Rear of Light Gas Gun.**

Due to the chosen size of the cylinders, a sabot was necessary to hold the specimens in the 1/2 inch barrel as they traveled down the gun. The sabots were fabricated from plastic and "stripped" off the projectile by the steel plate immediately past the barrel end. This plate allowed the projectile through and held the plastic sabot (although the sabots would typically break apart during the process after releasing the projectile). The projectiles would continue and impact the target. This impact was
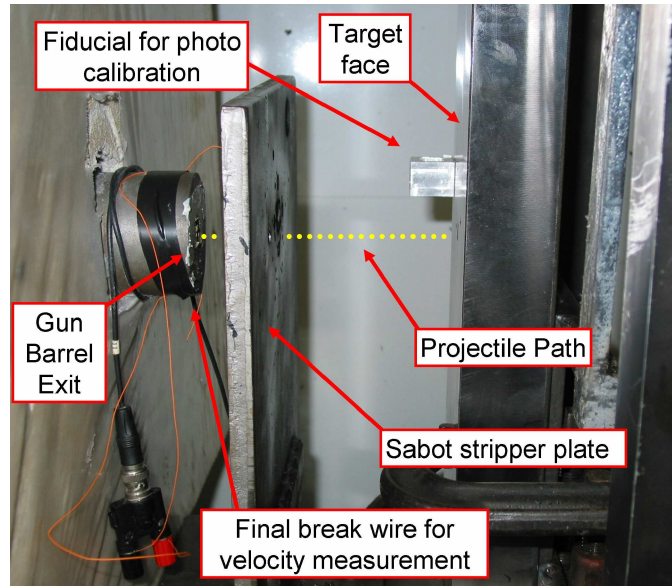
Figure 6.14:   **Exit End of Light Gas Gun.**

recorded via a high-speed digital camera with the capability to take a frame every 21 microseconds. This camera appears in Figure 6.15.
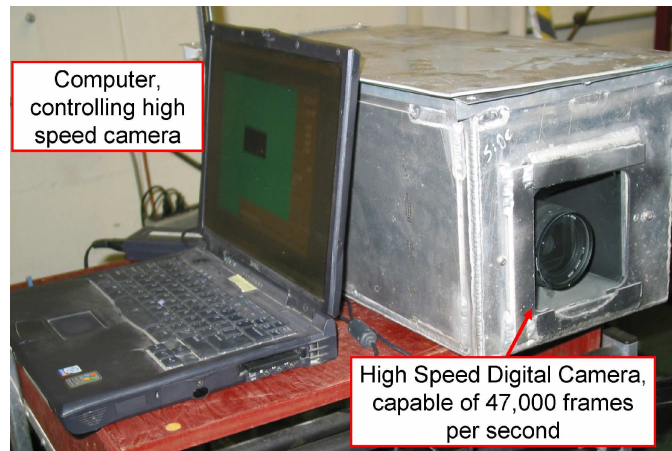
Figure 6.15:   **High Speed Phantom Digital Camera and Computer.**

The velocity of the projectile was measured with the use of trip wires across the barrel - two at various distances down the length of the barrel and one across the barrel exit. A computer would record the time difference between wire breaks and a velocity could be computed. This velocity was used to validate our primary technique of reading the impact velocity using the high-speed photographs. The

velocities from these two methods were within 10% of each other. The "fiducial" (of known dimensions) on the target face was used to calibrate distances in the digital photographs. Figure 6.16 illustrates an example high-speed photograph of a Taylor cylinder impact and the resulting deformation.
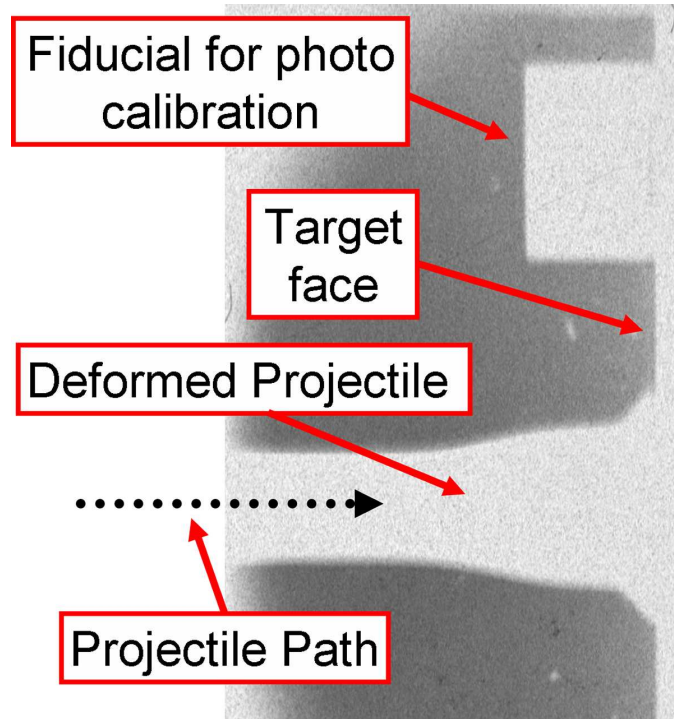
Figure 6.16:   **Example High Speed Photograph of Taylor Impact.**

6.3.2   Taylor Test Results.   Early in the process of conducting the Taylor Tests, the VascoMax 300 exhibited a very low tolerance for an off-axis impact. The brittle nature of the material led to projectile fracturing at very low impact velocities (as low as 75 m/s). In testing VascoMax, a very close to normal impact was required, and a low impact velocity. As the test procedure was improved and thereby the accuracy of the impact vector, more typical Taylor impacts were recorded. However, pushing the velocity up past 135 m/s resulted in fracture even with a normal impact. The 1080 steel projectiles experienced deformation in the typical fashion. Figures 6.17 and 6.18 show examples of post-test deformation.

Figure 6.17: **Deformation of VascoMax 300 Taylor Specimen (V10).**
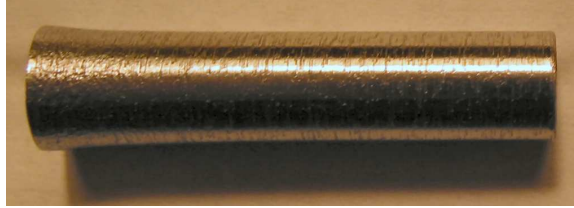
Figure 6.18: **Deformation of 1080 Steel Taylor Specimen (S6).**

Tables 6.1 and 6.2 summarize the Taylor impact results for VascoMax 300 and 1080 steel, where D_0 is the initial specimen diameter, L_0 is the initial specimen length, v_0 is the initial impact velocity (measured from the digital photographs), L_f is the specimen final length, D_f is the final mushroom diameter, and h_f is the undeformed section length (i.e. the remaining length of the cylinder that has not experienced any measurable diameter change). These quantities are illustrated in Figure 6.19.
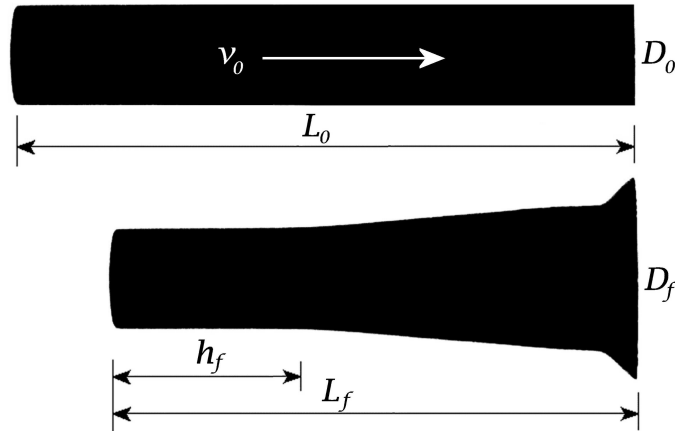
Figure 6.19: **Measured Characteristics from a Taylor Impact.**

6-13

Table 6.1:   Taylor Impact Results for VascoMax 300.

Test Shot	L_0 (mm)	D_0 (mm)	v_0 (m/s)	L_f (mm)	D_f (mm)	h_f (mm)
V5	60.08	5.89	64	59.95	6.07	59.93
V6	60.06	5.93	76	59.78	6.1	58.9
V7	60.04	6.01	92	59.52	6.25	58.1
V9	30.02	6.08	83	29.81	6.22	27.5
V10	30	6.17	99	29.73	6.24	22.7
V11	59.91	5.88	107	59.4	6.01	53.4
V12	60.03	5.99	111	59.48	6.2	52.7
V13	89.92	5.93	111	89.04	6.12	83.3
V15	89.93	5.86	101	88.88	6.11	83.5

Table 6.2:   Taylor Impact Results for 1080 Steel.

Test Shot	L_0 (mm)	D_0 (mm)	v_0 (m/s)	L_f (mm)	D_f (mm)	h_f (mm)
S1	60	6	39	59.75	6	60
S2	60	6	134	57.46	6.6	41.32
S3	30	6	218	27.35	8.1	14.43
S5	29.96	6	207	27.44	7.9	16.44
S6	30	6	156	28.44	6.97	17.1
S7	30	6.01	263	25.94	9.59	11.29
S8	59.91	6	128	57.74	6.52	42.26
S9	59.95	5.89	148	57.19	6.6	39.96
S11	90.01	5.95	112	87.24	6.4	65.62

The high-speed camera provided an opportunity to examine the impact in a time resolved manner. The capability of our equipment in this case, however, prevented a detailed investigation of that deformation. We simply did not possess sufficient resolution to track the plastic wave or measure mushroom diameter as a function of time after impact. The photographs offered a way to verify a normal impact and evaluate qualitative aspects of the event. The post-test measurements of the specimens were the only data in terms of deformation that we could reliably gather.

Selected test shots are presented in this work to illustrate the character of the impact event. These appear in Figures 6.20 to 6.24. In some of these Figures the sabot material is seen behind the specimen because the sabot broke apart and came through the stripper plate. In others, the final trip wire is seen as it is being pushed out of the way by the cylinder. Each frame is separated by 21 microseconds (which allows us to adjust for the single shot in which the camera time stamp function malfunctioned). Figure 6.22 shows a normal impact of VascoMax 300 that resulted in a classic 45° fracture of the tip along the line of maximum shear stress.
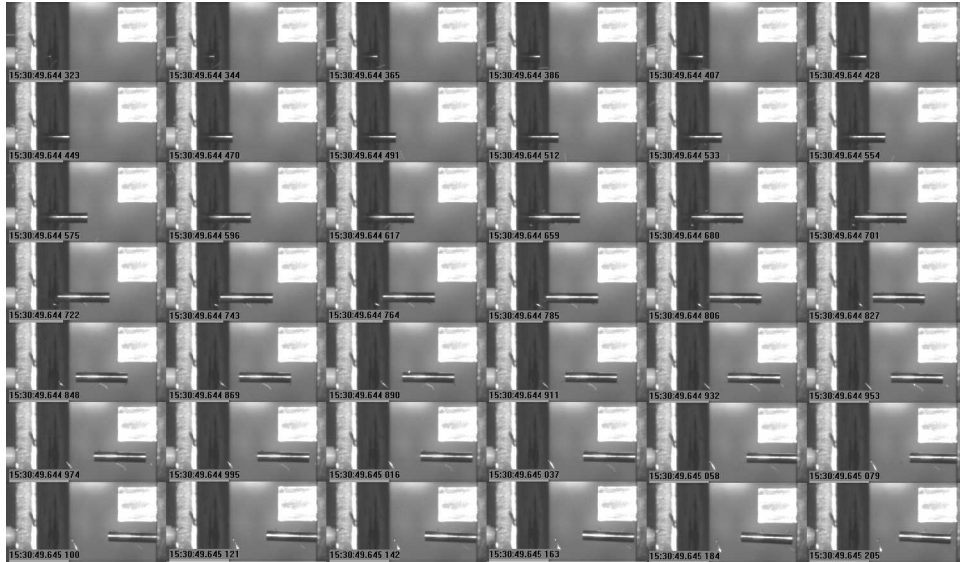
Figure 6.20:   **High-Speed Camera Photographs of Specimen V10.**

Figure 6.21: High-Speed Camera Photographs of Specimen V15.
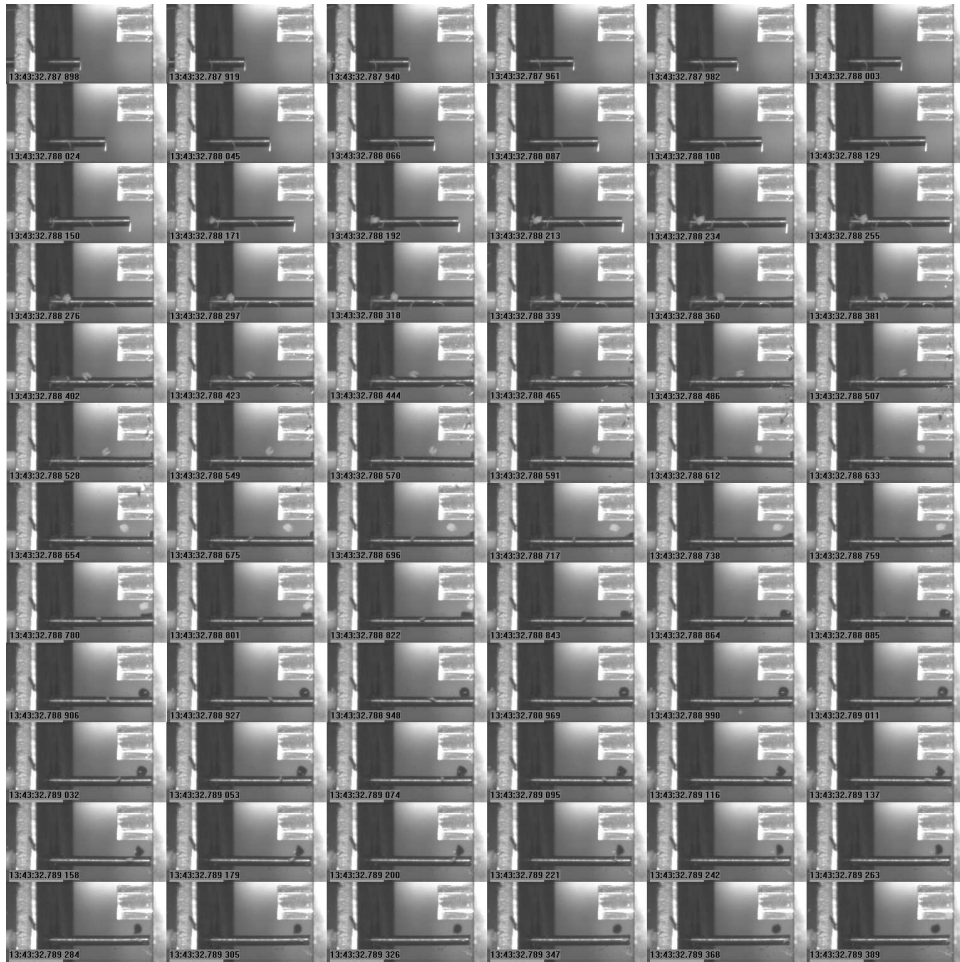
Figure 6.22: High-Speed Camera Photographs of Specimen V14.
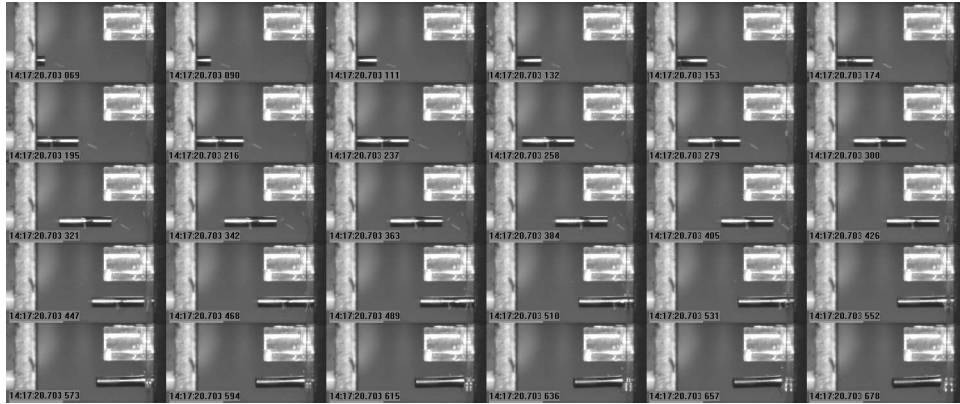
Figure 6.23: **High-Speed Camera Photographs of Specimen S6.**

Figure 6.24: **High-Speed Camera Photographs of Specimen S8.**

6-17

6.3.3 Constitutive Model Validation via Taylor Tests. The Taylor Impact Tests were conducted prior to the flyer plate experiments. Therefore, two separate validations of the material flow models were performed. Initially, the Johnson-Cook material model appeared to be adequate for the effort to model hypervelocity impact, so the material model in Table 5.3 was used.

As an initial check on the validity of the Johnson-Cook coefficients determined by using the Split Hopkinson Bar data, a simple Lagrangian Finite Element Taylor Impact Test solver, authored by Cook (of the Johnson-Cook relationship) [37], was used. This solver allows the user to input an initial estimate of the Johnson-Cook parameters and the other material properties of a Taylor Impact Test and run the impact to see if the post-test geometry matches experimental data. Using the constants from the Hopkinson Bar test, this solver showed excellent agreement between theoretical deformations and those seen in experimentation. This tool was used primarily due to the fact that this code could complete a run in approximately 10 seconds on a desktop PC, whereas a similar impact in CTH requires approximately 1 hour using a state-of-the-art, multiple processor, parallel computing cluster.

Once we had established high confidence in these Johnson-Cook coefficients, the CTH model was constructed to perform the experimental tests. The CTH Taylor impact test model was created using a 0.002 cm mesh (as previously discussed as mesh convergence value) in a 2-D axisymmetric implementation. The details of this can be found in Kennen [60] and [32, 34]. A more detailed discussion of the CTH modeling of these Taylor tests appears in Section 6.5. The results of this series of numerical simulations were:

> !

- The CTH model achieves the correct D_f, L_f, and h_f within 2% of measured values and also matches the curvature of the mushroom for VascoMax 300
- The CTH model achieves the correct D_f, L_f, and h_f within 5% of measured values and also matches the curvature of the mushroom for 1080 steel

- The new 1080 steel material model is 100% more accurate and the VascoMax 300 model is 50% more accurate than the previously used model [104–109] for Iron and VascoMax 250 respectively

After the flyer plate tests were completed and the full-range constitutive models were developed, these tests were revisited to ensure that the new Zerilli-Armstrong model would replicate these good results. The new model was slightly better in most cases, and in no case worse than the previously reported match to the Taylor Impact Tests. The failure pressure used was the value arrived at using the method in Section 5.2.3.

Based on these results, the Zerilli- Armstrong material flow model presented in Table 5.5 was validated for the mid-range strain-rate impact tests. As part of the investigation into the HHSTT gouging problem, material coatings (see section 2.2.6) were also investigated using the Taylor test.

6.4   Study of HHSTT Coatings via Taylor Test

In order to study the two specific coatings currently in use at the HHSTT, experimental techniques to ascertain the friction coefficients at hypervelocity were explored. This effort proved problematic, in that hypervelocity friction studies do not exist. The highest friction values published between metals is in the neighborhood of 800 m/s (see Bowden and Freitag [16], where they found at these velocities that the friction mechanism was due to local adhesion and shearing between the contact surfaces). Additionally, the test facility at the Air Force Research Laboratories also could not create a laboratory friction test above this velocity range. Therefore, a novel technique was created to coat Taylor Impact specimens and use the test discussed in Section 6.3.1 to compare the deformation of specimens [14, 32, 34].

6.4.1   Coated Taylor Impact Test Overview.   A set of 1080 steel Taylor specimens were coated with iron oxide (hematite) and epoxy – which are the two coatings used on the rails at the HHSTT. An additional series of specimens were

coated with an experimental material, known as "nanosteel [43]." A series of Taylor impact tests were conducted against a VascoMax 300 target, with an effort made to examine deformation at various velocities and at those specific speeds that uncoated tests had been conducted. Figure 6.25 depicts the different Taylor impact specimens used in our testing. The iron oxide and epoxy coatings were applied by the HHSTT in the same manner as the rails are coated for sled test runs - specifically using the same techniques and thicknesses. The nanosteel specimens were coated by a NanoSteel, Inc. subcontractor (Engelhard), to the same thickness specifications.
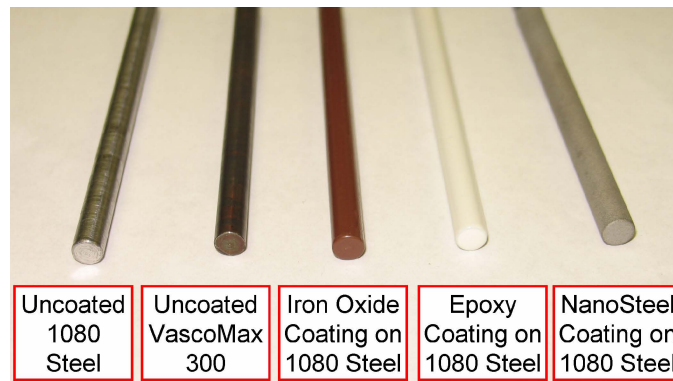
Figure 6.25: **Different Taylor Impact Specimens (Left to right: Uncoated 1080 Steel, VascoMax 300, Iron Oxide coated 1080, Epoxy coated 1080).**

6.4.2 Coated Taylor Impact Test Results. In the same manner as described in Section 6.3.1, a series of tests were conducted. The deformation was similar to those experienced for uncoated 1080 steel. Typical deformations can be seen in Figures 6.26 and 6.27. Note that the coatings tended to fracture off of the sides of the specimens during the impact process.

The coated specimens exhibited a greater radial deformation as compared to the uncoated specimens. Tables 6.3, 6.4, and 6.5 summarize the Taylor impact results for 1080 steel specimens coated with iron oxide, epoxy, and nanosteel.

Similar to Section 6.3.2, a series of selected test shots are presented in Figures 6.28 to 6.32 to illustrate the impact event with coatings. Note in the photographs that

Table 6.3:   Taylor Impact Results for Iron Oxide Coated 1080 Steel.

Test Shot	L_0 (mm)	D_0 (mm)	v_0 (m/s)	L_f (mm)	D_f (mm)	h_f (mm)
I1	30.32	5.98	161	28.61	7.18	15.85
I2	60.19	5.92	130	57.9	6.65	37.4
I3	90.21	5.93	110	87.38	6.44	54.4
I4	30.28	5.93	243	26.25	9.7	10.7
I5	60.25	5.85	144	57.25	6.74	32.25

Table 6.4:   Taylor Impact Results for Epoxy Coated 1080 Steel.

Test Shot	L_0 (mm)	D_0 (mm)	v_0 (m/s)	L_f (mm)	D_f (mm)	h_f (mm)
E1	30.53	6.04	151	28.7	7.13	20.8
E2	60.55	5.96	128	57.97	6.65	47
E3	90.55	5.96	108	87.68	6.41	78.85
E4	30.51	5.97	243	26.31	10.2	14.25
E5	60.48	5.97	144	57.37	6.9	39.4

Table 6.5:   Taylor Impact Results for Nanosteel Coated 1080 Steel.

Test Shot	L_0 (mm)	D_0 (mm)	v_0 (m/s)	L_f (mm)	D_f (mm)
N2	90.42	5.89	113	88.15	6.52
N4	60.28	5.95	118	58.76	6.44
N5	30.42	5.95	141	29.44	6.80
N6	30.47	5.95	254	26.85	9.50

6-21

Figure 6.26: **Deformation of Iron Oxide Coated 1080 Steel Taylor Specimen (I4).**

Figure 6.27: **Deformation of Epoxy Coated 1080 Steel Taylor Specimen (E5).**

the coating has very little resistance to the elastic deformation wave and therefore fractures off the side of the specimen.
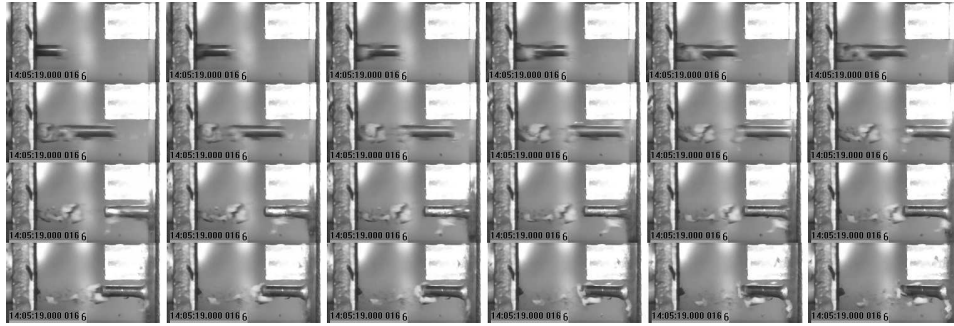
Figure 6.28: **High-Speed Camera Photographs of Specimen I4.**

The coated specimens deformation was characterized by greater mushroom growth (radial deformation against the target face) for the coated specimens versus the uncoated ones presented earlier. We know from estimates of the frictional coefficients that iron oxide has a lower coefficient than uncoated contact, and that epoxy has a lower one than iron oxide [108]. This is graphically illustrated by comparing the diameter growth ratio (D_f/D_0) versus impact velocity. This comparison appears in Figure 6.33. This clearly shows a relationship between increasing impact speed and the resulting mushroom diameter. Because the coatings act to reduce the

Figure 6.29:   **High-Speed Camera Photographs of Specimen I5.**
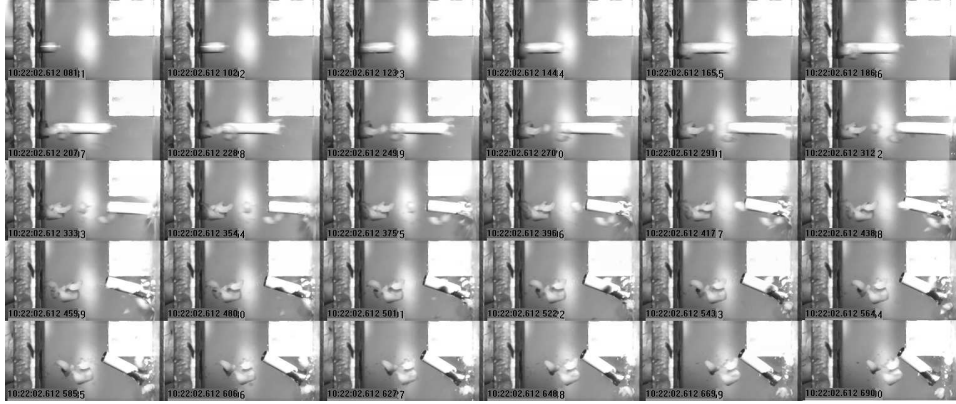
Figure 6.30:   **High-Speed Camera Photographs of Specimen E4.**

friction against the target face, it is apparent the epoxy has the lowest coefficient of friction, followed by iron oxide, nanosteel, and finally the non-coated state.

A simple one dimensional analysis is presented in the next section in an effort to quantify the difference in the coefficient of friction between these coatings.

6.4.3   One Dimensional Theory for Coating Comparison using the Taylor Impact Test.   In order to derive a simple relationship to compare the coefficients of friction between the three Taylor Impact cases (no coating, coated with iron oxide, and coated with epoxy), let's examine the deforming specimen in Figure 6.34. In this depiction, F_I is the force of impact, F_f is the force of friction, F_x is the force of deformation in the x-direction, and N is the normal force.

Figure 6.31: **High-Speed Camera Photographs of Specimen E5.**

Figure 6.32: **High-Speed Camera Photographs of Specimen N4.**

As we can see in the figure, the point of interest (the outside edge of the mushroom) can be thought of as experiencing the four forces depicted. To simplify this analysis, let us consider that F_I is constant over the time interval $0 \leq t \leq \Delta t_y$, where t is time, and Δt_y is the duration of the impact event in the vertical direction.

If we apply a simple impulse-momentum balance to the forces acting in the vertical direction, then it can be said that:

$$F_I \Delta t_y = m \Delta v_y \tag{6.1}$$
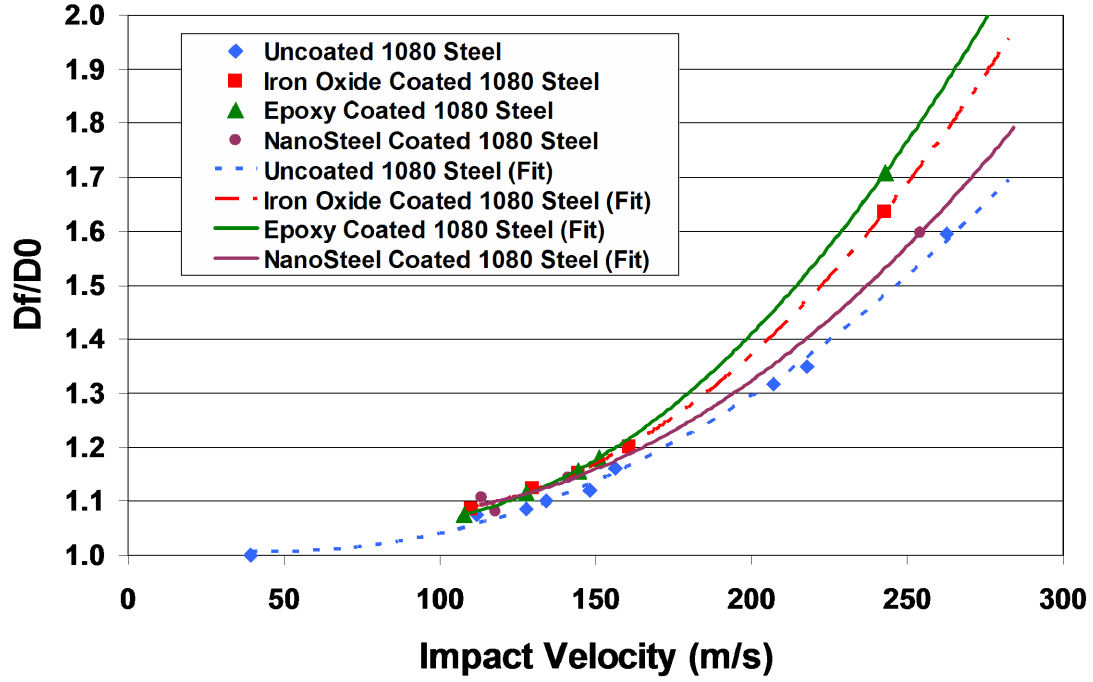
Figure 6.33: Comparison of Deformation for Coated Taylor Specimens.
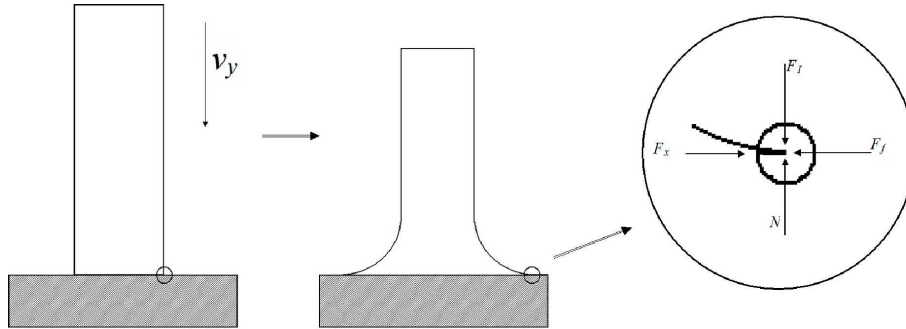
Figure 6.34: Diagram of Deforming Taylor Specimen.

where Δv_y is the impact velocity and m is the mass of the projectile. Since there is a force balance in the vertical direction, we know that:

$$N = F_I = \frac{m\Delta v_y}{\Delta t_y} \qquad (6.2)$$

If we consider that a state of dynamic equilibrium exists in the x-direction, then $F_f = F_x$. Applying kinematics to the expression of F_x yields:

$$F_x = ma_x = m\frac{\Delta v_x}{\Delta t_x} = m\frac{\frac{\Delta s_x}{\Delta t_x}}{\Delta t_x} = m\frac{\Delta s_x}{\Delta t_x^2} \tag{6.3}$$

where a_x is the acceleration of the deformation in the x-direction, Δv_x is the change in deformation velocity in the x-direction, Δt_x is the time duration of the deformation event in the x-direction, and Δs_x is the deformation in the x-direction. We also know that since $F_f = \mu N$ (where μ is the coefficient of friction), then:

$$\mu = \frac{F_f}{N} = \frac{\Delta s_x \Delta t_y}{\Delta v_y \Delta t_x^2} \tag{6.4}$$

Making a computation for the values of μ becomes problematic in that we do not have accurate experimental values for Δt_x or Δt_y. We could analytically estimate Δt_y by using elastic wave speed theory and assert that the specimen remains in contact with the target for the length of time that it takes the elastic wave to travel to the specimen end and return as a tensile wave (and thereby pulling the specimen off the target). Making that claim we arrive at:

$$\Delta t_y = \frac{2L_0}{c_0} = \frac{2L_0}{\sqrt{\frac{E}{\rho}}} \tag{6.5}$$

We note, then, that Δt_y becomes a constant for a particular shot geometry if we are interested in making a comparison between the various coatings options on the specimens. Additionally, if we take the comparison at a fixed impact velocity, the Δv_y is also a constant. Therefore:

$$\mu \sim C\frac{\Delta s_x}{\Delta t_x^2} \tag{6.6}$$

where C is a constant. Now, let us assume that the deformation speed, $\Delta s_x/\Delta t_x$, is a constant for a given geometry and impact velocity. That would lead to:

$$\mu \sim \frac{C'}{\Delta t_x} \tag{6.7}$$

where C' is a constant. Note that this implies that a greater deformation, Δs_x, would require a proportionally greater Δt_x for the deformation speed to remain constant. A greater Δt_x would result in a lower relative value for μ - which makes intuitive sense. This constant deformation implies that:

$$\Delta v_x = \frac{\Delta s_{x_1}}{\Delta t_{x_1}} = \frac{\Delta s_{x_2}}{\Delta t_{x_2}} \tag{6.8}$$

or

$$\Delta t_{x_2} = \frac{\Delta s_{x_2}}{\Delta s_{x_1}} \Delta t_{x_1} \tag{6.9}$$

Therefore, if we were to compare two shots of differing coatings:

$$\frac{\mu_1}{\mu_2} = \frac{\frac{C'}{\Delta t_{x_1}}}{\frac{C'}{\Delta t_{x_2}}} = \frac{\Delta t_{x_2}}{\Delta t_{x_1}} = \frac{\frac{\Delta s_{x_2}}{\Delta s_{x_1}} \Delta t_{x_1}}{\Delta t_{x_1}} = \frac{\Delta s_{x_2}}{\Delta s_{x_1}} \tag{6.10}$$

Again, we note that if $\Delta s_{x_2} > \Delta s_{x_1}$ that this relationship would require that μ_1 to be proportionally larger than μ_2. In a simple, one dimensional sense then, we can compare the relative coefficients of friction between coating states by comparing the resulting mushroom diameters in the Taylor impact test.

By re-examining Figure 6.33, we see that there is a distinct difference in mushroom diameter for the different Taylor specimens at the same impact velocity. The Figure includes a simple polynomial fit to the experiment data. We can take the point at 243 m/s to compare the coefficients of friction, which corresponds to a velocity at which we have a couple data points (and can extrapolate the other one). Additionally, at velocities higher that this range significant radial fractures in the mushroom occur. At this velocity (243 m/s):

$$\mu_{epoxy} = \frac{2.90mm}{4.23mm} \mu_{uncoated} = 0.69\mu_{uncoated} \tag{6.11}$$

and

$$\mu_{ironoxide} = \frac{2.90mm}{3.77mm} \mu_{uncoated} = 0.77\mu_{uncoated} \tag{6.12}$$

and

$$\mu_{nanosteel} = \frac{2.90mm}{3.15mm}\mu_{uncoated} = 0.92\mu_{uncoated} \tag{6.13}$$

Stated another way, with this simple analysis, the nanosteel coating appears to reduce the frictional effects by approximately 8%. The iron oxide coating reduces that friction by another 15%. The epoxy coating reduces that friction by another 11%, for a total reduction of friction over the uncoated rail of 31%.

As we have seen in the literature, frictional effects play an important role in this hypervelocity gouging problem. This experimental work and analysis indicates that there is a significant reduction in friction using the coatings.

While we have validated our constitutive models with respect to the uncoated Taylor tests, we need to also validate them in impacts involving the coating.

6.4.4 Constitutive Model Validation for Taylor Test Coated Specimens. Following the same procedure outlined in Section 6.3.3, the experimental tests were used to validate CTH models of the Taylor impact specimens impacting the VascoMax 300 target. In these cases, the model was modified to add a layer of coating (at a nominal thickness of 0.02 cm, which matches both the experimental specimens and the coating thickness used on the rail for the sled test at the HHSTT). A more detailed discussion of the CTH modeling of these Taylor tests appears in Section 6.5.

In the case of the coated specimens, a similar double set of validations for the flow models was performed - one validation using the SHB Johnson-Cook models [14,32,34,60], and a final one using the Zerilli-Armstrong full-range model. CTH had experimentally-based constitutive models and EOS models for both epoxy and iron oxide. Therefore, these CTH simulations of coated Taylor tests were also needed to validate the coatings models within the code.

! CTH runs were very similar for these two validation cases. Remarkably good agreement was achieved between experimental results and the numerical predictions. The CTH model achieves the correct D_f, L_f, and h_f within 5%

of measured values and also matches the curvature of the mushroom for 1080 steel with both iron oxide and epoxy coatings.

Figure 6.35 provides an illustrative example in which CTH has replicated the final deformation of Test E2 and the behavior of the coating - specifically the fracture of it off of the nose and sides of the projectile. The figure shows the post-test condition of Test E2 and the CTH simulation of the impact - the projectiles traveled right to left in this particular depiction. Both the deformation of the projectile and the damage to the coating was accurately predicted by the simulation.
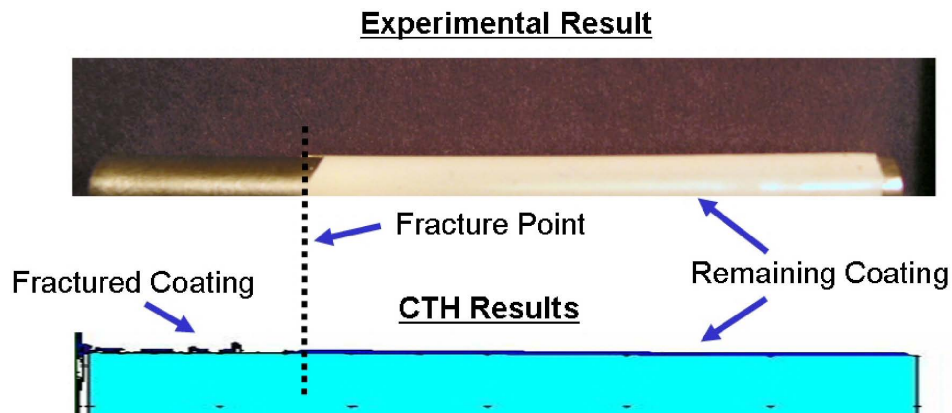
Figure 6.35: **Comparison of CTH results to Projectile, Test E2.**

These results establish confidence in both the developed constitutive models for the 1080 and VascoMax 300 steels and the ability of CTH to model deformations with and without coatings.

6.5 Modeling of Taylor Impact Tests in CTH

The validation of the material constitutive models within CTH necessitated a related study into how CTH handles the contact schemes before the Taylor impact model could be used.

6.5.1 CTH Contact Schemes. One of the primary areas of study within the hypervelocity gouging phenomenon is the topic of friction, the heat generated by it, and how this interaction can be accurately reflected in a numerical model. CTH has

several contact algorithms for describing material interactions on the interface which were carefully examined [83, 84].

There are three methods for defining the interface between materials in CTH. The first is the "no-slide" (default) condition. This approach assumes that the materials are joined upon contact, and the mixed cells (cells with two different materials within it) in the Eulerian mesh have strength characteristics weighted to the material volume fraction. This condition requires the materials to fail in shear for a sliding type action to occur. In order to attempt to solve this difficulty, a second algorithm was developed called the "slide-line." The slide-line artificially sets the material shear strength of the mixed cells to zero, which allows sliding action to occur. This fluid-like behavior leads to undesirable results in a penetration type impact in that the typically harder projectile experiences erosion during penetration. In order to correct this, a third algorithm was developed, known as the "boundary-layer" approach [98]. This algorithm moves the slide line into the target material in order to preserve the integrity of the penetrator. This approach is the only one in which the user may explicitly set a coefficient of friction between the materials.

In order to study these algorithms, a simple sliding model was developed in which a rod of VascoMax 250 slides within a stationary cylinder of iron (these being the closest materials in CTH to VascoMax 300 and 1080 steel at the time of the study) under continuous contact. The interior rod was not given a velocity vector to allow collision, and should not have interacted significantly with the target.

The slide-line algorithm developed significant numerical instability and created shear stresses within the target far away from the material interface. The result of the simulations was non-physical stresses and thermodynamic characteristics. The no-slide and boundary-layer algorithms produced similar results, with some numerical noise, but much better than the slide-line approach.

A further investigation was conducted in which a normal penetrating impact was evaluated using these various contact schemes. The outcome of this study was

to determine that the slide-line created unrealistic results and that careful use of both the no-slide and boundary-layer algorithms could yield good results. While the slide-line approach may be valid in some kinds of problems, the hypervelocity gouging problem requires a judicious application of the interface conditions.

The boundary-layer algorithm, however, was found to be valid only in a 2-D axi-symmetric case, and only using single-processor CTH computations. This limitation makes that particular algorithm of little use in the simulation of a full shoe/rail geometry model - which requires a 2-D plane-strain, multiprocessor mode. This particular limitation was unknown to previous investigators, with unknown impact on the results derived from using the boundary layer algorithm in this multi-processor, 2-D plane strain mode.

Therefore, the default contact scheme is the best choice to model hypervelocity impact. Eulerian hydrocodes, in general, have difficulty modeling sliding interfaces, friction, and contact [4]. However, the no-slide scheme selected offers the best opportunity to generate good results using CTH.

6.5.2 CTH Taylor Test Model. Having established the optimum contact algorithm for the simulation of the Taylor impact test, a model was created with CTH. As previously mentioned, a mesh convergence study was conducted by Szmerekovsky, in which the 0.002 cm cell size was found to be the limit of continuum mechanics for these steels and where the solution converged [108].

Figure 6.36 depicts the mesh used to simulate the Taylor specimens. The boundary conditions on the edges of the mesh were selected to be hydrodynamic conditions - which allow stress waves to pass (emulating a semi-infinite edge).

Lagrangian tracer points were included along the specimen edges to track material flow and to measure final diameter, length, and undeformed section length. A typical CTH simulation appears in Figure 6.37. In this particular case, the specimen has impacted the target and bounced back away. The fragments in the field are from the coating fracturing off of the specimen. An important note here is that the pres-
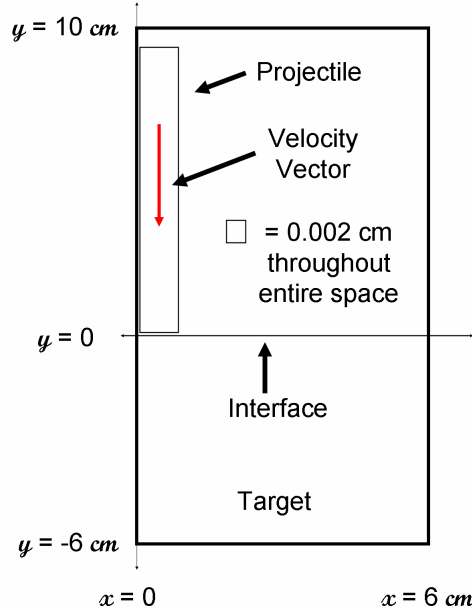
Figure 6.36:   **CTH Mesh for Taylor Impact Test Simulation.**

ence of the coating aided the mushroom development in the simulation in the same manner that it did in the experiment - acting as a sacrificial shear layer which reduced the effective friction between the projectile and the target.

Figure 6.38 illustrates one of the many possible plots available from CTH. In this case, the mid-range strain-rates of 10^4/sec and below are verified by observing the strain-rate of the early stages of deformation. After this initial stage, the strain-rates drop immediately to the 10^2/sec to 10^3/sec range - and then decrease as the event continues.

6.5.3   CTH Modeling Conclusion.   Based on a study conducted to ascertain the best contact scheme for use in simulation impact scenarios, the default no-slide condition was shown to be the most suitable. Additionally, previous work with the boundary layer algorithm may, in fact, be invalid due to the implementation of the algorithm within the CTH code. Finally, a CTH Taylor test model was developed and was successfully used to simulate the impact events.
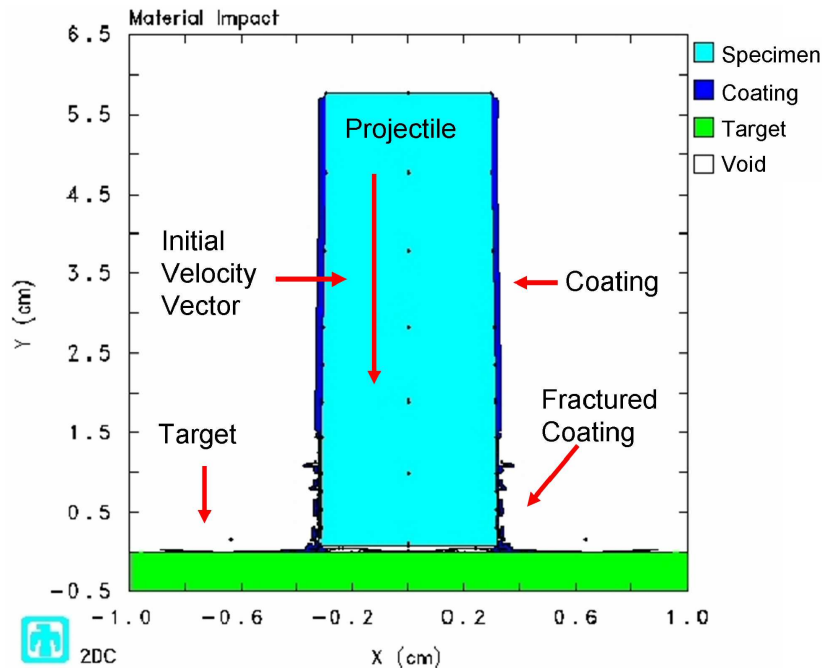
Figure 6.37: Example CTH Solution for Taylor Impact Test.
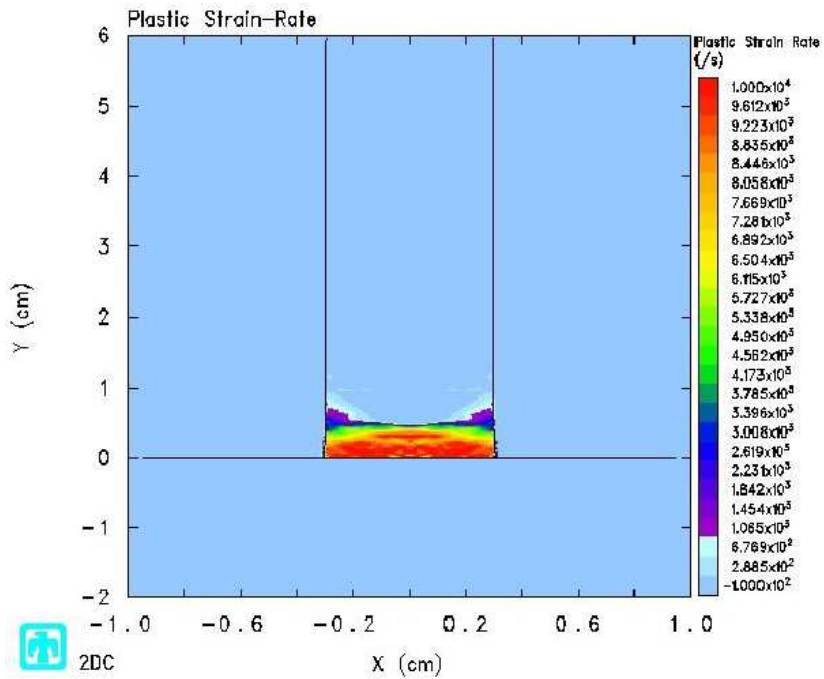
Figure 6.38: Example CTH Strain-Rate Solution for Taylor Impact Test.

6.6 Summary of Mid-Range Strain-Rate Model Validation

The mid-range strain-rate regime of the material constitutive models developed from experimentation in Chapter V were validated in a simulation of the SHB tests using a Lagrangian finite element code. The thermal characteristics that developed from these flow models, with respect to the creation of shear bands, were verified metallurgically. The flow models therefore demonstrated good fidelity in predicting material behavior in that type of test.

In order to transition the validation effort into the impact testing realm, a series of Taylor impact tests were conducted (with and without coatings). These tests were successfully simulated using CTH – which validated not only the mid-range portion of the full constitutive models, but also the CTH models for the coatings. These CTH models were developed after a tangential study concluded that the no-slide contact scheme in CTH was the most accurate for the simulation of impacts.

While the constitutive models have been validated at the mid-range strain-rate values, the hypervelocity gouging impact at the HHSTT also includes the high strain-rate regime. Therefore, to fully validate these models for application to that problem, a laboratory hypervelocity impact test was developed.

VII. Scaled Laboratory Hypervelocity Gouging Test

Validating the developed Zerilli-Armstrong constitutive models for VascoMax 300 and 1080 steel within the CTH hydrocode is necessary in order to ensure that simulations of the HHSTT sled scenario are accurate. Unfortunately, precise conditions at the point of gouging in the field are not known. That is, the HHSTT facility does not have the instrumentation arranged so that, where gouges occur, the sled parameters are recorded. Additionally, intentional gouging is not possible to arrange for analytical purposes. Therefore, the development of a laboratory hypervelocity gouging test was undertaken.

The dimensionality of the HHSTT sled makes full scale gouge tests prohibitive. In order to create a laboratory gouging test, the sled scenario is scaled down to in order to test in the laboratory. The purpose was to evaluate the HHSTT scenario in a scaled experiment. A mathematically rigorous scaling (via the Buckingham Pi technique) led to a geometry that was beyond the range of available laboratory facilities. To adjust for this eventuality, a one-dimensional penetration theory is developed to ensure laboratory tests will create gouging.

With this background, a series of hypervelocity gouging tests are conducted for the purpose of creating cases for CTH to match with our new constitutive models. The goal is to validate CTH's ability to generate correct predictions for hypervelocity gouging impacts, prior to its use in modeling the HHSTT scenario.

7.1   Scaled Gouging Test Development

In developing a laboratory hypervelocity gouging scenario, in which to examine this phenomenon of gouging and to establish test parameters to simulate within CTH, a mathematical scaling approach was utilized. The well-known Buckingham Pi technique, which has been applied on this type of problem previously [36,93,94,108], was adopted. The goal of this effort was to arrive at test parameters that could be replicated by the gun facility that was available. A very detailed presentation of this technique can be found in [108] and [90].

According to the Buckingham Pi Theorem, if a physical law consists of a number (m) of quantities, $\{q_i\}$, where $i = 1...m$, that have dimension and are products and powers of j independent fundamental dimensions, L_j, then a unit free fundamental law can be defined as

$$f(q_1, q_2, q_3, \cdots, q_m) = 0 \qquad (7.1)$$

where m is the number of dimensioned quantities to be used in the analysis [10,18]. A fundamental dimension is a quantity that is used to describe a dimensioned quantity. There are many different fundamental systems that can be used such as FLT (Force, Length, Time) and MLT (Mass, Length, Time). Take pressure for example, in the FLT system, pressure would be represented as FL^{-2}. In the MLT system, pressure is represented as $ML^{-1}T^{-2}$. It must be ensured that the fundamental dimensions alone can describe all dimensioned quantities.

As mentioned above, it is possible to represent any dimensioned quantity as a product of fundamental dimensions raised to some power:

$$q_i = \left[L_1^{d_1} L_2^{d_2} \cdots L_n^{d_n} \right]_i \qquad (7.2)$$

where q_i is a dimensioned quantity, L_j is a fundamental dimension, and d_k is the power the fundamental dimension is raised to. The dimensioned quantities can then be combined to form invariant Pi quantities:

$$\Pi = (q_1)^{\alpha_1} (q_2)^{\alpha_2} \cdots (q_m)^{\alpha_m} \qquad (7.3)$$

where the α_i's are an exponent to be determined. It then follows that:

$$\Pi = \left(L_1^{d_1} L_2^{d_2} \cdots L_n^{d_n} \right)_1^{\alpha_1} \left(L_1^{d_1} L_2^{d_2} \cdots L_n^{d_n} \right)_2^{\alpha_2} \cdots \left(L_1^{d_1} L_2^{d_2} \cdots L_n^{d_n} \right)_m^{\alpha_m} \qquad (7.4)$$

Rearranging this equation so that all of the L_i quantities are together leads to:

$$\Pi = (L_1)^{\beta_1} (L_2)^{\beta_2} \cdots (L_n)^{\beta_n} \tag{7.5}$$

where the exponents β can be described as:

$$\left\{ \begin{array}{c} \beta_1 \\ \beta_2 \\ \vdots \\ \beta_n \end{array} \right\} = \left[\begin{array}{cccc} d_{11} & d_{12} & \cdots & d_{1m} \\ d_{21} & d_{22} & & d_{2m} \\ \vdots & & \ddots & \vdots \\ d_{n1} & d_{n2} & \cdots & d_{nm} \end{array} \right] \left\{ \begin{array}{c} \alpha_1 \\ \alpha_2 \\ \vdots \\ \alpha_m \end{array} \right\} \tag{7.6}$$

Mathematically, $\{\alpha\}$ must exist in the null space of the dimension matrix, $[D]$, for the physical law to be dimensionally consistent. This requires that $\{\beta\} = \{0\}$. This requirement forces the solution of Equation 7.6 to give the products of dimensioned quantities that must remain invariant between models [18].

Also according to the theorem, if there are m dimensioned quantities and r fundamental dimensions, then there are $k = m - r$ independent dimensionless quantities. In the MLT system there will be $r = 3$ fundamental dimensions [18].

Careful selection of the variables to be used within the Buckingham Pi approach is required. Those characteristics, such as material density, which can be expressed as functions of other chosen parameters, are removed from consideration. Because the authors wish to scale the shoe/rail geometry, but still experiment with the materials at the HHSTT (VascoMax 300 and 1080 steel), some of the material properties (such as the wave speed of the material) are removed from consideration also. If that was not done, the Buckingham Pi theorem would dictate an experimental test in which two different materials (which result from the scaling of the material properties) should be shot in our laboratory hypervelocity scenario. Therefore, those properties that cannot be scaled are removed from consideration, and the dimension scaling rule is made mathematically more sound [9].

Table 7.1:   Buckingham Pi Dimensioned Quantities.

Dimensioned Quantity	Symbol	Fundamental Dimensions
Mass	m	M
Height	d	L
Length	l	L
Horizontal Velocity	u_x	LT^{-1}
Vertical Velocity	u_y	LT^{-1}
Compressive Yield Strength	$\sigma_{y,c}$	$ML^{-1}T^{-2}$
Elastic Modulus	E_0	$ML^{-1}T^{-2}$
Shear Modulus	G_0	$ML^{-1}T^{-2}$

It should be noted here that previous modeling of the sled/rail interaction was done in a plane-strain manner [104–109]. This choice and the implications to our scenario will be discussed later in this work in detail. At this point, however, the dimension of width (into the depth of a plane-strain implementation) is removed from consideration. Additionally, the rail dimensions are not scaled, since the rail appears as an infinite half-plane of material to the shoe (or scaled impact projectile) over the time scale of a gouging impact (approximately 10 microseconds). Therefore, taking the minimum number of fundamental characteristics from the sled/rail geometry, we arrive at the selected dimensioned quantities appearing in Table 7.1.

With these choices, the invariant parameter Π then becomes:

$$\Pi = (m)^{\alpha_1} (l)^{\alpha_2} (d)^{\alpha_3} (u_x)^{\alpha_4} (u_y)^{\alpha_5} (\sigma_{y,c})^{\alpha_6} (E_m)^{\alpha_7} (G_o)^{\alpha_8} (t)^{\alpha_9} \tag{7.7}$$

In fundamental dimension form, Equation 7.4 becomes:

$$\begin{aligned}
\Pi = &(M)^{\alpha_1} (L)^{\alpha_2} (L)^{\alpha_3} (LT^{-1})^{\alpha_4} (LT^{-1})^{\alpha_5} \cdot \\
&(ML^{-1}T^{-2})^{\alpha_6} (ML^{-1}T^{-2})^{\alpha_7} (ML^{-1}T^{-2})^{\alpha_8} (T)^{\alpha_9}
\end{aligned} \tag{7.8}$$

This reduces to:

$$\Pi = (M)^{\beta_1} (L)^{\beta_2} (T)^{\beta_3}$$

where,

$$\beta_1 = \alpha_1 + \alpha_6 + \alpha_7 + \alpha_8 \tag{7.9}$$

$$\beta_2 = \alpha_2 + \alpha_3 + \alpha_4 + \alpha_5 - \alpha_6 - \alpha_7 - \alpha_8$$

$$\beta_3 = -\alpha_4 - \alpha_5 - 2\alpha_6 - 2\alpha_7 - 2\alpha_8 + \alpha_9$$

Setting the values of β to zero and solving for $m = \alpha_1$, $l = \alpha_2$, and $u_x = \alpha_4$ one obtains:

$$\alpha_1 = -\alpha_6 - \alpha_7 - \alpha_8$$

$$\alpha_2 = -\alpha_3 + 3\alpha_6 + 3\alpha_7 + 3\alpha_8 - \alpha_9 \tag{7.10}$$

$$\alpha_4 = -\alpha_5 - 2\alpha_6 - 2\alpha_7 - 2\alpha_8 + \alpha_9$$

If these equations are rewritten in vector form, the result is:

$$
\begin{Bmatrix} \alpha_1 \\ \alpha_2 \\ \alpha_3 \\ \alpha_4 \\ \alpha_5 \\ \alpha_6 \\ \alpha_7 \\ \alpha_8 \\ \alpha_9 \end{Bmatrix}
=
\begin{Bmatrix} 0 \\ -1 \\ 1 \\ 0 \\ 0 \\ 0 \\ 0 \\ 0 \\ 0 \end{Bmatrix} c_3 +
\begin{Bmatrix} 0 \\ 0 \\ 0 \\ -1 \\ 1 \\ 0 \\ 0 \\ 0 \\ 0 \end{Bmatrix} c_5 +
\begin{Bmatrix} -1 \\ 3 \\ 0 \\ -2 \\ 0 \\ 1 \\ 0 \\ 0 \\ 0 \end{Bmatrix} c_6 +
\begin{Bmatrix} -1 \\ 3 \\ 0 \\ -2 \\ 0 \\ 0 \\ 1 \\ 0 \\ 0 \end{Bmatrix} c_7 +
\begin{Bmatrix} -1 \\ 3 \\ 0 \\ -2 \\ 0 \\ 0 \\ 0 \\ 1 \\ 0 \end{Bmatrix} c_8 +
\begin{Bmatrix} 0 \\ -1 \\ 0 \\ 1 \\ 0 \\ 0 \\ 0 \\ 0 \\ 1 \end{Bmatrix} c_9
$$

$$\tag{7.11}$$

The columns of Equation 7.11 represent a separate invariant. The invariant is found by associating each dimensioned quantity with its corresponding α value and raising

the dimensioned quantity to the power seen in the column vector. In this case, the invariants are given by:

$$\Pi = \left(\frac{d}{l}\right)^{c_3} \left(\frac{u_y}{u_x}\right)^{c_5} \left(\frac{\sigma_{y,c} l^3}{m u_x^2}\right)^{c_6} \left(\frac{E_m l^3}{m u_x^2}\right)^{c_7} \left(\frac{G_o l^3}{m u_x^2}\right)^{c_8} \left(\frac{t u_x}{l}\right)^{c_9} \tag{7.12}$$

The separate invariants are found by setting one $c_i = 1$ for a given i and the others to zero, which gives:

$$\pi_1 = \frac{d}{l}, \ \pi_2 = \frac{u_y}{u_x}, \ \pi_3 = \frac{\sigma_{y,c} l^3}{m u_x^2}, \ \pi_4 = \frac{E_m l^3}{m u_x^2}, \ \pi_5 = \frac{G_o l^3}{m u_x^2}, \ \pi_6 = \frac{t u_x}{l} \tag{7.13}$$

To maintain proper scaling, these six parameters must be matched in between the HHSTT sled and the developed laboratory hypervelocity impact scenario. Term π_1 of Equation 7.13 defines the geometry aspect ratio, π_2 defines the impact angle. Terms π_3 through π_5 relate material properties, length, mass, and horizontal velocity. Parameter π_6 is a time scale that can be used to compare two scenarios.

In order to scale the HHSTT sled problem, we begin with the known parameters from that gouging scenario. A nominal sled has a mass of 800 kg. The shoes that connect the sled to the rails are generally 20.32 cm long, by 10.8 cm wide, by 2.54 cm high. Taking a unit slice of the geometry for a plane-strain implementation (again, discussed later), the parameters for the HHSTT become those listed in Table 7.2.

Using these values for the HHSTT, the invariant parameters from the Buckingham Pi theorem can be computed. Those parameters can then be used in determining the required geometry of a scaled hypervelocity projectile. The π parameters establish ratios between these characteristics. Therefore, to arrive at a design for the laboratory test, we must constrain the solution space with real-world test limitations. Initially, we chose 0.6 cm as the hypervelocity projectile height, which allowed us to generate the remaining values. Unfortunately, this created a scenario which exceeded the capability of the guns available. Consequently, we optimized the available design variables

Table 7.2:　HHSTT Dimensioned Quantities [93,94].

Dimensioned Quantity	Symbol	Value
Mass	m	19.1 kg
Height	d	2.54 cm
Length	l	20.32 cm
Horizontal Velocity	u_x	1500 m/s
Vertical Velocity	u_y	-1 m/s
Compressive Yield Strength	$\sigma_{y,c}$	14.47 GPa
Elastic Modulus	E_0	180.7 GPa
Shear Modulus	G_0	70.42 GPa

(based on gun limitations) to arrive at the test geometry that best matched the π parameters. The impact angle selected was one that would guarantee gouging - due to a limited number of tests available to the authors (discussed in the next Section). Table 7.3 summarizes the parameters that results from the HHSTT geometry and the required scaled parameters for the laboratory tests. Parameter π_6 is not presented, as it is used to compare time scales and not geometry.

If strict adherence to the Buckingham Pi approach was possible, the test geometry would have been characterized according to the theoretical column in Table 7.3. However, the gun arrangement available restricted the geometry to projectiles of 4.78 g mass, 5.5 mm diameter, 25 mm long cylinders with hemispherical noses. The projectiles were limited due to a requirement to be aerodynamically stable in flight and sized for launch by the specific gun hardware. The maximum velocity achievable from our facility was 2225 m/s. As noted previously, this limitation prompted an increase in the impact angle in order to ensure sufficient energy was directed into the target rail to generate gouging (discussed in detail in the next Section).

Therefore, the theoretical scaled impact test was not possible to conduct given equipment limitations. Another approach needed to be developed to ensure that we

Table 7.3:   HHSTT Dimensioned Quantities [93,94].

Parameter	HHSTT Scenario	Theoretical Scaled Scenario	Actual Scaled Scenario
π_1	0.125	0.125	0.22
π_2	$-6.67 \cdot 10^{-4}$	$-6.67 \cdot 10^{-4}$	-0.1763
π_3	0.282	0.282	0.9851
π_4	35.619	35.619	125.4
π_5	13.984	13.984	48.88
Horizontal Velocity	1500 m/s	4809 m/s	2190 m/s
Vertical Velocity	-1 m/s	-3.2 m/s	-386 m/s

could create hypervelocity gouging impacts in the laboratory environment, given a launch velocity limits of 2225 m/s and the projectile limitations outlined above. A one-dimensional penetration theory was adapted to the gouging impact scenario to establish the test parameters. Using this approach, it was possible to create a laboratory gouging test that recreated the major characteristics of hypervelocity gouging. These laboratory gouges could then be used to validate the material flow model and CTH's ability to accurately simulate a hypervelocity gouging impact.

7.2   One-Dimensional Penetration Model

In order to better understand the gouging process, and to predict when gouging might occur in a scaled laboratory hypervelocity gouging experiment, a one-dimensional penetration theory is refined for use in this particular geometry [26].

7.2.1   Theoretical Foundations of the 1-D Penetration Model.   Cinnamon, et al. [19–23], developed a one-dimensional approach to predicting penetration depth and crater diameter based on previous analysis in [56, 61, 82, 115]. This theory was based on the penetrator being a rod of known geometry impacting a semi-infinite target material. This theory has application in the HHSTT hypervelocity gouging

problem in that the gouging process is considered to begin with rail damage from vertical impact (see Chapter II). Therefore, we re-examine the previously mentioned one-dimensional model and refine its presentation to be utilized as a design tool for a material combination that has no empirical data. That is, this one-dimensional theory can predict penetration depth (rail damage) based on known quantities in the HHSTT gouging problem or define a threshold impact velocity beyond which damage to the rail occurs. The analysis in [23] is reformulated here for clarity.

The general rod penetration process is detailed in Figure 7.1. An undeformed rod of known geometry (length L, and cross-sectional area, A_i) impacts a semi-infinite target at a known impact velocity, v_0. As the impact event unfolds, the head of the penetrator mushrooms into the target and material is ejected from the resulting hole - the undeformed section length is ℓ. When the event is complete, a measurable hole remains in the target material, with penetration depth z.
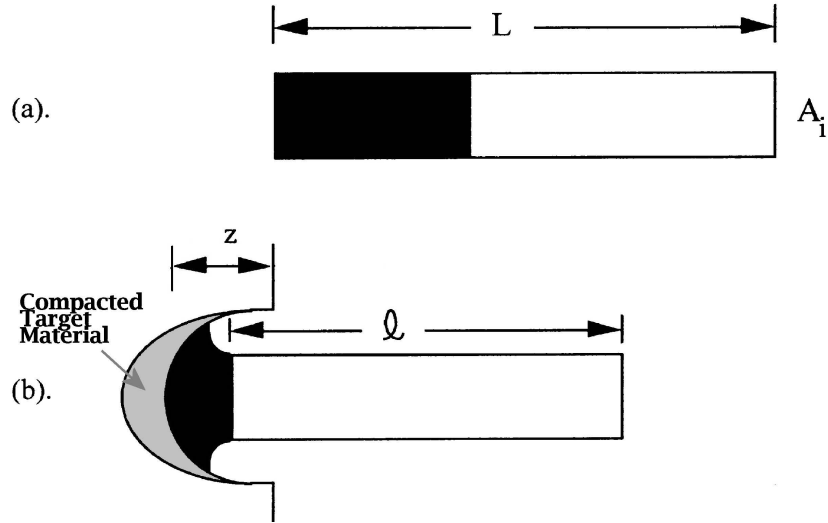
Figure 7.1: **Rod Penetration Event. a). Initial rod geometry, with a shaded region that will be lost to erosion. b). Penetration Event.**

Jones, et al. [56] developed the equation of motion of the undeformed section of the rod (by performing a momentum balance) as:

$$\ell\dot{v} + \dot{\ell}(v - u) = \frac{-P}{\rho(1 + e)} \tag{7.14}$$

where the dots refer to differentiation with respect to time, ℓ is the undeformed section length, v is the current undeformed section velocity, u is the penetration velocity, P is the average pressure on the penetrator tip, ρ is the penetrator density, and e is the engineering strain of the penetrator head.

By applying the conservation of mass across the plastic interface between the undeformed section and the mushroom another relation is determined:

$$e\dot{\ell} = v - u \tag{7.15}$$

Since the engineering strain, e, in the mushroom is compressive, and therefore negative,

$$e = \frac{A_i}{A} - 1 \tag{7.16}$$

where A is the instantaneous penetrator tip cross-sectional area.

This one-dimensional analysis can be improved by adding an initial transient phase, which is dominated by shock effects and complete mushroom growth. This phase precedes a steady state penetration phase in which further penetrator tip growth is not experienced. This addition was motivated by the observations of Ravid, et al. [92].

In applying this transient to the analysis, we assume that the undeformed section length does not experience appreciable deceleration (i.e. $\dot{v} \approx 0$). Therefore, $v = v_0$ during the mushrooming phase of penetration. During this transient, the initial cross-sectional area of the penetrator tip grows from A_0 to A_1. This cross-sectional area, A_1, at the end of the transient is maintained for the remainder of the penetration event (again, prompted by the experimental observations in [92]).

Ravid, et al. [92] also reported little change in the penetration velocity during this initial transient phase, which motivates the assumption that $u = u_0$ and hence Equation 7.14 becomes:

$$\dot{\ell}(v_0 - u_0) = \frac{-P}{\rho(1+e)} \tag{7.17}$$

and Equation 7.15 becomes

$$e\dot{\ell} = v_0 - u_0 \tag{7.18}$$

Equations 7.17 and 7.18 describe the mushrooming rod during the initial transient phase. We can arrive at an explicit expression for engineering strain by combining these equations.

$$e = \frac{-(v_0 - u_0)^2}{(v_0 - u_0)^2 + \frac{P}{\rho}} \tag{7.19}$$

This equation describes the strain during the initial transient, until the steady state penetration phase begins. At that point, the strain is fixed for the remainder of the event.

Once steady-state penetration is reached, the well-known modified Bernoulli equation is applied [56, 115]. This equation relates the pressure on the axis of the penetrator tip (p_a), the undeformed section velocity (v), the penetration velocity (u), and the material properties of the target and penetrator,

$$p_a = \frac{1}{2}\rho_t u^2 + R_t = \frac{1}{2}\rho(v-u)^2 + Y_p \tag{7.20}$$

where ρ_t is the target density, R_t is the target dynamic yield strength, and Y_p is the penetrator dynamic yield strength. We adopt a more explicit formulation of this equation in this work, contrasted to [23], for improved clarity. Making this relationship specific to our transient penetration analysis, Equation 7.20 becomes:

$$p_1 = \frac{1}{2}\rho_t u_0^2 + R_t = \frac{1}{2}\rho(v_0 - u_0)^2 + Y_p \qquad (7.21)$$

where p_1 is the axial penetrator tip pressure at the end of the transient. Similarly, Equation 7.19 becomes:

$$e_1 = \frac{-(v_0 - u_0)^2}{(v_0 - u_0)^2 + \frac{P_1}{\rho}} \qquad (7.22)$$

where e_1 is the engineering strain and P_1 is the average pressure on the penetrator tip, both quantities taken to be after the transient phase.

Equation 7.21 can be manipulated to solve for u_0 in terms of known quantities in the impact scenario (v_0, ρ, ρ_t, R_t, and Y_p). With a quantity for u_0, Equation 7.22 can be solved with only the additional quantity P_1. It is the determination of P_1 that is the foundation of this one-dimensional approach.

For the case that the target and penetrator have the same densities ($\rho = \rho_t$) and dynamic yield strengths ($Y_p = R_t$), Equation 7.21 algebraically reduces to:

$$u_0 = \frac{1}{2}v_0 \qquad (7.23)$$

This approximation of u_0 also applies for cases in which the impact velocities are relatively small [56].

For unequal dynamic yield strengths ($Y_p \neq R_t$) and equal densities ($\rho = \rho_t$), Equation 7.21 reduces to:

$$u_0 = \frac{\rho v_0^2 + 2(Y_p - R_t)}{2\rho v_0} \qquad (7.24)$$

The general penetration case ($Y_p \neq R_t$, $\rho \neq \rho_t$) is given by:

$$u_0 = \frac{-\rho v_0}{\rho_t - \rho} + \frac{1}{\rho_t - \rho}\left[\rho^2 v_0^2 - 2(\rho_t - \rho)(R_t - Y_p - \frac{1}{2}\rho v_0^2)\right]^{\frac{1}{2}} \qquad (7.25)$$

Therefore, e_1 in Equation 7.22 is a function of known parameters and the quantity, P_1.

At this point, we can also solve for some of the conditions at impact. For instance, the strain at impact, e_0, can be computed from Equation 7.19 if we know the average pressure on the penetrator tip at impact, P_0.

$$e_0 = \frac{-(v_0 - u_0)^2}{(v_0 - u_0)^2 + \frac{P_0}{\rho}} \tag{7.26}$$

The impact pressure on the penetrator tip axis, p_0, can be estimated from elementary shock physics relationships [89, 129]:

$$p_0 = \rho u_s u_0 \tag{7.27}$$

where u_s in the shock speed in the target. Values for u_s as a function of u_0 can be found in Shock Hugoniot tables, e.g. [76]. The presence of shock waves in these kinds of high energy impacts have been confirmed by various investigators in the field (for instance, [92]).

Calculation of P_0 from the estimation of p_0 is dependent on the assumed character of the pressure distribution. Previous works have assumed various distributions from constant to highly parabolic (see [22,23] for a full discussion). In general, P can be computed from:

$$P = \frac{1}{A_i} \int_{A_i} p \, dA_i \tag{7.28}$$

A number of pressure profiles were attempted, and it was noted that the more successful modifications to P_1 removed all the velocity dependence and instead assumed a single constant steady-state average tip pressure for the entire impact velocity range.

The mathematical model for the behavior of the penetrator is a rigid-plastic, instantaneously eroding rod model. As a result, the penetrator enters the target with some impact engineering strain e_0 that expands to e_1 during the transient. The impact pressure p_0 is usually very high relative to the steady state pressure p_1. Although this pressure decreases rapidly during mushroom formation in the transient phase, the values for p_0 can be significant. The mushroom diameter grows from the time of impact through the transient phase, and ceases at the beginning of the steady state portion of the event. The shock/impact stage takes place in a period of a few microseconds [92].

The instantaneous erosion assumption prevents the model from accounting for any additional erosion of the target - which occurs in actual practice. There is typically appreciable change in target geometry due to penetrator and target material ejection from the crater. As a consequence, the recovered targets will appear to have more cylindrical-type craters than the model would predict. Figure 7.2 illustrates the crater predicted by the mathematical model, and Figure 7.3 indicates how the actual geometry frequently appears.
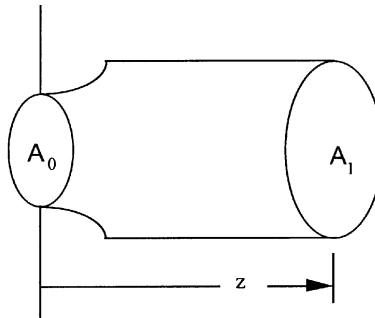
Figure 7.2:   **Idealized Crater Geometry.**

To this point, the one-dimensional theory can provide an estimate for penetrator strain, given an approximation for P_1. In order to compute the predicted penetration depth, we need to use the database of empirical test shots. A mathematically sound one-dimensional theory for predicting penetration depth remains elusive.
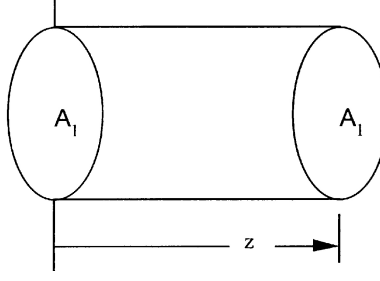
Figure 7.3:   **Actual Crater Geometry.**

For a number of years, investigators have observed a very strong correlation between impact kinetic energy and the resulting crater volume. For the velocity range of 1-6 km/s, this relationship is nearly linear [61, 82]. As a result, the crater volume, V_c, can be simply expressed as:

$$V_c = aE_0 + b \qquad (7.29)$$

where E_0 is the impact kinetic energy, a is the slope and b is the intercept of the linear crater volume/kinetic energy relationship. Of course, E_0 can be expressed as:

$$E_0 = \frac{1}{2}\rho A_i L v_0^2 \qquad (7.30)$$

The linear fit is performed for each shot combination. The results are highly dependent on the quality of the experimental data and sufficient discrete tests.

By utilizing a cylindrical approximation for the crater geometry (as in Figure 7.3), we can generate an estimate for penetration depths. The cross-sectional area of the target crater will be A_1, which is:

$$A_1 = \frac{A_i}{1 + e_1} \qquad (7.31)$$

The crater volume then becomes:

$$V_c = A_1 z \qquad (7.32)$$

We can then predict the penetration depth of an impact scenario by applying the appropriate crater volume/kinetic energy relationship. Combining Equations 7.29, 7.31 and 7.32 we get:

$$z = \frac{1}{A_i}(1 + e_1)(aE_0 + b) \tag{7.33}$$

Therefore, we have an estimation for the penetration depth based on an empirical crater volume/kinetic energy relationship and the strain at the end of the transient phase - which depends on an approximation of the average pressure on the penetrator tip at steady-state, P_1.

The determination of P_1 was the focus of previous work. The modified Bernoulli equation tends to over-predict penetration depth significantly as the impact velocities enter the hypervelocity range. A significant effort was made to create pressure profiles that tended to reduce the parabolic nature of the modified Bernoulli relationship [20, 57].

7.2.2 Results from the 1-D Penetration Model. Extraordinary results were obtained by disassociating the approximation of P_1 from a particular pressure profile, but simply assuming a constant steady state penetrator tip pressure for the entire velocity range. That is, the end of the transient and commencement of steady state penetration occurs at one particular value of average pressure for a specific set of materials. By examining a vast database of existing empirical data [21–23], a strong correlation between the P_1 that best fit the penetration data and the dynamic yield strength of the target was observed. A full discussion of the database used and the limitations of some of the experimental data can be found in [21, 22].

Figures 7.4 and 7.5 summarizes the data reduction from [19–23] and reports for the first time, in one location, the resulting crater volume/kinetic energy relationship and the estimate for P_1 that resulted in best fit matches to the empirical penetration depths. That is, estimates for P_1 were chosen for their ability to match experimental

data closely. In this process, discovering a correlation between these "best fit" choices of P_1 and physical parameters in the problem was a priority. It became clear that a strong correlation exists between the approximation of P_1 and the dynamic yield strength of the target. Figure 7.6 illustrates this correlation. The cases in which figures appear in this text are annotated by color highlighting around the entries.

Penetrator Material	Y_p (MPa)	ρ (kg/m³)	L (mm)	L/D	Target Material	R_t (MPa)	ρ_t (kg/m³)	a (thousands, mm³/kJ)	b (thousands, mm³)	P_1 (MPa)
Alum Alloy	200	2700	63.5	10	Lead	200	11200	1.28233	-1.405	128
1100-O Al	250	2720	9.525	3	1100-O Al	250	2720	2.67727	-.227	280
2024-T3 Al	675	2770	9.525	3	1100-O Al	250	2720	2.27238	-.006	280
7075-T6 Al	600	2804	9.525	3	1100-O Al	250	2720	2.69559	-.197	280
C1015 St.	600	7600	9.525	3	1100-O Al	250	2720	5.86367	-.174	280
Soft 4340	1263	7850	31.75	5	2024-T4 Al	400	2770	3.02053	-3.545	600
7075-T6 Al	600	2804	31.75	5	2024-T4 Al	400	2770	.97863	-.629	600
Hard 4340	1826	7850	31.75	5	7075-T6 Al	600	2804	1.861	-3.285	1050
Soft 4340	1263	7850	31.75	5	7075-T6 Al	600	2804	1.58951	-2.531	1050
1100-O Al	250	2720	9.525	3	C1015 St.	600	7600	.17751	-.046	1050
2024-T3 Al	675	2770	9.525	3	C1015 St.	600	7600	.185	-.051	1050
7075-T6 Al	600	2804	9.525	3	C1015 St.	600	7600	.18565	-.048	1050
C1015 St.	600	7600	9.525	3	C1015 St.	600	7600	.486	-.048	1050
4340 Steel	1600	7810	68.58	18	6061-T651 Al	600	2710	1.8191	-3.801	1050
1100-O Al	250	2720	9.525	3	2024-T3 Al	675	2770	.79216	-.069	1300
1100-O Al	250	2720	9.525	3	304 St.St.	675	7900	.14375	-.028	1300
2024-T3 Al	675	2770	9.525	3	2024-T3 Al	675	2770	.77581	-.051	1300
2024-T3 Al	675	2770	9.525	3	304 St.St.	675	7900	.15862	-.052	1300
C1015 St.	600	7600	9.525	3	2024-T3 Al	675	2770	1.37937	-.043	1300
C1015 St.	600	7600	9.525	3	304 St.St.	675	7900	.34775	-.01	1300
304 St.St.	675	7900	9.525	3	2024-T3 Al	675	2770	1.91916	-.24	1300
304 St.St.	675	7900	9.525	3	304 St.St.	675	7900	.43117	-.046	1300
C110W1	1200	7850	25	10	St37	750	7850	.4056	-.151	1400
C110W1	1200	7850	43	10	St37	750	7850	.39881	-.85	1400
C110W1	1200	7850	54	10	St37	750	7850	.4573	-1.373	1400
C110W1	1200	7850	25	10	St52	850	7850	.32086	-.088	1700
C110W1	1200	7850	43	10	St52	850	7850	.33567	-.448	1700
C110W1	1200	7850	54	10	St52	850	7850	.30658	-.674	1700
D17	2500	17000	28	10	St52	850	7850	.73457	-.291	1700
D17	2500	17000	60	10	St52	850	7850	.72127	-1.812	1700
C110W2	1100	7850	58	10	HzB,A	850	7850	.30214	-1.427	1700
Marag St	1000	7850	58	10	HzB,A	850	7850	.55887	-3.28	1700
Marag St	1000	7850	116	20	HzB,A	850	7850	.93885	-18.371	1700
35CrNiMo	2200	7850	54	10	HzB,A	850	7850	.33035	-2.768	1700
Elmet	2000	15500	58	10	HzB,A	850	7850	.51019	-1.189	1700
D17K	2500	17300	58	10	HzB,A	850	7850	.54269	-1.58	1700
D17	2500	17000	58	10	HzB,A	850	7850	.57631	-1.794	1700
W	2500	19300	60	10	HzB,A	850	7850	.67001	-2.742	1700
W75	2500	15500	58	10	HzB,A	850	7850	.49547	-1.264	1700
W90	2500	17000	58	10	HzB,A	850	7850	.55021	1.470	1700
D18	2500	18000	58	10	HzB,A	850	7850	.55090	-1.403	1700
H01T	2000	14500	58	10	HzB,A	850	7850	.31125	-.048	1700
D17.6	2000	17600	41.7	10	HzB,A	850	7850	.59808	-1.722	1700
D17.6	2000	17600	58	10	HzB,A	850	7850	.64719	-2.775	1700
Steel	1600	7850	58	10	HzB,A	850	7850	.1301	-.009	1700
D17	2500	17000	116	20	HzB,A	850	7850	.47207	-3.142	1700

Figure 7.4:   **Empirical Data Summary, Part 1.**

The fit in Figure 7.6 can be expressed as:

Penetrator Material	Y_p (MPa)	ρ (kg/m^3)	L (mm)	L/D	Target Material	R_t (MPa)	ρ_t (kg/m^3)	a (thousands, mm^3/kJ)	b (thousands, mm^3)	P_1 (MPa)
D18.5	2500	18500	58	10	HzB,A	850	7850	.50749	797	1700
H01T	2000	14500	58	10	HzB,A	850	7850	.5255	-2 544	1700
H60T	1600	13500	60	10	HzB,A	850	7850	.45625	-1.153	1700
H60T	1600	13500	58	10	HzB,A	850	7850	.53628	-2.431	1700
H70T	1400	13500	60	10	HzB,A	850	7850	.50427	-1.696	1700
H70T	1400	13500	58	10	HzB,A	850	7850	.51743	-1 364	1700
D17.6	2000	17600	101.5	17.5	HzB,A	850	7850	.743	-9.305	1700
D17.6	2000	17600	107.8	22	HzB,A	850	7850	.887	-16.427	1700
D17.6	2000	17600	110.25	22.5	HzB,A	850	7850	.35615	-1.552	1700
D17.6	2000	17600	156.8	32	HzB,A	850	7850	.36932	-2.853	1700
D17.6	2000	17600	163.2	32	HzB,A	850	7850	.90932	-19.938	1700
Hard 4340	1826	7850	60	6	RHA	1000	7850	.33074	-12.832	2200
OFHC Cu	300	8900	60	6	RHA	1000	7850	.44	-12.862	2200
Tantalum	500	16600	60	6	RHA	1000	7850	.59013	-6.425	2200
Hard 4340	1826	7850	95.25	7.5	RHA	1000	7850	.21294	-8.144	2200
Kenn W10	2500	17300	155.8	23	RHA	1000	7850	.60321	-23 912	2200
Kenn W10	2500	17300	121.75	23	RHA	1000	7850	57257	-13.244	2200
D17	2500	17000	28	10	W8	1000	7850	.49159	-.288	2200
U-3/4Ti	7000	18600	266.7	20	RHA	1000	7850	.54275	-165.234	2200
Kenn W10	2500	17200	50	10	Ger RHA	1000	7850	.47692	-1.299	2200
Teledy X27	2500	17330	78.74	10	RHA	1000	7850	50125	-5 403	2200
C110W1	1200	7850	25	10	Ger Arm St	1100	7850	.22431	-.094	2275
C110W1	1200	7850	43	10	Ger Arm St	1100	7850	.22444	- 359	2275
C110W1	1200	7850	54	10	Ger Arm St	1100	7850	.24157	-.97	2275
D17	2500	17000	28	10	Ger Arm St	1100	7850	.52198	-.335	2275
D17	2500	17000	60	10	Ger Arm St	1100	7850	.39291	- 897	2275
D17.6	2000	17600	17.4	3	Ger St	1200	7850	.57051	-1.474	2350
D17.6	2000	17600	29	5	Ger St	1200	7850	.58488	-1.431	2350
D17.6	2000	17600	42	10	Ger St	1200	7850	.86399	-7.527	2350
Soft 4340	1263	7850	31.75	5	Soft 4340	1263	7850	.2248	- 004	2400
7075-T6 Al	600	2804	31.75	5	Soft 4340	1263	7850	.12627	- 764	2400
Hard 4340	1826	7850	31.75	5	Soft 4340	1263	7850	.30299	- 884	2400
X21C	3500	17650	45.7	10	4340 Steel	1600	7810	.41786	-1.08	2500
Teledy X27C	2500	17400	81.6	10	4340 Steel	1600	7810	.35178	-1.915	2500
Teledy X27C	2500	17400	81.6	15	4340 Steel	1600	7810	.31052	-1.249	2500
Hard 4340	1826	7850	63.5	10	Hard 4340	1826	7850	.17261	-.562	2600
Hard 4340	1826	7850	47.63	7.5	Hard 4340	1826	7850	.16663	- 379	2600
Hard 4340	1826	7850	47.63	5	Hard 4340	1826	7850	.26591	-2.524	2600
Hard 4340	1826	7850	31.75	5	Hard 4340	1826	7850	.22845	- 73	2600
Hard 4340	1826	7850	63.5	5	Hard 4340	1826	7850	.24281	-3.068	2600
Hard 4340	1826	7850	31.75	3.33	Hard 4340	1826	7850	.27563	-1.211	2600
Hard 4340	1826	7850	31.75	2.5	Hard 4340	1826	7850	.25713	-1.228	2600
Soft 4340	1263	7850	31.75	5	Hard 4340	1826	7850	.26557	-.841	2600
OFHC Cu	300	8900	60	6	Hard 4340	1826	7850	.26425	-3.517	2600
Tantalum	500	16600	60	6	Hard 4340	1826	7850	.39113	2.931	2600
D17	2500	17000	28	10	D17	2500	17000	.22515	-.224	2900

Figure 7.5:   **Empirical Data Summary, Part 2.**

$$P_1 = 3.8[1 - e^{(-0.00135R_t)}] - 0.8 \qquad (7.34)$$

with P_1 expressed in GPa and R_t expressed in units of MPa in this instance.

Figures 7.7 and 7.8 illustrate the improvements this revised average pressure estimate makes in both the estimate of strain and penetration depths for a typical material combination - Kennenmetal W10 on Rolled Homogenous Armor (RHA).
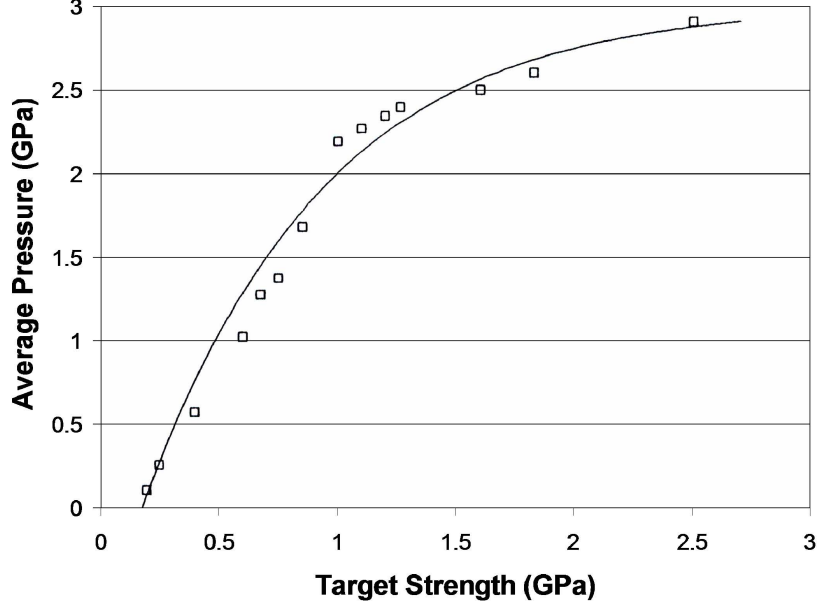
Figure 7.6: P_1 **vs. Target Dynamic Yield Strength.**

This combination is highlighted in gray in Figure 7.5. Figures 7.9 - 7.13 provide two additional examples to those presented in [23] to illustrate the capability of this theory to predict target damage - these cases are highlighted in red and blue in Figure 7.4. Figures 7.11 - 7.13 are chosen specifically to apply to the hypervelocity gouging scenario, discussed later.

7.2.3 Engineering Design Approach for using 1-D Penetration Model. One of the driving motivations for the development of this one-dimensional approximation is to develop an algorithm for engineering design efforts. That is, we wish to establish a database and a procedure for an estimation for target damage without the need to resort to expensive experimentation or time-intensive computational simulations. Of course, this would only serve as a first-order approximation. However, it promises to provide a good approximation prior to code simulations or gun range work.

The one-dimensional approach for predicting penetration depth can be used to make a first order approximation in impact scenarios that have not been experimentally performed. To establish this capability, we note that the modified Bernoulli equation and the theory developed rely on a few specific material parameters (i.e.
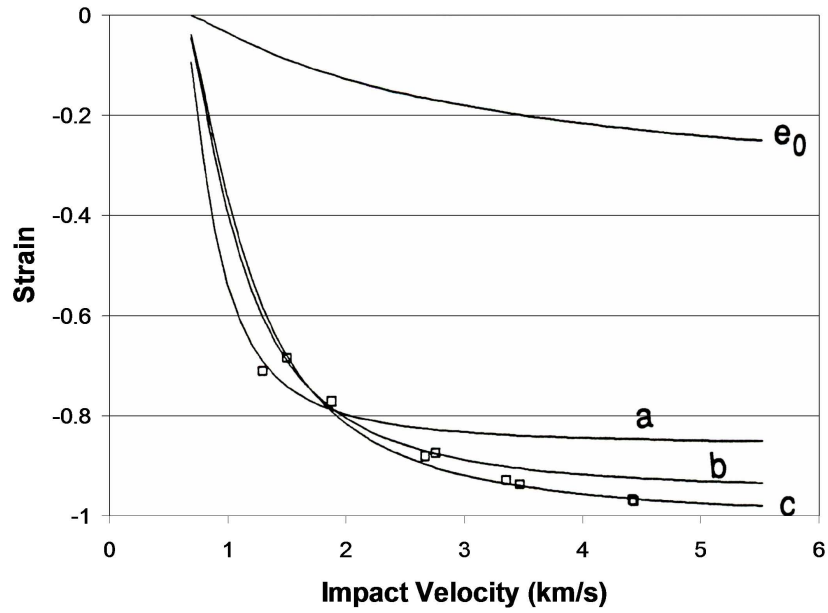
Figure 7.7:   Strain Comparison of Average Pressure Es-
timates, Kennenmetal W10 on RHA, (a) from approach
in [19, 20], (b) from approach in [57], (c) from approach
in [20, 21, 23, 26].
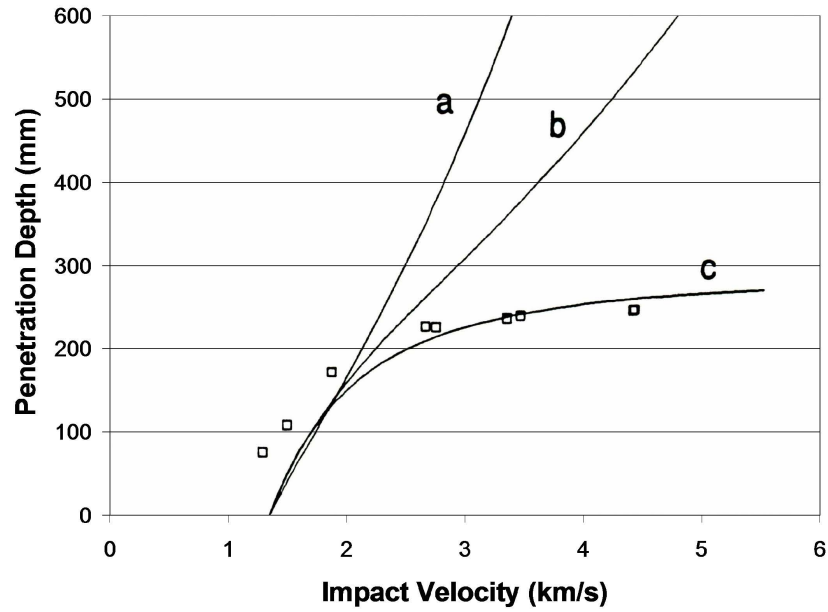
Figure 7.8:   Penetration Comparison of Average Pres-
sure Estimates, Kennenmetal W10 on RHA, (a) from
approach in [19, 20], (b) from approach in [57], (c) from
approach in [20, 21, 23, 26].
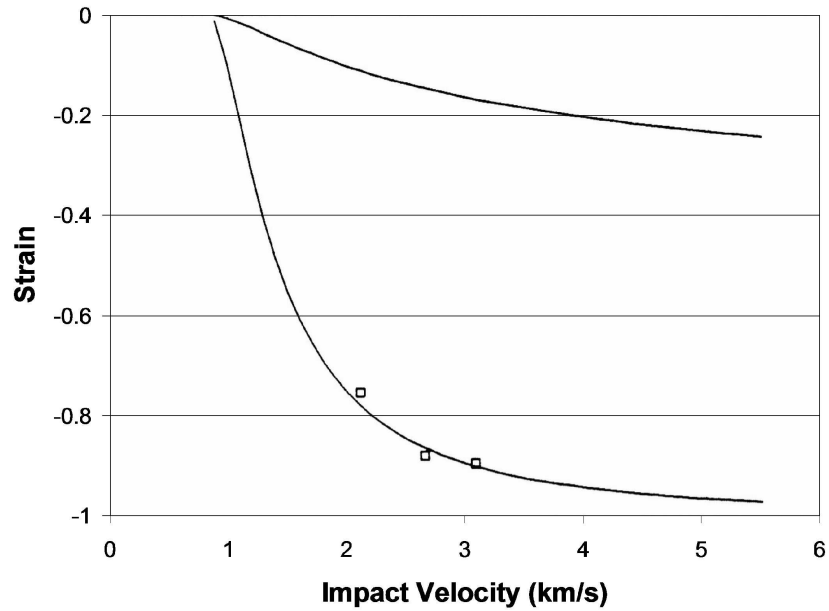
Figure 7.9: Strain, 4340 Steel on 6061-T651 Aluminum.
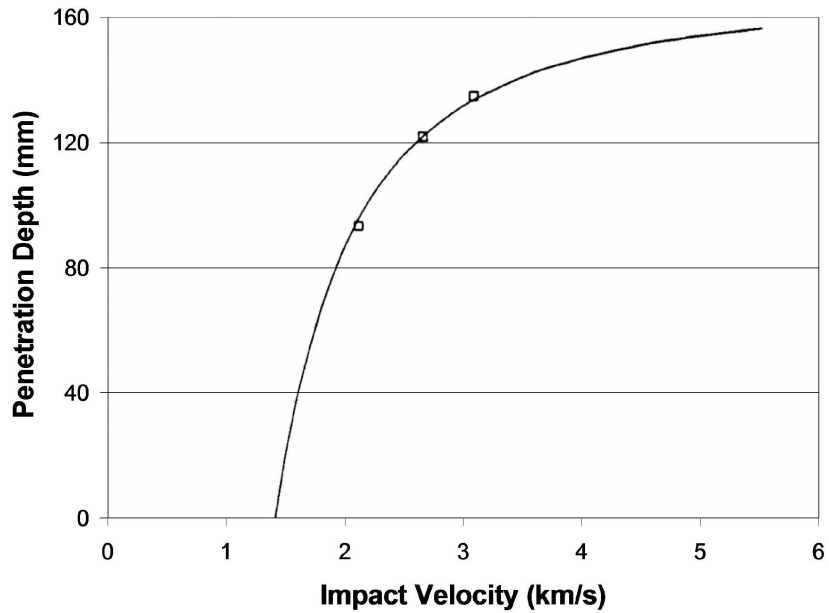
Figure 7.10: Penetration Depth, 4340 Steel on 6061-T651 Aluminum.

dynamic yield strength and density). If the materials to be evaluated can be found to closely match those presented in Figures 7.4 - 7.5, a simple algorithm can be followed to estimate the resulting damage to a target given a set of initial impact conditions.
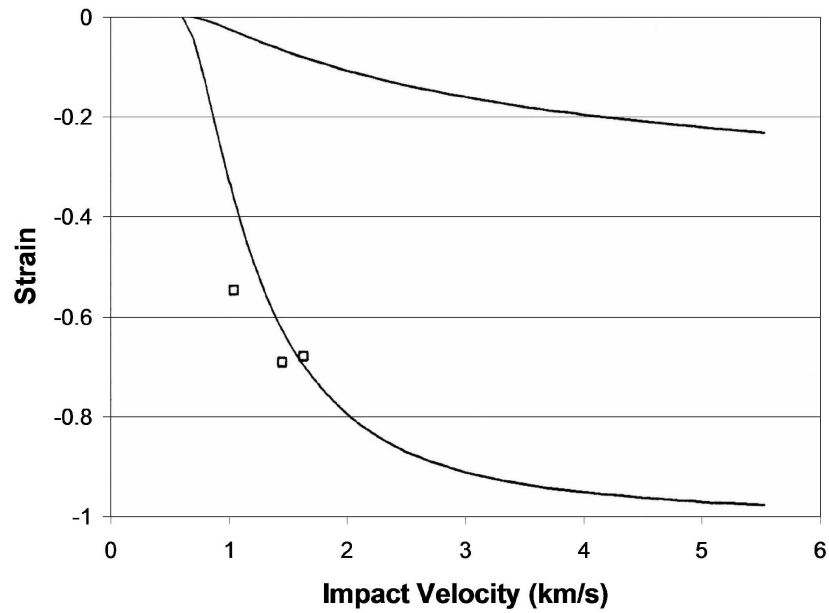
Figure 7.11:   **Strain, Steel on HzB,A.**
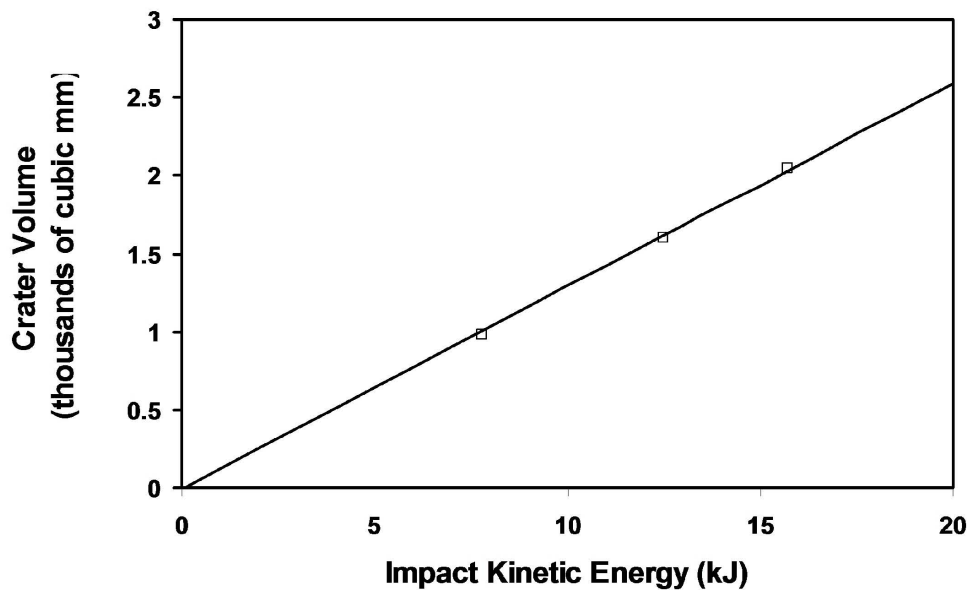
Figure 7.12:   **Crater Volume/Kinetic Energy, Steel on HzB,A.**

1. The first step would be to select a material combination in Figures 7.4 -
7.5 that matches fairly closely the density and dynamic yield strengths of a scenario
to be evaluated. The appropriate crater volume/kinetic energy relationship is then
selected. Note that a detailed discussion on estimating the dynamic yield strength is
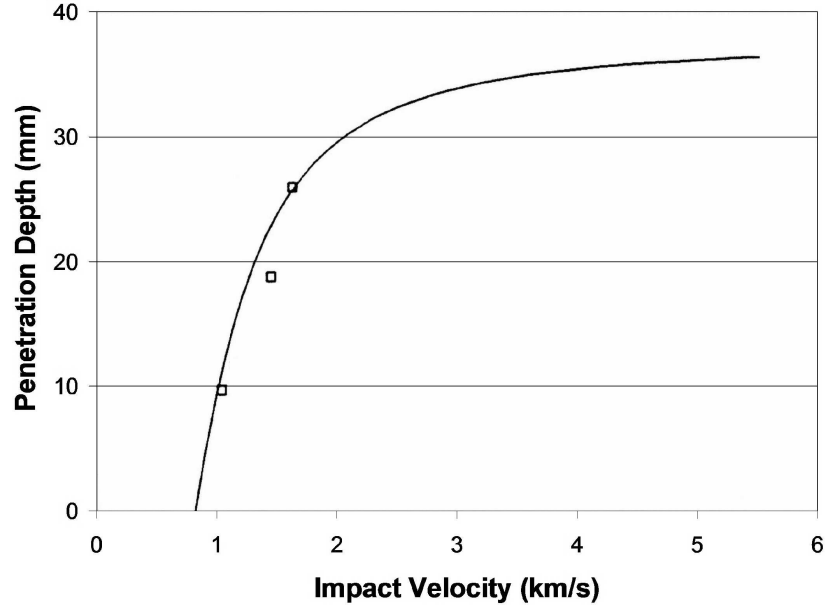
Figure 7.13:   **Penetration Depth, Steel on HzB,A.**

available elsewhere. Estimates for this flow stress is typically gained from other high strain-rate experimentation (e.g. Split Hopkinson Bar, Flyer Plate, Taylor Impact Tests, etc.).

2. Second, select the appropriate expression for u_0 from Equations 7.23 - 7.25 and compute the value. This value can then be inserted into Equation 7.22 with the appropriate value of P_1 from Figures 7.4 - 7.5 to arrive at e_1. In cases in which the estimated dynamic yield strength of the target material is not sufficiently close to the value reflected in Figures 7.4 - 7.5, P_1 can be computed from the relationship in Equation 7.34.

3. The crater cross-sectional area and the penetration depth can then be computed from Equations 7.31 and 7.33.

In this manner, a simple one-dimensional approximation for the penetration depth and crater diameter can be made using known quantities of a hypothetical scenario and the empirical relationships outlined in Figures 7.4 - 7.5.

For our specific application, we can use this simple approximation to estimate the required vertical velocity to damage the HHSTT rail and initiate gouging or work

from known rail damage to compute the velocities required for that damage to occur. Therefore, this penetration theory can be used to determine required laboratory configuration to ensure gouging - given the equipment capabilities. Additionally, this theory can be applied to the full HHSTT problem to serve as an analytical modeling tool that does not require significant computational resources to utilize. This application is presented in the next section.

In order to verify this one-dimensional theory is valid in our laboratory gouging environment, we can compare the theory results to known gouging parameters from the HHSTT problem. Successful estimation of those conditions will increase our confidence in this analytical approach.

7.2.4 Application of the 1-D Theory to the HHSTT Gouging Problem. The one-dimensional approach for predicting penetration depth can be used to predict the occurrence of gouging in the hypervelocity gouging impact found at the HHSTT. A great deal of work has been focused on determining a threshold velocity for gouging to occur. Many investigators have concluded that a vertical impact is necessary to initiate the gouging process [11, 12, 44, 64, 81, 113, 114]. They argue that an initial vertical deformation of the rail causes an asperity on the rail surface, which initiates the high pressure core and material mixing that characterizes gouging.

The one-dimensional approach described above can be utilized to compute the threshold vertical velocity component that creates a rail penetration and compare that against known parameters which lead to gouging at the HHSTT. To apply this approach to our hypervelocity gouging problem, we follow the computation steps presented in the previous section.

The material combination chosen in Figures 7.11 - 7.13 match closely with the values for density and dynamic yield strength of 1080 steel and VascoMax 300 found using the Split Hopkinson Bar Test (See Chapter V). This relationship is highlighted in blue in Figure 7.4. We then take the threshold penetration kinetic energy from Figure 7.12 as 69.5 J. Assuming that the nominal sled shoe assumed 1/4 of the sled

mass, a 200 kg mass would need to impact the rail at approximately 0.84 m/s. If we were to assume that some pitch or yaw in the sled had caused a single shoe to assume 1/2 the sled mass, then a 400 kg mass would need to impact the rail at about 0.59 m/s to begin penetrating the rail. This penetration would be the precursor, but not the guarantee, of gouging.

The values arrived at using this simple one-dimensional analysis are precisely within the range predicted by aerodynamic study and reported by the HHSTT as probable conditions during a hypervelocity test run [48]. Additionally, this magnitude (1-2 m/s) was used in the hydrocode, CTH, to initiate gouging by Szmerekovsky [105].

Taking this analysis one step further, we can assume that same 400 kg came down at 5 m/s and that the leading 10% of the shoe surface area impacted the rail (resulting from pitch angle, for instance). With nominal shoe dimensions of 20.32 cm x 10.8 cm, the resulting penetration depth would be 0.3 mm, which would be sufficient to cause gouging to initiate [105]. In fact, 0.1 mm was shown to be sufficient to initiate the typical gouge event within code simulations reported in [105]. If we further consider the penetrator surface to be 1% of the nominal shoe surface area, the resulting penetration depth would be 3.0 mm. This depth prediction approaches the magnitude of material removal ($\sim$5 mm) noted in Chapter IV from a gouged rail from the HHSTT.

Therefore, this one-dimensional theory does match previous CTH code computations and actual gouges in the field remarkable well and can provide insight into the parameters (such as vertical impact velocity and material dynamic yield strength) that govern hypervelocity gouging.

With this level of validation established for the one-dimensional penetration theory approach, the theory was used to establish the test parameters for the scaled laboratory hypervelocity gouging tests.

7.2.5   *Application of the 1-D Theory to the Laboratory Hypervelocity Gouging Tests.*   Using the same approach as described in the preceding section, the one-

dimensional theory was applied to the estimation of the experimental configuration for the laboratory hypervelocity gouging tests. Recall that the test limitations were a projectile of approximately 5 grams in mass, 5.5 mm in diameter, and 25 mm in length. Applying this dimensionality to the equations outlined in the previous section, the threshold penetration velocity yielded a striking angle of about 4.4°. If we use the previously reported value for minimum gouge depth in CTH models to create gouging of 0.1 mm, the angle would need to be approximately 8°.

Therefore, striking angles of 10° and 15° were chosen for the experimental tests. The critical nature of having these estimates prior to testing was that a small number of tests (four) was available. The tests were then conducted in order to generate hypervelocity gouging in the laboratory sense.

7.3 Laboratory Hypervelocity Gouging Experiments and Validation of the One-Dimensional Penetration Model

Based on the Buckingham Pi analysis presented earlier in this Chapter, and constrained by the capability of our laboratory gun facility, the test parameters for a scaled hypervelocity gouging test were chosen. While matching the parameters exactly was not possible, an attempt was made to establish a test geometry that reduced the difference between the theoretical parameters and the experimental parameters. The goal, of course, was to generate hypervelocity gouging within a laboratory scenario.

The experimental apparatus was available at the 46th Test Wing, Wright-Patterson AFB, Ohio. The projectile was fired by a 30mm powder gun as pictured in Figure 7.14. The projectile was held in the barrel by a sectioned sabot that split apart during free flight, as pictured in Figure 7.15. The sabot sections hit the "sabot stripper" plate and the projectile traveled through the hole to hit the target rail as shown in Figure 7.16.

The impact was digitally captured using two high-speed cameras at a frame rate of 47,000 frames per second. An attempt was made to "soft-catch" the projectiles -
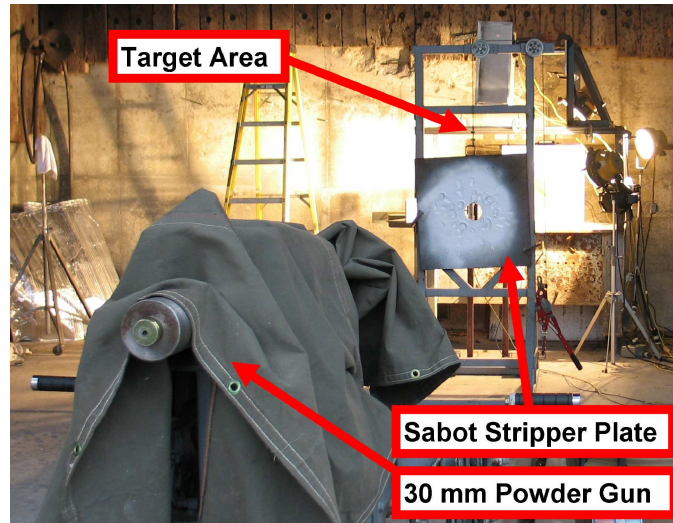
Figure 7.14:   **30 mm Powder Gun.**
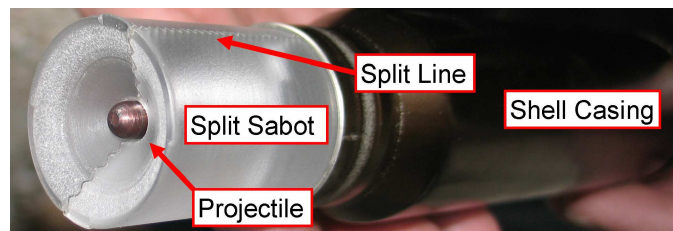
Figure 7.15:   **Projectile in Sabot.**
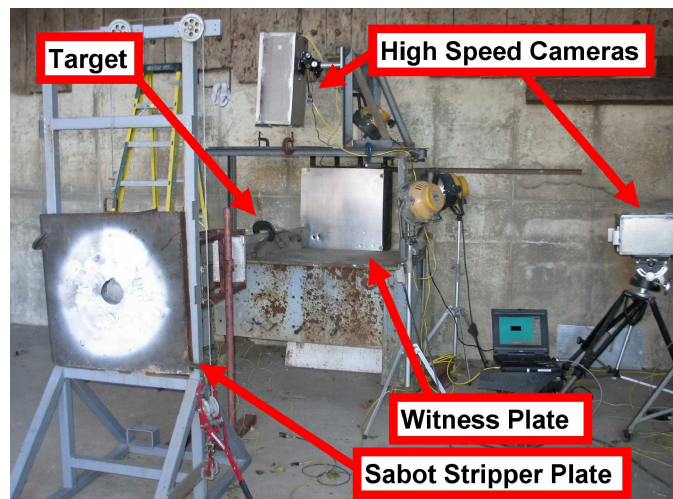
Figure 7.16:   **Target Area.**

which proved ultimately to be unsuccessful. The impact velocity was measured using

"break-sheets" immediately prior to the target. The electrical current breaks were recorded and the impact velocity was computed for each shot.

A series of equipment "check-out" shots were conducted in order to ensure the functionality of the configuration. For these initial qualification tests, stock steel was chosen for the target and the penetrator (304 stainless steel). Three tests shots were accomplished. The target plate was set at an oblique angle of 10° to the penetrator path to create a gouging type impact. Figure 7.17 illustrates a typical gouge generated in the 304 stainless steel (projectile motion was left to right). Table 7.4 summarizes the test results for this qualification test series.
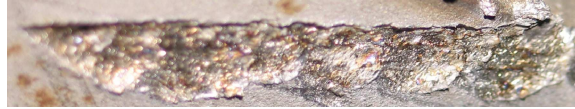
Figure 7.17:   **Gouged 304 Stainless Steel Target (Test ss-1).**

In order to further validate our one-dimensional model, we chose the 304 stainless steel on 304 stainless steel from Figure 7.4 (outlined in green). This gives us a crater volume/kinetic energy relationship. We can then compute u_0 and a penetration depth, z. This computation is made slightly more difficult because the projectile impacts along its long axis and therefore the cross-sectional area (in a one-dimensional sense) in contact with the target changes as a function of penetration depth. That is, as penetration depth is computed, more of the cylinder's cross-sectional area is in contact with the target, changing A_i. Therefore, Equation 7.33 is modified by a factor of $4/3\pi$ (to account for the hemispherical shape of the penetrating edge of the projectile) and a simple iteration scheme based on a cross-section calculation and predicted penetration depth converges to the values in Table 7.4. Of course, only the component of the velocity vector oriented into the target (i.e. normal to the target surface) is used to compute the penetration kinetic energy.

The measured crater depth for each shot also appears in Table 7.4. Good agreement between experimentation and the one-dimensional model was observed.

Table 7.4:   304 Stainless on 304 Stainless Steel Test
Series.

Test	Angle	Impact Velocity	z (predicted)	z (measured)
ss-1	10°	2584 m/s	0.99 mm	0.9 ± 0.1 mm
ss-2	10°	2147 m/s	0.73 mm	0.7 ± 0.1 mm
ss-1	10°	2157 m/s	0.73 mm	0.7 ± 0.1 mm

Therefore, the general approximation regarding penetration depth was been validated in another application.

After the laboratory configuration qualification test shots, the HHSTT materials were shot. During the initial tests of VascoMax 300 projectiles shot against the 1080 steel railroad rails used at the HHSTT, a 7.3 g projectile (5.5 mm diameter, 37.5 mm length) was used. These projectiles tended to tumble too much, and would not successfully go through the stripper plate hole. However, one of these tests provided an opportunity to validate our one-dimensional model in a more traditional normal impact scenario. One of these larger projectiles impacted the stripper plate with the long axis normal to the plate surface at 2226 m/s with a 0° of incidence. Figure 7.18 is of the resulting crater. Table 7.5 summarizes the measured and predicted quantities of this impact event. The crater volume/kinetic energy relationship used is the same for VascoMax 300 on 1080 steel because the stripper plate steel is a close match to 1080 steel.

Figure 7.18:   **Crater in Sabot Stripper Plate (Test sp-1).**

Table 7.5:   VascoMax 300 Impact on Steel Stripper
Plate.

Parameter (Test sp-1)	Predicted	Measured
Penetration Depth	2.41 mm	2.5 ± 0.1 mm
Crater Volume	2351.8 mm^3	2400 ± 300 mm^3
Crater Area	1261.5 mm^2	1200 ± 80 mm^2

The predicted values match the measured quantities closely. In fact, taking the computed impact kinetic energy of 18.16 kJ and the measured crater volume, we can add an additional point on the crater volume/kinetic energy relationship presented in Figure 7.12. The additional experimental point falls on the linear fit we have been using. Figure 7.19 shows this new relationship.
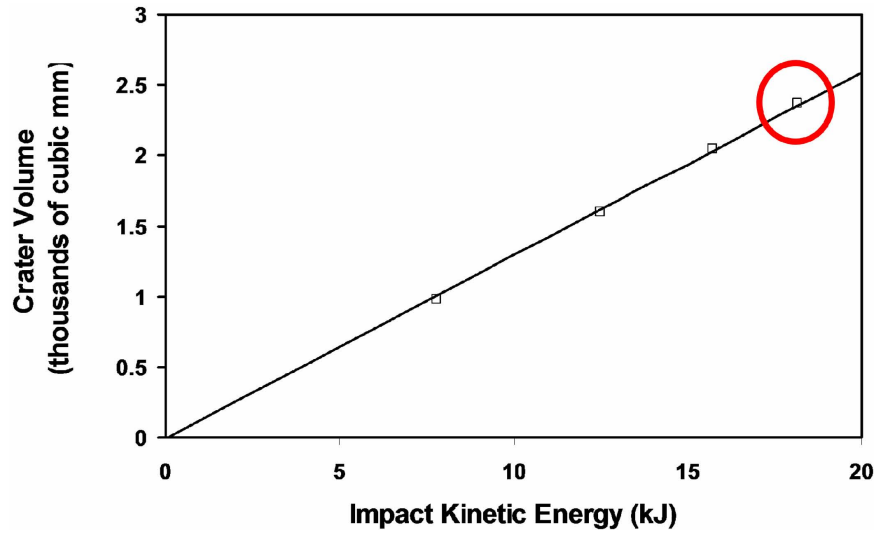
Figure 7.19:   **Updated Crater Volume/Kinetic Energy,
Steel on HzB,A.**

The test series of VascoMax 300 projectiles (4.78 g, 5.5 mm diameter, 25 mm length) was then conducted. Based on the predictions of penetration depth available using the theory, angles of 10 and 15 degrees were selected to create gouging. The gouging event was recorded via high-speed digital photography. The high energy/high thermal character of the event was immediately evident [31].

Figure 7.20 is a typical impact of the projectile against the rail (in this case coated with epoxy), with the impact event itself obscured by a bright fireball. The projectile enters the frame from the left and impact the rail face proceeding to the right.
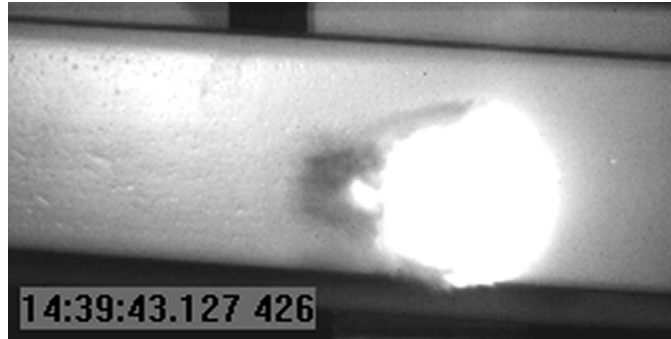
Figure 7.20:   **Typical High-Speed Photo of Gouging Event.**

Two rail targets were used. One was coated with iron oxide and the other coated with epoxy. These coatings represent the two used at the HHSTT on the rail to mitigate gouging. Figures 7.21 and 7.22 depict typical gouges on these targets.

Figure 7.21:   **Gouge in Iron Oxide Coated Rail (Test hi-2).**

Figure 7.22:   **Gouge in Epoxy Coated Rail (Test he-1).**

Table 7.6 summarizes the experimental results and the prediction generated by the one-dimensional theory. Again, close agreement is observed between theory and experiment. An important note is that there was no measurable difference in the gouges created in the rails coated with different materials.

Table 7.6:   VascoMax 300 on 1080 Steel Test Series.

Test	Coating	Angle	Impact Velocity	z (predicted)	z (measured)
hi-1	Iron Oxide	10°	2225 m/s	0.51 mm	0.5 ± 0.1 mm
hi-2	Iron Oxide	15°	2150 m/s	1.03 mm	1.0 ± 0.1 mm
he-1	Epoxy	15°	2147 m/s	1.03 mm	1.0 ± 0.1 mm
he-2	Epoxy	10°	2163 m/s	0.48 mm	0.5 ± 0.1 mm

These results further illustrate the ability of the one-dimensional model to predict penetration depth. Of course, because of the horizontal velocity and the nature of a gouging impact, the crater volume cannot be used to compare against the theory. That is, the gouging creates a much larger crater due to the horizontal velocity of the projectile.

In addition to these impacts, a couple of unintended impacts also allowed us to further validate this one-dimensional prediction. In order to prevent the projectiles from lodging into the sabot material during the explosive launch, a steel "pusher plate" (10 mm x 10 mm x 5 mm, 3.925 g) was constructed and placed at the rear of the projectile. In two of the tests (hi-2, he-1), the pusher plate also impacted the rail (in different locations from the primary gouge). The secondary impacts also gouged the rail and provided us with another opportunity to apply our theory. Figure 7.23 shows one of these pusher plate impacts.

Figure 7.23:   **Pusher Plate Impact on Rail (Test he-1).**

Table 7.7:   Pusher Plate Steel on 1080 Steel Impacts.

Test	Coating	Angle	Impact Velocity	z (predicted)	z (measured)
pp-1 (from hi-2)	Iron Oxide	15°	2150 m/s	0.91 mm	1.0 ± 0.1 mm
pp-2 (from he-1)	Epoxy	15°	2147 m/s	0.90 mm	1.0 ± 0.1 mm

In applying our approach to this impact combination, a material combination that most closely matches the dynamic yield strength and densities of the pusher plate steel and 1080 steel were selected from Figure 7.4 and outlined in orange. Table 7.7 summarizes the measured and predicted penetration depths from this material combination.

Despite being unintended impacts, these pusher plate gouges also demonstrate agreement between the one-dimensional theory and experimental results. Figure 7.24 summarizes the match between all of the experimental results and the predictions. The uncertainty in test measurement is depicted with the black error bars.
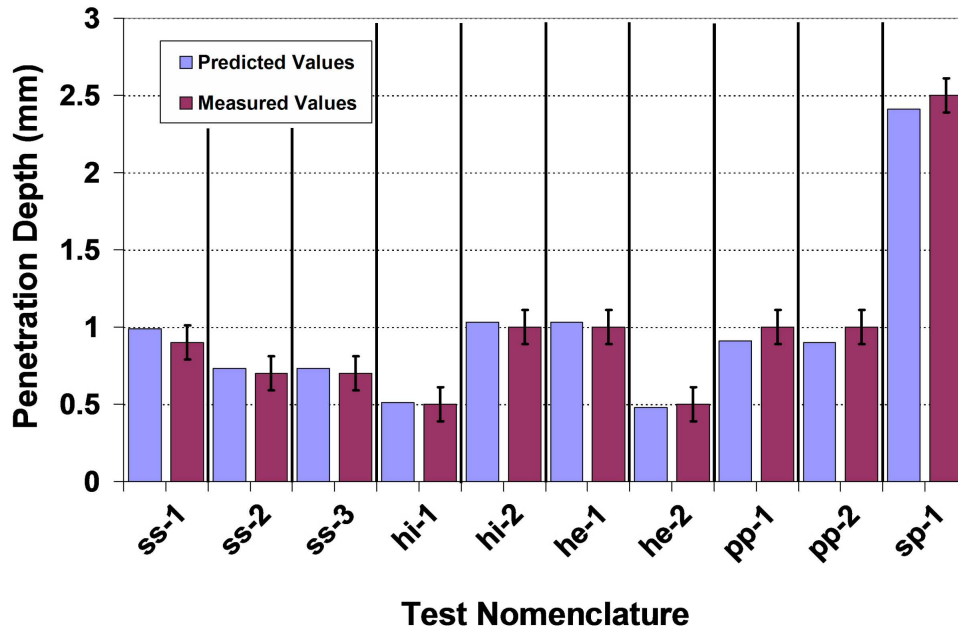
Figure 7.24:   **Penetration Depth Summary.**

The one-dimensional theory matches experimental results extremely well. The ability of it to match the experimental results, across the various material combinations, illustrates its flexibility. Specifically, the theory has been validated against experimental shots involving the materials in the HHSTT scenario. This, coupled with the previous analysis indicating the theory matches previous modeling of gouging and results from the field, confirm that this one-dimensional theory can be a powerful tool in predicting gouging.

As a final experimental examination of the scaled laboratory hypervelocity gouging tests, a metallurgical examination of the gouges was performed.

7.4 Metallurgical Examination of Hypervelocity Gouging Test Results

The in-depth characterization of gouging presented in Chapter IV indicated that one of the primary characteristics of the plastic deformation is a discernible heat zone in the post-test specimens. In an effort to verify that the gouging impacts generated with the scaled laboratory hypervelocity gouging tests presented in this Chapter generated the same phenomenon, a metallurgical study was performed on the gouged rails.

Utilizing the exact techniques outlined in Chapter IV, three of the four gouges were prepared for microscopy using the "as-polished" techniques. The samples were cut along the direction of projectile motion, down the middle of the gouge. The rail was then examined through the depth, in the plane parallel to projectile motion (exactly as in Chapter IV).

All of the gouged specimens exhibited the same evidence of a thermal pulse of sufficient magnitude as to austenize the 1080 steel (above 725°C). Figure 7.25 is characteristic of what was discovered.

In this figure, the microstructure of the steel near the gouge surface is modified from the unaffected microstructure shown on the same figure (which is taken at the rail surface in an undamaged section which still has its epoxy coating on it). The
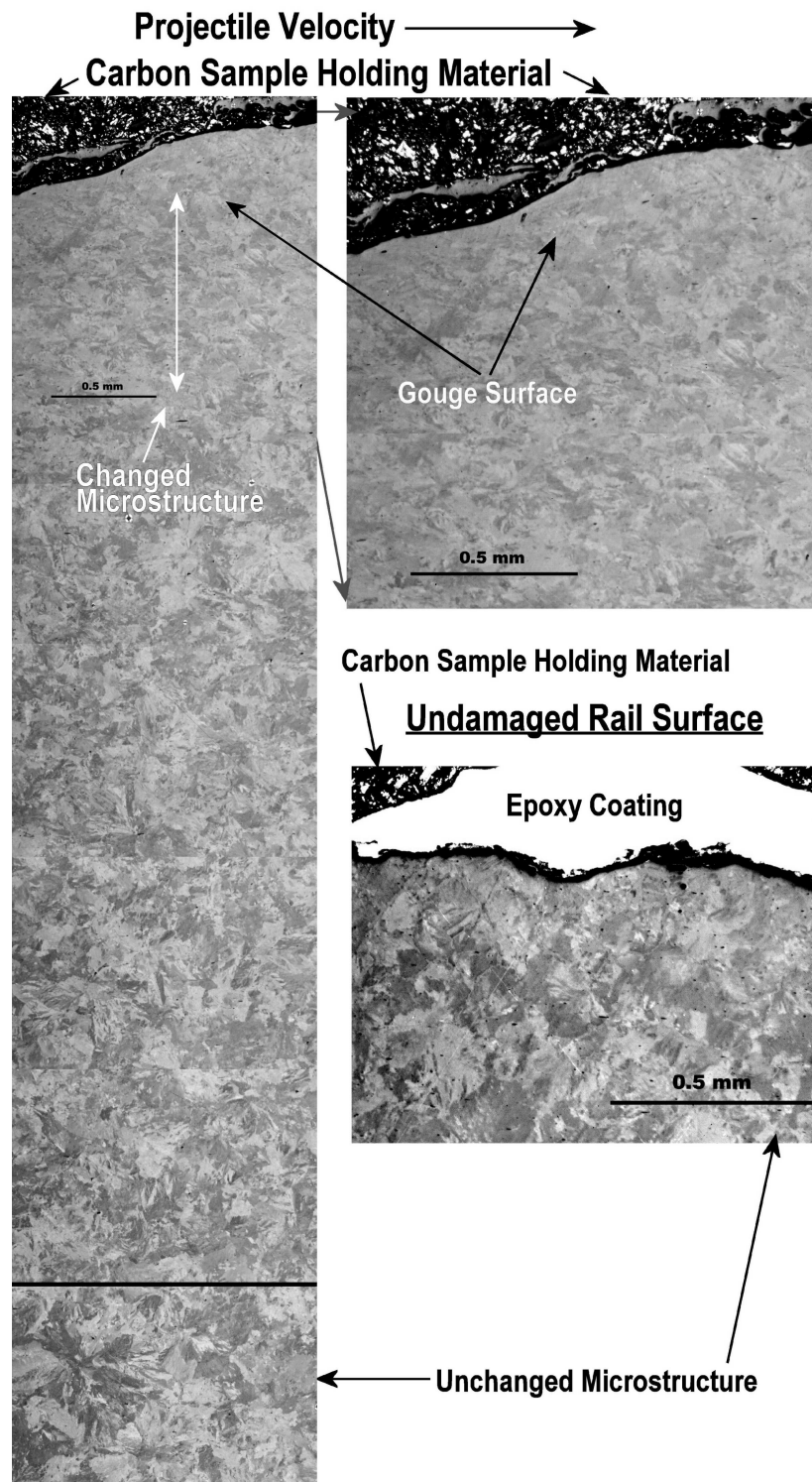
Figure 7.25: Metallurgical Examination of Gouge Test he-1.

microstructure of the gouged section changes back to an unaffected state at about 1.0 mm into the rail depth. The horizontal black line in the gouged section's micrograph indicates a jump to a location far away from the gouge surface (about 2 cm).

It is clear from this examination that the hypervelocity gouge tests conducted in the laboratory in a scaled form produced the same phenomenology as the full scale gouge from the HHSTT. More detail is provided on this metallurgical analysis in the next Chapter.

7.5   Summary of Scaled Laboratory Hypervelocity Gouging Test

A scaled hypervelocity gouging test was developed for a laboratory application. The goal was to create hypervelocity gouging experimentally for the purpose of validating our material constitutive models developed earlier in this work. A mathematical scaling approach was used to determine the experiment's parameters - which exceeded the available gun range capability.

A one-dimensional penetration theory was developed to aid in the determination of experimental parameters for a hypervelocity impact test that was feasible. The 1-D approach matched previous CTH models of the HHSTT problem, and data from the field, very well. The one-dimensional theory was then applied to the scaled hypervelocity experiment to set test parameters.

A series of hypervelocity impact tests were conducted. The one-dimensional theory was validated against several different material combinations and predicted the resulting penetration depths extremely well. Hypervelocity gouging impacts were created in a scaled laboratory experiment. These gouges were shown to have the same microstructural characteristics as full scale gouges from the HHSTT.

Therefore, this approach has yielded hypervelocity gouging impacts that can be modeled by CTH, with the newly developed full-range constitutive models, to validate the codes predictions of these gouging events.

VIII. Validation of Constitutive Models for High Strain-Rates in Hypervelocity Impact

In Chapter VI, the new material flow models of VascoMax 300 and 1080 steel (based on experiment) were validated in simulations of the Split Hopkinson Bar (SHB) tests and the Taylor Impact tests. These were mid-range strain-rate events. With the successful creation of a laboratory hypervelocity gouging test, the validation of the material constitutive models can be extended into the high strain-rate regime. Specifically, the CTH hydrocode can be used to simulate the hypervelocity gouging experiments to validate its ability, with the new flow models, to predict the observed behavior.

Prior to using CTH to model these laboratory hypervelocity gouging impacts, a discussion concerning modeling these events in a 2-D CTH environment is conducted. The gouging tests are then predicted using a CTH model. The ultimate goal of this effort is to validate CTH's ability to accurately predict hypervelocity gouging so that it may be used as an effective tool in the mitigation of gouging in the HHSTT scenario.

8.1 Examination of CTH Modeling

The effort to simulate these kind of hypervelocity impacts have been conducted for many years [47,77,96,97]. One of the most successful codes is the hydrocode, CTH. CTH is unique in that it possesses a large body of experimental data embedded in equation-of-state (EOS) tables. Additionally, CTH was written as a shock-physics code whose primary purpose is to simulate high-energy impact events. The primary limitation of this code is that it is extremely computationally intensive. Users of CTH typically create state-of-the-art computer clusters, or utilize time on some of the nation's fastest supercomputers, in order to have the computation time stay in the reasonable range. A simple problem, implemented in full 3-D, with all the associated optional subroutines engaged (i.e. heat conduction, etc.) can take two weeks to generate 10 microseconds of data. Therefore, many users model these impact problems

with plane-strain or 2-D axi-symmetric models to reduce computation time to the order of tens of hours and days.

With regard to the specific impact problem at the HHSTT, previous researchers performed a comparison between simulating the shoe/rail interaction in 2-D plane-strain versus a full 3-D implementation [66–69]. The conclusion was drawn that a plane-strain version of the impact event was significantly similar to the results from a 3-D solution. Based on this analysis, subsequent model development was done in plane-strain.

Szmerekovsky [104–109] developed a 2-D plane-strain model of the shoe/rail interaction by taking the sled arrangement and distributing the mass of the sled across the four shoes. The mass is then taken to distribute evenly through the width of the shoe, and a unit slice is removed and modeled. This process is depicted in Figure 8.1. This model was used very successfully to simulate the gouging phenomenon. Many of the features observed in the field and from experimental analysis of the gouges were generated by this plane-strain model in CTH [104–109]. Figure 8.2 illustrates a typical gouge created in CTH. Material mixing is created and represents one of the unique capabilities of this code. Based on the success of these plane-strain models, and the unreasonable computation times of 3-D implementations, a decision was made to model these impact events in 2-D plane-strain.

As mentioned previously, the major limitation of these earlier modeling efforts was the lack of specific material models in CTH for VascoMax 300 and 1080 steel. While suitable EOS models exist, the constitutive models governing the strength of the materials below EOS pressures are not available. Therefore, an extensive effort was undertaken to develop these material strength models (see Chapter V). In order to validate these material models, experimental Taylor Impact tests were conducted (see Chapter VI). The focus of this Chapter is to extend the validation into the hypervelocity impact regime.
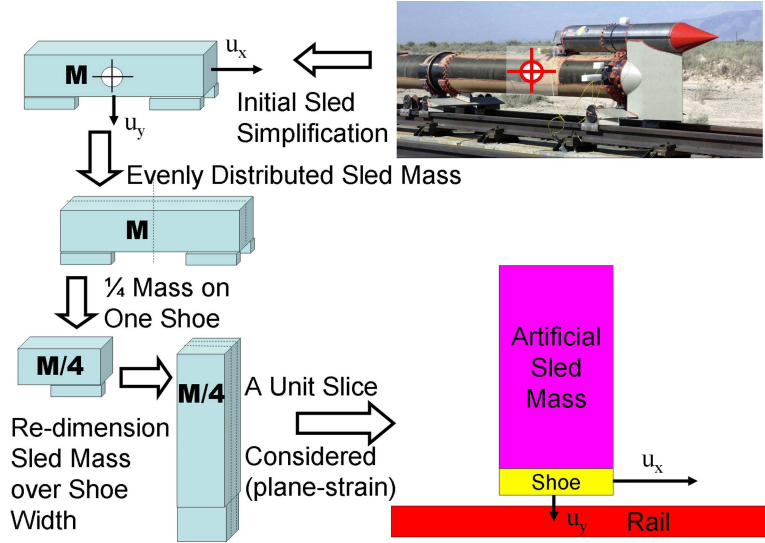
Figure 8.1: **Sled Plane-Strain Gouging Model Development [108].**
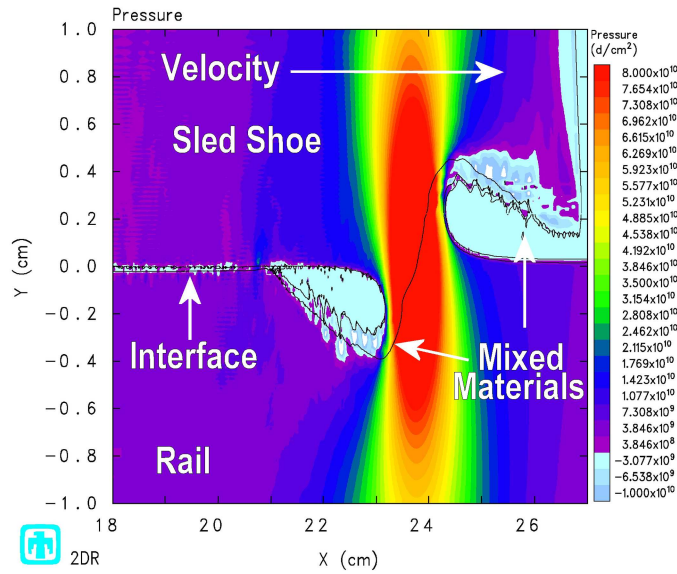
Figure 8.2: **Typical CTH Gouge Simulation.**

Related to the mid-range strain-rate validation of the strength models in CTH (using the Taylor Impact tests), an evaluation of the suitability of 2-D simulations was performed. In Chapter VI, a 2-D model was able to match post-test geometry of the Taylor Impact Test within 5% (which involves a cylinder of material impacting a non-deforming target at velocities around 200 m/s). Additionally, because of the nature of CTH's development, some additional features have been added to the code for specific

reasons. An evaluation of the three material contact schemes was undertaken, and the most numerically stable option was identified (designated as the no-slide line option within CTH).

As previously mentioned, in modeling our hypervelocity gouging tests, we are limited to choosing between plane-strain and a full 3-D model. CTH does have a 2-D axi-symmetric mode, but it is limited to a vertically oriented impact because it established a vertical line of symmetry and rotates a user-defined 2-D slice about it. Motivated by previous success in 2-D modeling, an investigation into the difference between an axi-symmetric mode and a plane-strain mode solution to impact problems was conducted [27, 36, 90].

8.1.1 Model Mode Comparison. For this examination, a penetration model was created based on our hypervelocity experimentation. The projectiles used in our gun tests were modeled to impact the rail at a normal incidence angle and at the velocity range corresponding to the vertical impact velocity of our hypervelocity shots (i.e. 375-555 m/s) from Chapter VII. The material flow relation used in our modeling was the Zerilli-Armstrong model. The material model constants were formulated from flyer plate experiments presented in Chapter V. Table 5.5 summarizes the material model constants used within CTH. The temperature constants, c_3 and c_4 are given in electron-volts - which is the unit used in CTH.

An axi-symmetric model, which represents the actual geometry of the experimental projectile, was compared against a plane-strain model of the same vertical impact. The impact geometry is depicted in Figure 8.3. The mesh size used was 0.002 cm, which was arrived at by a previous mesh convergence study. In this work, a representative case is examined, in which the projectile hits the target at 375 m/s. Figures 8.4 and 8.5 compare the axi-symmetric solution to the plane-strain solution at discrete times (in which the axi-symmetric solutions appears on the left, and the plane-strain on the right). Note that the penetrator deformation and penetration depth are in good agreement out to 10 microseconds - which corresponds both to

the event time of the hypervelocity gouging impact test and the gouge event in the HHSTT scenario.
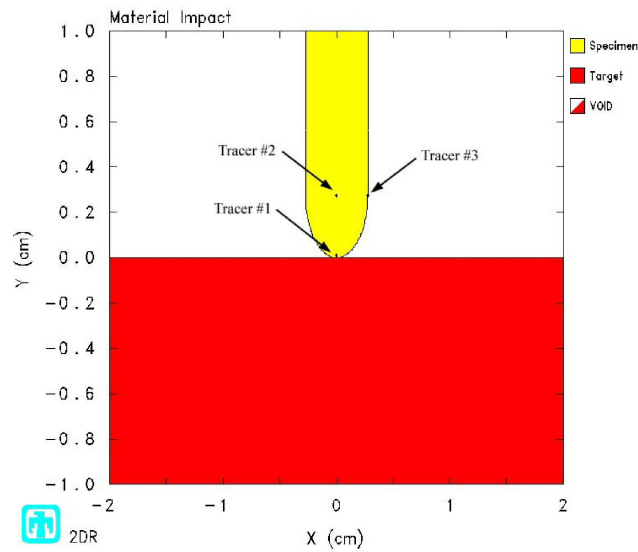
Figure 8.3:   **Typical CTH Solution Mode Comparison Model.**
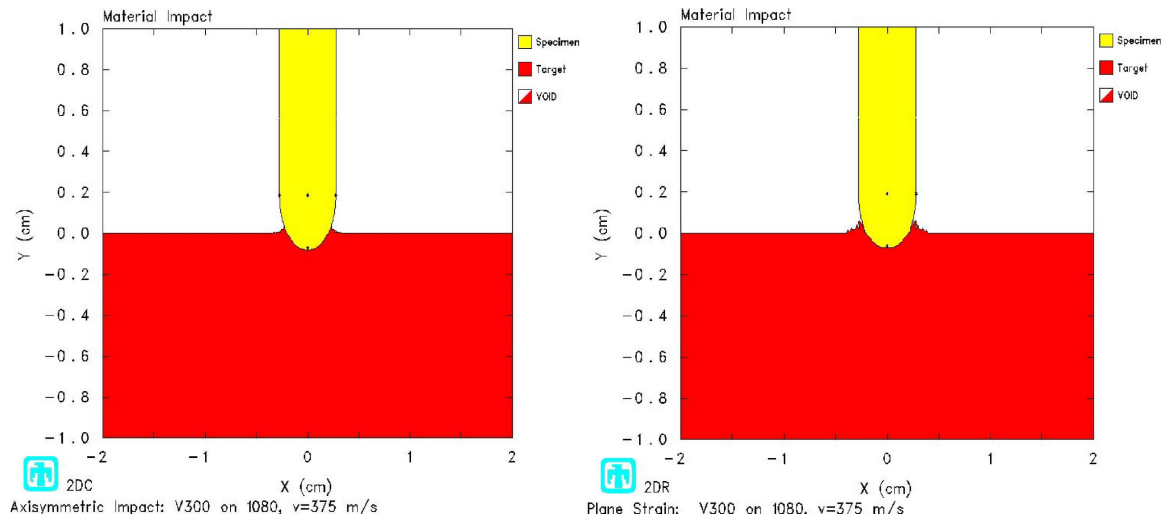
Figure 8.4:   **CTH Solution Mode Comparison Model at 2.5 μsec (axi-symmetric on the left, plane-strain on the right).**

In examining the difference in cell pressure generated in each of the solution techniques, six Lagrangian grid points were selected and the pressure was recorded at discrete points of time. Figures 8.6 and 8.7 illustrate the pressure profiles, where
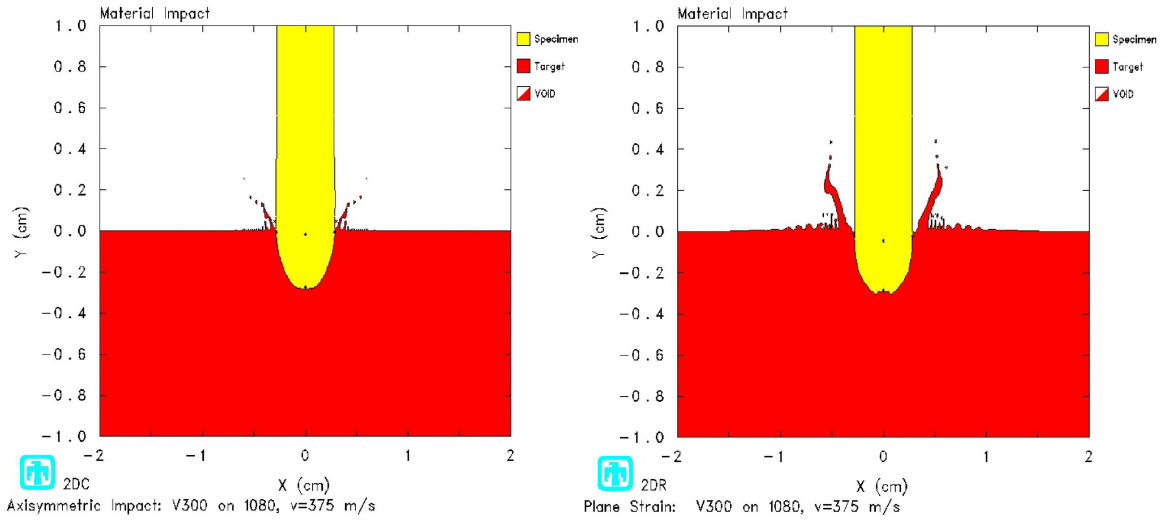
Figure 8.5:   **CTH Solution Mode Comparison Model at
10 μsec (axi-symmetric on the left, plane-strain on the
right).**

the black points in Figure 8.7 indicate the points where the pressure was compared.
While there appears to be some general differences in appearance, the magnitude of
the pressure variance is not excessive. Table 8.1 records the pressure differences at
each point and summarizes the results.
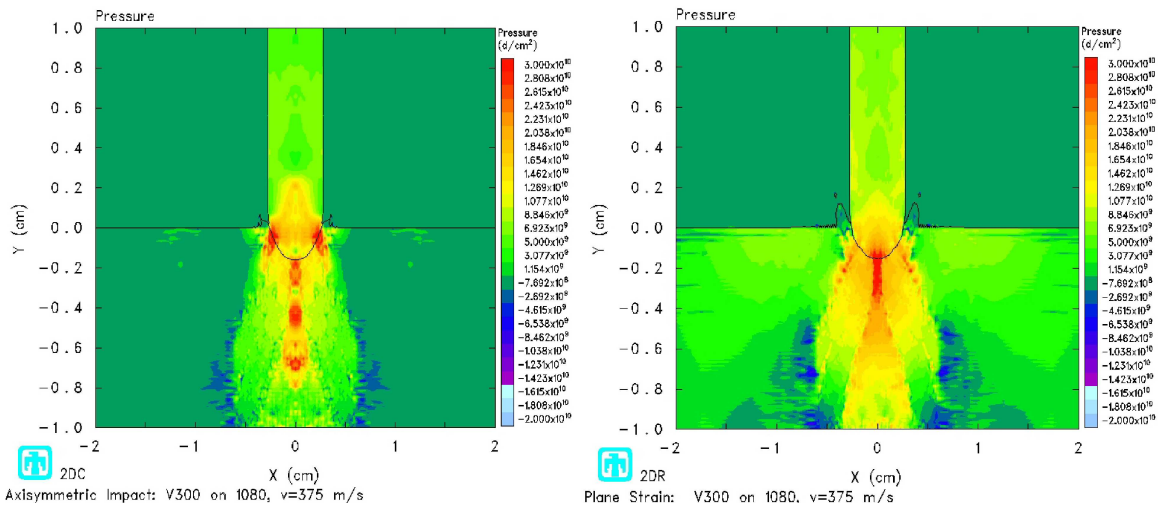
Figure 8.6:   **CTH Pressure Solution Mode Comparison
Model at 2.5 μsec (axi-symmetric on the left, plane-
strain on the right).**

8-6
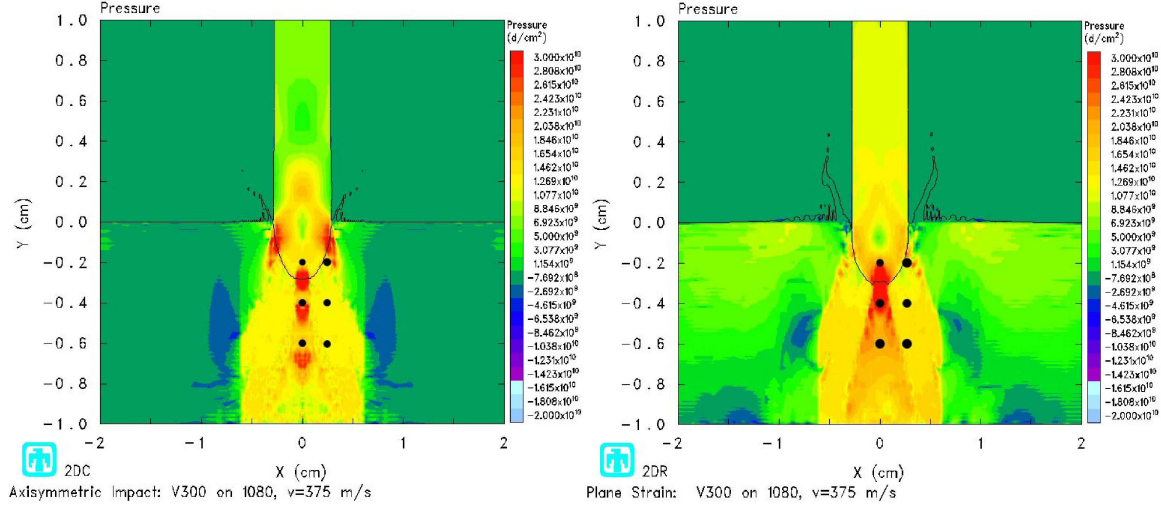
Figure 8.7:   **CTH Pressure Solution Mode Comparison Model at 10 μsec (axi-symmetric on the left, plane-strain on the right).**

So, while there is some measurable difference between the solution techniques, the magnitude of the difference are not significant. Additionally, the gross deformation predicted by the methods match very well. Note that in Figure 8.7, the penetrators are almost identical in diameter (0.26 cm for axi-symmetric, 0.25 cm for plane-strain, for a difference of 3.8%). Additionally, the penetration depth for both cases is also comparable (0.29 cm for axi-symmetric, 0.3 cm for plane-strain, for a difference of 3.4%). Even better agreement was noted in the 555 m/s impact case. Based on this evaluation, it can be concluded that the plane-strain solution technique can fairly accurately model this 3-D impact event. The 2-D axi-symmetric model would be employed for the modeling of our laboratory hypervelocity gouging test, but our impact geometry is not compatible with the implementation in CTH.

8.1.2   Model Mode Comparison Summary.   Therefore, based on this analysis, the laboratory hypervelocity impact test is modeled in 2-D plane strain. This approach matches those of previous investigators, and has been shown to be sufficiently accurate in the preceding section. Additionally, this approach will be used to model the sled/rail gouging phenomenon for the HHSTT problem. Of course, the

Table 8.1:   CTH Pressure Solution Mode Comparison - Plane-Strain compared against Axi-symmetric.

Discrete Point, x coordinate	Discrete Point, y coordinate	% Difference, t=5μsec	% Difference, t=10μsec
0	-0.2 cm	21%	16%
0	-0.4 cm	9%	14%
0	-0.6 cm	0%	16%
0.25 cm	-0.2 cm	17%	30%
0.25 cm	-0.4 cm	47%	0%
0.25 cm	-0.6 cm	36%	12%
	Average:	31%	14%

suitability of this approach can be judged based on its ability to accurately generate the experimental characteristics of the gouging tests.

8.2 Validation of CTH Hypervelocity Gouging Model

In order to establish the validity of CTH to model the full sled/rail interaction at the HHSTT, the newly developed material flow models and CTH are validated against the hypervelocity gouging tests presented in the Chapter VII.

8.2.1 CTH Model of Laboratory Hypervelocity Gouging Test.   With the investigation presented above, a 2-D plane-strain model of the hypervelocity gouging test was constructed. Using this approach, the cylinder with a hemispherical nose is modeled as a unit-thickness, plane-strain plate, with a rounded leading edge. Figure 8.8 illustrates this model. The high speed photography available from the impacts indicated that the projectile oriented during flight in such a manner as to impact the target rail as depicted in Figure 8.8. This is illustrated in Figure 8.9. This is a top-down view of the impact and represents the available photographic depiction. While

the velocity vector was still oriented at 10° or 15° to the rail surface, the long-axis of the projectile was aligned with the longitudinal axis of the target rail.
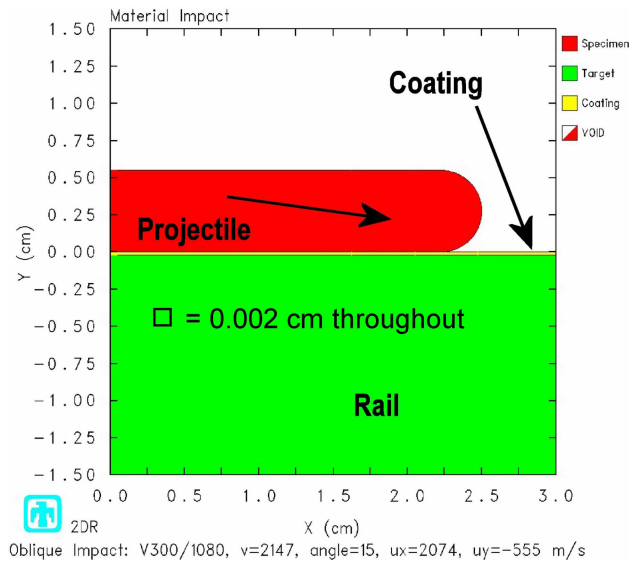
Figure 8.8:   **CTH Model of Hypervelocity Gouging Test (velocity vector indicated).**
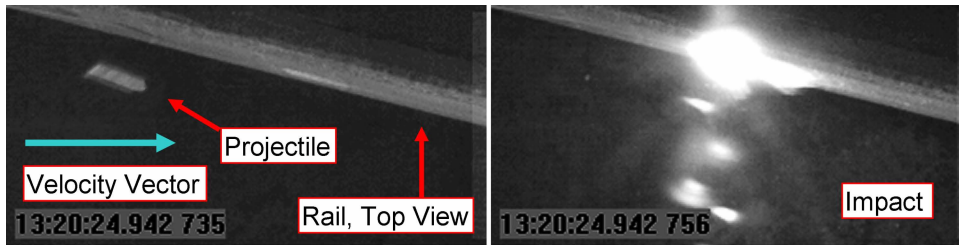
Figure 8.9:   **High Speed Photograph of Projectile Impact Orientation.**

Again, the appropriate mesh size was utilized - 0.002 cm. All four impact cases from Chapter VII were examined. A sample CTH input file is included in Appendix A.

8.2.2   CTH Simulation of Laboratory Hypervelocity Gouging Test.   The effort to model the hypervelocity gouging tests was extremely successful. A representative case is presented in Section. Figure 8.10 is of impact Test he-1, with an impact velocity of 2147 m/s and an impact angle of 15°. The solution shows the characteristic

material mixing and high plasticity of gouging. Additionally, Figure 8.11 illustrates the pressure and strain-rate associated with 10 μsec. Note that the strain-rates computed by CTH are predominately in the 10^4/sec - 10^6/sec range in the gouging region, but that the mid-range strain-rates are also indicated within the solution.
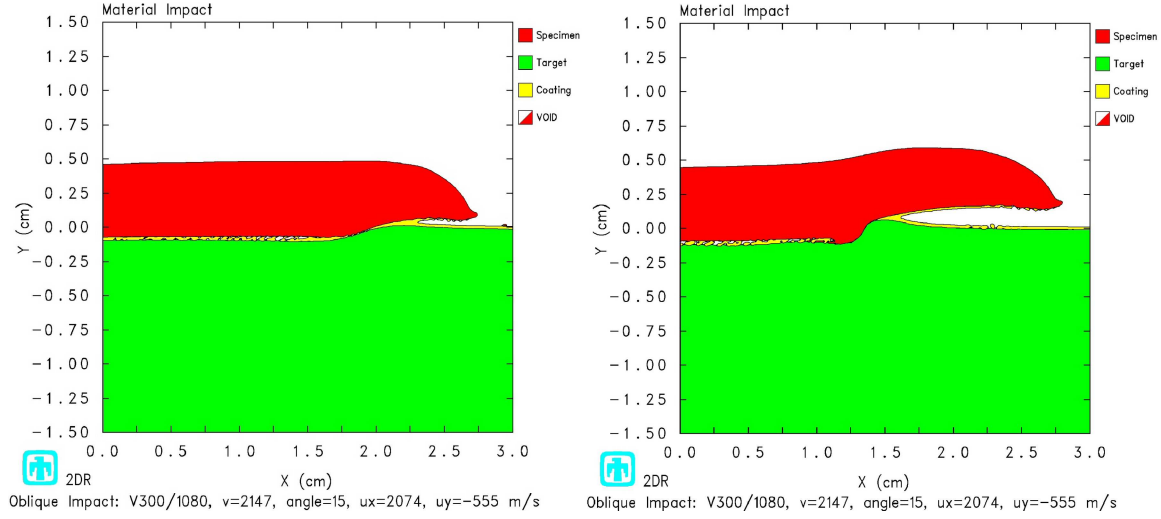
Figure 8.10:   **Simulation of Test he-1 at 5 μsec and 10 μsec.**
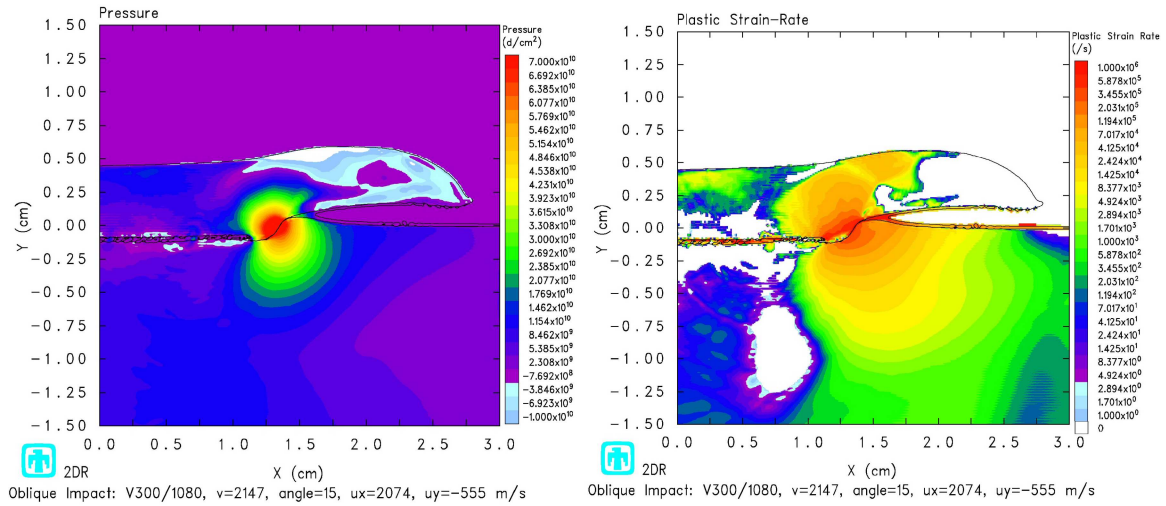
Figure 8.11:   **Simulation of Test he-1, Pressure and Strain-Rate, at 10 μsec.**

The gouge depth can be seen in Figure 8.10 to be approximately 1.1 mm, which agrees closely with the experiments presented in Chapter VII. Indeed, the simulated

Table 8.2:   CTH Simulation of VascoMax 300 on
1080 Steel Test Series.

Test	Coating	Angle	Impact Velocity	Gouge Depth (predicted)	Gouge Depth (measured)	Gouge Depth (simulated)
hi-1	Iron Ox.	10°	2225 m/s	0.51 mm	0.5 ± 0.1 mm	0.6 mm
hi-2	Iron Ox.	15°	2150 m/s	1.03 mm	1.0 ± 0.1 mm	1.1 mm
he-1	Epoxy	15°	2147 m/s	1.03 mm	1.0 ± 0.1 mm	1.1 mm
he-2	Epoxy	10°	2163 m/s	0.48 mm	0.5 ± 0.1 mm	0.5 mm

results are within the uncertainty range of the measurements of the experimental gouge depths. All four simulations of the laboratory gouging shots demonstrated excellent agreement to experimentally observed values for gouge depth. Table 8.2 summarizes these results. The one-dimensional theory predictions (using the approach outlined earlier in this Chapter) are presented in this table to show the agreement between the 1-D analytical approach and the computational simulation. Figure 8.12 summarizes the information in graphical form.

The characteristics of hypervelocity gouging, such as a high pressure concentration [104–108] at the gouge location, material jetting, and material mixing are evident in these simulations. Additionally, sufficient temperature was generated by the plasticity that could create the microstructural changes reported in the Chapter VII. Figure 8.13 illustrates the temperature profile of test he-1 as generated by the CTH simulation.

8.2.3 CTH Simulation of Thermal Characteristics of the Laboratory Hypervelocity Gouging Test.   As part of the CTH model validation for the laboratory hypervelocity gouging test, we can closely examine CTH's ability to match the microstructural observations from the gouges. As presented in Chapter VII, the gouges created in the scaled hypervelocity test exhibited the same kind of microstructural changes within the rail as the full scale HHSTT gouge. Returning to these metallur-
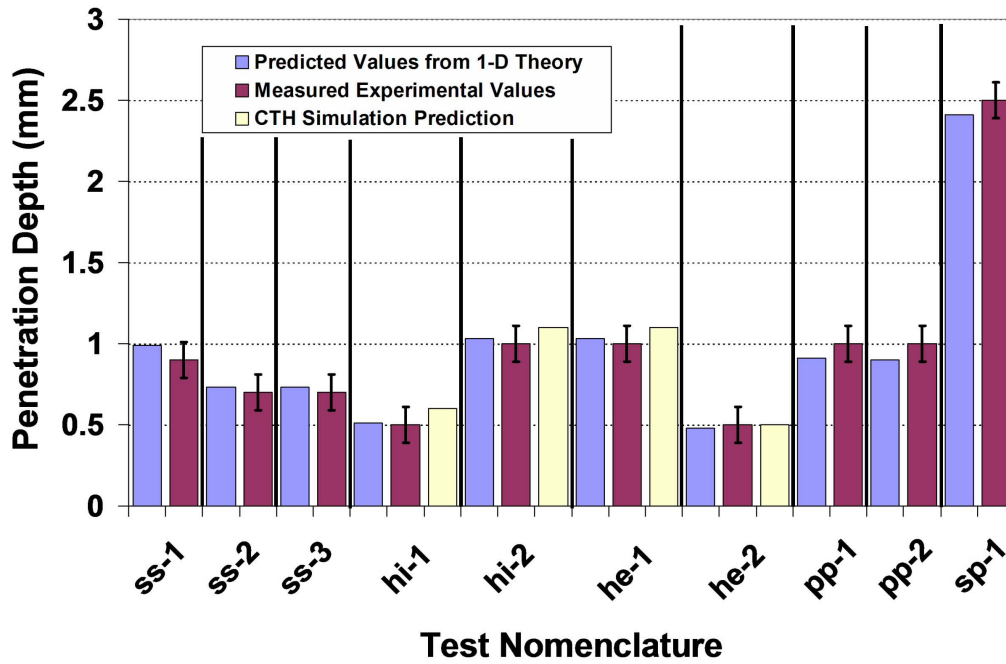
Figure 8.12:   Hypervelocity Gouge Test Series Results
Summary.
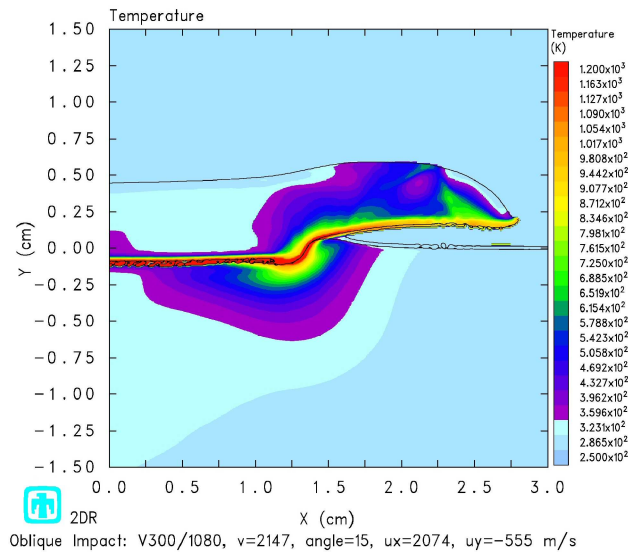
Figure 8.13:   Simulation of Test he-1, Temperature, at
10 μsec.

gical results, we can compare the CTH simulations of generated temperature to those
microstructural changes observed.

Figure 8.14 is a summary of the comparison between the CTH simulation of test he-1, and the metallurgical results. Note that the depth of microstructure change is matched, as well as the gouge depth (which was noted in Table 8.2). The austenzing depth is discussed in Chapter IV - and occurs when the temperature exceeds 1000°K. The CTH simulation portion of that figure comes from zooming in on the gouge in Figure 8.13.

Similar results are seen from examining Tests hi-1 (in Figure 8.15) and hi-2 (in Figure 8.16) . Again, the austenizing temperatures are matched against micrographs of the gouged rails.

8.2.4   Further Results from the Comparison of CTH Simulations to the 1-D Penetration Theory.   In the investigation of the hypervelocity gouging impact simulation within CTH, some additional impact conditions were examined. As noted in Chapter VII, the 1-D penetration theory was primary developed to estimate the laboratory configuration necessary to ensure gouge creation. In order to further validate the one-dimensional approach, the limiting case of a 5° impact was simulated in CTH, as well as one of 20° impact.

Figure 8.17 illustrates the impact velocity of Test hi-1 (2225 m/s) oriented at a 5° striking angle and simulated in CTH. The one-dimensional theory from Chapter VII predicts a gouge depth of 0.044 mm - or essentially no penetration. This type of impact is predicted by CTH - in which there is some negligible deformation of the rail and associated heating from small amounts of plasticity. Note that even with very little surface deformation, the temperatures have risen above the austenizing limit, which may point to the cause of the type of microstructure changes observed in non-damaged (in-service) rails from the HHSTT seen in Chapter IV.

When the impact angle is increased to 20°, the resulting prediction for the one-dimensional penetration theory becomes 1.52 mm. Figure 8.18 depicts how CTH creates the same result. In this case, more plasticity and gouge depth is generated and the temperature profile is correspondingly more significant.

Test he-1

Depth of Changed Microstructure ~ 1.0 mm

Unchanged Microstructure

CTH Simulation

Y (cm)

0.50
0.25
0.00
-0.25
-0.50

Simulated Gouge Depth: 1.1 mm

Austenized Depth: 2.1 mm

Depth of microstructure Change: 1 mm

Temperature (K)

1.200x10^3
1.163x10^3
1.127x10^3
1.090x10^3
1.054x10^3
1.017x10^3
9.808x10^2
9.442x10^2
9.077x10^2
8.712x10^2
8.346x10^2
7.981x10^2
7.615x10^2
7.250x10^2
6.885x10^2
6.519x10^2
6.154x10^2
5.788x10^2
5.423x10^2
5.058x10^2
4.692x10^2
4.327x10^2
3.962x10^2
3.596x10^2
3.231x10^2
2.865x10^2
2.500x10^2

Figure 8.14: **Comparison of CTH Simulation to Observed Microstructure, Test he-1.**

The fidelity of the one-dimensional penetration theory has been demonstrated to be beyond the several cases in which experimental tests were conducted. That is, the theory can be applied to a broader range of impact conditions and shows promise in the study of impacts that do not generate gouging - but create "wear."
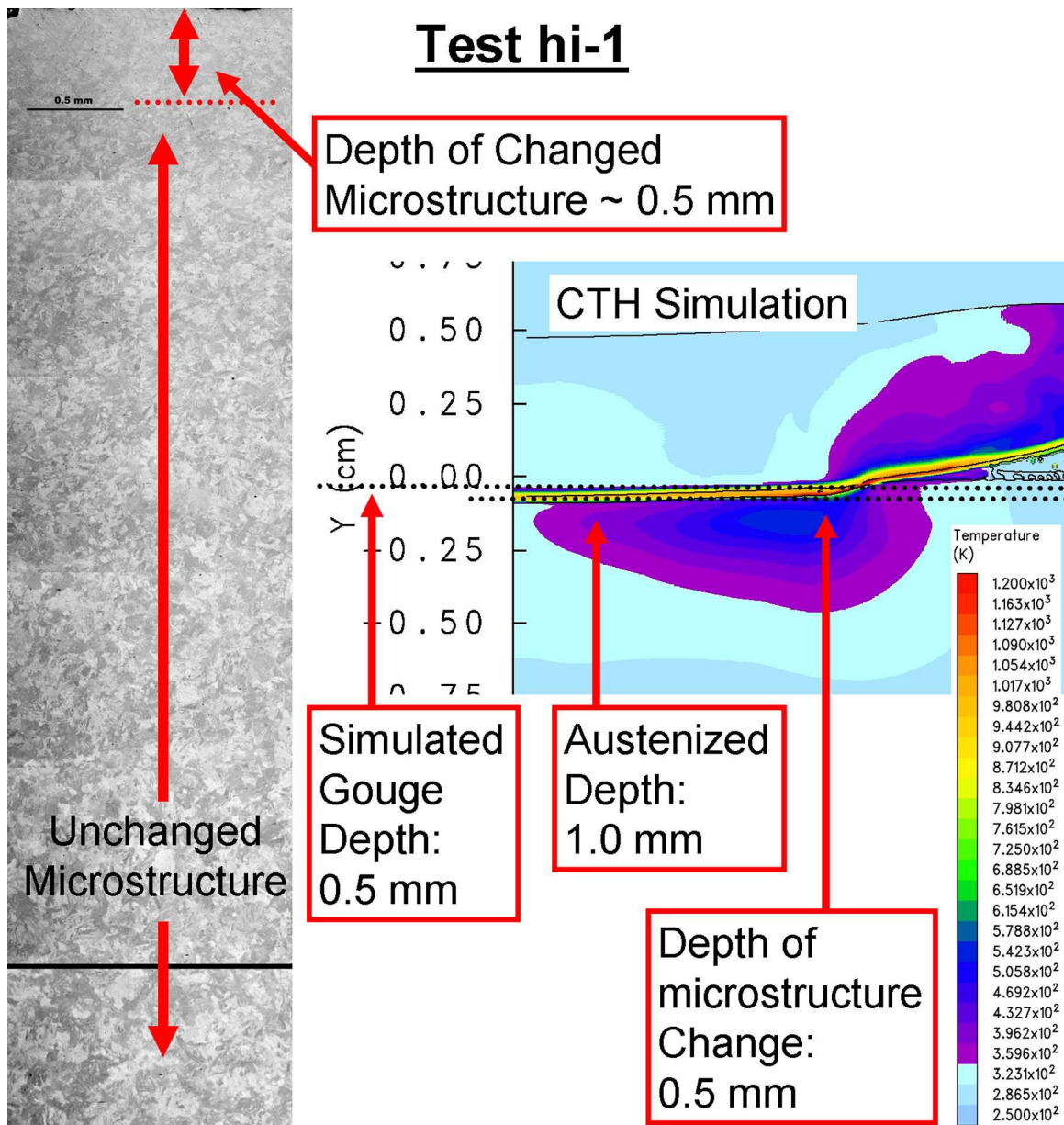
Figure 8.15: **Comparison of CTH Simulation to Observed Microstructure, Test hi-1.**

8.2.5 Summary of Validation of CTH Hypervelocity Gouging Model. A CTH model was validated against a series of laboratory hypervelocity gouging experiments. The simulations were able to match both gouge depth and temperature profiles generated by the plastic deformation of the materials. Additionally, the one-dimensional
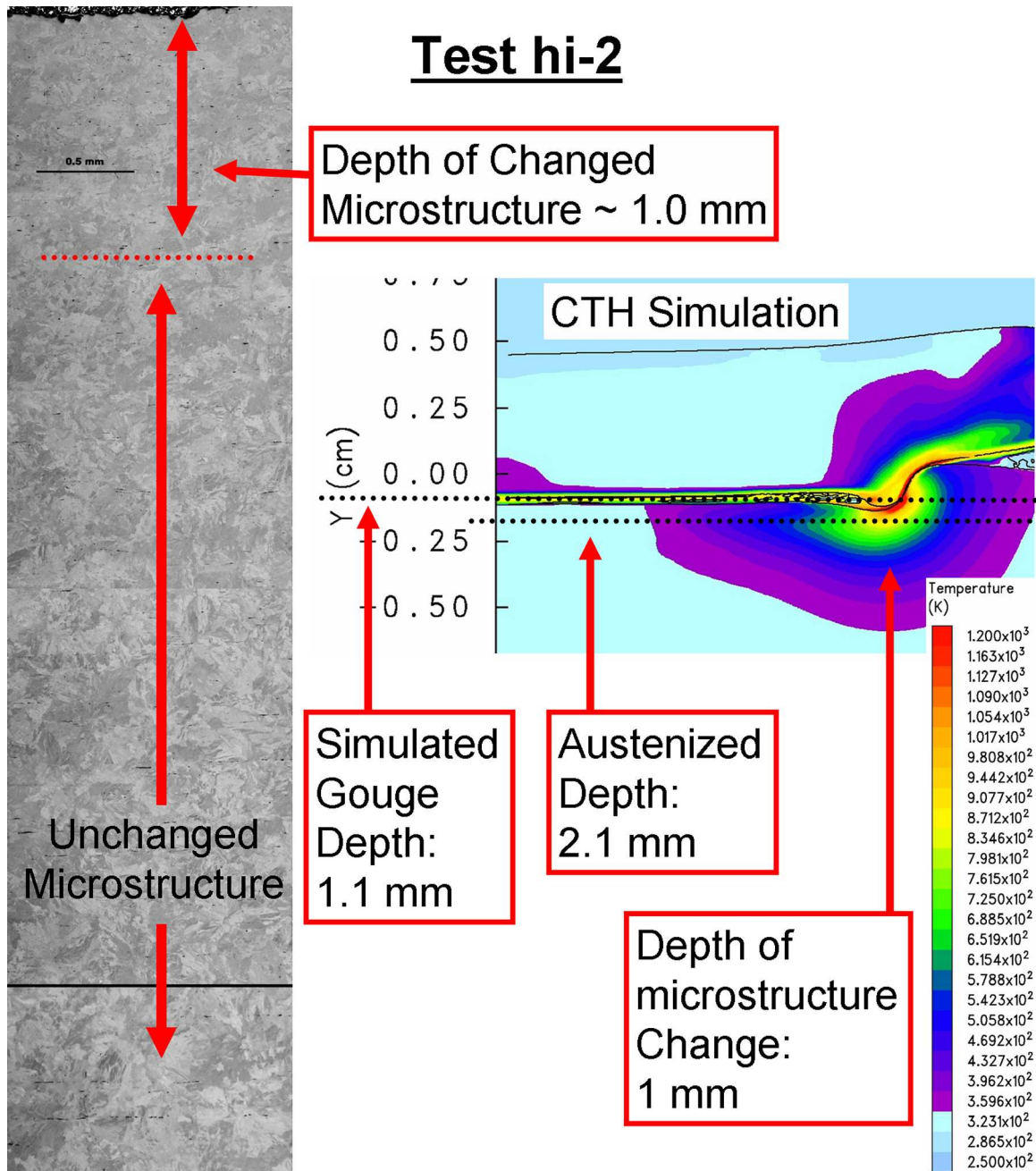
Figure 8.16: **Comparison of CTH Simulation to Observed Microstructure, Test hi-2.**

penetration theory was shown to successfully predict impacts beyond the range of impact conditions used in the experimental tests.
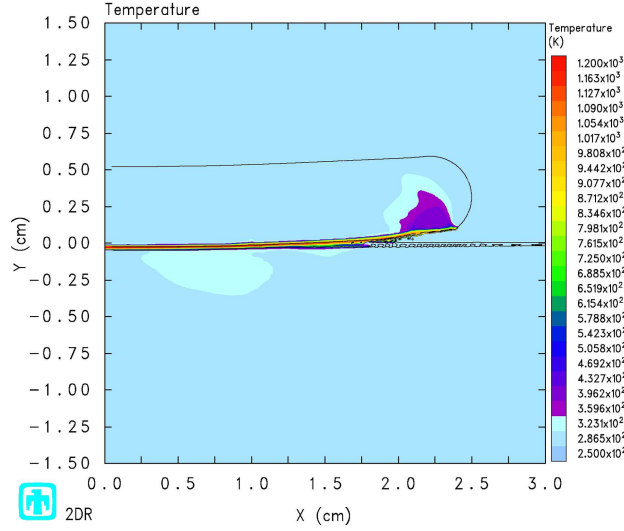
Figure 8.17: **Simulation of Test he-1, 5° Striking Angle, Temperature, at 10 μsec.**
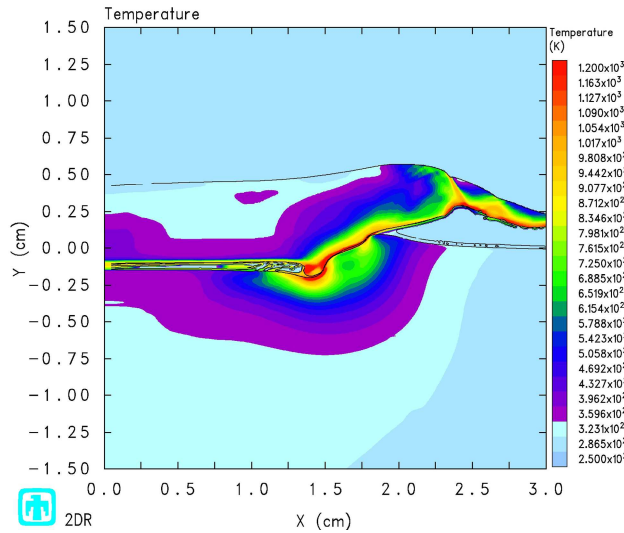
Figure 8.18: **Simulation of Test he-1, 20° Striking Angle, Temperature, at 10 μsec.**

8.3 Validation of Constitutive Models and CTH for Hypervelocity Modeling

The material constitutive models for VascoMax 300 and 1080 steel were tested in the high strain-rate regime using hypervelocity gouging impact experiments. The techniques and justification for modeling these impact events in a 2-D mode within CTH were presented. Using the full-range Zerilli Armstrong flow models developed in

this study, CTH demonstrated its capability to accurately capture the development of gouging, the resulting gouge depth (rail damage), and the temperature inputs that resulted in observed alteration to the target's microstructure.

Therefore, CTH and the constitutive models have been validated using experimentation for use in modeling hypervelocity gouging impacts. With this capability, the HHSTT sled scenario can be confidently modeled and evaluated.

IX. Simulation of HHSTT Hypervelocity Gouging Scenario

With the development of specific material constitutive models for VascoMax 300 and 1080 steel, and the validation of the ability of CTH to accurately model mid-range and high strain-rate impacts, the full scale HHSTT sled gouging problem can be confidently simulated in CTH. The previously developed CTH model for the shoe/rail interaction [108] was modified to include the new material flow models. Various impact cases were examined in order to replicate gouging in the CTH simulation that matches the experimental observations noted from HHSTT gouges. Based on the comparison of code predictions and the experimental record, conclusions are drawn concerning the character of the gouging experienced at the HHSTT.

Gouge modeling efforts previously conducted had concluded that gouging develops within the CTH solution when either sufficient vertical impact velocity or rail discontinuities were used [68,108]. This was verified with the new material flow models, and were simulated as three gouging cases. The first was to create a vertical impact velocity sufficient to initiate gouging. The second was an impact with an angle of incidence to the rail. The final case was created when the shoe encountered a rail discontinuity. For each case, the results are presented and comparisons to the experimental gouge characterization from Chapter IV are made. Because the goal of the HHSTT is to extend the velocity of the sled program to 3 km/sec, all simulations are conducted at that velocity.

9.1 CTH Modeling of the HHSTT Sled Scenario

Previous efforts in modeling the HHSTT sled gouging problem had not only yielded CTH as the optimum choice for modeling hypervelocity gouging, but a full-scale impact simulation was developed [104–109]. This model was a 2-D plane strain implementation, based on the conclusions made previously that the 2-D solution was substantially similar to results observed in a full 3-D simulation [66,68,69]. In Chapter VIII, further favorable comparisons were made in the scaled hypervelocity impact test simulations between 2-D axisymmetric and 2-D plane strain. As with that analysis,

the sled simulation will, over time, become more inaccurate as the reflected stress waves are not modeled in the 2-D plane-strain case. Szmerekovsky computed the time for those reflected wave to return to the gouge area to be 30 microseconds. Therefore the gouge simulations are typically considered accurate to a time of 20 microseconds.

Figure 8.1, adapted from [108], illustrates how the full 3-D dimensionality of the sled was reduced to a plane-strain model. The plane-strain model was modeled in CTH in a mesh geometry that was the result of a convergence study conducted by Szmerekovsky. Figure 9.1 illustrates the boundary conditions and mesh used to model the sled/rail interactions [108].
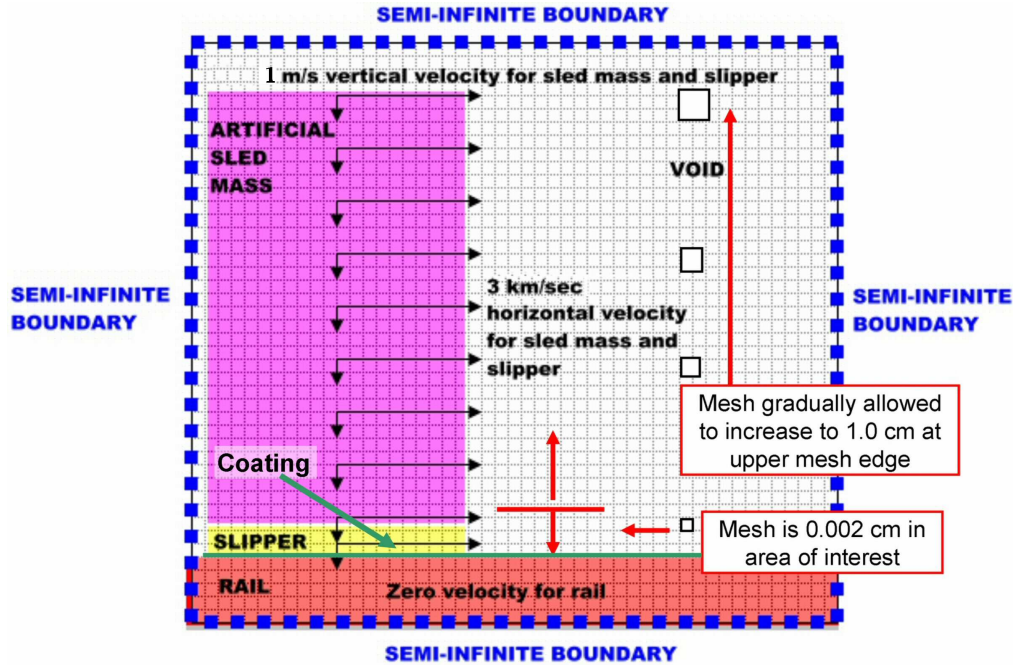
Figure 9.1:   **Mesh for CTH Simulation of HHSTT Scenario.**

The previously developed CTH model was modified to include the newly developed, strain-rate dependent Zerilli-Armstrong constitutive models for VascoMax 300 and 1080 steel. The EOS models, based on high energy experimentation (and which include non-equilibrium thermodynamic effects), were used for VascoMax 300 and 1080 steel. The EOS for the epoxy coating was also employed, as well as a elastic-

perfectly plastic flow model used successfully in the past simulations [14, 33, 36, 60]. Various impact scenarios were then investigated to better understand the gouging phenomenon. A sample CTH input file for these impact cases appears in Appendix B.

9.2 Gouging Case 1: Vertical Impact

In the first case, the HHSTT sled model is considered at various vertical impact velocities. In previous sled simulations [108], a vertical impact velocity of 1 - 2 m/s was evaluated, based on the results from an aerodynamic modeling effort [48, 49]. As indicated in Chapter VII, the one-dimensional penetration analysis indicates that this impact velocity would begin to deform the rail. However, the threshold kinetic energy (or threshold vertical impact velocity) for penetration is not necessarily the threshold for gouge initiation. As previous researchers have noted (see Chapter II), the development of a hump of material in front of the shoe is critical to gouge development. As another validation of the 1-D penetration theory, comparisons between CTH and the theory will be presented in this section.

9.2.1 Vertical Velocity of 2 m/s. The first impact case considered was the 2 m/s vertical impact (with the 3 km/sec downrange velocity). The one-dimensional theory estimated a 0.002 mm deformation - or a negligible penetration depth. Figure 9.2 illustrates the CTH simulation results. There is some wear, or localized material removal, in the coating surface, but no appreciable damage to the rail.

9.2.2 Vertical Velocity of 10 m/s. Increasing the vertical impact velocity to 10 m/s increased the deformation into the rail surface, but did not initiate gouging - this is due to the fact that the required hump of material was not created that begins the material jetting. The 1-D penetration analysis predicts a penetration depth of 0.06 mm for this case. Figure 9.3 illustrates that this depth was reflected by CTH as 0.1 mm and also highlights the temperature generated by the localized plasticity and non-gouging deformation.
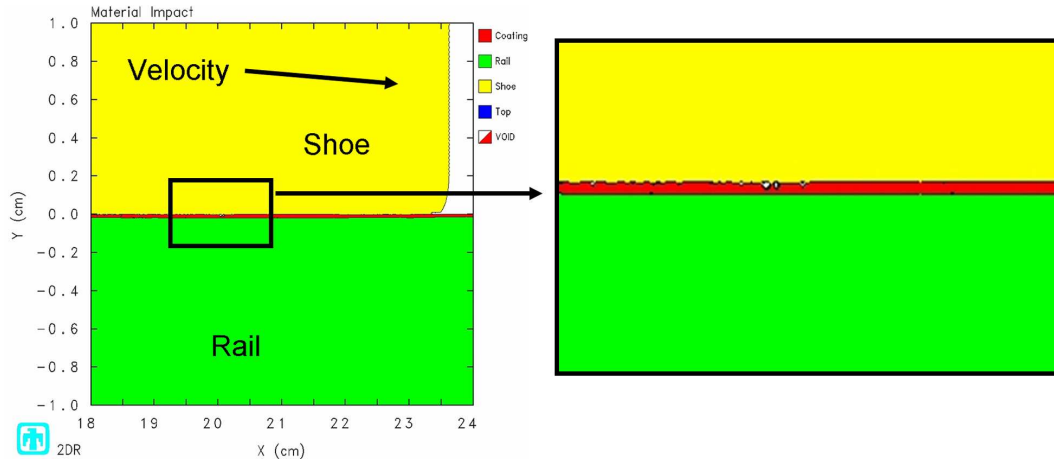
Figure 9.2: Sled, Vertical Impact of 2 m/s at 10 μseconds.
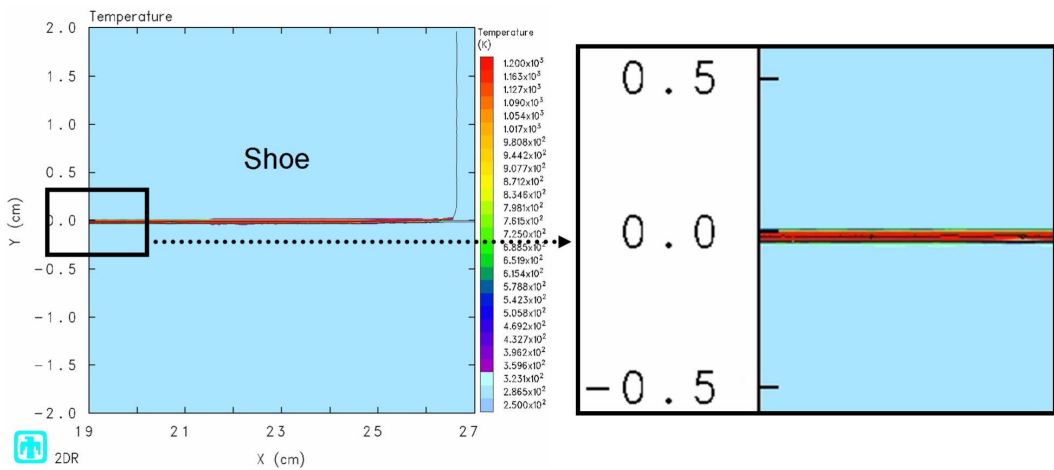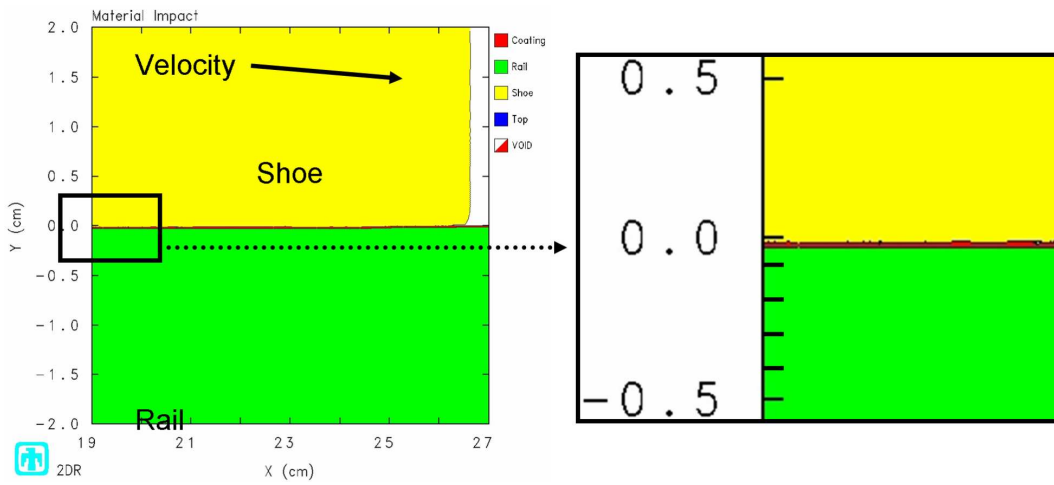
Figure 9.3: Sled, Vertical Impact of 10 m/s at 20 μseconds.

Note that the temperatures generated exceed the austenizing temperature of 1000 K.

9.2.3 *Vertical Velocity of 40 m/s.*   Increasing the sled vertical velocity beyond approximately 40 m/s increases the damage to the rail, but remains insufficient to generate gouging. In this case, the one-dimensional model predicts a penetration depth of approximately 0.95 mm. Figure 9.4 illustrates the CTH results - showing approximately a 1 mm deformation in the rail. As with the preceding figure, the resulting temperature profile is also depicted. Note that once again, localized temperature effects into the depth of the rail exceeds 1080 steel's austenizing temperature.
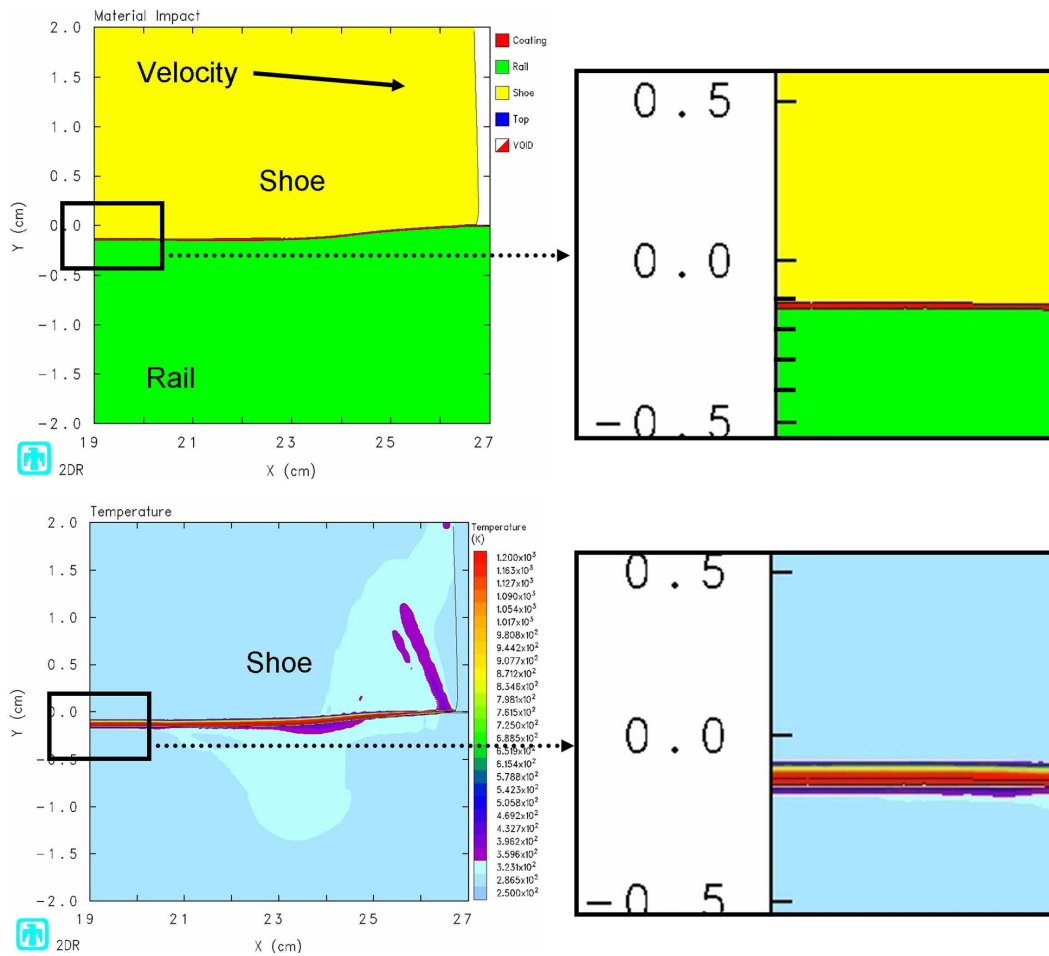
Figure 9.4:   **Sled, Vertical Impact of 40 m/s at 20 μseconds.**

9.2.4 Vertical Velocity of 75 m/s. The particular vertical velocity for gouging was not specifically ascertained in this study, but as the vertical velocity was increased to 75 m/s, gouging was observed. The one-dimensional theory predicts a penetration depth of 3.31 mm for this impact energy level. Figure 9.5 highlights the results of the simulation in terms of deformation. The penetration depth is approximately 3.5 mm in the region that is not involved in vertical material flow into the shoe and rail that characterizes gouging. The characteristics of material mixing is clear in this figure.
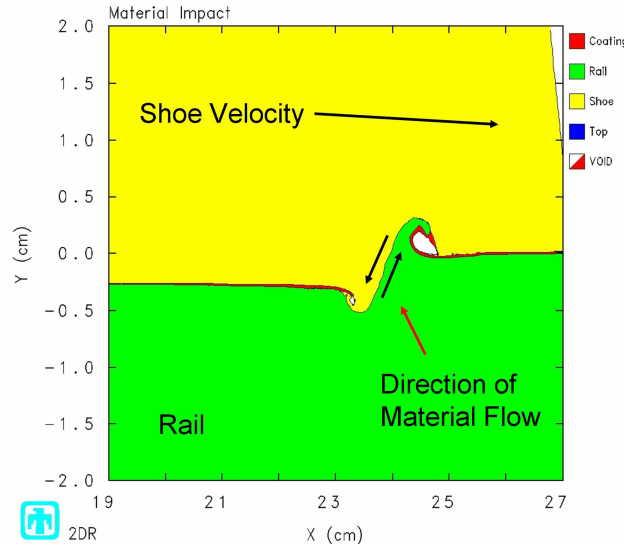
Figure 9.5:   **Sled, Vertical Impact of 75 m/s at 20 μseconds.**

Similar to other investigations, it appears that gouging begins with both the creation of a material hump and the contact of the shoe and rail materials with no intervening coating layer. This is illustrated in Figure 9.6.

The characteristic "high-pressure core" mentioned in previous work was also observed and appears in Figure 9.7. Note that the units in CTH are dynes/cm^3 - therefore the maximum value for this particular plot is 7 GPa when converted to more standard units.

The temperature profile that results from this plasticity is depicted in Figure 9.8. Note that a large portion of the rail is heated above the austenizing temperature.
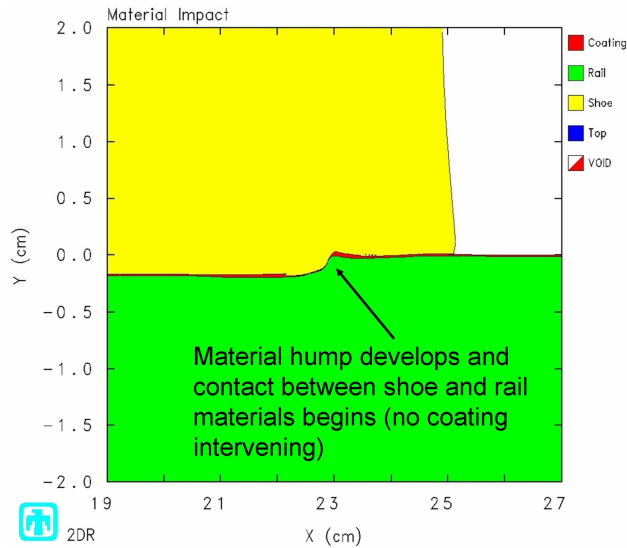
Figure 9.6: **Sled, Vertical Impact of 75 m/s at 14** μ**seconds.**
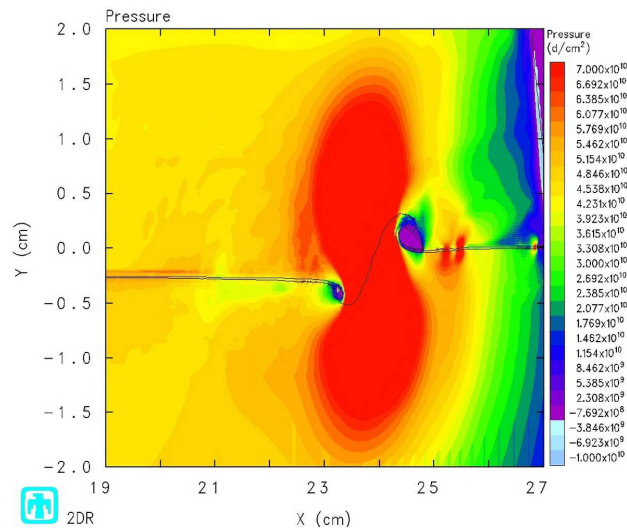
Figure 9.7: **Pressure, Vertical Impact of 75 m/s at 20** μ**seconds.**

Comparing this temperature to the experimental gouge analysis in Chapter IV, Figure 4.5, we arrive at Figure 9.9. This particular impact has generated results that match very closely to the metallurgical observations and subsequent thermal history that was suggested in Chapter IV.
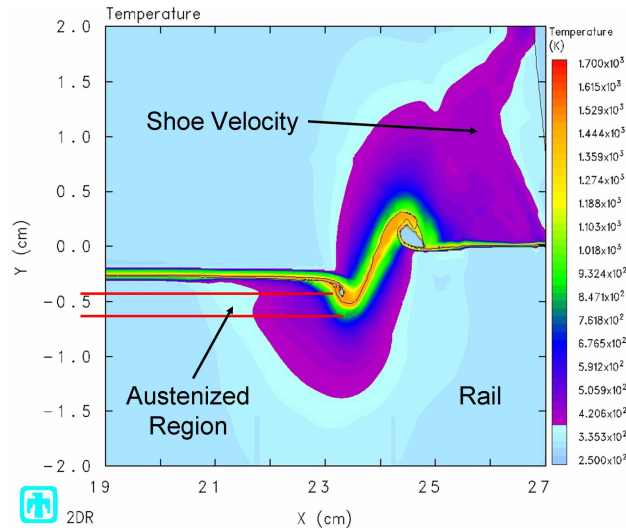
Figure 9.8:   **Temperature, Vertical Impact of 75 m/s at 20 μseconds.**
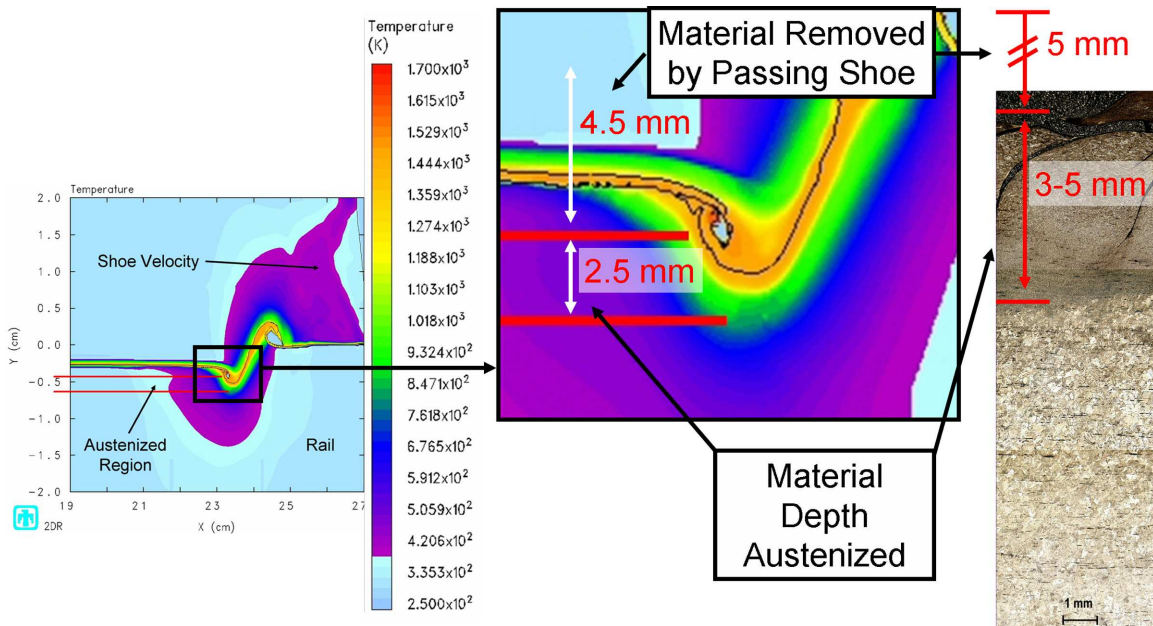
Figure 9.9:   **Temperature Profile Comparison, Vertical Impact of 75 m/s at 20 μseconds.**

This result is a key validation of both the material flow models, and CTH's ability to model hypervelocity impact. As we will see later in this Chapter, this kind of result can be obtained from the other type of impact cases. So, while a 75 m/s

vertical impact may not match well with aerodynamic models of the sled, other cases will match HHSTT conditions more closely.

9.2.5 *Vertical Velocity of 100 m/s.*   Increasing the vertical impact velocity simply increases the impact depth, and the size of the resulting gouge. Figure 9.10 illustrates the resulting deformation. At this impact velocity, the one-dimensional impact theory predicts a penetration depth of 5.8 mm. The CTH simulation indicates a penetration depth of approximately 4.5 mm. This result, and those of higher impact velocities, show a departure from the predicted penetration depths based on the one-dimensional theory. This is due to that fact that at these impact velocities, the penetration event is still occurring at 20 microseconds – where we end the simulation. So, while the 1-D theory may, in fact, predict the actual resulting depths more accurately, we cannot compare against CTH beyond about 75 m/s.
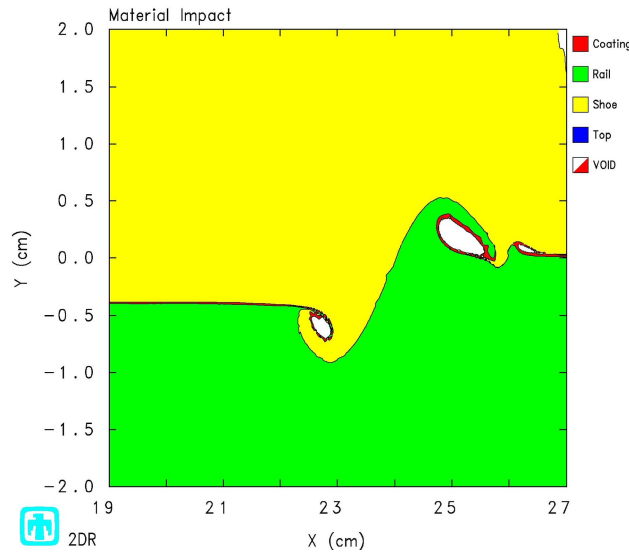
Figure 9.10:   **Sled, Vertical Impact of 100 m/s at 20 μseconds.**

Figure 9.11 shows the pressure generated by this higher energy impact, and Figure 9.12 illustrates the resulting temperature profile.
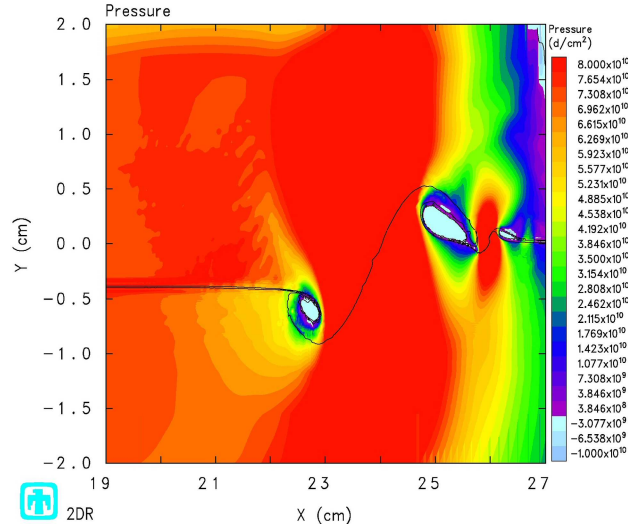
Figure 9.11: **Pressure, Vertical Impact of 100 m/s at 20 μseconds.**
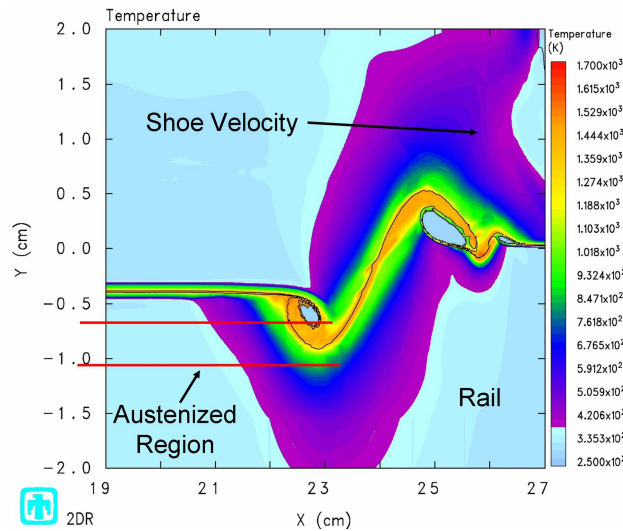
Figure 9.12: **Temperature, Vertical Impact of 100 m/s at 20 μseconds.**

Again, the temperature profile can be compared against the metallurgical examination of the HHSTT gouge. The results match fairly well for this particular case of gouging caused by high vertical impact velocity.

9.2.6 Vertical Velocity of 30 m/s on 10% Surface Area. As part of the examination of the gouging phenomenon, a smaller contact surface area was considered.

9-10
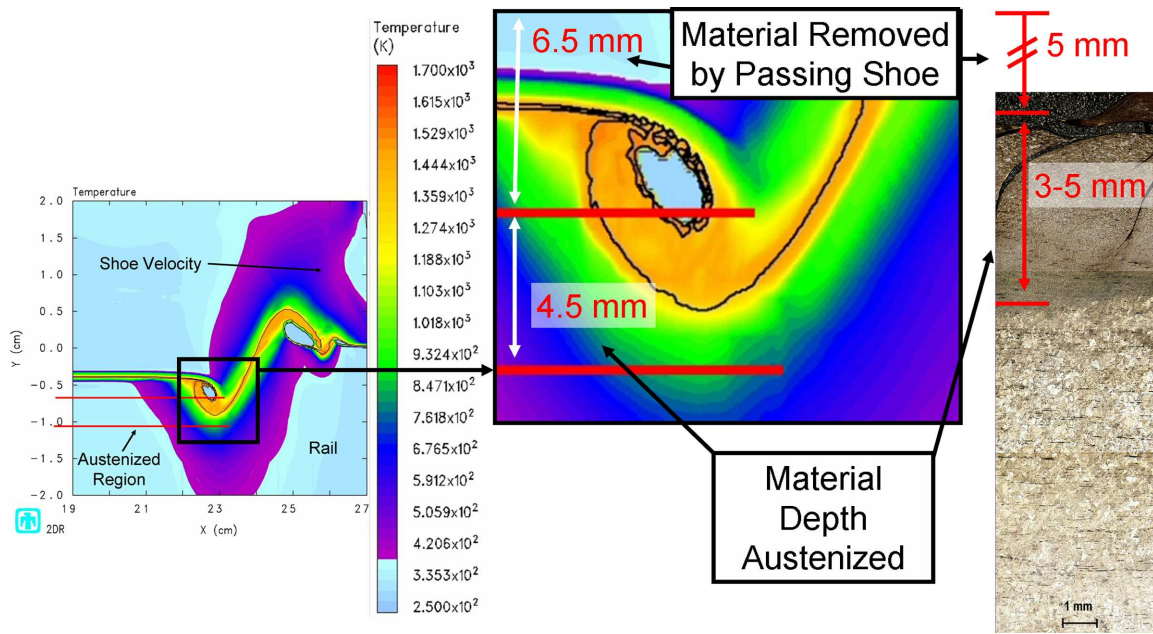
Figure 9.13: **Temperature Profile Comparison, Vertical Impact of 100 m/s at 20 μseconds.**

The plane-strain model presented in Figure 8.1 was re-dimensionalized so that the mass (200 kg) is carried by a shoe that is only 10% as long. Recalling the discussion in Chapter VII concerning the one-dimensional penetration theory's prediction of increased penetration depth with reduced impact area, a CTH model was created to emulate that phenomenon in plane-strain.

The one-dimensional penetration prediction for a 30 m/s impact on 10% of the shoe surface area is 5.32 mm. Figure 9.14 illustrates the result of the CTH simulation - which yields approximately 4.5 mm of penetration depth. Figure 9.15 illustrates the resulting pressure and temperature profiles.

Therefore, a decreased area of contact with the same mass and impact conditions, will increase the penetration depth and enhance the likelihood of gouge development.

9.2.7 Vertical Velocity of 100 m/s with Heated Shoe. One of the areas of continuing research in this field is the exploration of the effects of having the sled shoe heat during its run. Most simulations of these hypervelocity gouges involve
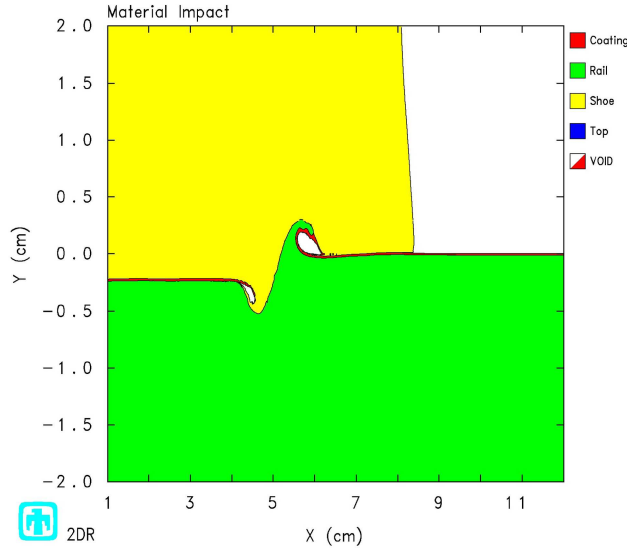
Figure 9.14:   10% Sled, Vertical Impact of 30 m/s at 20
μseconds.
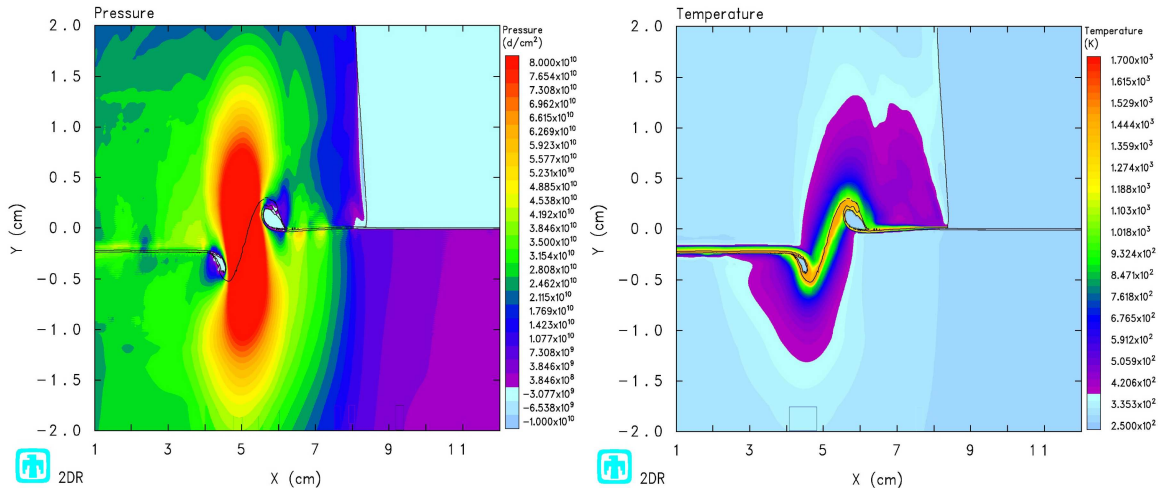
Figure 9.15:   10% Sled, Pressure and Temp, Vertical
Impact of 30 m/s at 20 μseconds.

room temperature materials coming into contact. For this particular evaluation, the
sled shoe was heated to 1200 K within CTH prior to initiating a 100 m/s vertical
impact velocity. This temperature represents a mid-range value from the frictional
analysis of Laird [68].

Figure 9.16 presented the results of the heated shoe run along with the previous
one in which the shoe was not heated. Although small differences can be noted (for

instance, there is a slight increase in gouge depth, austenized rail depth, and gouge depth into the shoe) they are relatively small variations in the solution. While this is certainly not an exhaustive study on the topic, it is interesting to note the small amount of contribution the heated shoe had to the overall results.
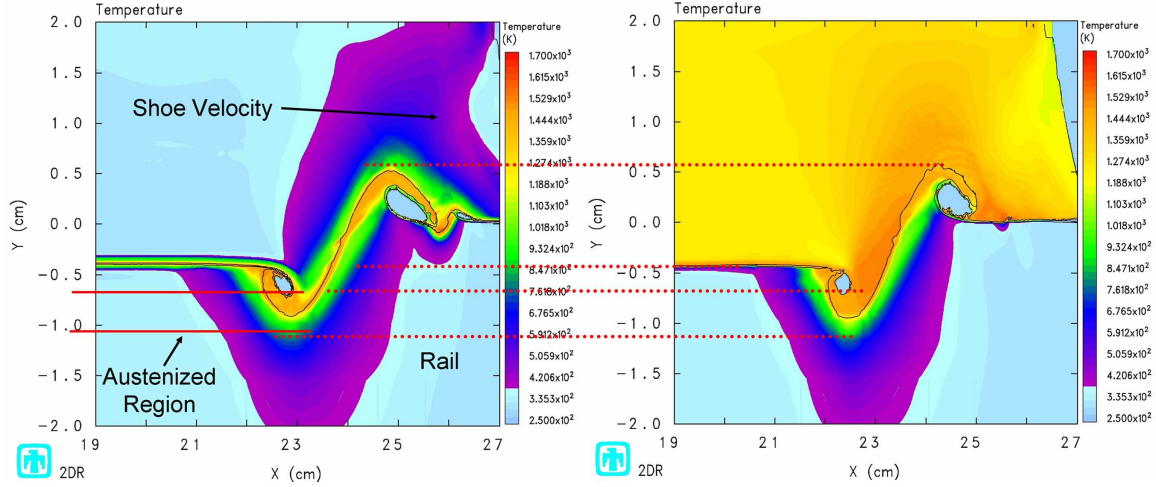
Figure 9.16: **Temperature Profile Comparison for Heated Shoe, Vertical Impact of 100 m/s at 20 μseconds.**

9.2.8 Summary of Vertical Impact Case. This section was a survey of the effect of the vertical impact velocity on the initiation of gouging with the new material constitutive models. Because the one-dimensional penetration model applied to these cases, a discussion of its predictions for each case was included.

Based on the estimated vertical impact velocities present in the HHSTT scenario (from aerodynamic models [48]), the CTH simulations indicate that gouging would not occur. If the impact velocities are increased, or the contact surface area is decreased, gouging does occur. The gouging events simulated do match the character and the thermal profiles seen experimentally. In addition, until the impact velocities are increased to a level in which the vertical penetration does not finish within 20 microseconds, the one-dimensional penetration theory fairly accurately predicted the results. Table 9.1 summarizes the comparison.

Table 9.1:   Comparison of Penetration Depth Predictions.

Vertical Velocity	z (1-D Theory)	z (CTH Simulation)
2 m/s	0.002 mm	0.0 mm
10 m/s	0.06 mm	0.1 mm
40 m/s	0.95 mm	1.0 mm
75 m/s	3.31 mm	3.5 mm
30 m/s (10% shoe)	5.32 mm	4.5 mm
100 m/s	5.8 mm	4.5 mm

9.3 Gouging Case 2: Angled Impact

A second type of impact that the sled could experience, and which does lead to gouging, is an "angled" impact. In this case, there is an angle of incidence between the rail and shoe such that the leading edge of the shoe contacts the rail first, before the remainder of the shoe impacts. The vertical velocity considered was 1 m/s.

One way in which this scenario can occur in the field is a rail height change over a length of rail. According to the HHSTT, the allowable rail height change is 0.025 inches over a length of 52 inches (0.0635 cm over a length of 132 cm) [50] - which is an angle of incidence of 0.03° (if considered over the entire length). The angle would, of course, be greater if the rail height change occurred over a smaller distance. As long as the height variation occurred within the entire test distance of 132 cm and was under 0.0635 cm in magnitude, the rail would be in tolerance. Therefore, a wide range of angles are possible. This tolerance will be referred to as the "rail height tolerance" in this work and is depicted in Figure 9.17.

Another manner in which an angled impact could occur is that the shoe gap can allow the rear of the sled to rise and thereby create an angle with the rail. This will be described in detail in section 9.3.1.
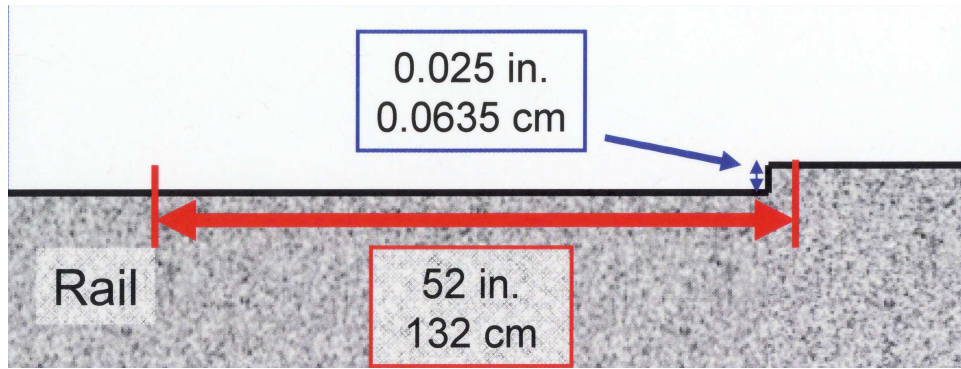
Figure 9.17:   **Rail Height Tolerance Illustration.**

Finally, this could also occur if a sloping rail discontinuity was encountered. According to the HHSTT, at the rail section seams, a sloping discontinuity of 0.075 inches over a 1 inch span (0.19 cm over 2.54 cm) is allowable [50] - which is an angle of 4.29°. Of course, if the discontinuity was joined with a smaller angle, it would be within tolerance. This tolerance will be referred to as the "rail seam tolerance" in this work and is illustrated in Figure 9.18. While a brief discussion of this type of impact is presented in this section, a much more detailed examination of the rail discontinuity case is presented in the next section.
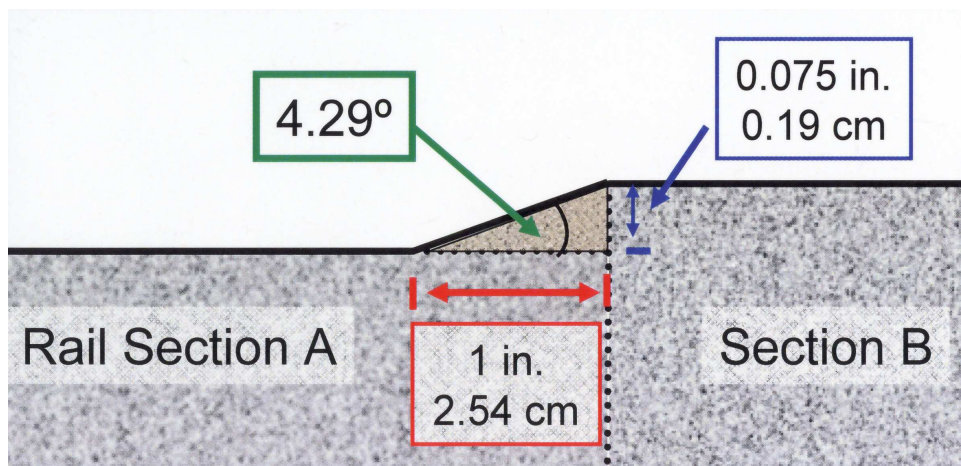
Figure 9.18:   **Rail Seam Tolerance Illustration.**

Both of these rail tolerances can be depicted in a graphical format - presented in Figure 9.19. In this diagram, the face angle of the discontinuity is shown as a

function of the discontinuity magnitude. The shaded areas represent the "operating area" where the rail discontinuity is within tolerances.
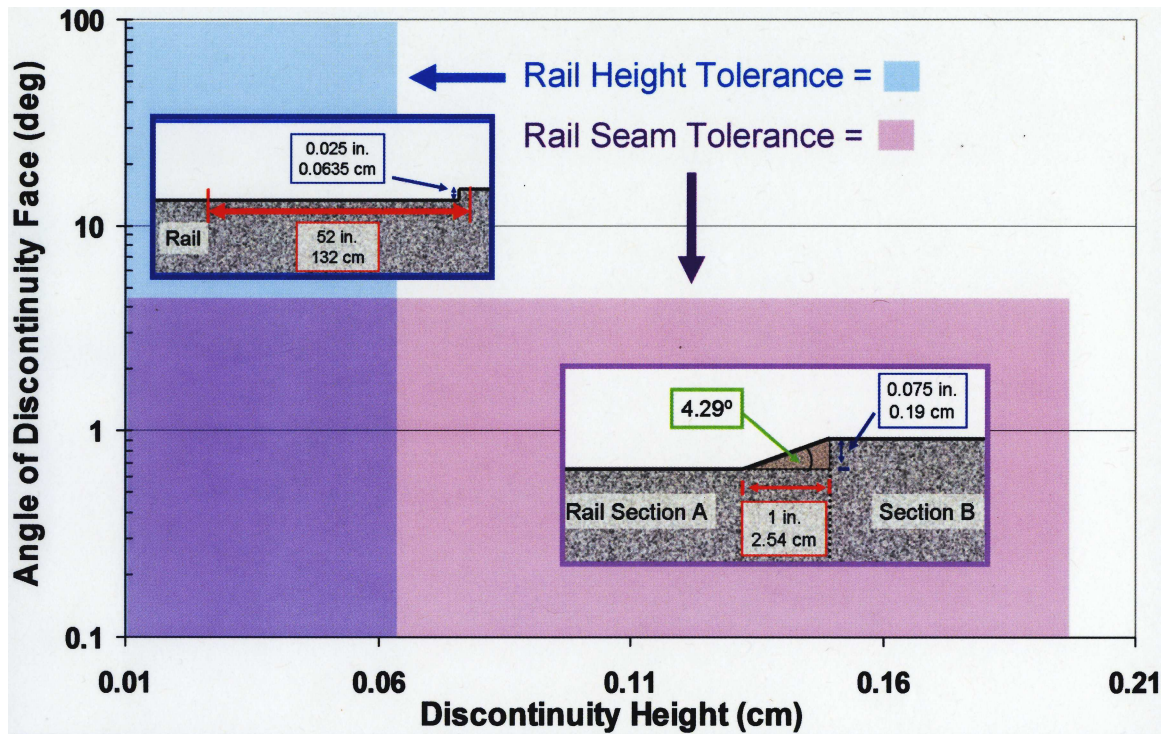
Figure 9.19:   **Rail Alignment Tolerance Summary.**

9.3.1   Incidence Angle of 0.14°.   In order to compute the maximum allowable incidence angle allowed in the HHSTT scenario considering only the shoe gap scenario, a simple computation is made. Taking the maximum shoe gap of 0.635 cm (which is the maximum gap between the shoe and the rail when the shoe is full travel in the up position) and the 2.5 m between the front and back shoes on the sled (see Figure 8.1), the maximum incidence angle of 0.14°. That is, if the sled is pitching down from the full up travel position, the leading edge of the front shoe can impact the rail at 0.14°.

Two models of this impact was evaluated - with very similar results. One was to angle the shoe and velocity vector within CTH and have the shoe impact the rail. The other technique applied was to angle the rail and have the shoe impact it in that manner.

In allowing the shoe/rail angle to be the maximum 0.14°, gouging did not occur. The resulting material response was very similar to Figure 9.3. This indicates that the maximum angle allowed by the shoe geometry would cause wearing type damage to the rail and some local elevated temperatures beyond the austenizing limit. Nearly identical results were obtained for an impact angle of 0.03°. Therefore, under normal sled operations (applied to the rail height tolerance and the allowable shoe gap scenario) only slight wearing will occur.

9.3.2 Incidence Angle of 1.65°. If the angle of incidence was allowed to increase beyond what the shoe design would allow but within the tolerance allowed for a rail section seam, to an angle of 1.65°, the impact would also not lead to gouging. However, a very important effect was noted. Figure 9.20 illustrates the wearing (or scraping) type damage to the rail and shoe during this type of impact. A small amount of plasticity is being generated and the pressure is correspondingly indicated in Figure 9.21.

Of particular interest is the temperature profile generated by this wearing type impact. Figure 9.22 depicts the temperature generated by the small amount of plasticity during this kind of non-gouging contact.

When we compare this generated heat profile from a non-gouging, wear-type impact, to those in-service rails (with no gouges) analyzed in Chapter IV, we arrive at a possible explanation for the observed microstructural changes. Since the scrape reported on the in-service rail specimen designated isrb was not measured and then painted over with coating, we cannot compare the material removal to that indicated in this simulation. However, that depth of austenization within the rail section matches very closely to that observed experimentally. Figure 9.23 compares the heat profile in this impact to the metallurgical analysis of specimen isrb (which sustained a slight gouge and remained in service at the HHSTT) that appears in Figure 4.23.

This indicates that a small, measurable amount of plasticity that was encountered in the field has caused a thermal pulse to enter the rail and change the mi-
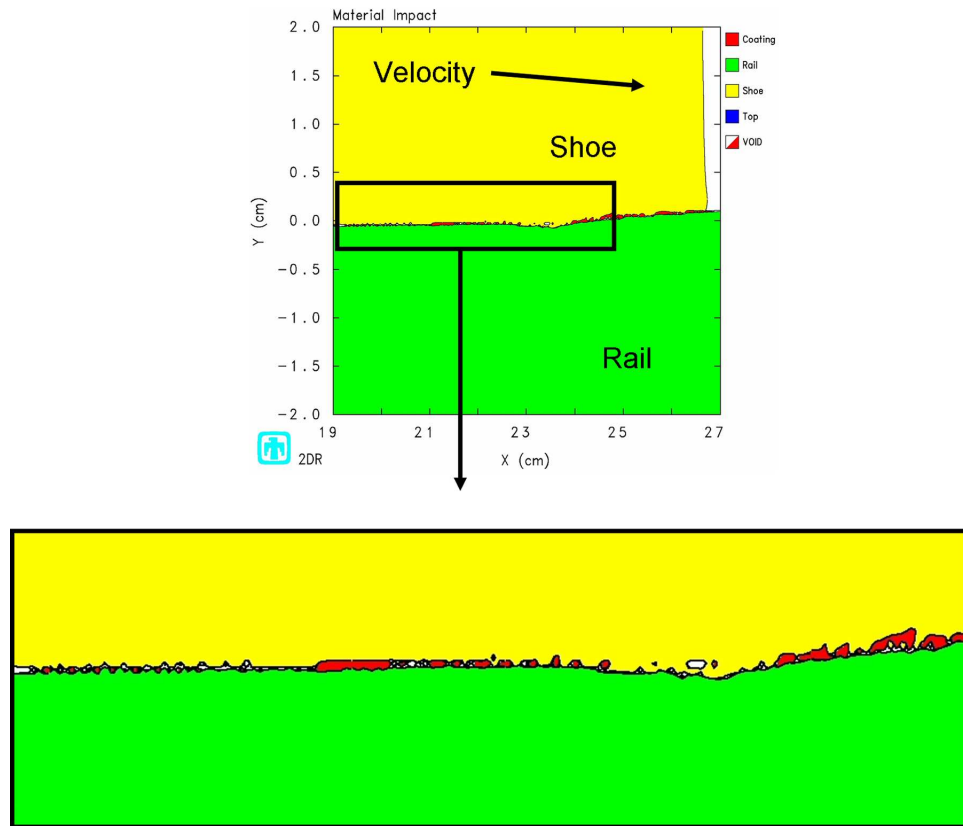
Figure 9.20:   **Sled, 1.65° Impact at 20 μseconds.**
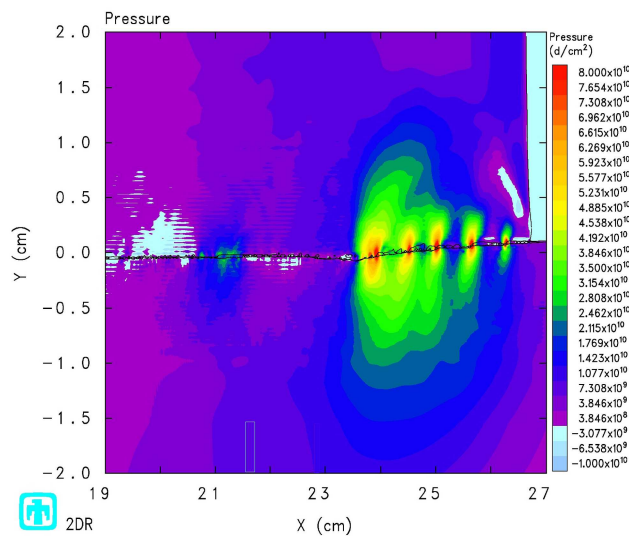
Figure 9.21:   **Pressure, 1.65° Impact at 20 μseconds.**

crostructure of the rail steel. CTH is able to model this temperature effect - which is confirmed by metallurgical analysis of the in-service rails sent from the HHSTT.
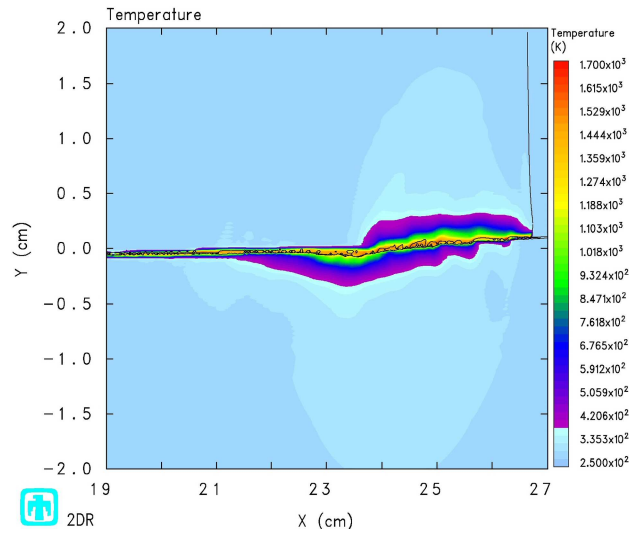
Figure 9.22:   **Temperature, 1.65° Impact at 20 μseconds.**
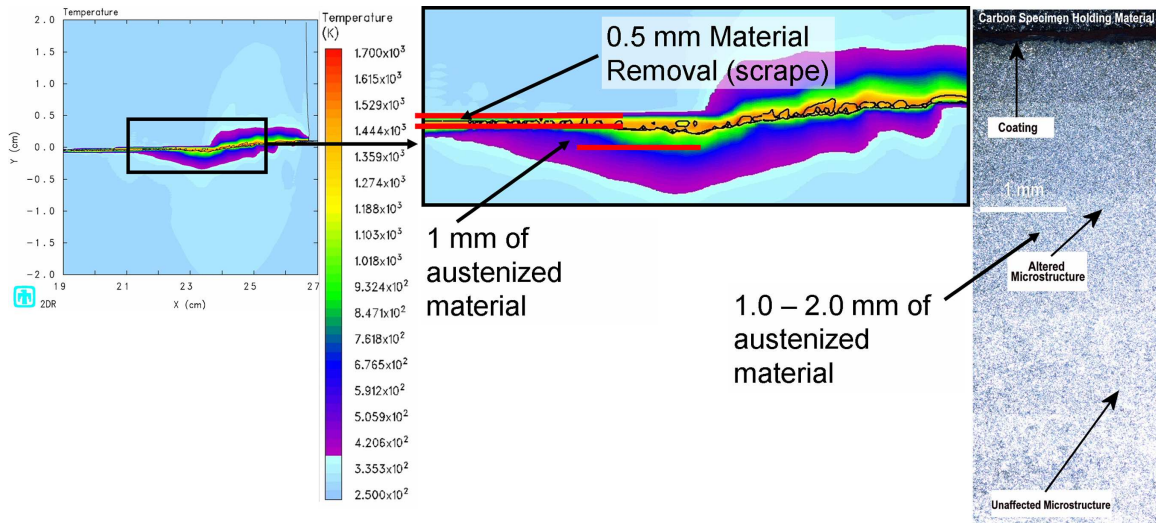
Figure 9.23:   **Temperature Profile Comparison, 1.65° Impact at 20 μseconds.**

9.3.3   Incidence Angle of 3°.   In order to ascertain the conditions at which gouging would occur in the angled impact case to the extent it might result in the type of gouging analyzed metallurgically in Chapter IV, the incidence angle was increased to 3°. This might occur if the rear shoes catastrophically failed and allowed the rear sled travel to rise to 13 cm above the rail and the sled came down at this angle on the front shoes. Alternately, this angle is also within the tolerance limit for the sloping discontinuity at the rail section seams.

Figure 9.24 illustrates the resulting deformation and pressure resulting from this kind of impact. The generated temperature profile is depicted in Figure 9.25. A comparison is made between this temperature profile and the experimentally examined gouge from the HHSTT in Figure 9.26. Note that the magnitudes of material removal and the depth of austenization is very close to those observed metallurgically.
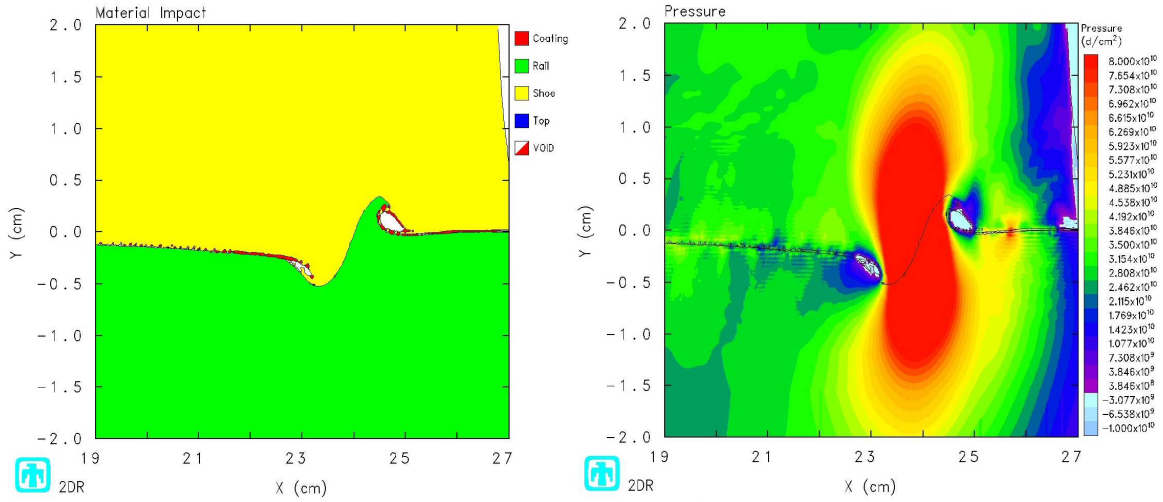
Figure 9.24:   **Deformation and Pressure, 3° Impact at 20 μseconds.**
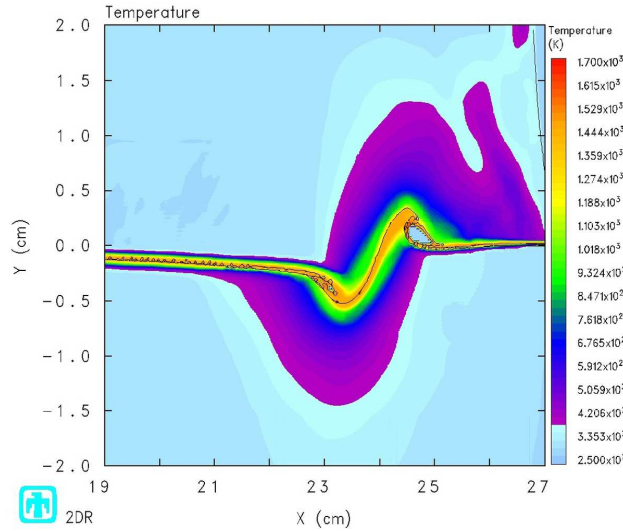
Figure 9.25:   **Temperature, 3° Impact at 20 μseconds.**

9.3.4   Summary of Angled Impact Case.   Gouging was not generated at the maximum incidence angle that can be expected during normal sled operations at the
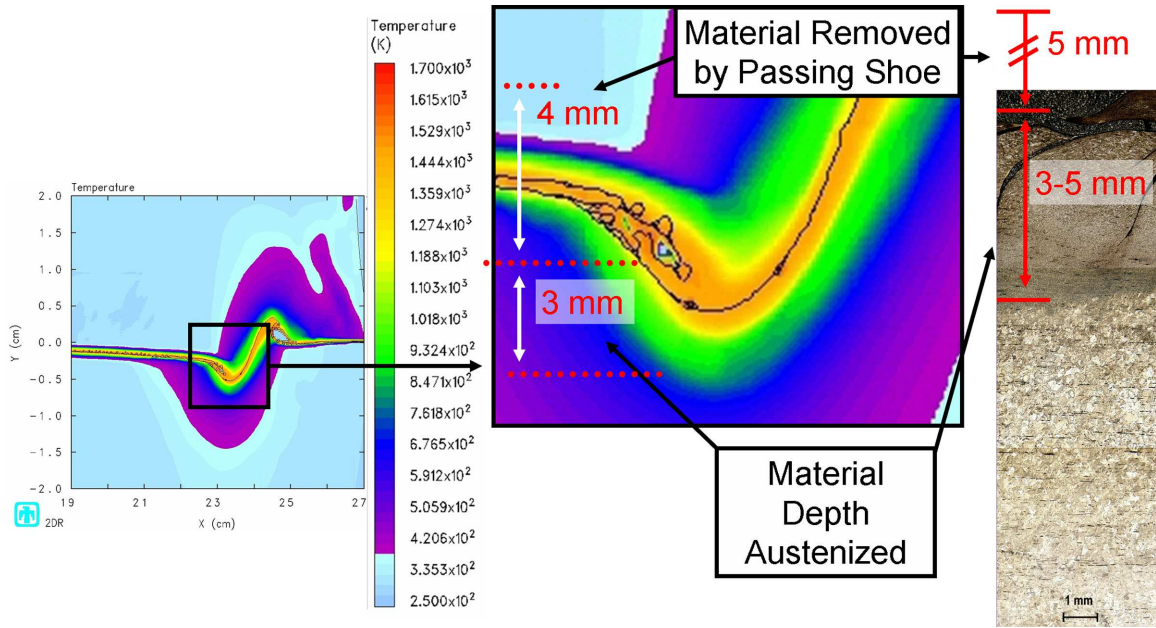
Figure 9.26:   **Temperature Comparison, 3° Impact at 20 μseconds.**

HHSTT when applied to the rail height tolerance. However, at angles within the allowable tolerances at the rail section seams, it was demonstrated that an impact at this angle could either create rail damage (wear and/or scraping) that could cause the microstructural changes seen in the non-damaged in-service HHSTT rails, or generate the kind of gouging impact that created the experimentally examined rail gouge that appears in Chapter IV.

These simulations increase our confidence in CTH modeling of hypervelocity impact and aid in determining which parameters in the HHSTT may lead to gouging.

9.4   Gouging Case 3: Rail Discontinuity

The final gouging case examined was the impact against, or into, a rail discontinuity. These continuities can take the form of an abrupt change in rail height, a smooth variation in rail height, or debris on the track (an asperity) [108]. This case is distinguishable from the angled impact scenario in that the rail discontinuity is not

a continuously angled rail - but a discrete section of rail that has a local rail height change.

In the modeling presented in this study, the type of rail discontinuity considered is a rail height change that might occur at the end of a rail section or might be inherent in the rail's condition. In all cases, the rail in considered to be coated with epoxy over its entire surface, including the discontinuity. In addition, the sled also has 1 m/s of vertical impact velocity. Of the cases examined, this is the most likely to occur in the field at the HHSTT. The allowable rail alignment tolerance used at the HHSTT is 0.0635 cm [50].

Initially, the discontinuities considered were "sharp" discontinuities, with a "face" angle of 90°. Figure 9.27 provides an overview of this test geometry. A discontinuity is placed in front of the sled and modeled to be coated.
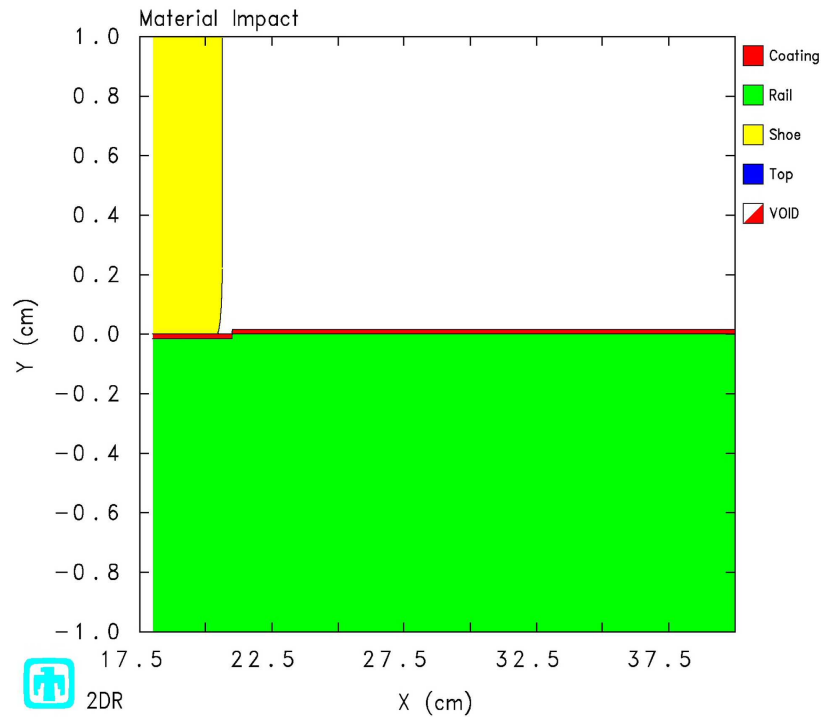
Figure 9.27:   **Overview of Sharp Rail Discontinuity.**

As the study progressed, it became clear that altering the face angle would have a dramatic impact on the occurrence of gouging. Figure 9.28 illustrates the terminology adopted to examine the rail discontinuity case more completely.
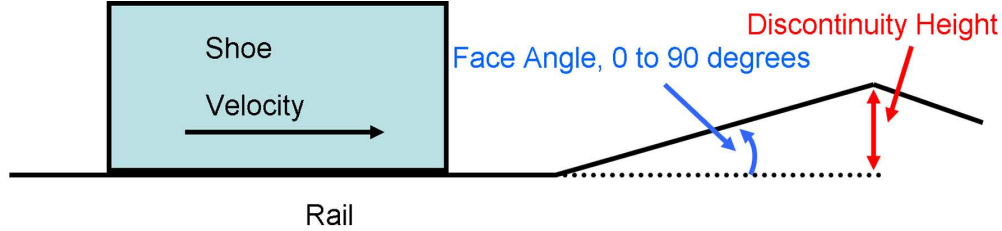
Figure 9.28:   **Overview of General Rail Discontinuity.**

Based on the rail alignment tolerances of 0.0635 cm over a span of 132 cm, the rail discontinuity would be a gradual slope. However, the method of checking for these rail height changes is a machine that runs down the track making measurements. This technique does not specifically flag local discontinuities as special cases. That is, the 0.0635 cm height change could occur in a sharp discontinuity and it would still be within track tolerances. Based on the results of the angled impact, a very gradual face angle would not generate gouging. Therefore, the sharp discontinuities (with face angles of 90°) were considered as "worse-case" scenarios and were the subject of the first series of simulations.

Following an examination of these sharp discontinuities, a much more extensive series of simulations was conducted to explore the effect of face angle to the generation of gouging. Of course, the goal of this study was to discover the approaches required at the HHSTT to mitigate the occurrence of gouging.

9.4.1   0.01524 cm Rail Discontinuity.   The first case examined is a rail discontinuity of 0.01524 cm - which is the nominal thickness (6 mils) of the coatings placed on the rails [108]. This specific case appears in Figure 9.27. This small discontinuity was compressed into the rail and, while it caused some wearing type damage to the shoe and rail, it did not initiate gouging. The deformation and temperature profile that CTH generates as the solution to this impact problem appears in Figure

9.29. This degree of discontinuity does not generate gouging, but does results in some localized plasticity and temperature development.
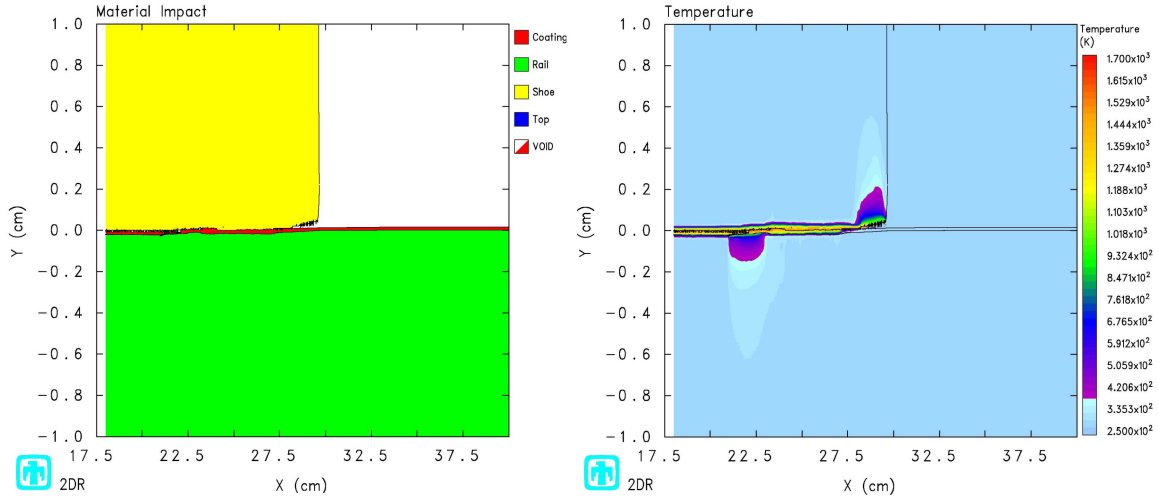
Figure 9.29:   **Sled, 0.01524 cm Rail Discontinuity at 20 μseconds.**

This amount of temperature generation is similar in magnitude to that seen on the non-damaged in-service rails examined in Chapter IV. Specifically, specimen "is" (see Figure 4.22) is depicted in Figure 9.30 along with the temperature profile created by this 0.01524 cm discontinuity impact. This provides another explanation for the microstructure changes seen in the rails that appear (visually) not to have any damage.

9.4.2   0.02 cm Rail Discontinuity.   In an effort to find a discontinuity that would initiate gouging, a 0.02 cm discontinuity was placed into the model, similar to that depicted in Figure 9.27. This level of discontinuity led to the creation of a typical gouging impact. Figure 9.31 depicts the resulting deformation and pressure plots for this case. Figure 9.32 indicates the plastic strain-rate and temperature results. Note that the strain-rate reaches the 10^6/sec level in some areas, and throughout the specimen the full range of strain-rates is being experienced. Additionally, the temperature plot indicates a portion of the material (shown in red) has reached the melt temperature (∼1650K). This matches more completely the experimental findings
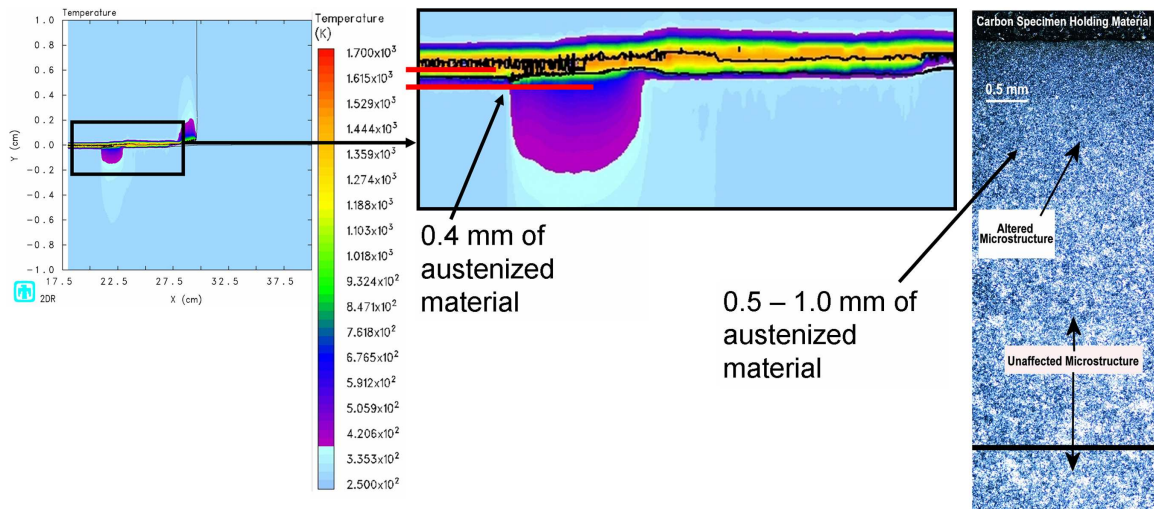
Figure 9.30: **Comparison of Temperature Profile, 0.01524 cm Rail Discontinuity at 20 μseconds.**

in the gouged specimen from the HHSTT - both in this work, and in Gerstle [42]. In the other gouging cases in this work, the melting temperature was not attained. This particular CTH simulation was allowed to run out to 25 microseconds to capture more of the event.
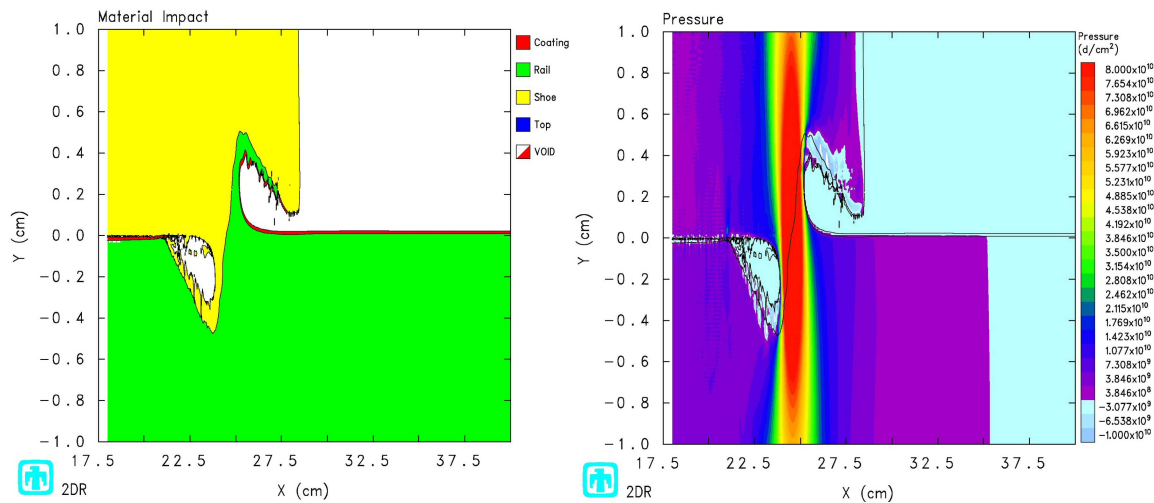
Figure 9.31: **Sled, 0.02 cm Rail Discontinuity at 25 μseconds.**

This 0.2 cm discontinuity case compares well against the experiment gouge analysis presented in Chapter IV. Figure 9.33 illustrates how the major elements of that gouge are matched with this simulation - to include melting at the gouge surface.
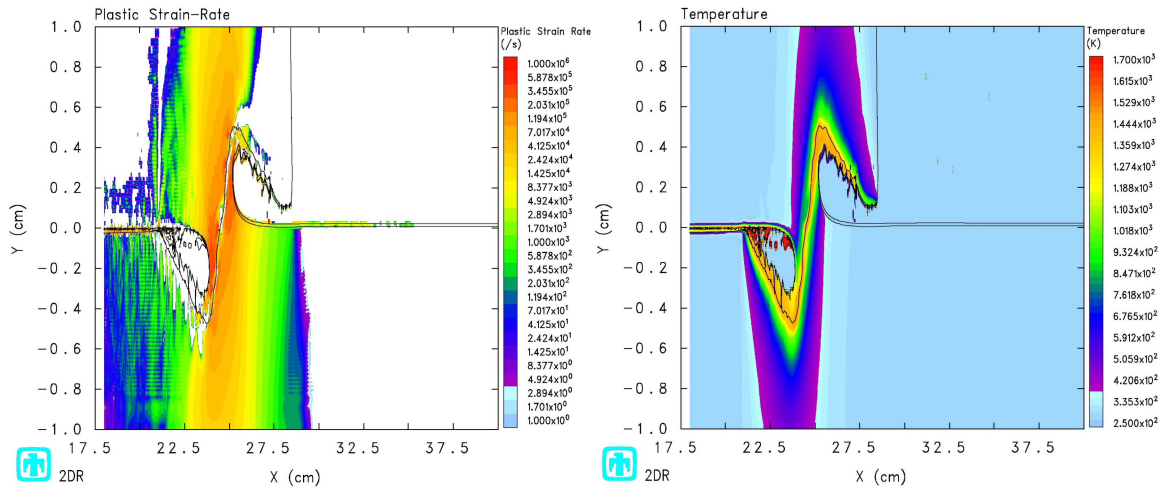
Figure 9.32:   **Sled, Strain-Rate and Temperature, 0.02 cm Rail Discontinuity at 25 μseconds.**
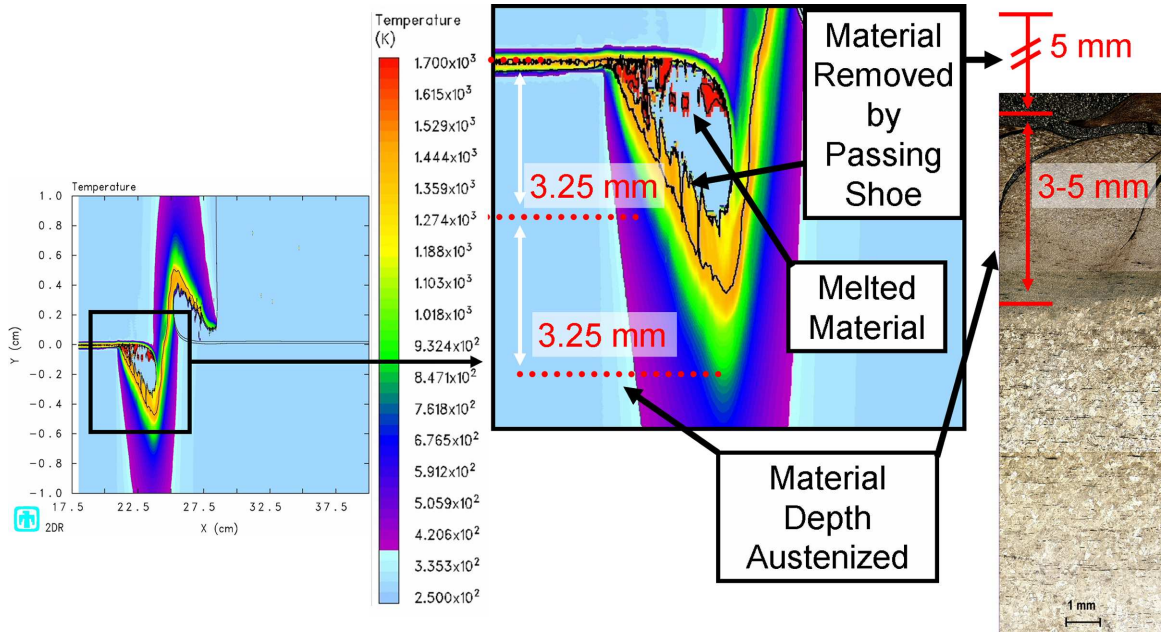
Figure 9.33:   **Temperature Profile Comparison, 0.02 cm Rail Discontinuity at 25 μseconds.**

9.4.3   0.03048 cm Rail Discontinuity.   The case of a discontinuity at twice the coating thickness was examined to further explore the phenomenon of gouging. Figure 9.34 illustrates the deformation and pressure plots, while Figure 9.35 depicts the strain-rates and temperature. This particular simulation was stopped at 20 microseconds to compare to the other types of gouging impacts examined in this work.
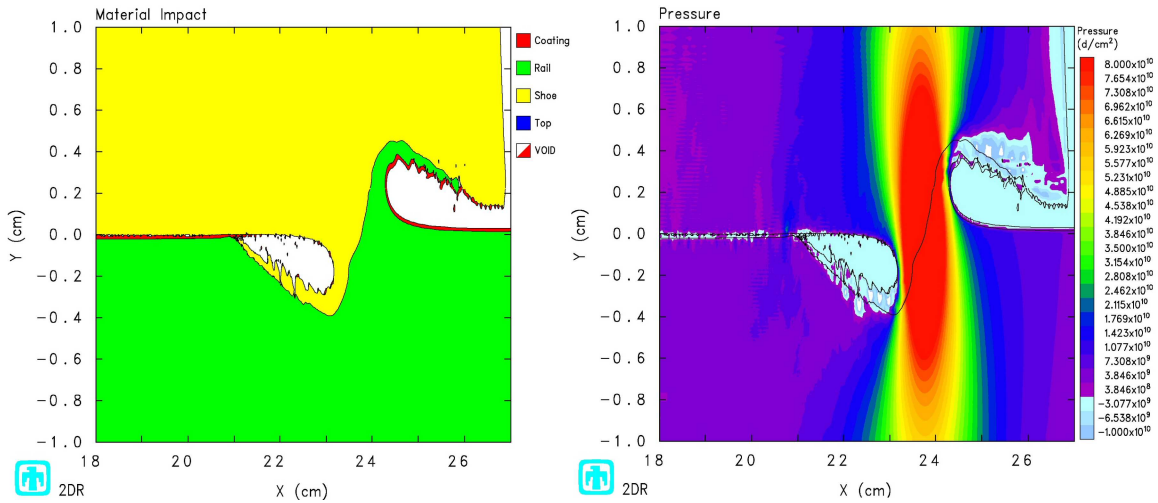
Figure 9.34:   **Sled, 0.03048 cm Rail Discontinuity at 20**
μseconds.
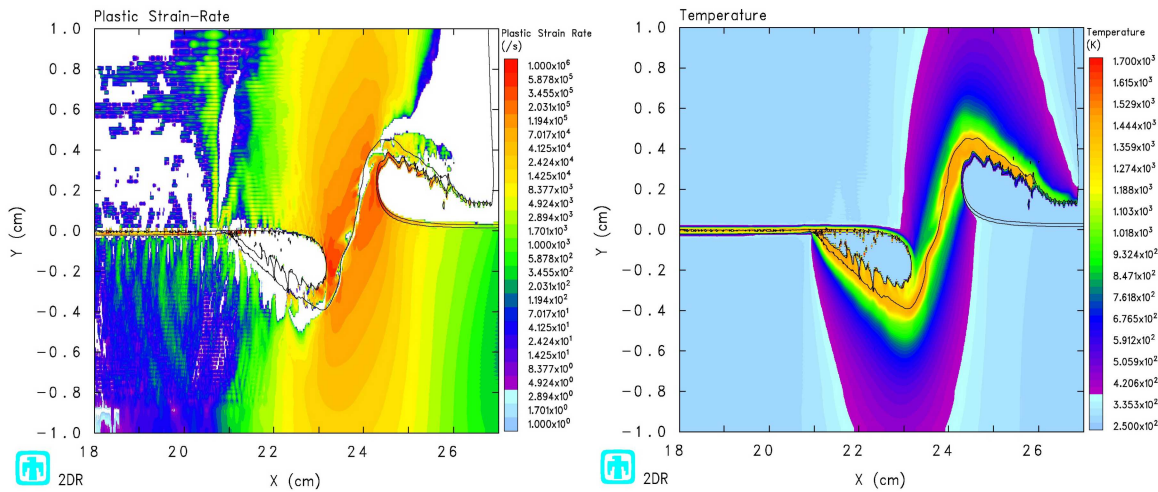
Figure 9.35:   **Sled, Strain-Rate and Temperature,**
0.03048 cm Rail Discontinuity at 20 μseconds.

Again, the strain-rates are focused in the high regime, but significant portions of the plasticity is occurring in the mid-range strain-rates - making the full-range constitutive model important to an accurate solution. The temperature profile in this case compares well with the metallurgical gouging evidence. Note that the deformations are not more pronounced due to stopping the simulation 5 microseconds before the 0.2 cm discontinuity case.
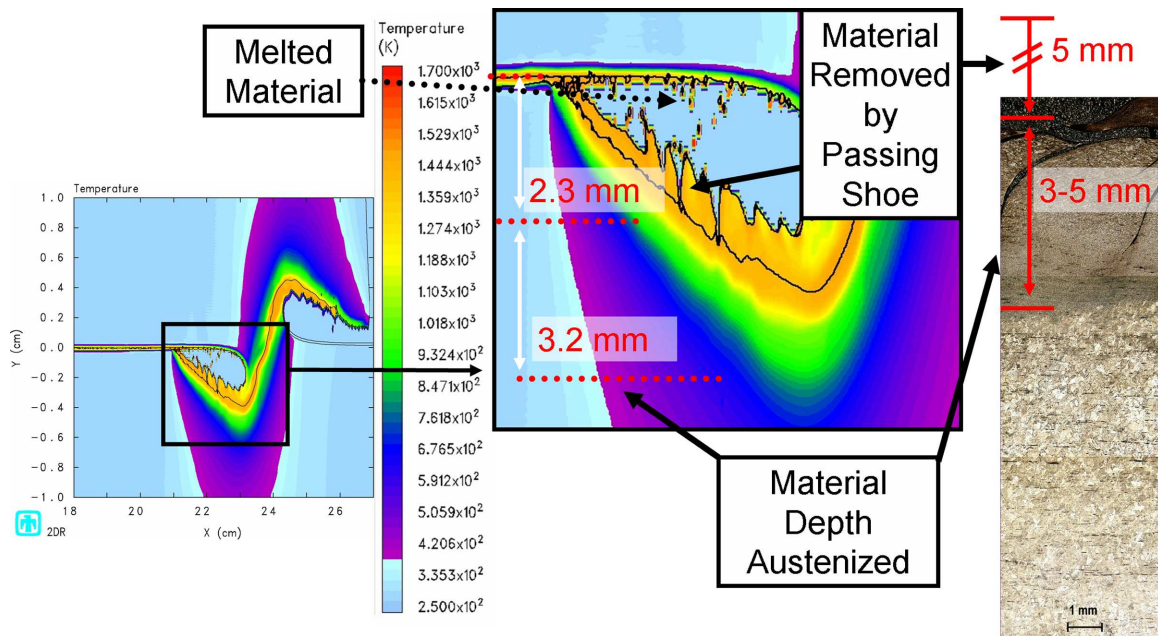
Figure 9.36:   **Temperature Profile Comparison, 0.03048 cm Rail Discontinuity at 20 μseconds.**

Of course, allowing the simulation to run further in time might create a profile that exactly matched the experimental gouge. However, the creation of the these very close matches between the CTH simulation and the experimental record allows the conclusion that the model is generating accurate results.

9.4.4   Discontinuity with Varying Face Angle.   Noting that the sharp discontinuity was one extreme version of this case, and that the angled impact could be viewed as the other extreme (that is, a discontinuity that occurred over an extended distance), an in-depth evaluation of numerous impact conditions was conducted. The goal was to find the combination of the discontinuity height and face angle (reference Figure 9.28) that created a gouging impact. Or more importantly, to define the set of parameters which would lead to a wearing type impact and allow the sled to pass without initiating gouging (and perhaps catastrophic failure).

To illustrate the type of impact that was created, a representative example is presented here. Figure 9.37 depicts an impact with a 0.0635 cm discontinuity which has a 2° face angle. This rail condition is within both rail alignment tolerances of

total rail height change over an extended distance, and the local tolerance for rail seams.
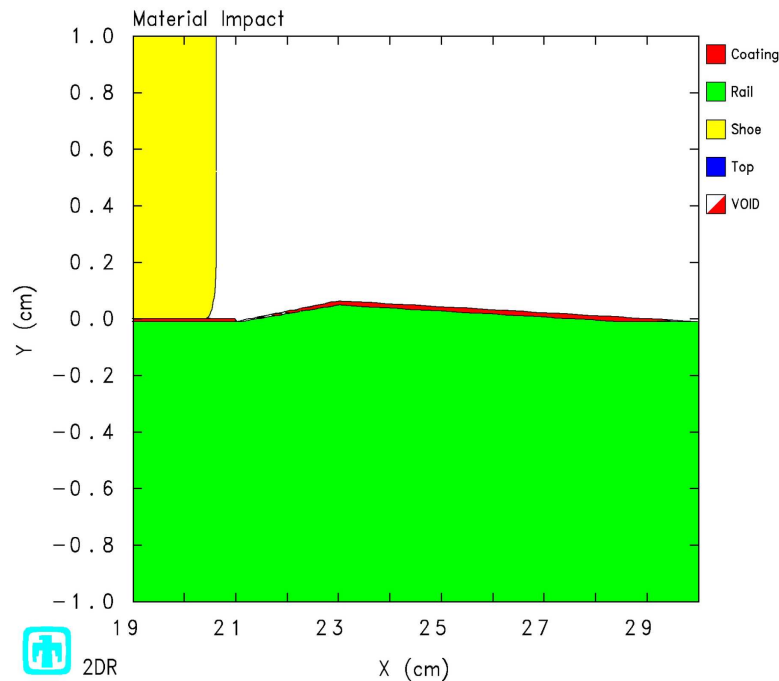
Figure 9.37:   **Example of Discontinuity with an Angled Face.**

As the impact progresses, the characteristic hump is created in front of the shoe and material mixing begins. This leads to the gouging type material interaction. Figure 9.38 shows this material flow beginning.

The type of gouging that results as the impact event unfolds close resembles those presented earlier in this Chapter. Figure 9.39 shows the deformation and pressure at 40 microseconds. The characteristic high pressure core is clearly evident. The strain-rates and temperatures generated by the impact are depicted in Figure 9.40. Once again, the strain-rates are throughout the entire range and there is a zone of austenized steel below the gouge.

This gouging case also compares well against the experimental gouge characteristics presented in Chapter IV. Figure 9.41 illustrates this comparison.
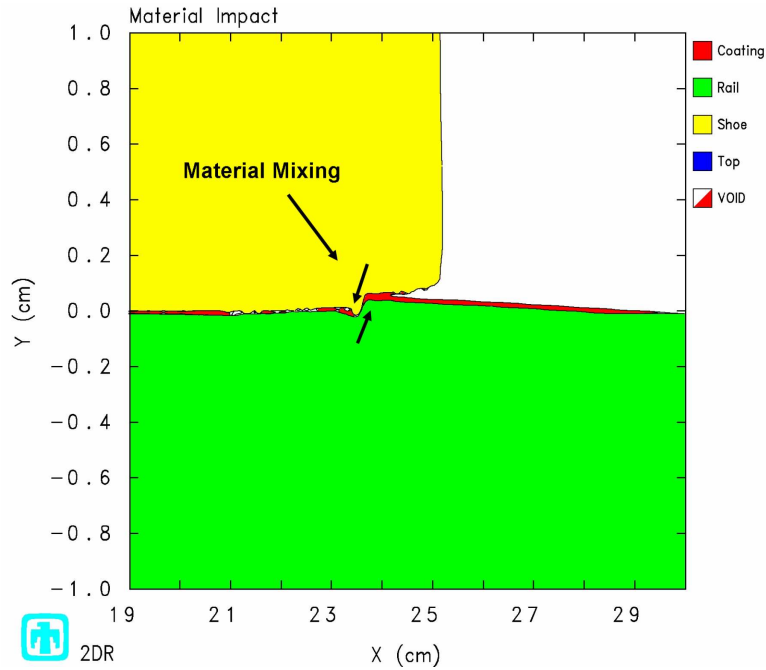
Figure 9.38:   **Example of Discontinuity with an Angled Face at 15 μseconds.**
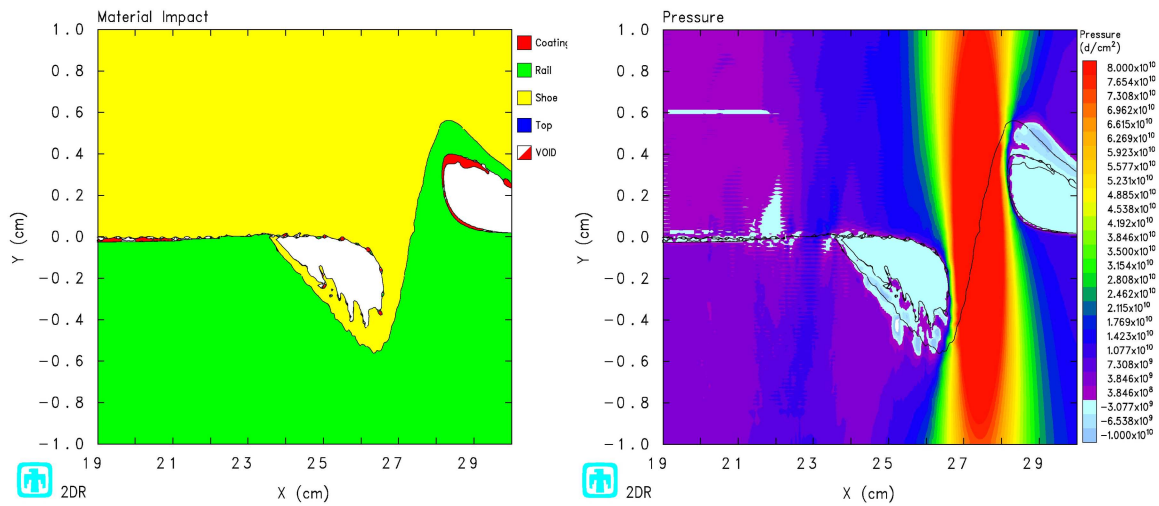
Figure 9.39:   **Example of Discontinuity with an Angled Face at 40 μseconds.**

Based on these findings (i.e. that gouging was affected by the face angle as well as the discontinuity height), a full complement of CTH simulations was conducted to define the parameter values that would only lead to a wearing type damage. Figure 9.42 summarizes the results of this extensive study.
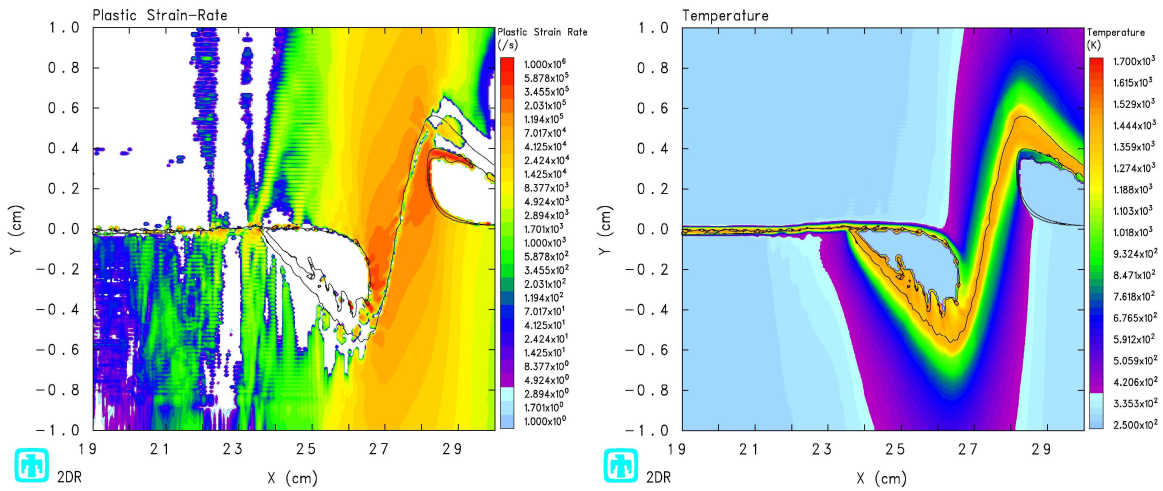
Figure 9.40:   **Example of Discontinuity with an Angled Face at 40 μseconds, Strain-rate & Temp.**
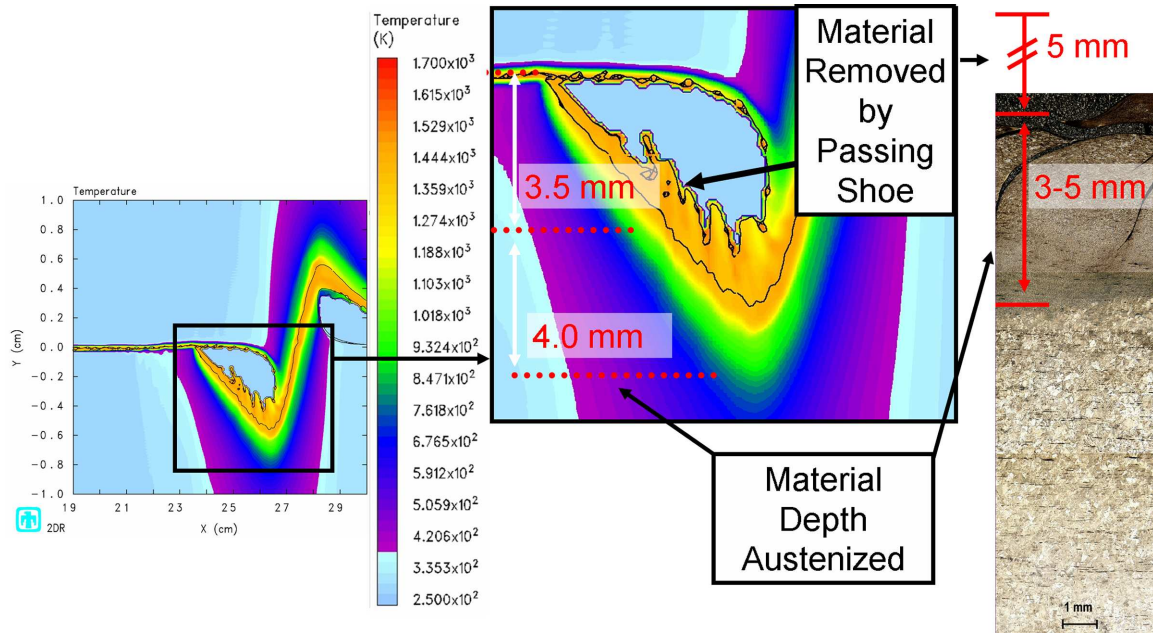
Figure 9.41:   **Example of Discontinuity with an Angled Face at 40 μseconds, Temp Profile Comparison.**

This information can be graphically presented in a manner which shows a distinct relationship between the parameters and the occurrence of gouging. Figure 9.43 shows these cases on a plot of discontinuity height versus face angle. The gouge and wear results are shown, with a threshold shown between the gouging and wearing damage cases. Because no gouging occurred below a face angle of 1.85°, that value is

Face Angle (deg)	Discontinuity (cm)	Damage
0.014	0.07	Wear
1.6	0.055	Wear
1.6	0.06	Wear
1.65	0.07	Wear
1.85	0.0635	Wear
1.85	0.07	Wear
2	0.05	Wear
2	0.06	Gouge
2	0.0635	Gouge
2	0.07	Gouge
3	0.0635	Gouge
3	0.07	Gouge
4	0.07	Gouge
5	0.035	Wear
5	0.045	Gouge
10	0.03	Wear
10	0.035	Gouge
20	0.025	Wear
20	0.03	Gouge
20	0.05	Gouge
20	0.0635	Gouge
40	0.02	Wear
40	0.025	Gouge
60	0.018	Wear
60	0.022	Gouge
60	0.035	Gouge
90	0.015	Wear
90	0.02	Gouge
90	0.03	Gouge
90	0.0635	Gouge

Figure 9.42:   **Summary of Discontinuity with an Angled Face Simulation Results.**

plotted using a dashed line. Additionally, a power-law fit is made to the wear data points and the threshold values until the angle decreases to the threshold gouging angle of 1.85°. In order to highlight the information at small angles, Figure 9.44 shows the same information, with the face angle depicted on a logarithmic scale.

Placing the current HHSTT tolerances for overall rail height variation and rail section seam discontinuity on a plot of the simulation results shows that the HHSTT is operating in the area of predicted gouging. This is illustrated in Figure 9.45. The area defined by a discontinuity below 0.0635 cm in magnitude (at any face angle) is the
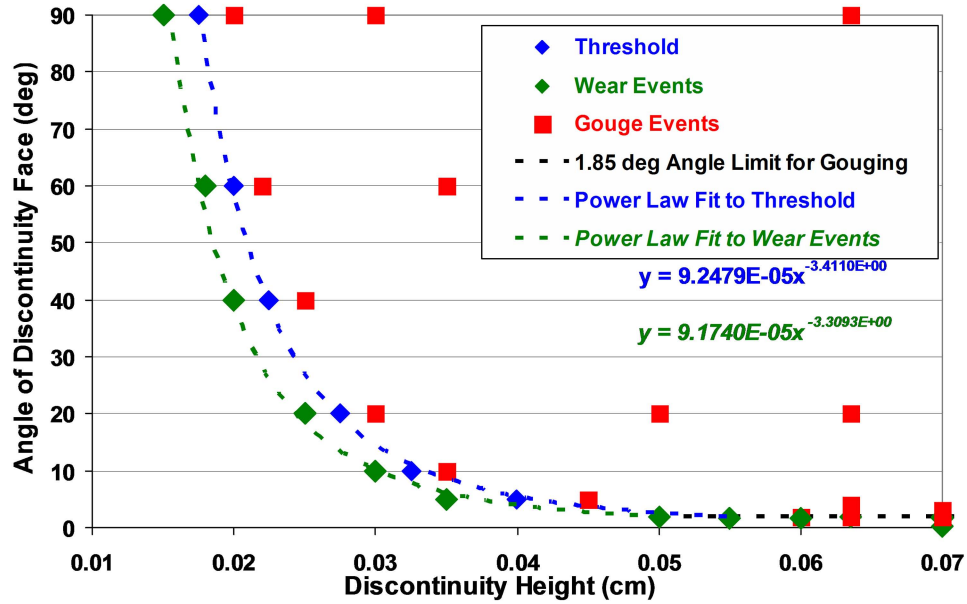
Figure 9.43: **Discontinuity with an Angled Face Simulation Results.**
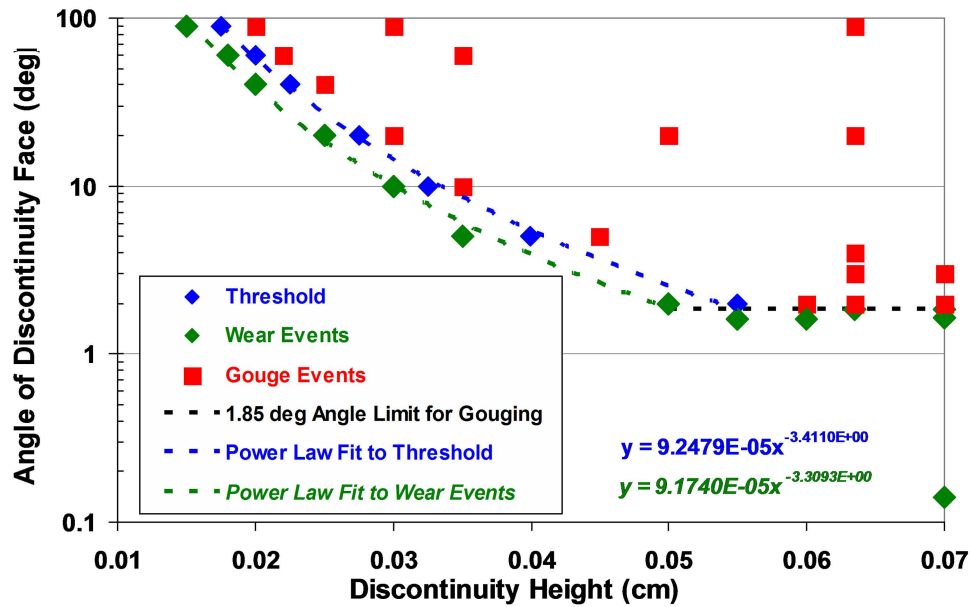
Figure 9.44: **Discontinuity with an Angled Face Simulation Results (Logarithmic Scale).**

current rail height tolerance. The area defined by an angle below 4.3° face angle and a discontinuity less than 0.19 cm represents the current rail seam tolerance. Therefore,

the HHSTT operates in these areas on Figure 9.45 that the CTH simulations show lead to hypervelocity gouging.
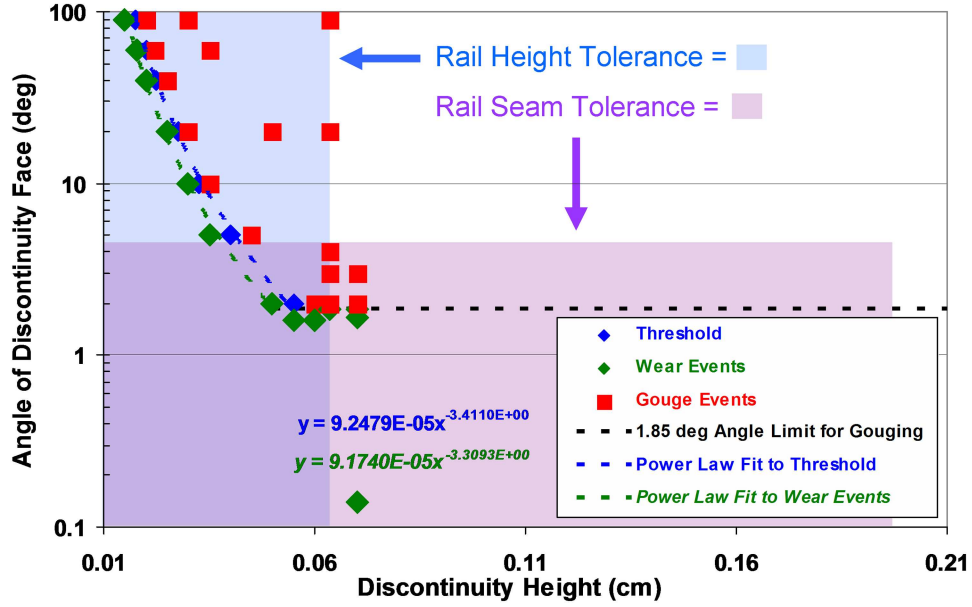
Figure 9.45: **Discontinuity with an Angled Face Simulation Results versus HHSTT Tolerances.**

This clearly indicates that the gouging experiences at the HHSTT can occur when the rail is prepared per their current rail alignment tolerances. Therefore, in order to prevent gouging in future sled run, the alignment criteria must be adjusted to remain within the zone of predicted wear. Expressed in an equational sense, and using the wear power fit results, the new criteria would be:

$$Face\ Angle\ (\text{deg}) = \max[(9.174 \cdot 10^{-5} \cdot Discontinuity\ (cm)^{-3.309}),\ 1.85°]$$
$$Face\ Angle\ (\text{deg}) = \max[(4.196 \cdot 10^{-6} \cdot Discontinuity\ (in.)^{-3.309}),\ 1.85°]$$

(9.1)

That is, the maximum allowable face angle, as a function of discontinuity height, is expressed in above. This rule can be used as the new rail alignment tolerance limit which, according to the CTH simulation predictions, would prevent the occurrence of hypervelocity gouging.

9.4.5 Summary of Rail Discontinuity Case.   In this particular gouging case, the hypervelocity gouging was initiated by discontinuities in the rail height. This is a very plausible condition at the HHSTT. Noting that the rail alignment tolerances used at the HHSTT, gouge initiation can occur within those tolerances. Additionally, the character of the gouging was a better fit to the experimental evidence presented in Chapter IV in that the material in the gouge reached the melting temperature.

9.5 HHSTT Hypervelocity Gouging Scenario Simulation Conclusions

In this Chapter, three different techniques were employed in the CTH model of the HHSTT hypervelocity gouging scenario to initiate the gouging process. The results of this study was the identification of key aspects of gouging that was evident in the metallurgical examination of rail gouges and other rail sections (see in Chapter IV).

The first was the vertical impact velocity approach. Using this technique, only when the vertical velocity was increased to levels much higher than those present in the HHSTT scenario, did gouging occur. Throughout a majority of the cases, the one-dimensional penetration theory predicted the resulting penetration depth fairly well. In the impacts that did not gouge, localized plasticity generated temperature above the austenizing temperature, but not down to the depths observed in the rail samples examined in Chapter IV. In the impacts that gouged, assuming sufficient vertical velocity was applied, the characteristics of the gouging matched the metallurgically-examined gouge from the HHSTT. A heated shoe was also modeled, which demonstrated very little difference from the unheated shoe case.

The second technique was to induce an angled impact. When the maximum allowable angle (i.e. possible without shoe structural failure) was applied to a flat rail, no gouging occurred. However, if the rail was angled within the tolerances allowable for rail alignments at the section seams, a wearing type impact phenomenon generated an austenizing temperature profile down to 1 mm into the rail - which matches fairly closely to the in-service rail sections examined in Chapter IV. Hypervelocity gouging

was created by increasing the incidence angle beyond the nominal maximum for a flat rail, but also within the seam tolerances at the HHSTT. This gouge also matched well to the HHSTT gouge.

The final approach used was to establish a rail discontinuity and allow the shoe to run into it. Rail discontinuities well below the rail alignment tolerances created gouging. However, at the discontinuity value equal to the coating thickness, no gouging occurred - but a wearing type impact generated austenizing temperatures that could explain the microstructural variations observed in the in-service rails examined in Chapter IV. When the discontinuities were increased, gouging on the order of that evaluated from the HHSTT gouge was observed - including material melting and austenizing temperatures into the depth of the rail that matched measured values. Additionally, an extensive study of various discontinuities and face angles resulted in the description of a gouging limit that could be used to prevent gouging at the HHSTT.

In making a judgment concerning which scenario is the most plausible, aside from the fact that the gouging only occurs in the first case when the simulation conditions exceed the normal limits of a sled run, one can look at the gouges themselves. In comparing the shape of the generated gouge, the amount of shoe material deposited in the rail, and the creation of melted material in the gouge, the rail discontinuity case creates better results. Figure 9.46 illustrates this comparison. The gouges represent the best matches from each case to the HHSTT gouge (from Chapter IV) and have only been altered to make the gouges in the correct aspect ratio and the same length in the diagram.

The first two techniques generate gouges which leave too much shoe material in the rail material, and which do not match the gouge shape reported in the literature. The rail discontinuity case, however, matches all aspects of the experimentally examined gouge more closely - including the shape.
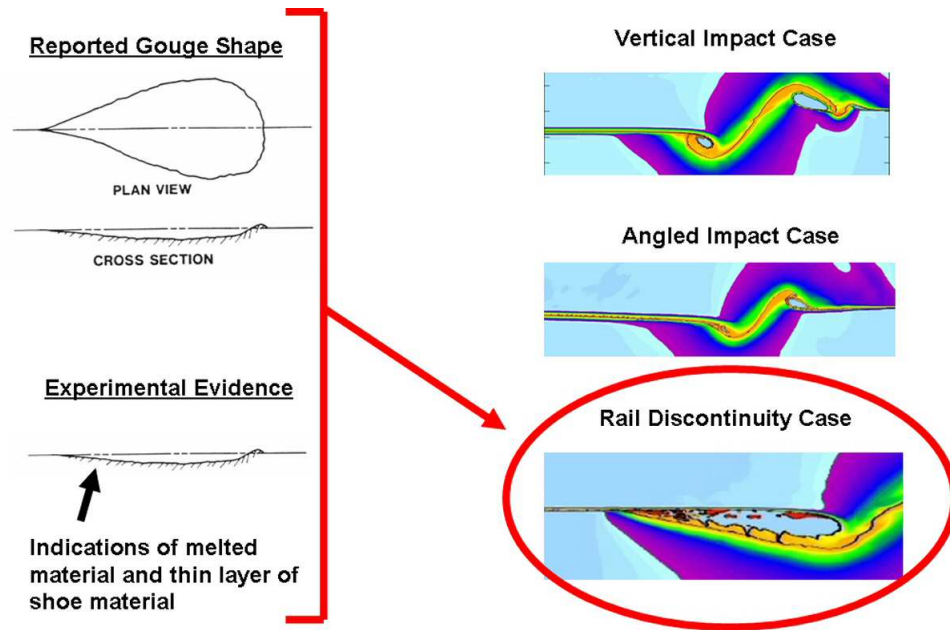
Figure 9.46:   **Comparison of Gouge Characteristics.**

Based on the study performed in this Chapter, it is clear that the gouges being created during the HHSTT sled runs are most likely rail discontinuity induced. These gouges occur with the validated CTH model, using the newly developed material constitutive models, and rail alignments below the HHSTT tolerances. Therefore, in order to avoid gouging on the rail, the discontinuities must be reduced to below the limits described in Equation 9.1.

X. Conclusions

This study examined the phenomenon of hypervelocity gouging and resolved several of the limitations of previous efforts in the field. Through a rigorous experimental process, material models were developed and validated against observed results. A computational model was created that captures the non-linear nature of the constitutive models and the non-equilibrium thermodynamic nature of the equation of state. A full range strain-rate material flow model was shown to generate results that match experimentation. This model was applied to the HHSTT gouging problem, and observations were made on the origin of the damage and nature of its development.

10.1 Review of Previous Research in the Field

A summary of the past research efforts in the field of hypervelocity gouging revealed several shortcomings and illuminated the direction that further investigations should take. In order to span the wide number of approaches to this phenomenon, this study acknowledged both the analytical and experimental nature of the endeavor and successfully joined them in a single work.

One of the primary avenues available in the effort to analyze and model hypervelocity gouging is the experimental evidence from the HHSTT. While instrumenting a gouge while it occurs or purposely creating a gouging impact is not possible, many experimentally-verifiable aspects of the phenomenon can be utilized. This study, then, sought to examine the gouging problem using state-of-the-art laboratory equipment and techniques.

The inability to generate instrumented or intentional gouging on the sled track had led past investigators into the creation of laboratory experiments to create gouging. Based on the valuable nature of having a hypervelocity gouge created under measurable and controlled condition, this study created a hypervelocity gouging experiment to use as a validation of modeling efforts.

Past modeling efforts in the field have been extensive. While the most recent efforts have established an optimum computational code choice (CTH) and resulted in the simulation of gouging within the code solution, the codes were relying on inexact material constitutive models for the materials in the HHSTT scenario. Additionally, the material model for VascoMax 300 was a strain-rate independent implementation. Finally, the contact algorithms utilized were not the optimum choice for numerical stability. This study corrected those deficiencies by determining an experimentally-based material flow model for each material and validating the models with a CTH code simulation of impact events.

In this way, the review of past research efforts established the areas to focus this study in order to generate the most accurate results possible. The remainder of this Chapter will summarize each of these specific areas and highlight the conclusions available from them.

10.2 Theoretical Foundations

The theoretical foundation of this research study revolves around the manner in which the hypervelocity gouging problem can be modeled within a computational code. Central to this approach is the understanding of how these types of problems are solved.

The solution of this type of scenario within the CTH code involves dividing the problem into two regimes. In the high pressure and temperature portion of the deformation event, the material equation of state dominates the solution. CTH is able to model this in a uniquely capable manner by relying on experimentally determined material states within the code. These values capture all of the effects present in high energy deformation - including the various non-equilibrium thermodynamic effects. The EOS models used were specific to VascoMax 300 and 1080 steel.

Within the regime that is dominated by the material strength and constitutive models, the specific flow formulation is the essential element. Two primary strain-rate

dependent formulations are available within CTH that can be created from experimentation.

Finally, the material failure model was summarized. The choice selected was the most commonly used, and most accurate, for metals undergoing non-explosive deformation.

10.3 Gouge Characterization

Using experimental techniques not applied to the HHSTT gouging phenomenon previously, a gouge was rigorously examined to understand the nature of the deformation process. Additionally, various other sections of rail were examined to better understand the conditions at the HHSTT.

A hypervelocity gouge was sectioned and examined through the depth to ascertain the key aspects of hypervelocity gouging. It was immediately evident that the material had experienced a thermal pulse that had changed the material microstructure during the post-gouge cooling. Various state-of-the-art techniques were applied to the specimen and a thermal profile was determined.

The experimentally observed thermal profile was modeled using a one-dimensional heat conduction model. The model, based on the heat conduction capabilities of 1080 steel, was able to replicate the observed microstructure. Therefore, a verified thermal history was established for the gouged specimen. This served to provide a set of conditions to validate computational simulations against.

In addition to examining a hypervelocity gouge, other rail sections from the HHSTT were examined in a similar manner. For rail sections that had never been placed in service, the manufacturing technique of head hardening was discovered to be taking place. On the rail section that had been in-service at the HHSTT, microstructural changes were noted that were similar (although to a lesser extent) to the gouged specimen. One section had a "wear" type impact that "scraped" the rail

and was later painted over with coating. The other two sections had no visible damage. All of these in-service section showed the same kind of thermal pulse evidence.

This examination of the rail at the HHSTT, including a hypervelocity gouge and a wearing impact, served to create validation points to match computational simulations against.

10.4   Development of Material Constitutive Models

In order to create accurate material constitutive models for use in the gouge modeling process, a series of experimental tests were conducted. These were designed to investigate and determine of the mid-range strain-rate and high strain-rate material responses.

The Split Hopkinson Bar test (SHB) was employed to test the mid-range (10^3/sec) strain-rate material behavior. Both VascoMax 300 and 1080 steel were tested and their material dynamic yield strength was computed. With these experiments, it was possible to generate the constitutive models.

A high strain-rate experiment, the flyer impact plate, was conducted on the two materials to define the material response in the 10^4/sec to 10^5/sec strain-rate range. In order to generate the constitutive models, the flyer plate experiments were modeled within CTH – using its experimental equation of state models. The material flow models were determined in an iterative process that sought to match the stress curves measured in the flyer plate experiments. Any non-equilibrium thermodynamic effects present in the flyer experiments were being modeled by the particular equation of state model in CTH - which is based on high energy experimentation and measurement.

To create material constitutive models that matched the high strain-rate experiments and also maintained a fit to the mid-range data, the Zerilli-Armstrong model formulation was selected as the appropriate choice for use in CTH modeling.

10.5 Validation of the Constitutive Models for Mid-Range Strain-Rates

While the hypervelocity gouging problem has areas that are at high strain-rates and in the realm of equation of state computations, much of the solution occurs within the mid-range strain-rate regime. Therefore, a study was conducted to validate the new material flow models at impact in the mid-range regime.

In order to validate the Split Hopkinson Bar (SHB) tests, a finite element code model was developed using ABAQUS. This code was able to create the post-test geometry of the SHB specimens using the new Johnson-Cook constitutive model (the code could not implement the Zerilli-Armstrong formulation). At these strain-rates, the Zerilli-Armstrong and the Johnson-Cook formulations are fairly close in the estimate of flow stress.

The SHB specimens were sectioned and metallurgically examined to ascertain if their microstructure matched the flow and shear band characteristics observed in the finite element model. Those elements were experimentally verified in the deformed microstructure.

To establish a mid-range strain-rate impact experiment to validate CTH's capability to model accurately with these material models, a Taylor impact test was constructed. A series of tests with VascoMax 300 and 1080 steel projectiles were conducted and simulated within CTH. With the new material flow models, the accuracy of the results was one-half to one order of magnitude better than with the material models used by previous researchers. The material deformation was matched within 5%.

In a related effort, a series of Taylor tests were conducted with the nose of the projectile coated with the materials used at the HHSTT to mitigate gouging and another candidate coating. The impact results demonstrated that there was a relative difference in the coefficient of friction between the coatings. Epoxy was shown to be the most effective coating, especially when compared against an uncoated rail - reducing friction by 31%.

Simulations of the coated Taylor tests were conducted, and similarly good results were obtained for the coated specimens. In addition, the behavior of the coatings were replicated by CTH, validating the flow models and equation of state models for the coatings within the code.

The CTH simulation techniques, boundary conditions, and contact algorithms were discussed - based on a related study of those topics. The conclusion of that exploration was that the contact algorithm needed to be the default (no-slide) condition in CTH and that an approach used by previous investigators may lead to unstable simulation results.

10.6   Development of a Scaled Hypervelocity Impact Experiment

A laboratory hypervelocity gouging test was desired to fully validate the material flow models for modeling in CTH. This hypervelocity test would serve to provide measurable data at known condition that could be used to check the CTH simulations.

To this end, a study was performed to determine the mathematically scaled version of the HHSTT scenario within the laboratory environment. The Buckingham Pi approach was used to scale the full problem. It was found that the gun range facility available was not able to conduct experiments of the velocity and geometry desired. Therefore, an optimum test configuration was arrived at by attempting to match the Buckingham Pi parameters within the constraints of the test facility.

Based on the small number of tests available, an approach was needed to ensure gouging was created by the laboratory test. To estimate this configuration, a novel one-dimensional penetration theory was developed and applied to the gouging scenario. This theory is empirically grounded and provides a penetration depth estimate based on impact geometry. The theory was applied to the HHSTT sled gouging problem and demonstrated that it matched some of the known conditions which lead to gouging. The one-dimensional theory was then applied to the scaled hyperveloc-

ity gouging test to determine the required impact angle for the projectiles to create gouging.

The computed test configuration was utilized and a series of hypervelocity impact tests were conducted. The one-dimensional penetration theory demonstrated remarkable agreement to the various type of impacts that were generated. Additionally, gouging was created by the laboratory test and accurately predicted by the one-dimensional theory.

Finally, the gouges created by the laboratory experiment were metallurgically examined to ascertain if the same kind of thermal history witnessed in the HHSTT gouge was observed. Indeed, the microstructure of the laboratory gouges contained the same kind of changes that had been seen in the HHSTT gouge.

The hypervelocity gouging tests, then, created gouges that could be used as validation points for the CTH simulation to achieve. In addition, the thermal profiles generated by CTH would be used to match against the observed metallurgical evidence.

10.7   Validation of the Constitutive Models for High Strain-Rates

To ensure that CTH simulation results are accurate for modeling efforts in hypervelocity impact problems, the hypervelocity gouge tests were used as a validation.

A general discussion of plane-strain solutions to 3-D gouging problems was presented. This summarized a related study that demonstrated good agreement between a 2-D axisymmetric simulation in CTH to a 2-D plane strain simulation conducted to the point in time in which reflected waves would affect the area of interest.

With this 2-D plane strain implementation shown to be accurate, the laboratory hypervelocity gouge tests were modeled within CTH using the material flow models developed in this study. The CTH model was shown to match the deformation measured in the tests, as well as the temperature profile observed in the microstructure.

That is, CTH was capable of matching all the major aspects of gouging that was experimentally noted in the hypervelocity gouging tests.

Additionally, the results from the hypervelocity gouging tests were shown to match between experiment, the one-dimensional penetration theory, and CTH simulations for the cases examined. This established confidence in both the one-dimensional theory and the CTH results.

In this manner, the use of CTH to model hypervelocity impacts with the new material constitutive model was validated. The CTH simulations were able to capture the deformation of the material and the associated temperature profiles resulting from the plasticity.

10.8   Simulation of the HHSTT Gouging Scenario

Having developed a specific material constitutive model for the materials in use at the HHSTT, and establishing the accuracy of CTH simulations of hypervelocity impacts, the model of the HHSTT gouging scenario was evaluated. Similar to results from previous researchers, three major techniques are used to generate gouging impacts in CTH.

The first case examined was having the sled shoe come down with a given vertical velocity while traveling down the rail at 3 km/s. Impacts velocities on the order reported as the conditions during sled runs did not generate gouging - but did show some small amount of plasticity in the coating and did generate a small zone of localized heating beyond the austenizing temperature. In order to create gouging of the magnitude seen in the metallurgically examined gouge from the HHSTT, a much higher vertical impact velocity was required. If that velocity was applied, gouging and the associated temperature profile that matches the HHSTT gouge was created. Additionally, reducing the contact surface area of the shoe led to increased gouging. Finally, a heated shoe scenario was presented and shown to not significantly modify the overall results (out to 20 microseconds). Throughout this analysis, the

one-dimensional penetration theory matched the resulting penetration depths fairly well.

The second case studied was to create an angle of incidence between the shoe and rail at impact. This causes the leading edge of the shoe to contact the rail prior to the remainder of the shoe. Using the maximum angle of incidence allowed by the nominal shoe gap, the geometry of the test sled, and the HHSTT rail seam tolerances, the impact generated a wearing (non-gouging) impact. This wearing impact, however, generated enough local plasticity and temperature into the depth of the rail as to match the metallurgical results seen from the in-service (but visually undamaged) rail from the HHSTT. Increasing the impact angle (to one which cannot occur unless the rear shoes fail to hold the sled down on a flat rail or which can occur within the rail seam tolerances) resulted in gouging that matched the gouge examined from the HHSTT. Both the amount of damage and the generated temperature profiles matches the observed gouge characteristics.

The final case explored was the collision of the shoe into a rail discontinuity - typically the result of rail misalignment at the section end. Several rail discontinuities heights were examined. For a rail discontinuity of the nominal thickness of the coatings used at the HHSTT, the resulting impact generated a wear-type response. This impact created a temperature profile that would modify the microstructure of the rail to a depth of the magnitude seen in the in-service rails examination. Increasing the discontinuity height to 0.02 cm resulted in the type of gouging that could create the HHSTT gouge specimen. This height is only 32% of the allowable rail misalignment tolerance. This particular simulation was unique in that it also predicted the creation of melted material - which has been observed experimentally. A slightly larger misalignment height was also simulated, with similar results. A full study of varying rail discontinuity heights and face angles was conducted to determine the relationship between these parameters and the occurrence of gouging. A power-law fit was made to the threshold values which created wearing damage and prevented gouging. Current HHSTT tolerances were shown to be within the range of values that can lead

to hypervelocity gouging. Therefore, rail discontinuities that could exist in the field have been shown to create hypervelocity gouging in the CTH simulations. An new tolerance criteria was developed to ensure gouging will not occur in future test runs.

In making a judgment as to the probable cause of the hypervelocity gouging, the gouges predicted by CTH from the various techniques were compared qualitatively to the geometry seen at the HHSTT. The rail discontinuity type initiation of gouging was shown to be the most likely cause of hypervelocity gouging. In addition, the CTH model predicts gouging begins at values of rail misalignment that are within the current accepted tolerance standards at the HHSTT.

10.9   Concluding Remarks

In this study, several advances were made in the field of understanding and modeling hypervelocity gouging.

An experimental examination of the gouges from the HHSTT led to the discovery of a thermal history within the gouging process. This thermal evidence was also found in rails that had not experienced visual damage. The ability of the rail steel to conduct the plastically-generated heat rapidly enough to create the observed microstructures was verified.

A series of experimental tests were conducted to formulate the constitutive models for VascoMax 300 and 1080 steel that had not been previously accomplished. These models were validated using a series of experiments at various strain-rates and conditions. Additionally, the relative effect of the HHSTT coatings on friction was shown.

A scaled hypervelocity gouging test was created that successfully recreated this type of gouging in controlled conditions. Associated with this effort, a one-dimensional penetration theory was developed that can estimate penetration depth with a minimum of material information and no additional experimentation.

The CTH modeling of hypervelocity impacts was validated. Specific gouge characteristics, such as deformation and temperature profiles, was shown to match experimental measurements. These simulations relied upon the developed material constitutive models and the embedded non-equilibrium thermodynamic-based (experimental) equation of state information.

Finally, with the validated material flow models developed for the HHSTT scenario, a CTH model was utilized to determine that a rail discontinuity is the probable cause of hypervelocity gouging and that the CTH simulation recreates major aspects of the gouging experimentally observed. A new rail alignment criteria, based on numerous simulations, is proposed that should mitigate future incidences of hypervelocity gouging.

STATE OF OHIO
JOHN
D.
CINNAMON
E-70200
REGISTERED
PROFESSIONAL ENGINEER
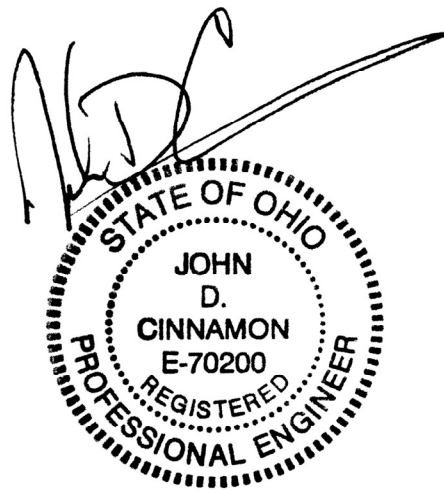
Appendix A. *Sample Scaled Hypervelocity Impact CTH Input File*

```
*eor* genin

Oblique Impact: V300/1080, v=2225, angle=10, ux=2192.2, uy=-386.37 m/s

* All output from CTHgen will have this title.
*
* This is an impact scenario of a Vascomax 300 projectile
* hitting a 1080 steel target.
*
control
  mmp3
  ep
  vpsave
endcontrol
*
*
*_____
*
mesh
  block 1  geom=2dr       type=e     * This section defines the mesh, not
                                       the cylinder or block.
                                     * 2dr = 2D rectangle (plain strain) -
                                       Use 2dc for axisymmetric.
                                     * e = Eulerian solution, the only
                                       current option

    x0=0.0                           * x0 = left starting value of x.
      x1  n=10 w=1.0  dxf=0.100      * x1,x2 = x subzone for defining
                                       different meshes along x.
      x2  n=50 w=0.5  dxf=0.010      * ALL DIMENSIONS MUST BE IN cm!
      x3  n=220 w=1.1 dxf=0.005      * n = # of cells; w = section width;
      x4  n=40 w=0.4  dxf=0.010      * dxf = dx first; dxl = dx last
                                       (optional)
      x5  n=20 w=2.0  dxf=0.100
    endx
    y0=-4.0                          * y has same inputs as x
      y1  n=20   w=2.0 dyf=0.10      * y0 = bottom starting position.
      y2  n=140  w=1.4 dyf=0.01
      y3  n=240  w=1.2 dyf=0.005
      y4  n=40   w=0.4 dyf=0.10
    endy
  endb
endmesh
*
*
*_____
*
insertion of material

  block 1
    package rod          * Insert rectangular rod and rotate
      material 1
      numsub 100
```

```
      xvel 2192.2e2       *  Change only the first number, leave 'e2'
                             this converts m/s to cm/s
      yvel -386.37e2

      insert box          *  This is where you input the cylinder.
         p1 0.0 0.0       *  Only model 1/2 of cylinder, and then
                             "mirror" in plotting.
         p2 2.225 0.55    *  Format: p1 = bottom center point of
                             cylinder
                          *  p2 = top right hand corner of cylinder.
                          *  Change p1 and p2 to define the size of rod.
      endinsert

      delete circle
         center 2.225 0.275
         radius 0.275
      enddelete
   endpackage

   package tip            *  Insert circular rod tip
      material 1
      numsub 100
      xvel 2192.2e2
      yvel -386.37e2

      insert circle
         center 2.225 0.275
         radius 0.275
      endinsert
   endpackage

   package target         *  Insert Rail Material
      material 2
      numsub 100
      insert box
         p1 0.0 -4.0
      p2 5.0 -0.02
      endinsert
   endpackage

   package coating
      material 3
      numsub 100
      insert box
         p1 0.0 -0.02
         p2 5.0 0.0
      endinsert
   endpackage

 endblock
endinsertion
*
```

```
*  _____
*
edit
  block1
  expanded
  endblock
endedit
*
*  _____
*
eos                         * Eq Of State
* Information for metals
    MAT1 SES STEEL_V300      * Sesame Eq of State tables, limited
                               material selection.
    MAT2 SES IRON            * Iron = closest material available to 1080
                               steel.
    MAT3 SES IRON            * iron oxide=MAT3 SES IRON, epoxy=MAT3 MGR
EPOXY_RESIN1
endeos

epdata                      * Elastic/Plastic data
 mix 3                      * mix 3 = normalized vol avg yield strength

    matep 1 ZE USER          * ZE coefficients for VascoMax 300.
       aze=1.42e10           * Dynes/cc
       nze=0.289
       c1ze= 4.0e10          * Dynes/cc
       c2ze=0.0
       c3ze=79.0             * 1/eV
       c4ze=3.0              * 1/eV
       c5ze=0.266e10         * dynes/cc
       poisson= 0.283

    matep 2 ZE USER          * ZE coefficients for 1080 steel.
       aze=0.825e10          * Dynes/cm^2
       nze=0.289
       c1ze=4.0e10           * Dynes/cm^2
       c2ze=0.0
       c3ze=160.0            * 1/eV
       c4ze=12.0             * 1/eV
       c5ze=0.266e10         * dynes/cc
       poisson= 0.27

    matep 3
       Yield = 0.1e8              * iron oxide=0.1e8, epoxy=0.5e7
       poisson=0.46               * iron oxide=0.46, epoxy=0.26

 vpsave
 lstrain
endep

*
```

A-3

```
*
*_____
*
*tracer
                  * Tracer input, starting at x1,y1 to ending x2,y2.
                  * n=number of tracers to distribute including
endpoints.
          * Projectile boundary
*   add 1.0 .01 to 3.0 .01 n=50
*endt
*
*
*_____
*
*eor* cthin

Oblique Impact: V300/1080, v=2225, angle=10, ux=2192.2, uy=-386.37 m/s

control               * Defines sys parameters for execution.
  mmp3                * mmp = multiple pressures and temps in mixed
material cells.
  tstop = 15.0e-6   * tstop = Problem stop time in seconds.
  cpshift=600.      * cpshift allows extra time for CTH to right data.
endc
*
*
*_____
*
Convct                         * Convection control input.
 convection=1                  * Convect internal energy based on
                                 energy density and mass
                               * density.  Discards kinetic energy.
 interface=high_resolution     * interface tracker, high_res
                                 recommended for 2D.
endc
*
*
*_____
*
fracts              * Fracture Strengh
 pfrac1=-2.2e10     * pfrac# = fracture pressure/stress of material #.
 pfrac2=-1.4e10
 pfrac3=-0.1e8      * iron oxide=-0.1e8, epoxy=-0.5e7
 pfmix=-2.0e10      * pfmix = fracture stress or pressure in cell with
                      mixed mat, no voids
 pfvoid=-2.0e10     * pfvoid = fracture press or strss in cell with
                      void.
endf
*
*
*_____
*
edit
  shortt
    tim 0.0, dt=1.0       * Restart data will be written every 'dt'
seconds.
```

```
      ends

   longt
      tim 0.0, dt=1.0          * Restart data will be written every 'dt'
seconds.
   endl

   plott
      tim 0.0 dt=0.5e-6        * cthplot data is written to restart file
every
                              * 'dt' seconds starting at 'tim'.
      endp                    * Beware - Restart file size limited to 2GB.

   histt
      tim 0.0 dt=0.5e-6      * History data will be written to hcta every
      htracer all            * 'dt' seconds.  Data will be written for all
                             * tracer points.
      endh

ende
*
*_____
*
boundary
   bhy                              * rigid boundaries all around
      bl 1
        bxb = 1, bxt = 1
        byb = 1, byt = 1
      endb
   endh
endb
*
*_____
*
vadd                                * Apply vel to keep gouge in mesh
   block=1
   tadd=0.0
   xvel=-2192.2e2
endvadd
*
*_____
*
cellthermo
 mmp3                    *  This was recommended by Eglin and appears
                         *  to give good results as well.
 ntbad 500000000
endc
*
*_____
```

Appendix B. Sample Sled Simulation CTH Input File

```
*
*eor* cgenin
*
*   cthgen input for Gouge simulation
*
*
*           _____
*           |     ----->    |
*           |       |       |
*           |       v       /
*   ---------------------------
*
*
*   vx=varies, vy=-1 m/s  V300 Steel Slider, 1080 Steel Rail, No Atm.
*   No Slide line. mix=1 frac=1 Rounded corner.
*   Added mass on top to simulate sled mass
*
 -1 m/s, 3.0 km/sec, 6 mil coating, .0020 cm mesh

control
  mmp3
  ep
  vpsave
endcontrol

*_/_/_/_/_/_/_/_/_/_/_/_/_/_/_/_/_/_/_/_/_/_/_/_/
* MESH AND BLOCK DEFINITION SET
*************************************************
*   geom=2DR(rectangular x,y)
*   geom=2DC(cylindrical x=radius, y=axis)
*   geom=3DR(rectangular x,y,z)
*   type=e (Eulerian)
*   x#=coordinate range for plot
*   y#=coordinate range for plot
*   dxf=width of first cell in the region
*   dxl=width of last cell in the region
*   n=number of cells added in this region
*   w=total width of this region in centimeters
*   r=ratio of adajacent cell widths
*_/_/_/_/_/_/_/_/_/_/_/_/_/_/_/_/_/_/_/_/_/_/_/_/
mesh
  block 1  geom=2dr      type=e
    x0=0.0000
      x1 w=15.00 dxf=5.00 dxl=0.002
      x2 w=3.000 dxf=0.0500 dxl=0.002
      x3 w=12.000 dxf=0.050 dxl=0.002
    endx
    y0=-4.000
      y1 w=2.200 dyf=0.100 dyl=0.0500
      y3 w=1.000 dyf=0.050 dyl=0.002
      y4 w=1.600 dyf=0.002 dyl=0.002
      y5 w=2.200 dyf=0.002 dyl=0.050
      y6 w=5.000 dyf=0.0500 dyl=0.100
```

```
        y7 w=35.500 dyf=0.100 dyl=10.00
      endy
    endblock
endmesh

insertion of material
  block 1

package rail
        material 2
        numsub 100
        xvel 0.0
        yvel 0.0
        insert box
        p1 0.0 -0.01
        p2 50.0 -4.0
        endinsert
endpackage


package coating
        material 1
        numsub 100
        xvel 0.0
        yvel 0.0
        insert box
        p1 0.0 0.0
        p2 21.0 -.01
        endinsert
 endpackage

package coat2
        material 1
        numsub 100
        xvel 0.0
        yvel 0.0
        insert triangle
        point 21.0 -0.01
        point 23.0 0.0635
        point 30.0 -0.01
        endinsert

        delete triangle
        point 21.1 -0.01
        point 23.0 0.04826
        point 28.5 -0.01
        enddelete
endpackage

package rail2
        material 2
        numsub 100
```

```
        xvel 0.0
        yvel 0.0
        insert triangle
        point 21.1 -0.01
        point 23.0 0.04826
        point 28.5 -0.01
        endinsert
endpackage

package shoe
        material 3
        numsub 100
        temperature = 2.53575e-2 * eV = 70F
         xvel 3.0e+5
         yvel -1.0e+2
        insert box
           p1 0.300, 0.0
           p2 20.62, 2.54

        endinsert
        delete circle
           center 20.42, 0.2
           radius 0.2
        enddelete
        delete box
           p1 20.42, 0.2
           p2 20.62, 0.0
        enddelete
     endpackage

     package sledsim
     material 4
     numsub 100
     temperature = 2.53575e-2 * eV = 70F
      xvel 3.0e+5
      yvel -1.0e+2
     insert box
       p1 0.300, 43.14
       p2 20.62, 2.54

     endinsert
     endpackage

     package sliderround
      material 3
      numsub 100
       temperature = 2.53575e-2 * eV = 70F
       xvel 3.0e+5
       yvel -1.0e+2
       insert circle
         center 20.42, 0.2
         radius 0.2
```

```
        endinsert
      endpackage
    endblock
endinsertion

edit
  block 1
  expanded
  endblock
endedit

*_/_/_/_/_/_/_/_/_/_/
* TRACER DEFINITION SET
*_/_/_/_/_/_/_/_/_/_/
*tracer
  *Target guider
*   add 20.40, -0.02 to 26.70, -0.02 n=10
  *Target slider
*   add 00.40, 0.02 to 20.40, 0.02 n=10
  *Target coating
*   add 20.40, -0.00725 to 26.70, -0.00725 n=10
  *Target slider boundary layer
*   add 00.40, 0.003 to 20.40, 0.003 n=10
endt

*_/_/_/_/_/_/_/_/_/_/_/_/_/_/
* EQUATION OF STATE DEFINITION SET
*_/_/_/_/_/_/_/_/_/_/_/_/_/_/
eos
*   MAT1 SESAME=GE1_RP EOS=7662* Reactive Graphite Epoxy
*   MAT1 MGR EPOXY_RESIN1
*   MAT1 SESAME=EPOXY EOS=7602* FEOS='seslan'
*   MAT1 SES EPOXY
    MAT1 SES GREPXY1 for epoxy
*   MAT1 SES IRON for iron oxide
    MAT2 SES IRON
    MAT3 SES STEEL_V300
    MAT4 MGR PLATINUM
endeos

epdata
  vpsave
  lstrain
  mix=3
  matep=1 *Epoxy Glider Coating
    poisson 0.46
    yield 1.0e8

  matep=2 ZE USER   * 1080 Steel rail
    aze=0.825e10     * dynes/cm^2
    nze=0.289
    c1ze=4.0e10      * dynes/cm^2
```

```
      c2ze=0.0
      c3ze=160.0          * 1/eV
      c4ze=12.0        * 1/eV
      c5ze=0.266e10    * dynes/cm^2
      poisson 0.27

   matep=3 ZE USER    * VascoMax 300 shoe
     aze=1.42e10        * dynes/cm^2
     nze=0.289
     c1ze=4.0e10        * dynes/cm^2
     c2ze=0.0
     c3ze=79.0          * 1/eV
     c4ze=3.0           * 1/ev
     c5ze=0.266e10      * dynes/cm^2
     poisson 0.283

   matep=4
     poisson .2
     yield 10e10

ende


*********************************************************************
*eor* cthin
-1 m/s, 3.0 km/sec, 6 mil coating, .0020 cm mesh

*_/_/_/_/_/_/_/_/_/_/_/_/_/_/_/_/_/_/_/_/_/_/_/_/_/_/
*CONTROL DATA SET
*********************************************************
*  mmp enables multiple material temps
*  and pressures in mixed cells
*  frac=1 changes fracture default
*******************************
* CELL THERMODYNAMICS INPUT SET
*******************************
* cellthermo
*  dtmax = max temp difference allowed in mixed cells
*  mmp distributes volume and energy based on volume
*  fractions of material in the cell
*  mmp=default
*  mmp1=same as mmp except uses new logic
*        and distributes volume and energy
*        based on volume fraction cubed divided
*        by mass of material in the cell
*  mmp2=allocation of work done on the cell is
*        dependent on material compressibility
*        and allows pressure relaxation between materials
*        in a cell
*  mmp3=new default that produces best results, see manual
* endc
*_/_/_/_/_/_/_/_/_/_/_/_/_/_/_/_/_/_/_/_/_/_/_/_/_/_/
```

```
control
  mmp3
  tstop = 40.00E-6
  nscycle=55000
  rdumpf=991800.
  cpshift=600.
  ntbad=99999999
*<<<<<<<<<<<<<<<<<<<<<<<<<<<<<<
* Courant condition multiplier
*<<<<<<<<<<<<<<<<<<<<<<<<<<<<<<
  dtcourant=0.6
endc

Convct
  convection=1
  interface=high_resolution
endc

fracts
pfrac1=-1.0e8
pfrac2=-2.0e10
pfrac3=-2.5e10
pfrac4=-1.2e10
pfmix=-1.20e10
pfvoid=-1.20e10
endfracts

edit
  shortt
    time = 0.0  , dt=1.0e-6
  ends
  longt
    time = 0.0e0  , dt = 1.0
  endl
  plott
    time  0.0e-6  dtfrequency 0.5e-6
  endp
  histt
    time  0.0e-6  dtfrequency 0.5e-6
    htracer all
  endhistt
ende

*_/_/_/_/_/_/_/_/_/_/_/_/_/_/_/_/_/_/_/_/_/_/_/_/_/_
* Hydrodynamic Boundary Conditions
************************************************************
* 0=symmetry
* 1=sound speed based absorbing
* 2=extrapolated pressure with no mass allowed to enter
* 3=extrapolated pressure but mass is allowed to enter
*_/_/_/_/_/_/_/_/_/_/_/_/_/_/_/_/_/_/_/_/_/_/_/_/_/_
```

```
boundary
  bhydro
    block 1
      bxbot = 1 , bxtop = 1
      bybot = 1 , bytop = 1
    endb
  endh
endb

*_/_/_/_/_/_/_/_/_/_/_/
* Heat conduction inputs
*_/_/_/_/_/_/_/_/_/_/_/_
*heatconduction
*   MAT1 TABLE=3
*   MAT2 TABLE=1
*   MAT3 TABLE=2
*endh

*   DEFTABLE=1 * 1080 STEEL
  *T(eV)    k(erg/s/eV/cm)
*   1.4684e-3 4.7700e10
*   1.0377e-2 4.8100e10
*   1.9090e-2 4.5200e10
*   2.7900e-2 4.1300e10
*   3.6711e-2 3.8100e10
*   4.5521e-2 3.5100e10
*   5.4332e-2 3.2700e10
*   6.3142e-2 3.0100e10
*   7.1953e-2 2.4400e10
*   8.9574e-2 2.6800e10
*   1.1111e-1 3.0100e10
*   endd

*   DEFTABLE=2 * VascoMax 300 Steel
  *T(eV)    k(erg/s/eV/cm)
*   3.6711e-3 2.4715e10
*   1.4684e-2 2.7424e10
*   2.9369e-2 2.9794e10
*   3.9158e-2 3.0132e10
*   endd

*   DEFTABLE=3 * Epoxy
  *T(eV)    k(erg/s/eV/cm)
*   3.6711e-3 6.5e8
*   1.4684e-2 6.5e8
*   2.9369e-2 6.5e8
*   3.9158e-2 6.5e8
*   endd

*_/_/_/_/_/_/_/_/_/_/_/_/_/_/_/_/_/
* Added velocity to maintain gouging in view
*_/_/_/_/_/_/_/_/_/_/_/_/_/_/_/_/_/
```

```
*vadd
*   block=1
*   tadd=0.0
*   xvel=-1.08333e+5
*endvadd

*mindt
*   time=0.  dt=1.e-12
*endn
maxdt
    time=0.  dt=.01
endx

cellthermo
mmp3
endc
```

Bibliography

1. Abrahamson, G.R. and J.N. Goodier. "The Hump Deformation Preceding a Moving Load on a Layer of Soft Material". *Journal of Applied Mechanics*, (61-APMW-5), 1961.

2. Abu-Al-Rub, Rashid K. and George Z. Voyiadjis. "Analytical and Experimental Determination of the Material Intrinsic Length Scale of Strain Gradient Plasticity Theory from Micro- and Nano-Indentation Experiments". *International Journal of Plasticity*, 20(6), 2003.

3. Allvac, Inc. "Technical Data Sheet", 2020 Ashcraft Ave, PO Box 5030, Monroe NC 28110, www.allvac.com, 2005.

4. Anderson, Charles F. "An Overview of the Theory of Hydrocodes". *Intenational Journal of Impact Engineering*, 5:33–59, 1987.

5. Anderson, John D. Jr. *Modern Compressible Flow: with Historical Perspective*. McGraw-Hill, Inc., New York, 2 edition, 1990.

6. Anderson, John D. Jr. *Hypersonic and High Temperature Gas Dynamics*. AIAA, Reston, VA, 2000.

7. Barber, J. R. and M. Ciavarella. "Contact mechanics". *International Journal of Solids and Structures*, 37:29–43, 2000.

8. Barber, John P. and David P. Bauer. "Contact Phenomena at Hypervelocities". *Wear*, 78:163–169, 1982.

9. Barenblatt, Dr G. I. "Private Communication concerning scaling the HH-STT problem", 5-11 November Orlando, FL, 2005. 2005 ASME International Congress.

10. Barenblatt, G. I. *Dimensional Analysis*. Gordon and Breach Science Publishers, New York, 1987.

11. Barker, L.M., T.G. Trucano, and L.W Munford. *Surface Gouging by Hypervelocity Sliding Contact*. Technical Report SAND87-1328, Sandia National Laboratories, Albuquerque, NM, September 1987.

12. Barker, L.M., T.G. Trucano, and A.R. Susoeff. "Railgun Rail Gouging by Hypervelocity Sliding Contact". *IEEE Transactions on Magnetics*, 25(1):83–87, 1988.

13. Benson, D. J. "Computational Methods in Lagrangian and Eulerian Hydrocodes". *Computer Methods in Applied Mechanics and Engineering*, 99:235–394, 1992.

14. Blomer, Mark A. *An Investigation for an Optimum Hypervelocity Rail Coating AFIT/GAE/ENY/05-J01*. Master's thesis, Air Force Institute of Technology, Wright-Patterson AFB, OH, May 2005.

15. Boehman, L.I., J.P Barker, and H.F. Swift. *Simulation of Friction, Wear, Anti Gouging for Hypersonic Guider-rail System*. Technical report, Arnold Engineering Development Center (PMP), November 1977.

16. Bowden, F.P. and E.H. Freitag. "The Friction of Solids at Very High Speeds". *Proceedings of the Royal Society, series A*, 248:350–367, March 1958.

17. Broek, David. *Elementary Engineering Fracture Mechanics*. Kluwer Academic Publishers, Dordrecht, The Netherlands, 4th edition, 1986.

18. Cengel, Yungas A. and John M. Cimbala. *Fluid Mechanics: Fundamentals and Applications*.

19. Cinnamon, J. D., S. E. Jones, J. W. House, and L. L. Wilson. "A One-Dimensional Analysis of Rod Penetration". *International Journal of Impact Engineering*, 12(2):145–166, 1992.

20. Cinnamon, J. D., S. E. Jones, L. L. Wilson, and J. W. House. "Further Results on the One-Dimensional Analysis of Rod Penetration". *Proceedings of the Sixteenth Southeastern Conference on Theoretical and Applied Mechanics*. SECTAM XVI, May 1992.

21. Cinnamon, John D. *Further One-Dimensional Analysis of Long-Rod Penetration of Semi-Infinite Targets*. Master's thesis, Department of Aerospace Engineering, University of Texas at Austin, Austin, TX, July 1992.

22. Cinnamon, John D. *Further One-Dimensional Analysis of Long-Rod Penetration of Semi-Infinite Targets*. Technical Report AFIT/CI/CIA-92-086, Air Force Institute of Technology, Wright-Patterson AFB, OH, 1992.

23. Cinnamon, John D. and S. E. Jones. "An Analysis of Rod Penetration of Semi-Infinite Targets Using an Average Pressure Estimate". *Proceedings of the ASME Pressure Vessel and Piping Conference*, 394:19–35, 1999.

24. Cinnamon, John D., S. E. Jones, Joseph C. Foster, and Peter P. Gillis. "An Analysis of Early Time Deformation Rate and Stress in the Taylor Impact Test". *Proceedings of the Sixth International Conference on the Mechanical Behavior of Materials*, 1:337–342, 1991.

25. Cinnamon, John D., S. E. Jones, J. W. House, and W. K. Rule. "Validating the High Strain-Rate Strength Estimates Generated from High-Speed Film Data and a Revised Elementary Theory for the Taylor Impact Test". *Proceedings of the ASME Pressure Vessel and Piping Conference*, 1:343–348, 2000.

26. Cinnamon, John D. and A. N. Palazotto. "Validation of a General Approximation for Impact Penetration Depth Considering Hypervelocity Gouging Data". *Journal of Applied Mechanics*, 1–12, Submitted for publication, 2006.

27. Cinnamon, John D., A. N. Palazotto, A. G. Szmerekovsky, and R. J. Pendleton. "Investigation of a Scaled Hypervelocity Gouging Model and Validation of Material Constitutive Models". *AIAA Journal*, 1–20, In Press, 2006.

28. Cinnamon, John D. and Anthony N. Palazotto. "Metallographic Analysis and Non-Equilibrium Thermodynamics for Hypervelocity Gouging". *Dayton-Cincinnati Aerospace Science Symposium*. AIAA, April 2005.

29. Cinnamon, John D. and Anthony N. Palazotto. "Metallographic Examination of Thermal Effects in Hypervelocity Gouging". *Proceedings of the 2005 ASME Pressure Vessels and Piping Division Conference*. ASME - Paper PVP2005-71613, July 2005.

30. Cinnamon, John D. and Anthony N. Palazotto. "Analysis of Hypervelocity Gouges Considering Non-Equilibrium Thermodynamics". *Dayton-Cincinnati Aerospace Science Symposium*. AIAA, April 2006.

31. Cinnamon, John D. and Anthony N. Palazotto. "Metallographic Examination and Validation of Thermal Effects in Hypervelocity Gouging". *ASME Journal of Pressure Vessel Technology*, 1–27, In Press, 2007.

32. Cinnamon, John D. and Anthony N. Palazotto. "Refinement of a Hypervelocity Model for the Rocket Sled Test". *Proceedings of the 2005 ASME International Congress*. ASME-Paper IMECE2005-80004, 5-11 November Orlando, FL, 2005.

33. Cinnamon, John D., Anthony N. Palazotto, and N. S. Brar. "Further Refinement of Material Models for Hypervelocity Gouging Impacts". *47th AIAA/ASME/ASCE/AHS/ASC Structures, Structural Dynamics, and Materials Conference*. AIAA, May 2006.

34. Cinnamon, John D., Anthony N. Palazotto, and Z. Kennan. "Material Characterization and Development of a Constitutive Relationship for Hypervelocity Impact of 1080 Steel and Vascomax 300". *Proceedings of the 2005 Hypervelocity Impact Symposium, International Journal of Impact Engineering*. October, In Press, 2005.

35. Cinnamon, John D., Anthony N. Palazotto, Z. Kennan, N. S. Brar, and D. Bajaj. "Johnson-Cook Strength Model Constants for VascoMax 300 and 1080 Steels". *14th APS Topical Conference on Shock Compression of Condensed Matter*. American Physical Society, July In Press, 2005.

36. Cinnamon, John D., Anthony N. Palazotto, Andrew G. Szmerekovsky, and Ronald J. Pendleton. "Further Investigation of a Scaled Hypervelocity Gouging Model and Validation of Material Constitutive Models". *47th AIAA/ASME/ASCE/AHS/ASC Structures, Structural Dynamics, and Materials Conference*. AIAA, May 2006.

37. Cook, William H. *2D Axisymmetric Lagrangian Solver for Taylor Impact with Johnson-Cook Constitutive Model*. Technical Report AFRL-MN-EG-TR-2000-7026, Air Force Research Laboratory, Eglin AFB, FL, 2000.

38. Davis, J. R. (editor). *Metals Handbook. ASM International. Desk Edition.* ASM, second edition, 1998.

39. George T. (Rusty) Gray, III. *Methods in Materials Research*, chapter High Strain-Rate Testing of Materials: The Split Hopkinson Bar. John Wiley and Sons, Inc., New York, Oct., 1987.

40. Gerstle, F.P. *The Sandia Rocket Sled Rail and Slipper Study.* Technical report, Sandia National Laboratories, Albuquerque, NM, 1968.

41. Gerstle, F.P. *Deformation of Steel During High Velocity Unlubricated Sliding Contact.* Ph.D. thesis, Duke University, 1972.

42. Gerstle, F.P., P.S. Follansbee, G.W. Pearsall, and M.L. Shepard. "Thermoplastic Shear and Fracture of Steel During High-Velocity Sliding". *Wear*, 24:97–106, 1973.

43. Goldman, Lee. "Steely Dan". *Forbes Magazine*, 12–13, December 23, 2002.

44. Graff, Karl F. and Berndt B. Dettloff. "The Gouging Phenomenon Between Metal Surfaces at Very High Speeds". *Wear*, 14:87–97, 1969.

45. Graff, Karl F., Berndt B. Dettloff, and H.A. Bolbulski. *Study of High Velocity Rail Damage.* Technical Report AA27 F29600-67-C-0043, Air Force Special Weapons Center, Kirtland AFB, NM, August 1970.

46. Hanagud, Sathyanaraya. "Thermomechanics of Impact and Penetration of Metallic Projectile into Isotropic and Granular Media", October 2002. A presentation to Drs. Mook, Hughes, and Palazotto at AFIT.

47. Hertel, E. S., R. L. Bell, M. G. Elrick, A. V. Farnsworth, G. I. Kerley, J. M. McGlaun, S. V. Petney, S. A. Silling, P. A. Taylor, and L. Yarrington. "CTH: A Software Family for Multidimensional Shock Physics Analysis". *Proceedings of the 19th International Symposium on Shock Waves*, 1.

48. Hooser, Dr Michael. "Simulation of a 10,000 Foot per Second Ground Vehicle". *21st AIAA Advanced Measurement Technology and Ground Testing Conference*, AIAA 2000-2290. AIAA, Denver, CO, 2000.

49. Hooser, Dr Michael. "Dynamic Design and Analysis System simulations", 2001. Unpublished data from Holloman AFB, NM.

50. Hooser, Dr Michael. "HHSTT Track Tolerances", 2006. Unpublished data from Holloman AFB, NM.

51. House, J. W. *Taylor Impact Testing.* Technical Report AFATL-TR-89-41, Air Force Armament Laboratory, Eglin AFB, FL, 1989.

52. Hoyt, Samuel L. (editor). *Metals Properties.* ASME Handbook, McGraw-Hill, New York, 1st edition, 1954.

53. Jiang, Tianci, Xia Lu, and Sathya V. Hanagud. "Time-Dependent Penetration Model for High-Velocity Impact & Penetration: Phase Transition Studies". *46th AIAA/ASME/ASCE/AHS/ASC Structures, Structural Dynamics, and Materials Conference*. AIAA, April 2005.

54. Johnson, Gordon R. and William H. Cook. "A Constitutive Model and Data for Metals Subjected to Large Strains, High Strain Rates, and High Temperatures". Proceedings of the 7th International Symposiumon Ballistics, 541–547. American Defense Preparation Organization, The Hague, Netherlands, April 1983.

55. Jones, S. E., J. A. Drinkard, W. K. Rule, and L. L. Wilson. "An Elementary Theory for the Taylor Impact Test". *International Journal of Impact Engineering*, 21:1–13, 1998.

56. Jones, S. E., P. P. Gillis, and J. C. Foster. "On the Penetration of Semi-Infinite Targets by Long Rods". *Journal of the Mechanics and Physics of Solids*, 35(121), 1987.

57. Jones, S. E., R. B. Marlow, J. W. House, and L. L. Wilson. "A One-Dimensional Analysis of the Penetration of Semi-Infinite 1100-0 Aluminum Targets by Rods". *International Journal of Impact Engineering*, 14(1-4), 1993.

58. Jones, S. E., Paul J. Maudlin, and J. C. Foster. "Constitutive Modeling Using the Taylor Impact Test". *High Strain Rate Effects on Polymer, Metal and Ceramic Matrix Composites and Other Advanced Materials*, 48:161–166, 1995.

59. Karpp, Robert R. *Progrees in Astronaitics and Aeronautics*, volume 155, chapter Warhead Simulation Techniques: Hydrocodes, 223–313. AIAA, 1993.

60. Kennan, Zachary. *Determination of the Constitutive Equations for 1080 Steel and VascoMax 300 AFIT/GAE/ENY/05-J05*. Master's thesis, Air Force Institute of Technology, Wright-Patterson AFB, OH, May 2005.

61. Kerber, M. W., S. E. Jones, C. A. Fisher, and L. L. Wilson. "Penetration and Cratering of Semi-Infinite Targets by Long Rods". *Proceedings of the 12th International Symposium on Ballistics*. 1990.

62. Korkegi, R.H and R.A Briggs. *Aerodynamics of Hypersonic Slipper Bearing*. Technical Report ARL 68-0028, Aerospace Research Laboratory, 1968.

63. Korkegi, R.H and R.A Briggs. "The Hypersonic Slipper Bearing - A Test Track Problem". *Journal of Spacecraft*, 6(2):210–212, February 1969.

64. Krupovage, Daniel J. and Hans J. Rasmussen. *Hypersonic Rocket Sled Development*. Technical Report JON:99930000, High Speed Test Track Facility, 6585th Test Group, Holloman AFB, NM, September 1982.

65. Krupovage, D.J. "Rail Gouging on the Holloman High Speed Test Track". *35th Meeting of the Aeroballistic Range Association*. 6585th Test Group, Test Track Division, Holloman AFB, NM, 1984.

66. Laird, D and A Palazotto. "Effects of Temperature on the Process of Hypervelocity Gouging". *AIAA Journal*, 41(11):2251–2260, 2003.

67. Laird, D and A Palazotto. "Gouge development during hypervelocity sliding impact". *International Journal of Impact Engineering*, 30:205–223, 2004.

68. Laird, David J. *The Investigation of Hypervelocity Gouging AFIT/DS/ENY 02-01*. Ph.D. thesis, Air Force Institute of Technology, Wright-Patterson AFB, OH, March 2002.

69. Laird, David J. and Anthony N. Palazotto. "Temperature Effects on the Gouging and Mixing of Solid Metals During Hypervelocity Sliding Impact". *43rd AIAA Structures, Structural Dynamics, and Materials Conference*. Denver, CO, April 2002.

70. Laird, David J., Anthony N. Palazotto, and Michael D. Hooser. "High Speed Test Track Slipper/Rail Gouging Phenomena Simulations". *Thermal Hydraulics, Liquid Sloshing, Extreme Loads, and Structural Response*, 61–68, 2001.

71. van Leer, B. "Towards the Ultimate Conservative Difference Scheme IV. A New Approach to Numerical Convection". *Journal of Computational Physics*, 23:276, 1997.

72. Lindholm, U. S. "Some Experiments with the Split Hopkinson Pressure Bar". *Journal of the Mechanics of Physical Solids*, 12:317–335, 1964.

73. Lofthouse, Andrew J., Montgomery C. Hughson, and Anthony N. Palazotto. "Hypersonic Test Sled External Flow Field Investigation Using Computational Fluid Dynamics". *40th AIAA Aerospace Sciences Meeting and Exhibit*, AIAA 2002-0306. AIAA, AIAA, Reno, NV, January 2002.

74. Lu, Xia and Sathya V. Hanagud. "Dislocation-Based Plasticity at High Strain-Rate in Solids". *45th AIAA/ASME/ASCE/AHS/ASC Structures, Structural Dynamics, and Materials Conference*. AIAA, April 2004.

75. Malvern, Lawrence E. *Introduction to the Mechanics of a Continuous Medium*. Prentice-Hall, Inc., Englewood Cliffs, NJ, 1969.

76. Marsh, Stanley P. (editor). *LASL Shock Hugoniot Data*. University of California Press, Berkeley, 1980.

77. McGlaun, J.M., S.L. Thompson, and M.G. Elrick. "CTH: A Three-dimensional Shock Wave Physics Code". *International Journal of Impact Engineering*, 10:351–360, 1990.

78. Mear, M. E. and J. W. Hutchinson. "Influence of Yield Surface Curvature on Flow Localization in Dilatant Plasticity". *Mechanics of Materials*, 4:395–412, 1985.

79. Meyers, Marc André. *3.4 Plastic Waves of Combined Stress*, 77–80. John Wiley and Sons, Inc., New York, NY, 1994.

80. Meyers, Marc André. *Dynamic Behavior of Materials.* John Wiley and Sons, Inc., New York, NY, 1994.

81. Mixon, L.C. *Assessment of Rocket Sled Slipper Wear/Gouging Phenomena.* F08635-97-C-0041. Applied Research Associates, Inc., Albuquerque, NM, 1997.

82. Murphy, M. J. "Survey of the Influence of Velocity and Material on the Projectile Energy/Hole Volume Relationship". *Proceedings of the 10th International Symposium on Ballistics.* 1987.

83. Nguyen, Minh C. *Analysis of Computational Methods for the Treatment of Material Interfaces AFIT/GAE/ENY 05-M15.* Master's thesis, Air Force Institute of Technology, Wright-Patterson AFB, OH, March 2005.

84. Nguyen, Minh C., Anthony N. Palazotto, and John D. Cinnamon. "Analysis of Computational Methods for the Treatment of Material Interfaces". *46th AIAA/ASME/ASCE/AHS/ASC Structures, Structural Dynamics, and Materials Conference.* AIAA, April 2005.

85. Nicholas, T., A. M. Rajendran, and D. J. Grove. "Analytical Modeling of Precursor Decay in Strain-Rate Dependent Materials". *International Journal of Solids and Structures*, 23(12):1601–1614, 1987.

86. Nicholas, T., A. M. Rajendran, and D. J. Grove. "An Offset Yield Criterion for Precursor Decay Analysis". *Acta Mechanica*, 69:205–218, 1987.

87. Nicholas, Theodore. "Tensile Testing of Materials at High Rates of Strain". *Experimental Mechanics*, 177–185, May, 1981.

88. Nicholas, Theodore and A.M. Rajendran. *High Velocity Impact Dynamics*, chapter 3 Material Characterization at High Strain Rates, 127–296. John Wiley and Sons, Inc., New York, 1990.

89. Nicholas, Theodore and Rodney F. Recht. *High Velocity Impact Dynamics*, chapter 1 Introduction to Impact Phenomena, 1–63. John Wiley and Sons, Inc., New York, 1990.

90. Pendleton, Ronald J. *Validation of a Scaled Plane Strain Hypervelocity Gouging Model AFIT/GAE/ENY/06-M26.* Master's thesis, Air Force Institute of Technology, Wright-Patterson AFB, OH, March 2006.

91. Ramjaun, Djameel, Ichiro Kato, Kazuyoshi Takayama, and Gopalan Jagadeesh. "Hypervelocity Impacts on Thin Metallic and Composite Space Debris Bumper Shields". *AIAA Journal*, 41(8):1564–1572, 2003.

92. Ravid, M., S. R. Bodner, and I. Holoman. "Analytical Investigation of the Initial Stages of Impact of Rods on Metallic and Ceramic Targets at Velocities of 1 to 9 km/s". *Proceedings of the 12th International Symposium on Ballistics.* 1990.

93. Rickerd, Gregory S. *An Investigation of a Simplied Gouging Model AFIT/GAE/ENY 05-M19.* Master's thesis, Air Force Institute of Technology, Wright-Patterson AFB, OH, March 2005.

94. Rickerd, Gregory S., Anthony N. Palazotto, and John D. Cinnamon. "Investigation of a Simplified Hypervelocity Gouging Model". *46th AIAA/ASME/ASCE/AHS/ASC Structures, Structural Dynamics, and Materials Conference*. AIAA, April 2005.

95. Schmitz, Craig P., Anthony N. Palazotto, and Michael Hooser. "Numerical Investigation of the Gouging Phenomena within a Hypersonic Rail-Sled Assembly". *AIAA*, AIAA 2001-1191. AIAA/ASME/AHS/ASC Structures, Structural Dynamics, and Materials Conference and Exhibit, Seattle, WA, April 16-19 2001.

96. Silling, S. A. *Stability and Accuracy of Differencing Schemes for Viscoplastic Models in Wavecodes*. Technical Report SAND91-0141, 1991.

97. Silling, S.A. "Algorithm for Eulerian simulation of penetration". *Winter Annual Meeting of the American Society of Mechanical Engineers*. ASME, Anaheim, CA, 1992.

98. Silling, Stewart A. "An Algorithm for Eulerian Simulation of Penetration". *ASME New Methods in Transient Analysis*, PVP 246, AMD 143:123–128, 1992.

99. Smith, Willam F. *Structure and Properties of Engineering Alloys*. McGraw-Hill, 1981.

100. Steinberg, D. and C. Lund. "A Constitutive Model for Strain Rates from 10^{-4} to 10^{6} sec^{-1}". *Journal of Applied Physics*, 65:1528, 1989.

101. Steinberg, Daniel J. *Equation of State and Strength Properties of Selected Materials*. Technical Report UCRL-MA-106439, Lawrence Livermore National Laboratory, Livermore, CA, February 1996.

102. Steinberg, D.J., S.G. Cochran, and M.W. Guinan. "A Constitutive Model for Metals Applicable at High-Strain Rate". *Journal of Applied Physics*, 51(3):1498–1504, March 1980.

103. Susoeff, A.R. and R.S. Hawke. *Mechanical Bore Damage in Round Bore Composite Structure Railguns*. Technical report, Lawrence Livermore National Laboratory, 1988.

104. Szmerekovsky, A. G. and A. N. Palazotto. "Structural Dynamics Considerations for a Hydrocode Analysis of Hypervelocity Test Sled Impacts". *American Institute of Aeronautics and Astronautics (AIAA) Journal*, (In Press), 2006.

105. Szmerekovsky, A. G., A. N. Palazotto, and W. P. Baker. "Scaling Numerical Models for Hypervelocity Test Sled Slipper-Rail Impacts". *International Journal of Impact Engineering*, 32(6):928–946, 2006.

106. Szmerekovsky, A. G., A. N. Palazotto, and M. R. Ernst. "Numerical Analysis for a Study of the Mitigation of Hypervelocity Gouging". *45th AIAA/ASME/ASCE/AHS/ASC Structures, Structural Dynamics, and Materials Conference*. AIAA, April 2004.

107. Szmerekovsky, A. G., A. N. Palazotto, and M. R. Ernst. "Numerical Analysis for a Study of the Mitigation of Hypervelocity Gouging". *Dayton-Cincinnati Aerospace Science Symposium*. AIAA, March 2004.

108. Szmerekovsky, Andrew G. *The Physical Understanding of the Use of Coatings to Mitigate Hypervelocity Gouging Considering Real Test Sled Dimensions AFIT/DS/ENY 04-06*. Ph.D. thesis, Air Force Institute of Technology, Wright-Patterson AFB, OH, September 2004.

109. Szmerekovsky, Andrew G., Anthony N. Palazotto, and John D. Cinnamon. "An Improved Study of Temperature Changes During Hypervelocity Sliding High Energy Impact". *47th AIAA/ASME/ASCE/AHS/ASC Structures, Structural Dynamics, and Materials Conference*. AIAA, May 2006.

110. Tachau, R. D. M., C. H. Yew, and T. G. Trucano. "Gouge Initiation in High-Velocity Rocket Sled Testing". *International Journal of Impact Engineering*, 17:825–836, 1995.

111. Tachau, R.D.M., C.H. Yew, and T.G. Trucano. *Gouge Initiation in High-Velocity Rocket Sled Testing*. Technical Report SAND94-1333C, Sandia National Laboratories, Albuquerque, NM, 1994.

112. Tachau, Robert D.M. *An Investigation of Gouge Initiation in High-Velocity Sliding Contact*. Technical Report SAND91-1732, Sandia National Laboratories, Albuquerque, NM, November 1991.

113. Tarcza, K. R. and W. F. Weldon. "Metal gouging at low relative sliding velocities". *Wear*, 209:21–30, 1997.

114. Tarcza, Kenneth Robert. *The Gouging Phenomenon at Low Relative Sliding Velocities*. Master's thesis, The University of Texas at Austin, Austin, TX, December 1995.

115. Tate, A. "A Theory for the Deceleration of Long Rods after Impact". *Journal of the Mechanics and Physics of Solids*, 15(387), 1967.

116. Taylor, G. I. "The use of flat-ended projectiles for determining dynamic yield stress I. Theoretical Considerations". *Proceedings of the Royal Society of London, Series A*, 194:289, 1948.

117. United States Steel, Inc. "Technical Data Sheet", 600 Grant St., Pittsburgh PA 15219, www.ussteel.com, 2005.

118. Voyiadjis, George Z. and Farid H. Abed. "Microstructural based models for bcc and fcc metals with temperature and strain rate dependency". *Mechanics of Materials*, 37(2-3):355–378, Feb-Mar 2005.

119. Voyiadjis, George Z. and Rashid K. Abu-Al-Rub. "Gradient plasticity theory with a variable length scale parameter". *International Journal of Solids and Structures*, 42(14):3998–4029, July 2005.

9

120. Voyiadjis, George Z., Rashid K. Abu-Al-Rub, and Anthony N. Palazotto. "Non-Local Coupling of Viscoplasticity and Anisotropic Viscodamage for Impact Problems Using the Gradient Theory". *Archives of Mechanics*, 55(1):39–89, 2003.

121. Voyiadjis, George Z., Rashid K. Abu-Al-Rub, and Anthony N. Palazotto. "Thermodynamic Framework for coupling of non-local viscoplasticity and non-local anisotropic viscodamage for dynamic localization problems using gradient theory". *International Journal of Plasticity*, 20(6):981–1038, June 2004.

122. Voyiadjis, George Z. and Rashid K. Abu Al-Rub. *Non-Local Coupling of Viscoplasticity and Rate-Dependent Damage for Impact Problems*. Technical Report 1, Department of Civil and Environmental Engineering, Louisiana State University, Baton Rouge, LA, August 2002.

123. Wiffen, A. C. "The use of flat-ended projectiles for determining dynamic yield stress II. Tests on various metallic materials". *Proceedings of the Royal Society of London, Series A*, 194:300, 1948.

124. Wilson, L. L., J. W. House, and M. E. Nixon. *Time Resolvable Deformation from the Cylinder Impact Test*. Technical Report AFATL-TR-89-76, Air Force Armament Laboratory, Eglin AFB, FL, 1989.

125. Yun, Su-Jin, John D. Cinnamon, and Anthony N. Palazotto. "Further refinement and validation of a viscoplastic model for VascoMax 300 and 1080 steel considering plastic deformation characterization". *Mechanics of Materials*, 1–24, Under Review, 2006.

126. Zerilli, F. J. and R. W. Armstrong. "Dislocation-mechanics-based constitutive relations for material dynamics calculations". *Journal of Applied Physics*, 61(5):1816–1825, March 1987.

127. Zukas, J.A. *High Velocity Impact Dynamics*, chapter Survey of Computer Codes for Impact Simulation, 593–623. John Wiley and Sons, Inc., New York, 1990.

128. Zukas, Jonas A. *Introduction to Hydrocodes*. Number 49 in Studies in Applied Mechanics. Elsevier, Oxford, UK, 2004.

129. Zukas, Jonas A., Theodore Nicholas, Hallock F. Swift, Longin B. Greszczuk, and Donald R. Curran. *Impact Dynamics*. Krieger Publishing Co., Malabar, FL, 1992.

Vita

    Major John D. Cinnamon graduated with academic distinction in May of 1991 from the United States Air Force Academy with a Bachelor of Science in Engineering Sciences degree and was commissioned in the United States Air Force. He was awarded a graduate school scholarship to pursue an accelerated Master's degree program. In August of 1992, John earned a Master of Science in Engineering, Aerospace Engineering, from the University of Texas at Austin.

    Major Cinnamon was then assigned to USAF pilot training. He graduated in October of 1993 and was assigned to Dover AFB, Delaware to fly C-5 Galaxies. After achieving the rating of Aircraft Commander, he was sent back to the USAF Academy, in March 1997, as an instructor in the Department of Astronautics and to instruct Introductory Flight Training in the T-3 Firefly aircraft. In January of 1999, John was assigned to Beale AFB, California as a T-38 Talon instructor pilot. There he served as the Director of Operations Support for the Operations Support Squadron and as a T-38 evaluator pilot for the U-2 program.

    In July of 2003, Major Cinnamon was selected as the Air Force Institute of Technology's sole Central Selection Board-designated Intermediate Developmental Education (IDE) PhD student for the inaugural IDE program. He was directed to attend the Air Force Institute of Technology for a PhD in Aerospace Engineering. In April of 2005, John earned his Professional Engineering License from the State of Ohio.

    Major Cinnamon is a Senior Pilot in the USAF with over 2600 hours of flight time in the C-5, T-3, T-37, and T-38. Major Cinnamon has pursued research in the field of high energy material deformation, penetration mechanics, and materials characterization for many years and has several technical publications in that field.

REPORT DOCUMENTATION PAGE

Form Approved
OMB No. 0704–0188

1. REPORT DATE *(DD–MM–YYYY)*	2. REPORT TYPE	3. DATES COVERED *(From — To)*
13–06–2006	Doctoral Dissertation	Sept 2003 — Jun 2006

4. TITLE AND SUBTITLE

Analysis and Simulation of
Hypervelocity Gouging Impacts

5a. CONTRACT NUMBER

N/A

5b. GRANT NUMBER

5c. PROGRAM ELEMENT NUMBER

6. AUTHOR(S)

John D. Cinnamon, Major, USAF

5d. PROJECT NUMBER

ENY 05-259

5e. TASK NUMBER

5f. WORK UNIT NUMBER

7. PERFORMING ORGANIZATION NAME(S) AND ADDRESS(ES)

Air Force Institute of Technology
Graduate School of Engineering and Management
2950 Hobson Way
WPAFB OH 45433-7765

8. PERFORMING ORGANIZATION REPORT NUMBER

AFIT/DS/ENY/06-01

9. SPONSORING / MONITORING AGENCY NAME(S) AND ADDRESS(ES)

AFOSR/NM
Attn: Dr. John Schmisseur
4015 Wilson Blvd, Rm 713
Arlington, VA 22203-1954

10. SPONSOR/MONITOR'S ACRONYM(S)

11. SPONSOR/MONITOR'S REPORT NUMBER(S)

12. DISTRIBUTION / AVAILABILITY STATEMENT

Approval for public release; distribution is unlimited.

13. SUPPLEMENTARY NOTES

14. ABSTRACT In this work, a summary of past and present research efforts, as well as the theoretical foundation, of hypervelocity gouging is presented. As the Holloman AFB High Speed Test Track (HHSTT) sled's speed has increased to Mach 8.5, material interactions develops which causes "gouging" - this can result in catastrophic failure. A characterization of gouging, including a thermodynamic history, is developed from an examination of a gouged rail. An extensive study is performed that determines the specific material flow models for VascoMax 300 and 1080 steel. The models are validated utilizing several experimental tests which are successfully simulated using CTH - a state-of-the-art shock wave physics hydrocode. Additionally, a penetration theory is developed which provides insight into the gouging problem using an analytic approach that does not require the use of computationally intensive codes. Based on the detailed examination of the materials and the validation of the material models within CTH, an evaluation of the HHSTT gouging phenomenon is performed. These simulations of the gouging problem replicate the experimentally observed characteristics and lead to recommendations to mitigate the occurrence of hypervelocity gouging.

15. SUBJECT TERMS

hypervelocity, gouging, impact, constitutive models, VascoMax 300, 1080 steel

16. SECURITY CLASSIFICATION OF:

a. REPORT	b. ABSTRACT	c. THIS PAGE	17. LIMITATION OF ABSTRACT	18. NUMBER OF PAGES	19a. NAME OF RESPONSIBLE PERSON
U	U	U	UU	312	Dr. Anthony N. Palazotto

19b. TELEPHONE NUMBER *(include area code)*
(937) 255–3636, ext 4599

Standard Form 298 (Rev. 8–98)
Prescribed by ANSI Std. Z39.18